Crystallography Reports, Vol. 47, No. 3, 2002, pp. 347–361. From Kristallografiya, Vol. 47, No. 3, 2002, pp. 391–405.

DIFFRACTION AND SCATTERING OF X-RAY AND SYNCHROTRON RADIATION

To the Memory of Riitta Kurki-Suonio

Indications of the Magnetic State in the Charge Distributions in MnO, CoO, and NiO. I: Para- and Antiferromagnetism of MnO[1]

Jean-Pierre Vidal*, Genevieve Vidal-Valat*,

Kaarle Kurki-Suonio, and Riitta Kurki-Suonio**†**

** Laboratoire d'Analyse Multipolaire des Repartitions de Charges Experimentales, Université Montpellier 2, 34095 Montpellier Cedex 05, France*

e-mail: jpgvidal@univ-montp2.fr

*** Physics Department, P.O. Box 9, FIN-00014 University of Helsinki, Finland*

Received May 28, 2001

Abstract—X-ray diffraction intensities from MnO and CoO were measured above and below their Néel temperatures and from NiO, below the Néel temperature. To detect possible characteristics of the paramagnetic and antiferromagnetic states of the crystals, the data were subjected to direct multipole analysis of the atomic-charge densities. For MnO, both spherical and nonspherical accumulation-of-charge densities indicate the exchange of the roles played by manganese and oxygen in the magnetic phase transition. Both spherical and nonspherical features characteristic of the ionic nature are inherent in both states. The electron counts of the density peaks correspond to Mn^{2+} and O^{1-}, with the tenth electron of O^{2-} being distributed in a wider region. In the paramagnetic state, there is an electronic Mn–Mn bond which seems to be formed due to coupling with the tenth electron of O^{2-} and builds up a three-dimensional net of the charge density with the "cages" surrounding oxygen atoms. In the antiferromagnetic state, some Mn–Mn bonds disappear, while the preserved nonspherical ionic features enhance the role of oxygen atoms in electronic coupling. *© 2002 MAIK "Nauka/Interperiodica".*

INTRODUCTION

There is a growing interest in transition-metal monoxides. The systematic study of their electronic structure can improve the understanding of the metal–oxygen chemistry, provide the basis for important corrosion research and a better understanding of the structural and electronic mechanisms necessary for their widespread use as catalysts and in various high-temperature applications.

This study is focused on three monoxides—MnO, CoO, and NiO—with the simple rock salt structure, sp. gr. *Fm3m* (n^0225). All three monoxides are insulators undergoing the transition from the paramagnetic to the antiferromagnetic state at the Néel temperatures 122, 289, and 523 K, respectively [1]. Antiferromagnetism preceding the transition into the superconducting state is characteristic of high-temperature superconductors. Therefore, the study of these compounds can clarify the role of an oxygen anion in the mechanisms of high-temperature superconductivity.

Among the above three materials, MnO is conceptually the simplest one to deal with because of the pronounced exchange splitting of a Mn^{2+} ($3d_5$) ion resulting in the division of the 3*d* level into the occupied spin-up and the empty spin-down components. The NiO oxide is certainly the most studied one, both experimentally and theoretically, of all the transition metal oxides. For several decades, it served as the benchmark system for understanding the electronic structure of transition metal compounds [2]. It was most difficult to interpret the data on CoO in terms of the common models that seemed to be appropriate for MnO and NiO.

There are numerous publications on these compounds—from the experimental studies of magnetic and dielectric properties (spectroscopic investigations of the electronic structure) and neutron diffraction studies of the magnetic structure to the theoretical treatment of the electronic structure with the use of various sophisticated models suggested to attain better agreement with the observed properties, the structure, and the review articles.

The principal magnetic susceptibilities of MnO single crystals were measured and their temperature dependences were studied in [3]. It was concluded that

† Deceased.

[1] This article was submitted by the authors in English.

the antiferromagnetic ordering consisted in the formation of ferromagnetic ⟨111⟩ sheets with antiferromagnetic stacking of the (111) planes. Srinivasan [4] reported high-resolution measurements of magnetic susceptibility near T_N in polycrystalline MnO, CoO, and NiO. Seino [5] performed ultrasonic measurements of sound velocity in an antiferromagnetic MnO single crystal. The observed discontinuities of the magnetic susceptibility and of the elastic constants c_{11} and c_{11}–c_{12} at T_N indicate the first-order phase transition.

Seehra and Helmick [6] measured the dielectric constant of MnO along the ⟨111⟩ direction. The anomaly observed below T_N was attributed to exchange striction. Seehra *et al.* [7] studied the temperature dependence of the static dielectric constant $\varepsilon_{\|}$ of MnO in the electric fields parallel and perpendicular to the spin-easy axis, but they failed to explain the signs and the magnitudes of $\varepsilon_{\|}$ and $\varepsilon_{\perp}$.

Ksendzov *et al.* [8] studied the electronic structure of MnO using the reflection spectra of chemically polished MnO crystals. Drokin *et al.* [9] studied the spectral, temperature, and relaxation characteristics of the photoconductivity of MnO single crystals and came to the conclusion that MnO is a wide-band antiferromagnetic semiconductor.

Lad and Henrich [10] studied photoemission spectra of cleaved MnO single crystals with the use of synchrotron radiation and reported data consistent with the localized Mn 3*d* orbital, which indicates that MnO is an insulator with charge transfer rather than a Mott insulator. Mochizuki *et al.* [11] studied photoluminescence in antiferromagnetic and paramagnetic MnO with the invocation of magnon processes and short-wavelength collective excitations. Fujimori *et al.* [12] used photoemission spectroscopy and obtained for MnO a high energy of *d*-charge transfer from the ligand to Mn indicating the pronounced ionic nature of Mn–O bonding.

McKay and Henrich [13] discussed the structure of valence- and conduction-band levels in NiO based on the experimental photoemission and photoabsorption of single crystals. They concluded that NiO is a Mott insulator whose insulating nature is associated with correlation effects. At the same time, Sawatzky and Allen [14] came to the opposite conclusion based on the photoemission and inverse-photoemission spectroscopy data. Hüfner *et al.* [15] studied the photoemission and inverse-photoemission spectra of thin NiO films grown on Ni substrates. On the basis of these data, the 4.0 eV optical gap in NiO was attributed to the charge-transfer transition O2*p* ⟶ Ni3*d*. Zschech *et al.* [16] studied the fluorescence yield from the photoabsorption spectra of bulk NiO. It was shown that self-absorption induces ~50% error in the coordination number. A thorough study of the optical-gap nature in NiO was performed by Hüfner [2].

New data on CoO were obtained from the studies of X-ray absorption and photoemission spectra. Kim [17] paid attention to surface contamination of CoO samples. Van Elp *et al.* [18] found that CoO is a highly correlated insulator. Okada and Kotani [19] considered the Co 2*p* core level by the methods of X-ray absorption and photoemission in CoO based on the CoO_6-cluster model.

Several theoretical studies of MnO have been undertaken both above and below the Néel temperature (118 K). Kanamori [20] indicated that antiferromagnetism can be caused by the mechanism of superexchange interactions. Mattheiss [21] made an attempt to explain the insulating properties of MnO in both antiferromagnetic and paramagnetic states by calculating energy bands. Terakura *et al.* [22] used another approach to band calculations for MnO. They stated that MnO is an insulator only in those cases where magnetization allows the existence on a particular antiferromagnetic spin structure observed experimentally. Terakura *et al.* [23] made an attempt to derive the electronic structure of insulating antiferromagnetic transition metal compounds by considering them as prototypes of a Mott insulator and using the energy band theory based on the model of local spin-density exchange and correlation.

Hugel and Carabatos [24] used the LCAO method to calculate both the valence band and the lowest conduction band of MnO. A new attempt made by Anisimov *et al.* [25] showed that the band-structure calculations with the use of the corrections for the potential of nonoccupied states provided an adequate description of the available spectral data measured for transition-metal monoxides with strong electron correlations.

Bocquet *et al.* [26] emphasized that the one-electron theory fails to describe the electronic structure of the transition-metal compounds discovered recently. Using the cluster-type charge-transfer model calculation, Bocquet *et al.* [26] managed to reproduce the core-level 2*p* X-ray photoemission spectra of a large number of transition metal oxides and sulfides, including MnO and NiO. They concluded that the basic Mott–Hubbard description of the charge fluctuations becomes invalid and that charge-transfer interactions are the most important for understanding the electronic structure of these compounds.

Nolting *et al.* [27] used the model taking into account the metal 3*d* and the oxygen 2*p* subbands, which explains the temperature-dependent electronic and magnetic properties of transition-metal oxides. They explained different properties by different interband and intraband couplings. The insulating properties require an integral number n of 3*d* electrons exceeding four, whereas antiferromagnetism is caused by $10 - n$ half-filled (exactly) 3*d* subbands and $n - 5$ completely filled subbands. This model correctly predicts the fact that MnO, CoO, and NiO are antiferromagnetic insulators.

Anisimov *et al.* [28] present a scheme for calculating photoemission spectra of transition metal oxides from first principles without any adjustable parameters.

The application of this method to NiO provided good agreement of the calculated and the experimental photoemission spectra and also their consistency with the oxygen K_α X-ray-emission spectra. They also reviewed the alternative approaches for calculating the properties of NiO.

In principle, the most direct means for obtaining the information on the magnetic structure is neutron diffraction. However, Roth [29, 30] indicated that magnetic scattering from polydomain single crystals cannot yield detailed information on the magnetic structure, because the distribution of the magnetization within the unit cell is averaged over the domains. To avoid this shortcoming, Bloch *et al.* [31] used the external mechanical stresses along the [111] direction and the external magnetic field to determine the order-parameter discontinuity in the magnetic transition in MnO.

More recently, Shaked *et al.* [32] studied the antiferromagnetic structure of MnO using high-resolution neutron diffraction from a polycrystalline MnO sample at 8 K. They found that, within the experimental resolution attained, the spin axis is perpendicular to the unique [111] direction.

Hermann-Ronzaud *et al.* [33] performed intense neutron diffraction studies on CoO samples subjected to stresses or magnetic fields to obtain monodomain crystals with the aim of analyzing the antiferromagnetic phase.

Chang *et al.* [34] studied the neutron-scattering factors of antiferromagnetic NiO using the calculations by the cluster model. The calculations took into account asphericity of the spin density around each Ni atom. The data obtained could be compared with the experiment only based on relative formfactor data for NiO. The agreement between the calculated and the experimental parameters depended mainly on the parameter nature.

A few X-ray diffraction studies of the charge densities of these compounds have been performed, but, unfortunately, so far they did not provide a better understanding of the electronic mechanism of magnetic ordering. These studies were performed mainly on the paramagnetic phases of MnO and NiO. The data obtained concern the net atomic charges and their radii.

Kuriyama and Hosoya [35] made an attempt to detect nonsphericities of the atomic charge distributions in MnO by the method of powder diffraction at room temperature. They concluded that both the Mn and O in the structure are in the state of divalent ions. Uno [36] subjected several transition metal monoxides to detailed powder-diffraction studies and tried to find evidence on superexchange atomic interactions. Meisalo and Inkinen [37] analyzed these data more thoroughly by the spherical-partitioning method and came to the conclusion that CoO behavior is essentially different from the behavior of MnO and NiO. Sasaki *et al.* [38] made a new X-ray diffraction study of spherical MnO crystals. They concluded that the ions were in doubly ionized states but were not considerably deformed in comparison with the ions in the free-atom superposition model. In view of the easy deformability of oxygen ions, this fact is a bit surprising.

Encouraged by our earlier experience in precision X-ray diffraction measurements and their direct multipole analysis (see, e.g., [39–41]), we decided to make an attempt to find the evidence of the magnetic states of these compounds by this method and, possibly, some indications to the bonding nature and the electronic mechanisms of the magnetic ordering. With this aim, we made high-accuracy X-ray diffraction measurements on MnO and CoO at 85 and 298 K and on NiO at 298 K, thus covering the antiferromagnetic phases of all three compounds and the paramagnetic phase of the first two compounds, and then performed the multipole analysis of the atomic-charge distributions.

EXPERIMENTAL

1. Sample

A stoichiometric MnO single crystal was kindly provided by the *Laboratoire de Chimie des Solides*, Université d'Orsay, France. It was synthesized by float-zone refining techniques from high-purity 5N powder. In this method, a high degree of mosaicity is provided by minimizing the extinction effect on the diffracted intensities so that the conventional extinction corrections are quite satisfactory, as was stated in [42]. Crystal stoichiometry was checked and confirmed by the optical and crystallographic methods, as is described elsewhere [43].

The crystal was cleaved several times along the (001) crystal faces. It was rather hard and, if sufficiently thin, fully optically transparent and had a bright green color, indicating both its stoichiometry and crystalline quality. The cleavage surface was perfectly smooth. Indeed, the crystalline quality is very important, whereas many studies reported in the literature were performed on poorly crystallized samples. The sample chosen for the X-ray diffraction measurements had the shape of a $0.182 \times 0.152 \times 0.114$-mm^3 parallelepiped. The as-cleaved sample was coated with plastic to avoid its oxidation. This protective film was perfectly transparent to the X-ray beam.

2. Data Collection

A precision X-ray diffraction study of MnO was carried out both above and below the Néel temperature, at 298 K for the paramagnetic phase and at 85 K for the antiferromagnetic one. The temperature was maintained within about 1 K. Neither magnetic field nor mechanical stresses were applied to the sample during X-ray diffraction measurements.

The precision X-ray diffraction measurements on magnetic polydomain crystals show that, at temperatures below the Néel point, the antiferromagnetic dis-

tortion of the NaCl-type structure is not perceptible. All the crystals studied had face-centered cubic lattices.

Roth [30] indicated that the magnetic scattering from a polydomain single crystal cannot be used in the detailed determination of the magnetic structure, since the latter is formed as a consequence of both the distribution of magnetic moments within the unit cell and the distribution of domains present in both powder and single crystal. This argument also holds for X-ray diffraction studies.

Bloch *et al.* [31] suggested avoiding this effect by applying mechanical stresses along the [111] direction, or an external magnetic field, or both. However, in this way, the magnetization of all the domains is forced along the same direction independently of lattice orientations in the domains. Therefore the results obtained are not related to the real crystalline magnetic field. Therefore, we did not apply an external field in our studies. Thus, if our results involve cubic symmetrization, the results obtained relate to the true field in the crystal and not to an artificially distorted one.

The lattice constants 4.431(2) and 4.425(2) Å for MnO at 298 and 85 K, respectively, were obtained by the least-squares refinement based on X-ray diffraction data.

Relative integrated intensities of all the reflections with $\sin\theta/\lambda$ up to about 1 $Å^{-1}$ in three octants were collected three times at both temperatures on an automated four-circle Enraf-Nonius CAD-4 diffractometer (MoK_α radiation). The data thus obtained included 26 independent reflections.

The integration was done in the θ–2θ scan mode with programmed scan and the aperture at the scanning rate of $2^\circ\ s^{-1}$. The dead-time correction was automatically taken into account by the analyzer.

The multiple-scattering effect was eliminated using different settings of the crystallographic and diffractometer axes. As a check, all the forbidden reflections were measured in the whole octant. No effect was detected.

The background, Lorentz, and polarization corrections were introduced into the intensities, as described earlier [44]. We also introduced the Busing and Levy absorption corrections [45] using the linear absorption factors 14.712 mm^{-1} and 14.772 mm^{-1} for MnO at 298 and 85 K, respectively.

The TDS contamination was evaluated by the Merisalo and Kurittu program [46] using the elastic constants from [47]. The effects were small (less than 3% in intensity) because of the high hardness of these compounds.

The observed intensity of a reflection was averaged over the intensities of all the equivalent reflections measured in three experiments.

THE REFERENCE MODEL

Our "direct multipole analysis" is based on the use of a reference model "asymptotically reliable" in the reciprocal space. As far as the condition of asymptotical reliability is fulfilled, the model itself does not affect the interpretation of the results, which can be expressed in terms of the deviations of the experimental charge-density characteristics from those of the model or, when added to the model values, in terms of purely experimental values of these characteristics [41]. In calculations of the model values, an asymptotically fitted Gaussian representation of the theoretical atomic factors can be used to account for the residual terms [48].

According to the conventional rigid-core assumption, the asymptotical reliability can be achieved within sufficient accuracy by using the current theoretical free-atom scattering factors with the appropriate atomic positions and motion parameters. For this purpose, the model should be refined to find the values of these parameters and, at the same time, to bring the observed structure factors to the absolute scale and correct them for extinction and anomalous scattering.

For Mn^{2+}, the relativistic Hartree–Fock values from the International Tables for Crystallography [49] were used and for O^{2-}, the atomic scattering factors suggested by Sanger [50] and the anomalous scattering factors $f' = 0.295$ and $f'' = 0.729$ for Mn^{2+} and $f' = 0.008$ and $f'' = 0.006$ for O^{2-} suggested by Cromer and Liberman [51] (MoK_α).

The structure factors were scaled to the fcc unit cell with four molecules with the origin of the representation being taken at the cation position. The atomic positions (0, 0, 0) and (1/2, 0, 0) for Mn^{2+} and O^{2-} are fixed by the crystal symmetry and have the cubic site symmetry *m*3*m*. Thus, we have to refine the isotropic Debye–Waller factors of the two ions.

In principle, the refinement can be performed either as a local Fourier-refinement of the difference densities at the atomic positions or as an "asymptotic" least-squares refinement of the structure factors at high $\sin\theta/\lambda$ values.

Since no procedure has been developed to include the extinction parameters in our iterative local Fourier refinement, at the first stage, we used the Linex program written by Becker and Coppens [52] to refine the extinction model together with the scale and the Debye–Waller factors.

All the possible combinations of the extinction models were tried—isotropic and anisotropic, mosaic-spread and particle-size type, with and without primary extinction. Isotropic mosaic-spread extinction gave a lower *R* factor, 0.005 and 0.004, than the particle-size extinction, 0.006 and 0.005 for MnO at 298 K and 85 K, respectively, and yielded the values $0.032(2) \times 10^4$ rad^{-1} and $0.039(2) \times 10^4$ rad^{-1} for the mosaic spread parameter *g* and $B(\mathrm{Mn}) = 0.300(16)$ $Å^2$, $B(\mathrm{O}) = 0.395(47)$ $Å^2$ and $B(\mathrm{Mn}) = 0.260(16)$ $Å^2$, $B(\mathrm{O}) = 0.379(47)$ $Å^2$, for the iso-

Table 1a. Structure factors for MnO at 298 K

h k l	2sinθ/λ, Å^{-1}	F_0	F_c	δF_0	*y*
0 0 0	0.0000		132		
1 1 1	0.3909	51.83	52.51	0.27	0.894
2 0 0	0.4514	93.21	92.99	0.41	0.704
2 2 0	0.6383	73.48	73.86	0.34	0.869
3 1 1	0.7485	39.88	40.79	0.18	0.959
2 2 2	0.7818	62.69	61.96	0.28	0.929
4 0 0	0.9027	54.41	53.80	0.22	0.953
3 3 1	0.9837	33.33	32.41	0.15	0.983
4 2 0	1.0093	47.11	47.87	0.19	0.962
4 2 2	1.1056	43.50	43.39	0.17	0.974
3 3 3	1.1727	27.71	27.11	0.14	0.991
5 1 1	1.1727	27.10	27.11	0.12	0.990
4 4 0	1.2766	37.35	37.09	0.13	0.985
5 3 1	1.3352	23.48	23.59	0.07	0.992
4 4 2	1.3541	35.45	34.79	0.18	0.987
6 0 0	1.3541	34.98	34.79	0.16	0.985
6 2 0	1.4273	32.93	32.87	0.13	0.988
5 3 3	1.4799	21.40	21.13	0.07	0.994
6 2 2	1.4970	30.69	31.22	0.12	0.990
4 4 4	1.5636	30.72	29.78	0.14	0.991
5 5 1	1.6117	19.10	19.30	0.10	0.996
7 1 1	1.6117	18.90	19.30	0.09	0.995
6 4 0	1.6274	28.37	28.51	0.09	0.990
6 4 2	1.6888	27.31	27.36	0.01	0.991
5 5 3	1.7335	17.81	17.84	0.08	0.996
7 3 1	1.7335	17.99	17.84	0.07	0.996
8 0 0	1.8055	25.22	25.36	0.10	0.993

Table 1b. Structure factors for MnO at 85 K

h k l	2sinθ/λ, Å^{-1}	F_0	F_c	δF_0	*y*
0 0 0	0.0000		132		
1 1 1	0.3914	51.97	52.59	0.30	0.874
2 0 0	0.4520	93.47	93.16	0.40	0.661
2 2 0	0.6392	74.14	74.15	0.15	0.858
3 1 1	0.7495	40.93	41.01	0.18	0.954
2 2 2	0.7828	62.89	62.36	0.30	0.914
4 0 0	0.9039	54.50	54.28	0.19	0.943
3 3 1	0.9851	33.45	32.73	0.14	0.980
4 2 0	1.0106	48.40	48.41	0.19	0.959
4 2 2	1.1071	43.69	43.99	0.18	0.968
3 3 3	1.1743	27.98	27.49	0.12	0.989
5 1 1	1.1743	27.56	27.49	0.12	0.988
4 4 0	1.2784	37.99	37.79	0.18	0.981
5 3 1	1.3370	23.54	24.04	0.10	0.992
4 4 2	1.3559	35.61	35.54	0.16	0.984
6 0 0	1.3559	35.31	35.54	0.19	0.982
6 2 0	1.4293	33.44	33.66	0.12	0.985
5 3 3	1.4819	22.38	21.63	0.11	0.994
6 2 2	1.4990	31.73	32.05	0.10	0.987
4 4 4	1.5657	30.89	30.65	0.15	0.988
5 5 1	1.6139	20.40	19.85	0.10	0.995
7 1 1	1.6139	19.33	19.85	0.10	0.995
6 4 0	1.6296	29.29	29.42	0.15	0.990
6 4 2	1.6911	28.59	28.31	0.14	0.988
5 5 3	1.7359	17.98	18.44	0.10	0.995
7 3 1	1.7359	18.52	18.44	0.09	0.996
8 0 0	1.8079	26.01	26.36	0.10	0.991

tropic Debye–Waller factors at 298 and 85 K, respectively. No more significant improvement was achieved when using any of the more sophisticated models.

The "experimental" structure factors thus obtained were then used as the initial values for a further iterative local Fourier-refinement of the scale and the Debye–Waller factors (cf. [53]). The data obtained at 298 K lead to a further change in the scale by 0.2%, while the scale factor for the data obtained at 85 K remained unchanged. The final refined values, B(Mn) = 0.305 Å^2, B(O) = 0.426 Å^2 and B(Mn) = 0.257 Å^2, B(O) = 0.368 Å^2, were adopted as the Debye–Waller factors of the reference model at 298 and 85 K, respectively.

The refinement also yields experimental structure factors F_0 on an absolute scale corrected for isotropic mosaic-spread extinction and anomalous dispersion. In what follows, these values, listed in Table 1 together with the extinction factors δF_0^2, are subjected to the multipole analysis. The uncertainties F_0 in the table are the standard errors of the mean.

To verify the nature of the residual experimental information, a number of refinement cycles of the Debye–Waller factors were performed for partial data, where the higher order reflections above different cut-off values of sinθ/λ were omitted, with the scale factor fixed at the value found with the total set of the data. It was found that, with increasing cut-off value, the thermal parameters smoothly approach their final values and remain stable beyond 0.8 Å^{-1}. This suggests that, beyond that limit, the X-ray data cannot give the deviations of the ionic formfactors from their theoretical values. Thus, the higher order reflections do not contain any further information on the electronic deformations and are not used in the subsequent multipole analysis.

RESULTS

Once the reference model has been fixed, the calculations required for the multipole analysis of atomic-charge densities can be straightforwardly performed. The principles of the analysis were considered earlier in different contexts [5, 44, 54–56]. Each *i* atom is discussed separately on the basis of the site-symmetric multipole expansion of the crystal charge-density centered at the atom site

$$\rho_i(\mathbf{r}) = \sum_n \rho_{in}(r_i) K_n(\theta, \varphi),$$

where r_i denotes the radial distance from the atomic site, and on the basis of the corresponding form factor expansion

$$f_i(\mathbf{b}; R_i) = \sum_n f_{in}(b; R_i) K_n(\theta, \varphi),$$

which is the Fourier transform of the charge-density expansion cut at a computational spherical-partitioning radius R_i of the ion. K_n are the cubic harmonics O_e corresponding to the point symmetry *m*3*m* [58], and the angular variables θ and φ refer to the local axes, which, in this case, are parallel to the axes of the cubic crystal.

Figure 1 shows the radial accumulation-of-charge densities

$$s_{i0}(r_i) = 4\pi\rho_{i0}(r_i) r_i^2$$

and the radial electron counts

$$Z_{i0}(R_i) = \int_0^{R_i} s_{i0}(r) dr$$

around the ionic sites.

Table 2 is related to Fig. 1 and gives the following spherical characteristics of the ionic charge distributions:

(1) The radii r_0 of best separation at which the radial accumulation-of-charge densities r_0 reach their minima as a measure of the size or the effective "range" of the ionic charge distribution;

(2) the corresponding minimum radial density $s_{0\min} = s_0(r_0)$ as a measure of the nonseparability of the ion from its surroundings;

(3) the electron count $Z_0 = Z_0(r_0)$ within the radius of best separation, as a measure of the charge concentrated in the main bulk of the ionic charge density peak; and

(4) the radii r_{2+} and r_{2-}, where the electron counts reach the values 23*e* and 10*e* corresponding to the doubly ionized states.

Figure 2 presents the radial multipolar scattering factors $f_{in}(b; R_i)$ as deviations from the reference model. The partitioning radii R_{Mn} = 1.25 Å and R_O = 1.30 Å were deduced on the basis of Fig. 1 and were assumed to be slightly larger than the radii r_0 of best separation [59].

Because of the normalization of the cubic harmonics to the maximum value, 1, the curves directly show the maximum contribution (to be multiplied by 4 for an fcc unit cell) of the component to the structure factors of the crystal as a function of the reciprocal-vector magnitude $b = 2\sin\theta/\lambda$. Their error bars indicate also the significance of the components with respect to the errors of the mean of the structure factors. All the components up to the 10th order were calculated. The first three nonspherical components of orders 4, 6, and 8 are of about the same significance, while the 10th-order component is insignificant and, therefore, is not shown.

For visualization and easier interpretation, the same components are also represented in real space in terms of the multipolar accumulation-of-charge densities $s_{in}(r_i) = B_n \rho_{in}(r_i) r_i^2$ around the ionic sites shown in Fig. 3. Again, the curves represent the deviations from the reference model. The normalization constants $B_n = \int_{K_n > 0} K_n(\theta, \varphi) d\Omega$ [53] ensure that the areas under the curves give the electron counts under the positive lobes of $K_n(\theta\varphi)$ within the radii R_i. These multipolar electron counts serve as nonspherical integral characteristics of the ionic charge distributions, as is indicated by the numbers in the figures.

The results are visualized in Fig. 4 in terms of difference-density maps representing the multipole expansions at the ionic sites, as composed by the components shown in Figs. 2 and 3. For each ion map, the three main lattice planes (100), (110) and (111) passing through the ionic site are shown.

For comparison, the conventional Fourier difference-density maps in the same planes are shown. Finally, views on the 3-dimensional nature of the ionic multipole expansions are shown in Fig. 5 to support the discussion of results.

DISCUSSION

The comparison of the radial densities s_0 of the reference model at two different temperatures presented by the dotted lines in Fig. 1 and by the corresponding parameters in Table 2 shows that the effect of the temperature factors on the nature of the ionic-charge distributions is negligible. Thus, the differences in the character of the experimental curves and the parameters at the two temperatures are of electronic origin and can be attributed to the differences in the magnetic states. They are evident from the deviations of the experimental curves from the reference curves in Fig. 1 and in the numerical values listed in Table 2. On a larger scale, they are shown by the Δs_0 curves in Fig. 3.

The radial density $s_0(r)$ in the region of overlap around the oxygen atom is obviously reduced in comparison with that for the reference model. The peaks are compressed and the minima are sharpened, thus improving the separation of the atoms from their sur-

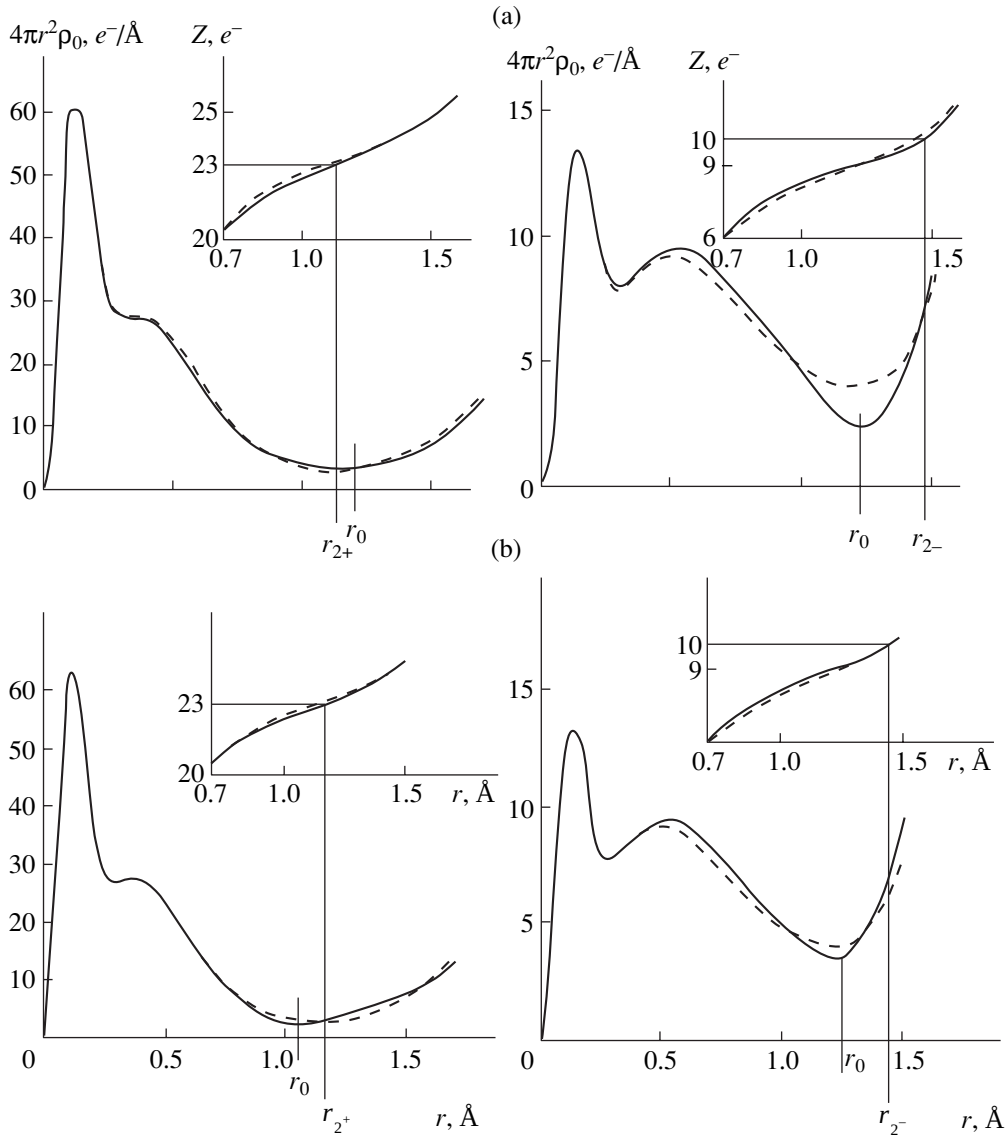

Fig. 1. Radial accumulation-of-charge densities $s_0(r)$ and electron counts $Z_0(r) = s_0(r)dr$ around the ionic sites of Mn^{2+} and O^{2-}, solid lines—experiment, dashed lines—reference model. (a) The paramagnetic state (298 K), (b) the antiferromagnetic state (85 K). The radii r_0 of the "best separation" or minimum s_0 and the radii r_{2^+} and r_{2^-}, where the electron counts corresponding to the double ionization of the ions are indicated for the experimental curves.

roundings and yielding well-defined radii of best separation of the ions from their surroundings. These features typical of ionic crystals [44, 53] are exceptionally strong in the paramagnetic state. In both states, the oxygen peak is about 9*e*, a value known for several other oxides [54, 57]. The radius r_{2^-} corresponding to the double ionization of oxygen or 10*e* is obviously larger, thus indicating that the tenth electron is distributed in a wider region between the main density peaks.

In manganese, the deviations from the reference model are of a different nature. In the antiferromagnetic state, the "ionic" sharpening of the separating minima is seen. However, it is caused by a slight expansion of the outer part of the ion. In the paramagnetic state, the minimum is flattened because of a somewhat inner expansion leading to a rather undetermined separation radius and to a higher value of the minimum density, which is more typical of covalent bonding. The electron counts indicated in Table 2 differ only because of the different radii used. In both states, the electron count of the manganese peak is very close to 23*e* corresponding to double ionization.

It should also be noted that the radial accumulation-of-charge densities at the minima are essentially higher than could be expected for an ionic crystal (cf. [54] and [44]). Manganese and oxygen in paramagnetic MnO have the highest and the least values, respectively. Both

Table 2. Spherical characteristics of the ionic electron distributions: radius r_0 of the best separation at which the radial accumulation-of-charge density $s_0(r)$ reaches its minimum; the minimum radial density $s_{0\min} = s_0(r_0)$; the electron count $Z_0 = Z_0(r_0)$ within the radius of the best separation, and the radii r_{2+} and r_{2-}, where the electron counts reach the values 23*e* and 10*e* corresponding to the doubly ionized states

Mn^{2+}	r_0	$s_{0\min}$	Z_0	r_{2+}
experiment				
298 K	1.20 Å	4.42 *e*/Å	23.34 *e*	1.12 Å
85 K	1.05 Å	3.23 *e*/Å	22.59 *e*	1.16 Å
reference model				
298 K	1.15 Å	3.57 *e*/Å	23.15 *e*	1.11 Å
85 K	1.10 Å	3.57 *e*/Å	22.97 *e*	1.10 Å
O^{2-}	r_0	$s_{0\min}$	Z_0	r_{2-}
experiment				
298 K	1.22 Å	2.61 *e*/Å	9.00 *e*	1.47 Å
85 K	1.25 Å	3.75 *e*/Å	9.21 *e*	1.45 Å
reference model				
298 K	1.20 Å	4.13 *e*/Å	8.80 *e*	1.44 Å
85 K	1.20 Å	4.20 *e*/Å	8.80 *e*	1.44 Å

these values pronouncedly change in the transition to the antiferromagnetic state, but along different directions.

The above differences indicate the exchange of the roles of the two ions as a result of the magnetic phase transition. The nonspherical radial accumulation-of-charge densities $\Delta s_n = 4.6$ and 8 in Fig. 3 throw some further light on their 3-dimensional nature.

Considering the angular behavior of the cubic harmonics schematically presented in Figs. 2 and 3 (cf. [60]), it is possible to note that at distances with positive values of $\Delta(r)$, the 4th-order component transfers electrons from the ⟨111⟩ to the ⟨100⟩ directions, the 6th-order component from the ⟨110⟩ mainly to the ⟨111⟩ and, to a somewhat lesser extent, to the ⟨100⟩ directions, while the 8th-order component collects electrons rather sharply to the ⟨100⟩ and, to some extent, also to the ⟨110⟩ directions from the intermediate directions. For negative values of $\Delta(r)$, the transfer has the opposite sense. Thus, considering the sign combinations in the inner and outer regions and comparing them, one can roughly deduce the 3-dimensional nature of the combined components to be related to the nature of the different electronic effects in two atoms in two magnetic states.

Here, the map representations in Fig. 4 give important support. However, it should be noted that, in the local map representations, only those features are significant which are significant in the angular-integral representation in Fig. 3. Thus, the difference densities at the ionic centra in any of the maps can be ignored. Similarly, no local features of the Fourier maps that are not seen in the multipolar maps in Fig. 4 can arise from the integral systematics of the low-order multipoles and, thus, can be regarded insignificant. The comparison with the multipolar maps allows us to follow how features seen in the Fourier maps originate from the electronic behavior of different atoms [41].

In paramagnetic MnO, the most striking feature is the concentration of electrons in the Mn^{2+} ion in the twelve equivalent ⟨110⟩ directions. This is clearly seen from all the maps constructed through the Mn site, because they have a common ⟨110⟩ line. In the Fourier maps, this can give rise to bondlike concentrations of electrons indicating the electronic Mn–Mn interactions between each Mn ion with its twelve Mn neighbors. This explains the flattening of the separating minimum of the radial density in Fig. 1.

The origin and nature of this formation is somewhat unclear. In the Mn multipole maps, the formation seems to be caused mainly by the electrons of the Mn ions participating in both internal and external coupling. However, it extends beyond the radius r_{2^+} of double ionization. Nevertheless, the formation is also visible in the oxygen multipole maps, which is obvious from the comparison of the multipole and the Fourier maps in the (100) and (110) planes, where it is seen to bridge the neighboring oxygen atoms. In the 3-dimensional view in Fig. 5, it appears as a cage surrounding an oxygen ion. In the periodic crystal structure, these cages build up a 3-dimensional net with a pocket for each oxygen atom. Therefore, although this formation lies beyond any reasonable separating radius, the oxygen ion probably plays a certain role in its formation. Then, some electronic Mn–O interactions should be involved. There should also be the space to hide the "lacking tenth electron" of O^{2-}.

The formation of a net structure is a parallel phenomenon to the formation of an oxygen net structure observed in beryllium oxide [5]. A closer look at the results of the multipole analysis of some other oxides [54] shows that the formation of such interatomic nets might be a more general phenomenon in oxides.

In addition, the multipole maps show the significant deformation of both ions. In oxygen, this appears as an additional concentration of electrons in the ⟨100⟩ directions. In manganese ions, the charge density is significantly reduced in these directions. These features are similar in nature to the ionic deformations observed in ionic crystals [44, 54]. While they are caused by electrostatic cation–anion interactions, they are electronically internal features of each ion.

The peak that appears on the (110) Fourier map at the empty 1/4, 1/4, 1/4 position is a local feature that cannot be attributed to any systematic integral behavior of the charge density. In integration, it is found to be an accumulation of 0.016 electrons only, i.e., is negligible. Thus, it is a typical artefact of the local Fourier representation.

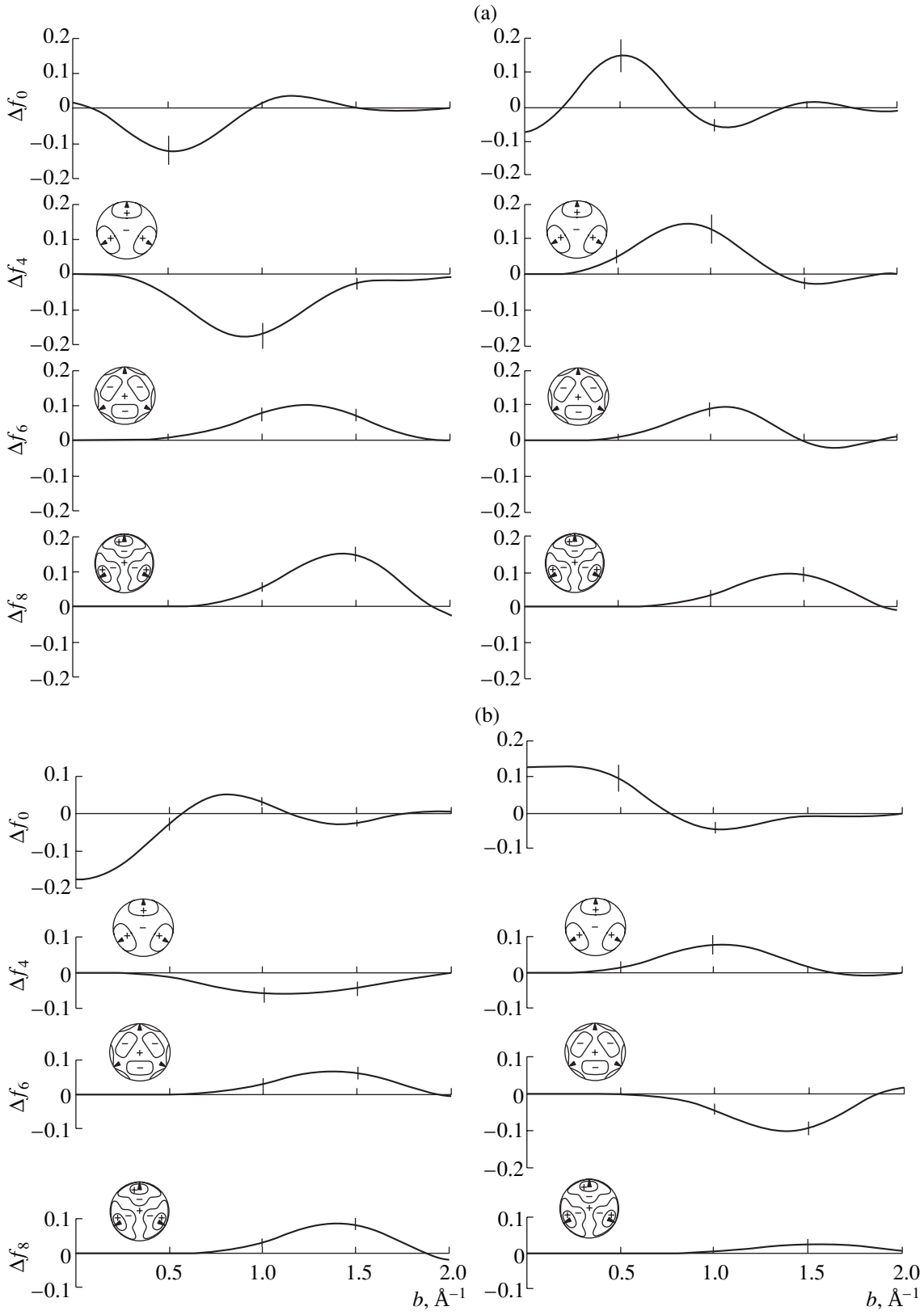

Fig. 2. Radial multipolar scattering factors of the Mn^{2+} and O^{2-} ions within the partitioning radii R_{Mn} = 1.25 Å, R_O = 1.30 Å. The results are related to cubic harmonics normalized to the maximum value $K_n(\theta\varphi) = 1$, and the curves represent the deviations Δf_n from the reference model. (a) The paramagnetic state (298 K), (b) the antiferromagnetic state (85 K).

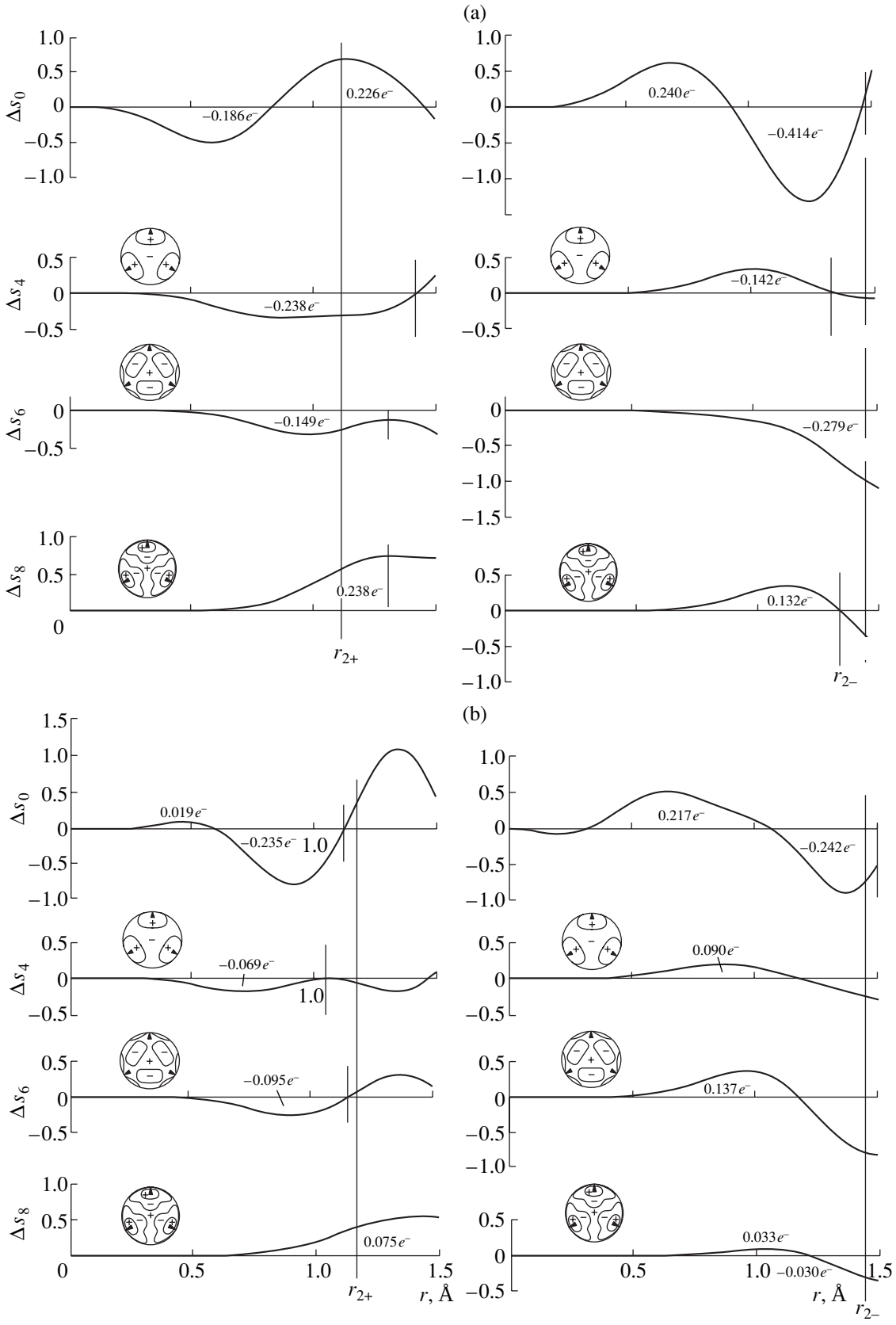

Fig. 3. Multipolar accumulation-of-charge densities $s_n(r)$ around the ionic sites of Mn^{2+} and O^{2-}. The curves represent deviations Δs_n from the reference model. (a) The paramagnetic state (298 K), (b) the antiferromagnetic state (85 K).

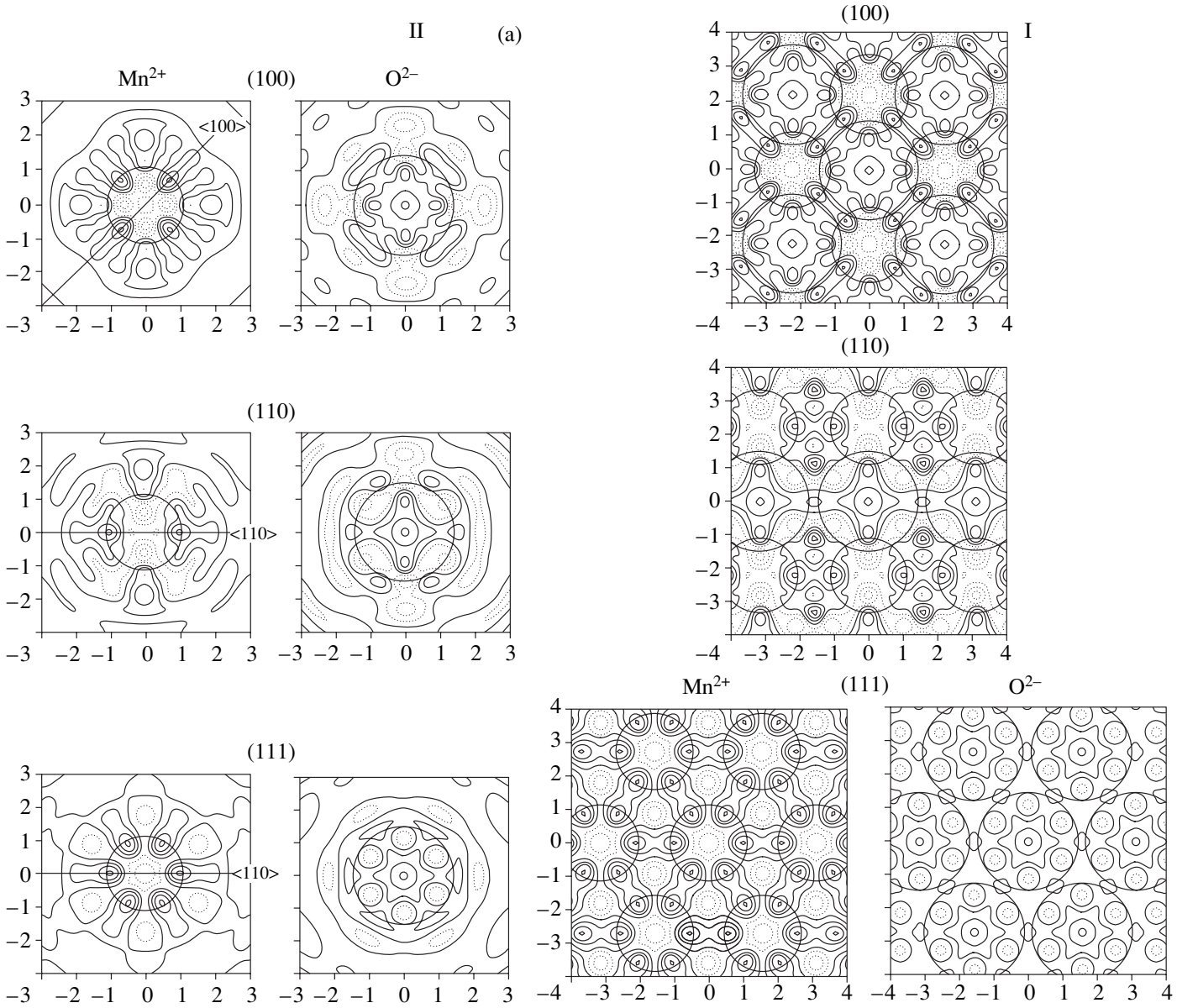

Fig. 4. Difference density maps of the multipole expansions up to $n = 8$ together with the corresponding Fourier difference-density maps on the (100), (110), and (111) planes passing through the ionic sites. Circles indicate the radii of doubly ionized ions. (a) The paramagnetic state (298 K), (b) the antiferromagnetic state (85 K). Solid lines indicate positive, dashed lines indicate negative, and dotted lines indicate zero values; the contours are spaced by 0.1 eÅ^{-3}.

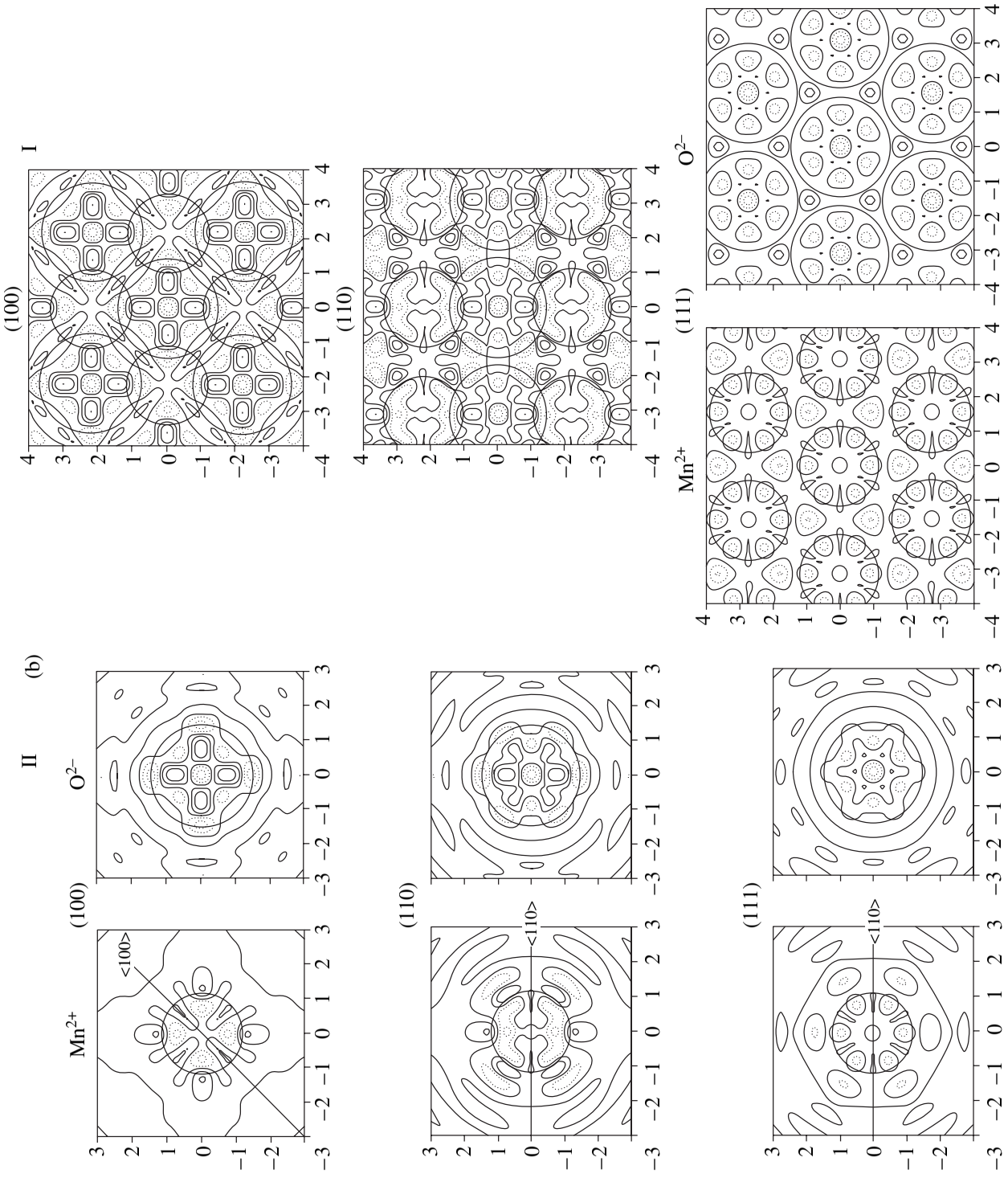

Fig. 4. (Contd.)

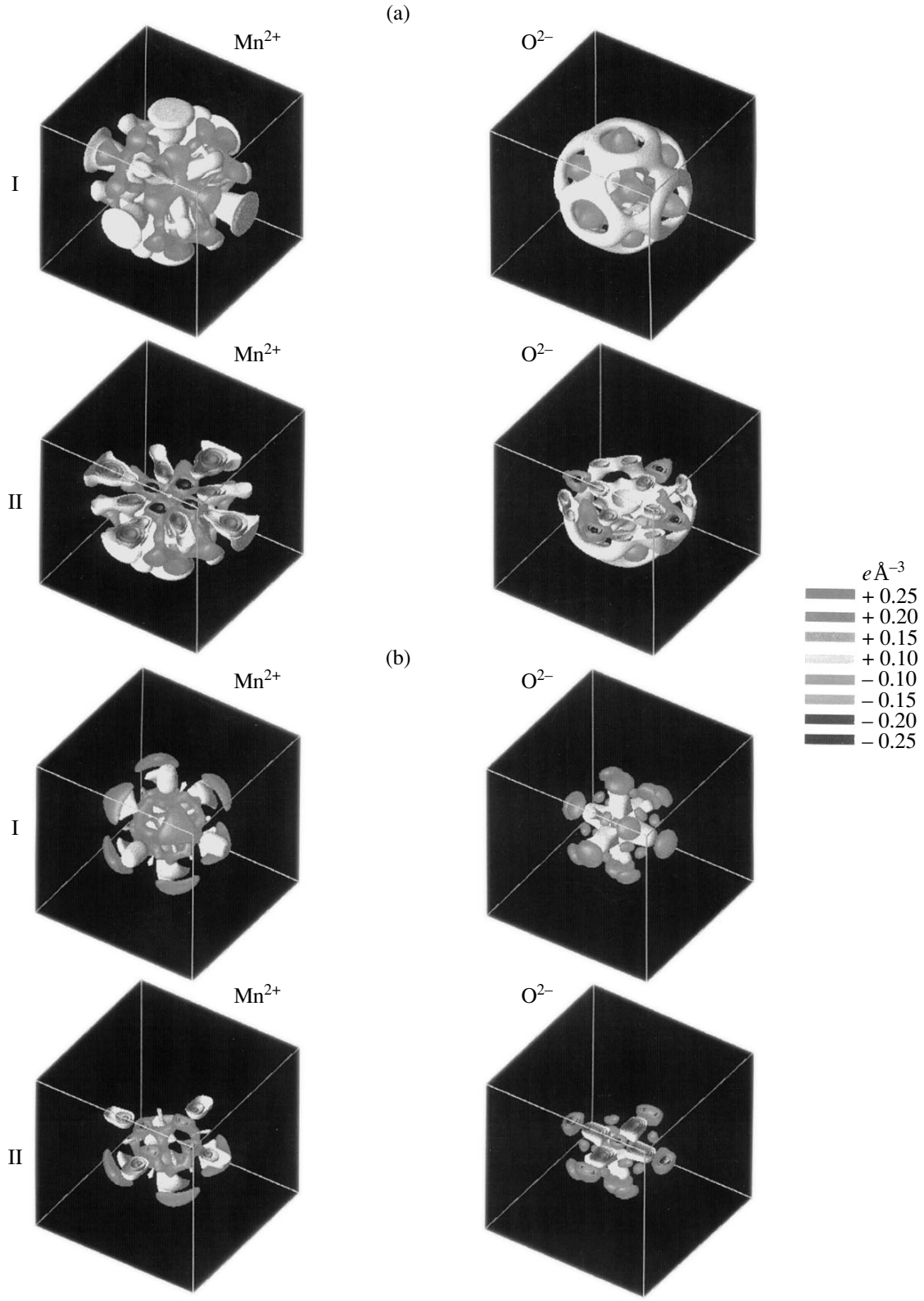

Fig. 5. Three-dimensional view on the ionic multipole expansions, extracts from a video presentation of the 3-dimensional distributions of MnO [61]. Surface-representations +0.1 and –0.1 eÅ^{-3} and section-representations +0.25 to –0.25 eÅ^{-3}; the zero value is omitted. Contours are spaced by 0.05 eÅ^{-3}. (a) The paramagnetic state (298 K), (b) the antiferromagnetic state (85 K).

The most obvious changes caused by the transition to the antiferromagnetic state is the disappearance of strong Mn–Mn bonding. There are some traces of such bonding, but the effect is much weaker than in the paramagnetic state. Now, there is no bridging between oxygen atoms, and it is unclear whether the net formation is still continued, although the areas of low but continuous additional charge density surrounding the oxygen in the multipolar maps and on the (111) Fourier map give a slight indication that the net formation still proceeds.

The general appearance of the deformations attributed to the electrostatic cation–anion interaction have not changed essentially. In manganese, they are weaker, as can be seen from the reduction of the 4th- and 6th-order radial densities (Fig. 3). In oxygen, these components interchanged their roles, which leads to the general impression that the effect has become somewhat stronger. This and the obviously higher minimum value of the spherical density in Fig. 1 indicate the presence of some electronic O–Mn coupling.

The combination of two positive and two negative peaks around the empty 1/4, 1/4, 1/4 position on the (110) Fourier map is a local feature and an obvious artefact.

REFERENCES

1. J. Kübler and A. R. Williams, J. Magn. Magn. Mater. **54–57**, 603 (1986).
2. S. Hüufner, Adv. Phys. **43** (2), 183 (1994).
3. M. S. Jagadeesh and M. S. Seehra, Phys. Rev. B **23** (3), 1185 (1981).
4. G. Srinivasan and M. S. Seehra, Phys. Rev. B **28** (11), 6542 (1983).
5. D. Seino, J. Magn. Magn. Mater. **28**, 55 (1982).
6. M. S. Seehra and R. E. Helmick, Phys. Rev. B **24** (9), 5098 (1981).
7. M. S. Seehra, R. E. Helmick, and G. Srinivasan, J. Phys. C **19**, 1627 (1986).
8. Ya. M. Ksendzov, I. L. Korobova, K. K. Sidorin, and G. P. Startsev, Fiz. Tverd. Tela (Leningrad) **18** (1), 173 (1976) [Sov. Phys. Solid State **18**, 99 (1976)].
9. N. A. Drokin, S. G. Ovchinnikov, and L. I. Ryabinkina, Fiz. Tverd. Tela (Leningrad) **29** (6), 1625 (1987) [Sov. Phys. Solid State **29**, 935 (1987)].
10. R. J. Lad and V. E. Henrich, Phys. Rev. B **38** (15), 10860 (1988).
11. S. Mochizuki, B. Piriou, and J. Dexpert-Ghys, J. Phys.: Condens. Matter **2**, 5225 (1990).
12. A. Fujimori, N. Kimizuka, T. Akahane, *et al.*, Phys. Rev. B **42** (12), 7580 (1990).
13. J. M. McKay and V. E. Henrich, Phys. Rev. Lett. **53** (24), 2343 (1984).
14. G. A. Sawatzky and J. W. Allen, Phys. Rev. Lett. **53** (24), 2339 (1984).
15. S. Hüfner, J. Osterwalder, T. Riesterer, and F. Hulliger, Solid State Commun. **52** (9), 793 (1984).
16. E. Zschech, L. Troger, D. Arvanitis, *et al.*, Solid State Commun. **82** (1), 1 (1992).
17. K. S. Kim, Phys. Rev. B **11** (6), 2177 (1975).
18. T. Van Elp, J. L. Wieland, H. Eskes, *et al.*, Phys. Rev. B **44** (12), 6090 (1991).
19. K. Okada and A. Kotani, J. Phys. Soc. Jpn. **61** (2), 449 (1992).
20. J. Kanamori, J. Phys. Chem. Solids **10**, 187 (1959).
21. L. F. Mattheiss, Phys. Rev. B **5** (2), 306 (1972).
22. K. Terakura, T. Oguchi, A. R. Williams, and J. Kübler, Phys. Rev. B **30** (8), 4734 (1984).
23. K. Terakura, A. R. Williams, T. Oguchi, and J. Kübler, Phys. Rev. Lett. **52** (20), 1830 (1984).
24. J. Hugel and C. Carabatos, Solid State Commun. **60** (4), 369 (1986).
25. V. J. Anisimov, M. A. Korotin, and E. Z. Kurmaev, J. Phys.: Condens. Matter **2**, 3973 (1990).
26. A. E. Bocquet, T. Mizokawa, T. Saitoh, *et al.*, Phys. Rev. B **46** (7), 3771 (1992).
27. W. Nolting, L. Haunert, and G. Borstel, Phys. Rev. B **46** (8), 4426 (1992).
28. V. J. Anisimov, P. Kuiper, and J. Nordgren, Phys. Rev. B **50** (12), 8257 (1994).
29. W. L. Roth, Phys. Rev. **110** (6A), 1333 (1958).
30. W. L. Roth, Phys. Rev. **111** (3B), 772 (1958).
31. D. Bloch, R. Maury, C. Vetter, and W. B. Yelon, Phys. Lett. A **49 A** (5), 354 (1974).
32. H. Shaked, J. Faber, and R. L. Hittrman, Phys. Rev. B **38** (16), 11901 (1988).
33. D. Hermann-Ronzaud, P. Burlet, and J. Rossat-Mignot, J. Phys. C **11**, 2123 (1978).
34. H. Chang, J. F. Harrison, T. A. Kaplan, and S. D. Mahanti, Phys. Rev. B **49** (22), 15753 (1994).
35. M. Kuriyama and S. Hosoya, J. Phys. Soc. Jpn. **17** (6), 1022 (1962).
36. R. Uno, J. Phys. Soc. Jpn. **20** (3), 308 (1965).
37. V. Meisalo and O. Inkinen, Ann. Acad. Sci. Fenn., Ser. A6 **240**, 4 (1967).
38. S. Sasaki, K. Fujino, Y. Takeuchi, and R. Sadanaga, Acta Crystallogr., Sect. A: Cryst. Phys., Diffr., Theor. Gen. Crystallogr. **36**, 904 (1980).
39. J.-P. Vidal, in *Symposium Franco–Finlandais. Structure de la Matiere. Reparitions Electroniques dans les Cristaux, Paris, 1993*, Ed. by J.-P. Vidal (Montpellier, 1994), p. J1.
40. G. Vidal, in *Symposium Franco–Finlandais. Structure de la Matiere. Reparitions Electroniques dans les Cristaux, Paris, 1993*, Ed. by J.-P. Vidal (Montpellier, 1994), p. I1.
41. K. Kurki-Suonio, in *Symposium Franco–Finlandais. Structure de la Matiere. Reparitions Electroniques dans les Cristaux, Paris, 1993*, Ed. by J.-P. Vidal (Montpellier, 1994), p. F1.
42. J.-P. Vidal, G. Vidal-Valat**,** and C. M. E. Zeyen, Nucl. Instrum. Methods **228**, 569 (1985).
43. A. Revcolevschi, Rev. Int. Hautes Temp. Refract. **7**, 73 (1970).

44. J.-P. Vidal, G. Vidal-Valat, M. Galtier, and K. Kurki-Suonio, Acta Crystallogr., Sect. A: Cryst. Phys., Diffr., Theor. Gen. Crystallogr. **37**, 826 (1981).
45. W. R. Busing and H. A. Levy, Acta Crystallogr. **10**, 180 (1957).
46. M. Merisalo and J. Kurittu, J. Appl. Crystallogr. **11**, 179 (1978).
47. K. G. Subhadra and D. B. Sirdeshmukh, Indian J. Pure Appl. Phys. **16**, 693 (1978).
48. R. Sälke and K. Kurki-Suonio, *Report Series in Physics* (Univ. of Helsinki, 1984), HU-P-233.
49. *International Tables for X-ray Crystallography* (Kluwer, Dordrecht, 1999), Vol. C.
50. P. L. Sanger, Acta Crystallogr., Sect. A: Cryst. Phys., Diffr., Theor. Gen. Crystallogr. **25**, 694 (1969).
51. D. T. Cromer and D. Liberman, J. Chem. Phys. **53**, 1891 (1970).
52. P. J. Becker and P. Coppens, Acta Crystallogr., Sect. A: Cryst. Phys., Diffr., Theor. Gen. Crystallogr. **31**, 417 (1975).
53. G. Vidal-Valat, J.-P. Vidal, K. Kurki-Suonio, and R. Kurki-Suonio, Acta Crystallogr., Sect. A: Found. Crystallogr. **48**, 46 (1992).
54. G. Vidal-Valat, J.-P. Vidal, and K. Kurki-Suonio, Acta Crystallogr., Sect. A: Cryst. Phys., Diffr., Theor. Gen. Crystallogr. **34**, 594 (1978).
55. K. Kurki-Suonio and R. Sälke, in *Local Density Approximations in Quantum Chemistry and Solid State Physics*, Ed. by J. P. Dahl and J. Avery (Plenum, New York, 1984), p. 713.
56. K. Kurki-Suonio and R. Sälke, Kristallografiya **31**, 776 (1986) [Sov. Phys. Crystallogr. **31**, 458 (1986)].
57. G. Vidal-Valat, J.-P. Vidal, K. Kurki-Suonio, and R. Kurki-Suonio, Acta Crystallogr., Sect. A: Found. Crystallogr. **43**, 540 (1987).
58. M. Kara and K. Kurki-Suonio, Acta Crystallogr., Sect. A: Cryst. Phys., Diffr., Theor. Gen. Crystallogr. **37**, 201 (1981).
59. K. Kurki-Suonio, Acta Crystallogr., Sect. A: Cryst. Phys., Diffr., Theor. Gen. Crystallogr. **24**, 379 (1968).
60. J.-P. Vidal, K. Kurki-Suonio, G. Vidal-Valat, and R. Kurki-Suonio, Video-film "Visualization of Spherical, Cubic and Icosahedral Harmonics," Ed. by J.-P. Vidal, Distributed by service du Film de Recherche Scientifique (Vanves, France, 1995).
61. J.-P. Vidal, K. Kurki-Suonio, G. Vidal-Valat, and R. Kurki-Suonio, Video-film "Is It Possible to Visualize the Multipole Expansion in Three Dimensions?," Ed. by J.-P. Vidal, distributed by Service du Film de Recherche Scientifique (Vanves, France, 1993).

Crystallography Reports, Vol. 47, No. 3, 2002, pp. 362–369. Translated from Kristallografiya, Vol. 47, No. 3, 2002, pp. 406–414.

DIFFRACTION AND SCATTERING OF X-RAY AND SYNCHROTRON RADIATION

Stochastic Structural Changes in Deformed Hydrogen-Saturated Pd–Ta Alloys from the Kinetic X-ray Data

V. M. Avdyukhina, A. A. Katsnelson, G. P. Revkevich, Han Ha Sok, and A. Sedletskiĭ

Physics Faculty, Moscow State University, Vorob'evy gory, Moscow, 119899 Russia

Received July 17, 2000; in final form, November 28, 2001

Abstract—The structural evolution of the deformed hydrogen-saturated Pd–Ta alloy has been studied by X-ray diffraction methods. It is established that, within the first 20–25 hours upon saturation with hydrogen, the expansion of the crystal lattice due to hydrogen dissolution in the system is accompanied by the transformation of defect–metal (D–M) complexes into hydrogen–defect–metal (H–D–M) ones, which provides the anisotropic contraction of the lattice. It is also shown that relaxation of inhomogeneities (H–D–M complexes and the surrounding transient regions) formed at the early stages of the process are, in fact, dynamic dissipative structures. The stochasticity of the structural changes is associated with the specific features of diffusion motion of atoms between the complexes, transient regions, and the matrix. © *2002 MAIK "Nauka/Interperiodica".*

INTRODUCTION

As is well known [1, 2], a deformable solid is a self-organizing system whose evolution results in the formation and transformation of dissipative structures. Metal–hydrogen systems belong to this type, because hydrogen absorbed by a metal gives rise to internal stresses deforming the metal lattice [3, 4].

Earlier [4], it was revealed that upon saturation of the Pd–W alloy (11.3 at. % W) with hydrogen, the intensities of the 200 and 400 X-ray diffraction maxima and the logarithms of their ratio oscillated with time and, upon a short period of broadening of these maxima, their intensities showed stochastic changes with time.

The change in the logarithm of the intensity ratio with time revealed in [4] shows, in accordance with [5], the alternative appearance and disappearance of small clusters, which proves the occurrence of self-organization processes in the cluster subsystem of the Pd–W–H alloy.

In the deformed two-phase Pd–Er alloys saturated with hydrogen, phase transformations of a stochastic nature were first observed in [6–8]. This phenomenon was explained by the fact that, upon saturation with hydrogen, the defect–metal (D–M) complexes existed in the alloy prior to saturation with hydrogen were transformed into hydrogen–defect–metal (H–D–M) ones. As a result, the inhomogeneities in this system acquire a multilevel nature. Under certain conditions, similar systems can be considered as fractal ones. At certain relationships of the relaxation times of the system variables and sufficient concentrations of the H–D–M complexes, the behavior of these systems should be described by a strange attractor, whereas the system evolution should acquire stochastic character. The data obtained also prove the cooperative nature of the processes occurring in different parts of the system [9]. All these facts indicate that the self-organization processes characteristic of metal–hydrogen systems occur not only in the defect subsystem.

Obviously, although these phenomena are associated with the specific features caused by the saturation of the defect subsystem with hydrogen, their temporal and other characteristics should be essentially dependent on the electronic structure of a dopant, the diffusion coefficient, and the direction of the diffusion flows. Therefore, it is very important to establish the objects and their initial states characterized by the nontrivial kinetics of phase transformations. As was shown elsewhere [8], the nontrivial kinetics is characteristic of systems which, in the initial state, were subjected to some perturbation-inducing treatment. Therefore, one of the major directions today is the search for alloys which, being saturated with hydrogen, would have the nontrivial kinetics of phase transformations. Since palladium is a hydrogen-absorptive metal, the problem reduces, first and foremost, to the determination of the Pd–M alloys with really nontrivial kinetics. The present study is dedicated to such a nontrivial kinetics in the Pd–Ta–H system, which has never been considered before.

EXPERIMENTAL

The study was performed by the methods of X-ray diffractometry [6–9] on a PC-controlled DRON-UM2 diffractometer providing the acquisition and the treatment of experimental data. The 111, 200, 220, 311, and 222 diffraction lines were recorded using the monochromatic Cu–$K_{\alpha 1}$ radiation. All these diffraction maxima were measured prior to alloy saturation with hydro-

gen, upon the first and the second cycles of such saturation, and also in the process of alloy relaxation. The measurements were made immediately upon completion of the saturation cycles for quite a long time (every day within a period of about eight days). We measured the reflections in the sequence 200, 220, 311, etc. This provided the collection of the data on the kinetics of displacement of the diffraction maxima, the changes in their shape, and, thus, on the evolution of the structure and the elastic stresses in the coherent-scattering regions of different orientations with respect to the hydrogen flow.

The samples of the Pd–7 at. % Ta alloy were prepared by melting pure (99.98 wt %) components in an electric-arc furnace in the titanium atmosphere with the use of a Ti getter. The samples thus prepared were subjected to one day (24 h) homogenizing annealing under a pressure of ~10^{-6} mm Hg at 900°C. Upon homogenization, the samples were cut by the electric-spark method. Then, the working surface of a sample was ground and polished with the aid of various diamond pastes until the attainment of a mirror-smooth surface. The diffuse diffraction maxima showed that the above treatment resulted in the deformation of a surface layer with a thickness of 10-μm exceeding the penetration depth of X-rays. The samples prepared by the above method had the shape of disks 16–18 mm in diameter and 2–5 mm in thickness. Hydration was performed in an aqueous (double distilled) 4%-NaF solution in an electrolytic bath at room temperature. The sample played the role of a cathode and the anode was a Pt plate. The initial 15-min-long cycle of hydration was performed at a current density of 40 mA/cm^2; then, upon 176-h-long measurements, the samples were subjected to a new 15-min-long cycle of hydration at a current density of 80 mA/cm^2. The amount of electricity passed through the surface unit of the sample attained 36 C in the first and 72 C in the second saturation cycles.

It should be indicated that, according to the latest data [10], the Ta solubility in Pd is close to 15 at. % Ta; in the two-phase region, the face-centered cubic and the ordered (by the $TiAl_3$-type) body-centered tetrahedral phases coexist. The microprobe analysis of the diffusion layers in this systems also showed the existence of a number of nonequilibrium phases [11]. The ability of Ta to absorb hydrogen results in the formation of two Ta hydrides—TaH and Ta_2H [12]. However, the solubility of oxygen in the alloys studied decreases with an increase in the Ta concentration [13].

As was shown in [14–16], the grinding and polishing of the samples of Pd alloys gave rise to elastic stresses σ resulting, in turn, in such an increase in interplanar spacings with the Miller indices *hkl* that the experimentally observed values of $a_{hkl} = d_{hkl}(h^2 + k^2 + l^2)^{1/2}$ were often inconsistent.

In this case, the dependence of a_{hkl} on (*hkl*) has the form

$$a_{hkl} = a_0 + a_0\sigma K_{hkl}, \quad (1)$$

where a_0 is the lattice parameter of a cubic crystal in the absence of elastic stresses σ; $K_{hkl} = -(\mu/E)_{hkl} = S_{12} + S_0\Gamma$; μ is the Poisson ratio; E is the Young's modulus; $S_0 = S_{11} - S_{12} - S_{44}/2$ is the anisotropy constant; S_{11}, S_{12}, and S_{44} are the elastic-compliance constants; and $\Gamma = (h^2k^2 + l^2h^2 + k^2l^2)/(h^2 + k^2 + l^2)^2$. If σ is negative (the interplanar spacings along the surface normal are overestimated), then $a_{100} > a_{111}$; if σ is positive, then $a_{100} < a_{111}$. The above expressions were obtained by Reuss [17] for the model in which the local stresses acting onto individual crystallites in the system were assumed to be equal.

Since the $a_0\sigma K_{hkl}$ value does not exceed 1% of a_0, then σa_0 in Eq. (1) can be replaced by σ'. The a_0 and σ' values were calculated from the experimental data by the least squares method.

EXPERIMENTAL RESULTS

The most valuable results were obtained for the 200, 220, and 311 reflections. The characteristic diffraction curves recorded for these reflections in various states of the sample upon the first and the second cycles of saturation with hydrogen are shown in Figs. 1–6. The a_{hkl}, a_0, and σ' values calculated from these data for the initial state and the states upon 50–176-h-relaxation are indicated in table.

The first reflection measured upon saturation with hydrogen was 200 (Figs. 1, 2). The initial plot (Fig. 1a) was a slightly broadened Lorentzian curve. Upon 0.5-h-saturation of the first cycle, the shape of this curve had considerably changed (Fig. 1b). On the side of smaller 2θ angles, an additional peak was formed, which was displaced by 0.2° with respect to the main peak. The intensity of the additional peak drastically decreased upon 3.3-h-saturation with hydrogen and approached the position of the main peak (Fig. 1c). The resulting maximum turned out to be displaced by 0.3° towards larger angles with respect to its position in the previous state. Upon 3.2-h-saturation, it displaced by 0.1° more toward larger angles (Fig. 1d). Then, the position, the shape, and the asymmetry of this maximum showed stochastic oscillations within the whole time of the subsequent observation (171 h). These effects were the most pronounced for the 220 and 311 reflections and, therefore, they are considered in detail together with the other data for these reflections, whereas now we only indicate that the shape of the 200 maximum had changed after 23.5- and 171-h saturation.

Consider the change of the 200 diffraction maximum upon the second saturation cycle (Fig. 2). The initial curve obtained 171 h after the first saturation cycle

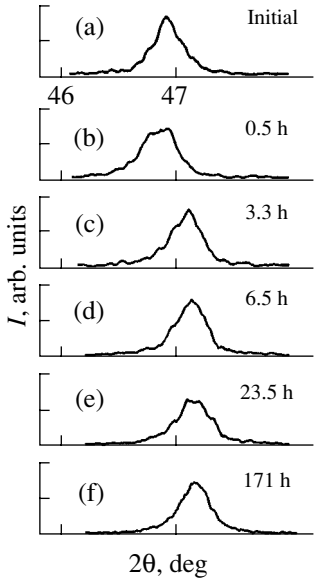

Fig. 1. Temporal change in the position and profile of the (200) diffraction line upon the first cycle of saturation with hydrogen.

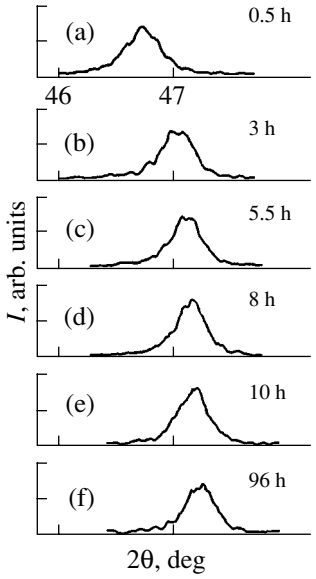

Fig. 2. Temporal change in the position and profile of the (200) diffraction line upon the second cycle of saturation with hydrogen.

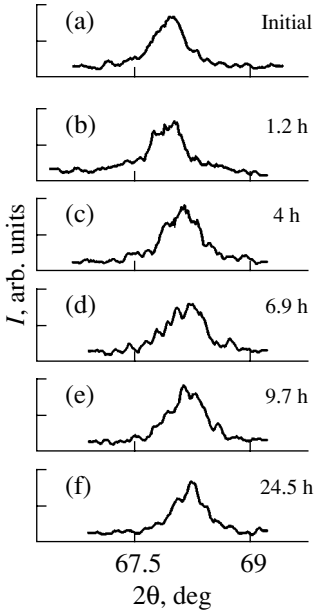

Fig. 3. Temporal change in the position and profile of the (220) diffraction line upon the first cycle of saturation with hydrogen.

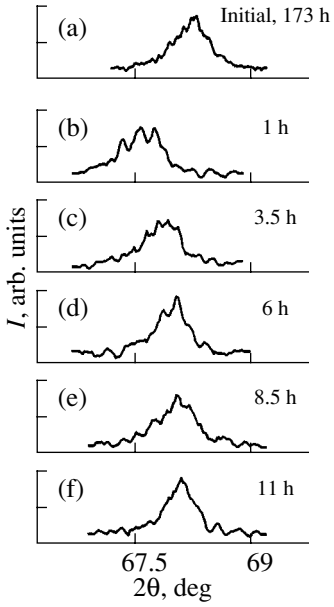

Fig. 4. Temporal change in the position and profile of the (220) diffraction line upon the second cycle of saturation with hydrogen.

is almost symmetric (Fig. 1f). Half an hour after this saturation cycle, the line is displaced by almost one degree toward smaller angles and becomes broader and less symmetric (Fig. 2a); 3 h later, it is displaced by half a degree more toward larger 2θ and becomes even broader and more asymmetric (Fig. 2b). Still 2.5 h later, the line is displaced by 0.1° in the same direction; its top becomes narrower but its base is broadened (Fig. 2c). After the next 2.5 h, the top of the curve becomes still narrower, but the maximum is only slightly displaced in the same direction (Fig. 2d). Two hours later, the shape of the maximum becomes pronouncedly asymmetric (Fig. 2e) (here, the asymmetry is understood as the merging of a weak additional max-

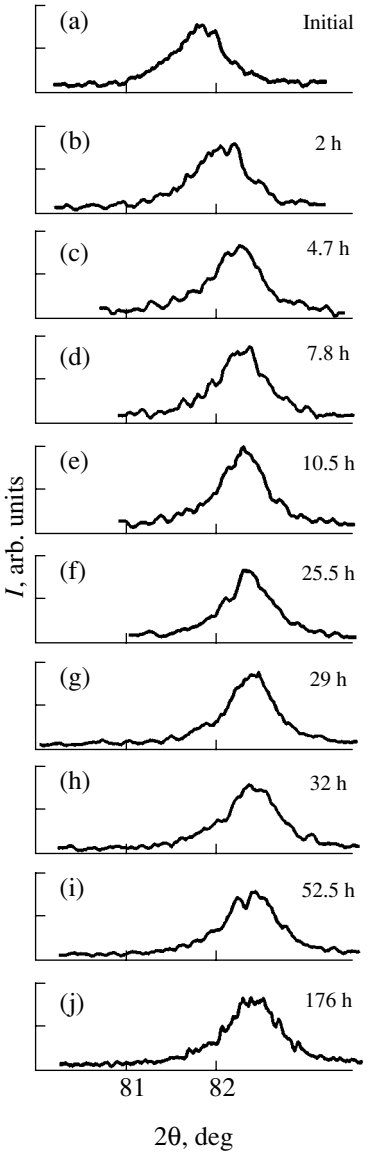

Fig. 5. Temporal change in the position and profile of the (311) diffraction line upon the first cycle of saturation with hydrogen.

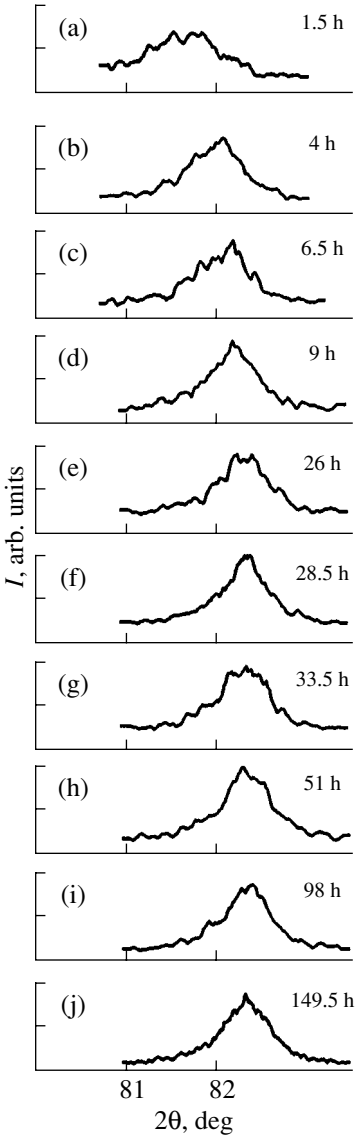

Fig. 6. Temporal change in the position and profile of the (311) diffraction line upon the first cycle of saturation with hydrogen.

imum with one of the sides of the main maximum). The existence of this maximum on the side of smaller diffraction angles corresponds to the negative sign of asymmetry. A further increase in the time upon the second and the first saturation cycles results in oscillations of the positions, shapes, and asymmetry of the diffraction curves.

Thus, the behavior of the 200 diffraction maximum in the first hours upon the first and the second saturation cycles is quite different. Half an hour after the first saturation cycle, the diffraction maximum consisted of two merged maxima, with the position of the first one being unchanged, whereas the position of the second one was displaced by 0.2° toward smaller angles. The same time after the second saturation cycle, the diffraction maximum showed almost 20% broadening and was displaced by 0.7° toward smaller 2θ angles. With an increase in the time upon the first and the second saturation cycles, the maximum was displaced toward larger angles. However, upon the first saturation cycle, the maximum was displaced from the 2θ value close to the value observed for the unsaturated sample, whereas upon the second saturation cycle it was displaced from the 2θ value attained upon the considerable displacement of the maximum toward smaller angles caused by its saturation with hydrogen.

The characteristic features of the displacement of the 220 diffraction maximum are similar to those observed for the 200 maximum: the diffraction profiles in some states consist of several components, which

Lattice parameters a_{hkl} and a_0 and σ

hkl	In the initial state, Å	Upon the first cycle of saturation (50–176-h relaxation)	Upon the second cycle of saturation (50–150-h relaxation)
111	3.8989	3.8902	3.8938
200	3.9084	3.8823	3.8815
220	3.9012	3.8879	3.8879
311	3.9040	3.8843	3.8855
222	3.9004	3.8905	3.8928
400	3.9072	3.8819	3.8815
a_0, Å	3.8961	3.8934	3.8971
σ, kg/mm^2	–50	50	70

Note: $\Delta a = 0.0007$ Å and $\Delta\sigma = 4$ kg/mm^2.

indicates the multiphase state of the alloy in the corresponding states (Figs. 3, 4) (in accordance with [18], here, a phase is understood as a homogeneous region of the substance). Thus, upon each cycle of saturation with hydrogen (Figs. 3b, 4b), the diffraction curves consisted of several well-resolved maxima. The most interesting feature is that the character of the multipeak diffraction curves changed every few hours. The changes in the diffraction curves (Figs. 3b–3f, 4b–4f) directly reflect the formation and the transformation of several phases (since these phases are nonequilibrium, this phenomenon is consistent with the Gibbs rule) associated with the redistribution of Pd and Ta atoms between different regions of crystallites. The changes in the number of the formed and the transformed phases and their volume ratios indicate their stochasticity.

The 311 reflection (Figs. 5, 6) was first measured 1.5–2.0 h after each saturation cycle. It was established that the first signs of the lattice expansion appear only after the second saturation cycle. In the initial state (prior to saturation) (Fig. 5a), the 311 maximum had a diffuse Lorentzian shape. Two hours after saturation with hydrogen, the maximum was displaced toward larger 2θ angles with the top of the maximum being asymmetric and considerably broadened (Fig. 5b). Upon 2.7-h-relaxation, the top of the maximum became narrower (Fig. 5c), and 3.1 h later, broadened again (Fig. 5d); then, still 2.7 h later, the maximum became narrower with both its wings becoming lower. The diffraction curve became more symmetric (Fig. 5e). The above transformations of the shape of the maximum were accompanied by its displacement by about half a degree toward larger 2θ angles (in comparison with the position in the initial state), which corresponded to a 0.02 Å decrease in interplanar spacings. The complex transformations of the diffraction maximum were also observed upon keeping the sample in air for a long period. Thus, the curves obtained after 25.5- (Fig. 5f), 29- (Fig. 5g), 32- (Fig. 5h), and 52.5-h- (Fig. 5i) relaxation of the sample in air showed oscillations of the point of the maximum and the asymmetry sign, which indicated the complex nature of the diffraction-pattern evolution upon the first cycle of saturation accompanied by a multiple redistribution of atoms in the system including the multiple changes of the ratio of the coexisting phases and their defect structures. It should also be noted that the top of the diffraction maximum observed after 176-h relaxation (Fig. 5j) also indicated considerable inhomogeneity of the sample and, possibly, the two-phase state of the system.

The experimental data obtained from the different states of the samples upon the second saturation cycle (performed 176 h after the first cycle) are shown in Fig. 6. An hour and a half later, after the second saturation cycle, the diffraction maximum was transformed into a curve consisting of three to four maxima (Fig. 6a); 2.5 h later, the shape of the diffraction curve was simplified (Fig. 6b), but it had obvious asymmetry with the negative sign. After another 2.5 h, the additional maximum on the side of small angles became more pronounced (Fig. 6c), and, 2.5 h later, it was transformed into an upper wing (Fig. 6d). Seventeen hours later, the diffraction maximum slightly broadened (Fig. 6e), but 2.5 h later this broadening disappeared (Fig. 6f). However, after the next 5 h, the top of the maximum broadened again (Fig. 6g), and, at the same time, a weak, although clear, maximum was formed on the side of small diffraction angles. Then, 17.5 h later, the top of the diffraction maximum became slightly narrower (Fig. 6h), but the weak maximum on the side of small angles was still observed for 98 h after the saturation (Fig. 6i). This maximum disappeared only after 150-h-relaxation (Fig. 6j). It should be indicated that, unlike the data obtained 176 h after the first saturation cycle, this state showed no signs of inhomogeneity or evidence of being a two-phase state.

The above transformations of the diffraction-maximum shape were accompanied by its displacement. Thus, 1.5 h after saturation, the maximum was displaced by more than half a degree toward smaller 2θ angles, but then it started moving in the opposite direction (for 24 h). Then the diffraction maximum showed small oscillations about its average position.

The table shows the a_{hkl} values obtained for the initial state and the states attained 50–176 h after the first and second cycles of saturation with hydrogen. These data show that, prior to saturation with hydrogen, the a_0 and σ values were equal to 3.8961 Å and –50 kg/mm^2, respectively. Upon the first saturation cycle followed by 50 to 176-h-relaxation, these values changed to 3.8934 Å and +50 kg/mm^2, and, upon the second saturation cycle and approximately the same relaxation, to 3.8971 Å and +70 kg/mm^2. This signifies that, like other systems studied [6, 15, 16], the saturation of our system with hydrogen results in the change of the elastic-stress sign. Moreover, it is seen that the a_0 value upon the first saturation cycle is less than that of the initial samples. This effect can readily be interpreted if one takes into

account that the data obtained in [19–21] attest to the appearance of a large number of vacations in hydrogen-saturated palladium-containing systems.

Thus, the study of the changes in the diffraction patterns upon saturation with hydrogen and the subsequent relaxation of the deformed Pd–Ta alloy showed

—the regular displacement of the diffraction maxima which indicated first the expansion and then the anisotropic contraction of the crystal lattice, which were different upon the first and the second saturation cycles;

—the stochastic change of the diffraction-maximum positions with time upon the completion of the above processes, which proved the dynamic character of the H–D–M complexes;

—the considerable complication of the diffraction curves upon the saturation of the system with hydrogen-broadening of the curves, the formation of asymmetry, and their "multipeak nature" at some stages of sample relaxation;

—the stochastic transformation of the diffraction-maximum profiles with time, which indicated the diffusion motion of atoms and their redistribution between different coherent-scattering regions; and, finally,

—the formation of multilevel hierarchic defect structure of crystallites [22].

It should also be emphasized that we managed to reveal, for the first time, signs indicating the dynamic nature of the formation of a defect structure, which, in turn, gives rise to elastic stresses. This directly follows from the fact that the positions of the diffraction-profile maxima show stochastic oscillations during relaxation after the completion of both first and second cycles of system saturation with hydrogen in the direction of larger angles.

DISCUSSION

For the first time, we have revealed the nontrivial kinetics of the structural evolution in deformed hydrogen-saturated Pd–Ta–H alloys and established its characteristic features. The structural evolution was studied for more than 150 h after one- and two-cycle saturation of the system with hydrogen. The experimental data showed that the main changes taking place in both cases consist in the displacement of the diffraction maxima and the change in their shapes. The specific features of these changes depend on the number of the saturation cycle, the time passed after saturation with hydrogen, and also on the crystallographic orientation of the reflecting planes with respect to the hydrogen flow in the coherent-scattering regions. We begin the analysis of the nature of these phenomena with diffraction-peak displacements.

First, compare the data obtained 150–175 h after the first and second saturation cycles. The a_0 and σ values obtained after these cycles turned out to be different (see table). Upon the first cycle, σ was equal to 50 kg/mm^2, which indicated that the complete change in σ attained 100 kg/mm^2. Despite the double current density, the total change in σ upon the second saturation cycle was 120 kg/mm^2, which exceeded by 20% the total change in σ attained after the first cycle. This signifies that, already upon the first cycle, the number of the H–D–M complexes formed in the system is close to its possible maximum value. During the subsequent process, this number increases only insignificantly. The a_0 value for the states corresponding to the relaxation times 50–170 h turned out to be less by 0.0027 Å than the a_0 value in the initial state (we ignore small positional oscillations of the tops of the diffraction maxima). This result can be explained by the fact that the saturation with hydrogen results in the formation of a large number of vacancies which can form various complexes [19–21]. At the same relaxation time upon the second saturation cycle, the a_0 value was slightly higher than the a_0 value in the initial state and much higher (by 0.0037 Å) than the a_0 value upon the first saturation cycle. This result shows that the amount of hydrogen preserved in the system upon the second cycle is much higher than upon the first cycle.

Now, consider the evolution of the positions of the diffraction maxima between the initial state of the system and its final state. Consider the a_{hkl} values upon the first saturation cycle. The data obtained showed that in our system the anisotropic contraction of the crystal lattice along the surface normal with the transformation of the complexes takes place not later than 2 h after the saturation which is associated with the transformation of complexes suggested in [6]. The reflections measured within the period of 1.5 h after the second saturation cycle showed a considerable increase in the unit-cell parameters (much more pronounced than after the first cycle) and then, similar to the case of the first saturation cycle, the anisotropic contraction of the lattice is observed.

According to [15–17], the positions of the diffraction maxima in the systems considered above are determined by the lattice parameters and the σ values. The changed positions of the diffraction maxima upon the first and second cycles of saturation can be explained as follows. Within the first two hours after the second saturation cycle, the changes are provided mainly by the expansion of the crystal lattice caused by dissolved hydrogen. The signs of this expansion are observed only within 1.2 h after the first cycle. Then, the anisotropic lattice contraction is clearly seen, which results in the change of the sign of σ and can be explained only under the assumption that saturation with hydrogen changes the D–M complexes characteristic of the initial state into H–D–M complexes playing the role of traps of hydrogen atoms and, possibly, also of atoms of some metals.

With due regard for data [7–9, 23], the above results indicate that, upon the first saturation cycle, a considerable number of hydrogen atoms move toward the com-

plexes and transform these complexes into "lattice-contracting" traps, which, finally, results in anisotropic elastic compression. In the second cycle of saturation, hydrogen atoms move mainly to the matrix and expand it, whereas only a small number of hydrogen atoms can participate in trap formation. Therefore, the resulting a_{hkl} values 150–175 h after both saturation cycles turned out to be rather close.

It is interesting that 25–30 h after saturation with hydrogen, we observed the effect of stochastic oscillations about some average values of interatomic distances. These average values considerably differ from the corresponding values for an unperturbed matrix. This behavior of the system indicates that, in addition to the global minimum, the dependence of the thermodynamic potential on the interatomic distances also has some metastable local minima and, therefore, the system preliminarily perturbed by defects and hydrogen atoms and relaxed upon saturation with hydrogen can go into one of these metastable minima. It seems that the minimum corresponding to a metastable state is rather deep, and the system can exist in this minimum for quite a long time. It should also be indicated that some signs of similar behavior were also observed for the Pd–Er–H system [7–9]. The dynamic character of the structural changes in hydrogen-saturated systems was also indicated in our earlier studies [24–26].

Simultaneously with the change in interatomic distances during system relaxation after its saturation with hydrogen, the diffraction maxima also change their shapes. These changes consist in the formation of a multipeak profile, the broadening of the top or the base of the maxima, and the appearance and transformation of the asymmetry. It is clear that these characteristics of the shape of the maxima stochastically change with time (see, e.g., Figs. 5a–5j, 6a–6j). In the first hours after saturation with hydrogen, the shapes of the maxima considerably change every few hours. However, the noticeable changes in the shape of the maxima are also clearly seen within the whole time of observation (150–175 h). Different changes of peak shapes indicate the existence of numerous differently directed diffusion flows varying with time, which determines the stochastic nature of the temporal dependence of phase transformations.

The following fact is of special interest. The displacements of the maxima are provided by the transformation of the complexes of defects caused by their saturation with hydrogen. Depending on their nature, these complexes can result either in the contraction or expansion of the crystal lattice because of the changes in the interatomic distances in the matrix. The change of the shapes of the maxima is associated with the fact that the interatomic distances change differently in different regions of the matrix. Also, in parallel with the change of the interatomic distances, the atoms of different kinds move from some regions of the matrix to others. Obviously, the second effect is possible only under the assumption that metal atoms also participate in this motion. The similar stochastic nature of the temporal changes of various diffraction characteristics indicates the relation between the formation of complexes of defects and the diffusion motion of metal atoms in the matrix. It seems that we deal here with several different effects—the motion of atoms between the complexes and the transient regions or specific "clouds" and also between these clouds and the matrix. First of all, this indicates that these complexes are dynamic and not static formations. The clouds are also dynamic formations. Thus, we can draw the conclusion that the real structure of crystals is of a multilevel nature. Sometimes, various processes observed in different regions of the crystal proceed almost independently, but sometimes they occur in the whole crystal volume.

Thus, extensive X-ray diffraction studies of the structural evolution in some palladium–metal–hydrogen systems (Pd–H, Pd–W–H, Pd–Sm–H, Pd–Er–H, Pd–Mo–H, Pd–Fe–H, and Pd–Ta–H studied above) allow us to state that the structural evolution observed at certain stages in all these systems is of an oscillatory nature. This is associated not only with the nonequilibrium state of the systems but, to a considerable extent, also with the fact that the structural evolution cannot be reduced only to the motion of hydrogen atoms in the solid-state system. An active part in the structural evolution is also played by the motion of metal atoms. The specific feature of the latter motion should be dependent on the initial defect structure and its transformation caused by the saturation of the system with hydrogen and its subsequent relaxation. In turn, this is associated with the fact that, although the oscillatory (often stochastic) nature of some stages of this evolution was revealed in all the above systems, the oscillating fragments of the structure are different in different alloys. Thus, in the Pd–W–H alloy, the alternating appearance and disappearance of small defect clusters was observed, which, sometimes, was changed to the formation and dissociation of large dislocation loops [4]. In the Pd–Er–H [3, 7–9], Pd–Sm–H [21], Pd–Mo–H [23], and Pd–Ta–H systems, the nonmonotonic changes of the volume ratios of coexisting phases were observed. In Pd–Mo–H [27] and Pd–Ta–H, this change was accompanied by a nonmonotonic change in the number of the components forming the diffraction maxima and the interplanar spacings.

Thus, it was shown that the saturation of the deformed Pd–Ta alloy with hydrogen results not only in the expansion of the crystal lattice caused by dissolved hydrogen but also in the transformation of the D–M complexes initially present in the alloy into the H–D–M complexes giving rise to the elastic compression of the lattice. Upon the first cycle of the system saturation with hydrogen, the second of these processes becomes prevalent. The process is almost completed within the first saturation cycle and, therefore, in the second saturation cycle, the dynamics of the process is determined mainly by the dissolution of hydrogen in the matrix

with the subsequent partial degassing of the system. The structural state formed as a result of the above processes is metastable, and, thus, the complexes and the clouds formed are dynamic formations. The gradient and ascending diffusion flows between the complexes, clouds, and the matrix (for two-phase systems, one has to consider two matrices) determine the stochastic nature of the structural changes upon the completion (on the whole) of the formation of the complexes and partial degassing of the Pd–Ta system. We believe that the processes taking place in the system studied here should also occur in all the other preliminarily deformed systems saturated with hydrogen.

ACKNOWLEDGMENTS

The authors are grateful to A.A. Anishchenko for participating in a number of experiments.

This study was supported by the Russian Foundation for Basic Research, project no. 99-02-16135 and the Program "Russian Universities," project no. 990156.

REFERENCES

1. V. S. Ivanova, A. S. Balankin, I. Zh. Bunin, and A. A. Oksogoev, *Synergetics and Fractals in Materials Science* (Nauka, Moscow, 1994).
2. A. I. Olemskoĭ and A. Ya. Flat, Usp. Fiz. Nauk **163** (12), 3 (1993) [Phys. Usp. **36**, 1087 (1993)].
3. V. M. Avdyukhina, A. A. Katsnel'son, and G. P. Revkevich, Poverkhnost, No. 2, 30 (1999).
4. A. A. Katsnel'son, A. I. Olemskoĭ, I. V. Sukhorukova, and G. P. Revkevich, Usp. Fiz. Nauk **165** (3), 331 (1995) [Phys. Usp. **38**, 317 (1995)].
5. M. A. Krivoglaz, *Theory of X-ray and Thermal Neutron Scattering by Real Crystals* (Naukova Dumka, Kiev, 1983; Plenum Press, New York, 1969).
6. V. M. Avdyukhina, A. A. Katsnel'son, N. A. Prokof'ev, and G. P. Revkevich, Vestn. Mosk. Univ., Ser. 3: Fiz., Astron. **39** (2), 94 (1998).
7. V. M. Avdyukhina, A. A. Katsnel'son, and G. P. Revkevich, Kristallografiya **44** (1), 49 (1999) [Crystallogr. Rep. **44**, 44 (1999)].
8. V. M. Avdyukhina, A. A. Katsnel'son, D. A. Olemskoĭ, *et al.*, Fiz. Met. Metalloved. **88** (6), 63 (1999).
9. V. M. Avdyukhina, L. Dombrovskiĭ, A. A. Katsnel'son, *et al.*, Fiz. Tverd. Tela (St. Petersburg) **41** (9), 1532 (1999) [Phys. Solid State **41**, 1402 (1999)].
10. *State Diagrams of Binary Metal Systems*, Ed. by N. P. Lyakishev (Mashinostroenie, Moscow, 1999), Vol. 3.
11. A. Brunsh and S. Steeb, Z. Naturforsch. **2**, 274 (1971).
12. *Hydrogen in Metals*, Ed. by G. Alefeld and J. Völkl (Springer-Verlag, New York, 1978; Mir, Moscow, 1981), Vol. 2.
13. Y. Sakamoto, K. Kajihara, T. Kikumura, and T. B. Flanagan, J. Chem. Soc., Faraday Trans. **86** (2), 371 (1990).
14. Ya. D. Vishnyakov, A. N. Dubrovina, Ya. S. Umanskiĭ, and V. S. Khaĭmovich, Zavod. Lab. **33** (3), 297 (1967).
15. G. P. Revkevich, M. K. Mitkova, and A. A. Katsnelson, J. Alloys Compd. **216**, 183 (1995).
16. G. P. Revkevich, M. K. Mitkova, A. A. Katsnel'son, *et al.*, Vestn. Mosk. Univ., Ser. 3: Fiz., Astron. **34** (6), 70 (1993).
17. A. Reuss, Z. Angew. Math. Mech. **9** (1), 49 (1929).
18. M. A. Leontovich, *Introduction to Thermodynamics. Statistical Physics* (Nauka, Moscow, 1983).
19. G. P. Revkevich, A. A. Katsnel'son, and V. M. Khristov, Metallofizika **11** (3), 57 (1989).
20. Y. Fukai and N. Okuma, Phys. Rev. Lett. **73**, 1640 (1994).
21. S. Miraglia, D. Fruchart, E. K. Hlil, *et al.*, J. Alloys Compd. **317**, 77 (2001).
22. A. A. Katsnel'son, M. A. Knyazeva, and A. I. Olemskoĭ, Fiz. Tverd. Tela (St. Petersburg) **41** (9), 1621 (1999) [Phys. Solid State **41**, 1486 (1999)].
23. A. V. Knyaginichev, Khan Kha Sok, V. M. Avdyukhina, *et al.*, Fiz. Tverd. Tela (St. Petersburg) **43** (2), 200 (2001) [Phys. Solid State **43**, 207 (2001)].
24. V. M. Avdjukhina, A. A. Katsnelson, G. P. Revkevich, and E. A. Goron, http://ru.arXiv:cond-mat/0004097 (2000).
25. V. M. Avdyukhina, A. A. Katsnel'son, and G. P. Revkevich, Vestn. Mosk. Univ., Ser. 3: Fiz., Astron. **38** (3), 44 (1997).
26. V. M. Avdyukhina, A. A. Katsnel'son, G. P. Revkevich, *et al.*, Al'tern. Energ. Ekol. **1** (1), 11 (1999).
27. V. M. Avdyukhina, A. A. Anishchenko, A. A. Katsnel'son, and G. P. Revkevich, Perspekt. Mater., No. 6, 52 (2001).

Translated by L. Man

Crystallography Reports, Vol. 47, No. 3, 2002, pp. 370–371. Translated from Kristallografiya, Vol. 47, No. 3, 2002, pp. 415–416.

DIFFRACTION AND SCATTERING OF X-RAY AND SYNCHROTRON RADIATION

Indexing of Diffraction Patterns from Triclinic Polycrystals[1]

V. P. Serykh

National Research Center, Kharkov Physicotechnical Institute, Kharkov, Ukraine

Received May 14, 1997; in final form, February 10, 1998

All the algorithms suggested for indexing diffraction patterns from triclinic polycrystals are based on the use of the quadratic form

$$q_i = h_i^2 x + k_i^2 y + l_i^2 z + h_i k_i A + h_i l_i B + k_i l_i C, \quad (1)$$

where $x = q_{100}$, $y = q_{010}$, $z = q_{001}$, $A = 2\sqrt{xy}\cos\gamma^*$, $B = 2\sqrt{xz}\cos\beta^*$, and $C = 2\sqrt{yz}\cos\alpha^*$. Here $q_i = 1/d_i^2$, $x = (\mathbf{a}^*)^2$, $y = (\mathbf{b}^*)^2$, $z = (\mathbf{c}^*)^2$, $\mathbf{a}^*$, $\mathbf{b}^*$, and $\mathbf{c}^*$ are the translation (unit) vectors of the reciprocal lattice; α^*, β^*, and γ^* are the angles formed by these vectors; and d_i are the interplanar spacings.

If the $(hkl)_i$ indices are selected, six Eqs. (1) provide the determination of the x, y, z, A, B, C parameters. The number of these equations can be reduced to three if we put $x = q_i, y = q_j, z = q_l$, where q_i, q_j, q_l are the minimum elements of the array $\{q_m\}$, $m = 1, \ldots, n$. This choice, with due regard for all the possible (hkl) combinations satisfying the condition $V < V_m$, where V is the unit-cell volume and $V_m = 1/(2\pi\Delta q\sqrt{q_n})$ is its limiting value, makes this indexing algorithm exhaustive [1–3].

If the reflections with $(hk0)_i$ indices in the low-angle range dominate, then one has to modify the universal algorithm [1–3].

Let $\boldsymbol{\sigma}_1$, $\boldsymbol{\sigma}_2$, and $\boldsymbol{\sigma}_3$ be the shortest coplanar reciprocal-lattice vectors not related by the collinearity condition, and q_l, q_j, and q_m be the quadratic forms corresponding to these vectors. Putting $x = q_l$ and $y = q_j$, we can determine the angular parameter by Eq. (1)

$$A = (q_m - h_m^2 x - k_m^2 y)/h_m/k_m. \quad (2)$$

Similar to [2], we obtain the formulas for exhaustive sorting of all the indices with the automatic satisfaction of the condition $S^* > S_m^*$, where $S^* = \sqrt{xy(1 - \cos^2\gamma^*)}$ is the area and S_m^* is the limiting area of the reciprocal unit cell [2]:

$$S_m^* = \sqrt{\sqrt{q_n}/V_m}. \quad (3)$$

Combining the expression for S^* and $A = 2\sqrt{xy}\cos\gamma^*$, we obtain a particular quadratic form $q_m = h_m^2 x + k_m^2 y + 2h_m k_m\sqrt{xy - (S^*)^2}$. Following the reasoning used in [2] for more general expression (1), we obtain

$$\begin{aligned} 0 \le h_m \le \sqrt{yq_m}/S_m^*; \quad k_1 \le k_m < k_2; \\ k_{2,1} = (-h_m A \pm \sqrt{(h_m A)^2 + 4y(q_m - h_m^2 x)})/2/y, \end{aligned} \quad (4)$$

where $A = 2\sqrt{xy - (S_m^*)^2}$. If $S_m^* < \sqrt{xy}$, the h_m and k_m vary within the range of real numbers, whereas the continuity of functions (4) provides the sampling of possible $(hk0)_i$ combinations. All the planar cells calculated by formulas (2)–(4) are refined using the set of the indexed reflections selected in accordance with their maximum reliability [4]

$$D = \sum_{i=1}^{n}(1 - \pi\Delta q_i/S^*).$$

As an example of the z parameter, consider the minimum element w_1 of the $\{w_1\}$ array consisting of those q_i which do not belong to the subset of reflections with the $(hk0)$ indices. Now, B and C can be determined by solving the system of equations

$$\begin{aligned} h_j l_j B + k_j l_j C = w_j - R_j - l_j^2 z, \\ h_m l_m B + k_m l_m C = w_m - R_m - l_m^2 z, \end{aligned} \quad (5)$$

where w_j and w_m are the minimum elements of the $\{w_1\}$ array and R_j and R_m are selected from the ordered set $R_m = h_m^2 x + k_m^2 y + h_m k_m A$. Since $z \gg x, y$, we can put $l_j = l_m = 1$.

Now, let us index the diffraction pattern from the compound $W[Al_2(SO_4)_3 \cdot 18H_2O]$ with $w = 2$ taken from [5] (see table).

The use of $x = q_1$, $y = q_2$ and reference value $q_m = 4q_3$ allows the calculation of the array of possible (h_m, k_m) indices. At $V = 1500$ Å^3, $\Delta q = 0.003$ and $S_m = 0.047$ calculated from (5), this array consists of 27 elements. The refinement of the results by (2) and the simplified tran-

[1] The article is deposited at VINITI, RAS, 1999, no. 12 (334).

Table

n	*d*	*q*	*h k l*	*n*	*d*	*q*	*h k l*
1	13.5	0.005487	0 2 0	11	5.049	0.039227	1 $\bar{4}$ 0
2	7.35	0.018511	1 0 0	12	4.918	0.041345	$\bar{1}$ 1 1
3	7.17	0.019450	1 $\bar{1}$ 0	13	4.884	0.041923	1 4 0
4	7.04	0.020180	1 1 0	14	4.704	0.045192	$\bar{1}$ 2 1
5	6.73	0.022080	0 4 0	15	4.643	0.046388	$\bar{1}$ $\bar{2}$ 1
6	6.55	0.023309	1 $\bar{2}$ 0	16	4.489	0.049625	0 6 0
7	6.37	0.024645	1 2 0	17	4.390	0.051888	$\bar{1}$ 3 1
8	6.01	0.027685	0 0 1	18	4.329	0.053361	1 $\bar{1}$ 1
9	5.79	0.029829	1 $\bar{3}$ 0	19	4.275	0.054718	1 5 0
10	5.601	0.031876	1 3 0	20	4.187	0.057042	1 $\bar{2}$ 1

sition to the primitive basic according to a procedure $x/4 \longrightarrow x, y \longrightarrow y, A/2 \longrightarrow A$ at $h = 1$, $k = 2$ singles out the setting of the axes with the parameters $x = 0.013803$, $y = 0.18460$, $A = 0.00342$ at the confidence $D = 11.13$. Putting $z = q_8 = w_1$, $w_j = w_2 = q_{12}$, and $w_m = w_3 = q_{14}$ and solving system (5) relative to B and C, we arrive (after the refinement) at the Bravais parallelepiped that differs from the parallelepiped reported earlier only by the setting; namely, $a = 26.932$ Å, $b = 7.431$ Å, $c = 6.049$ Å, $\alpha = 97.68°$, $\beta = 90.09°$, $\gamma = 91.91°$, $V = 1199$ Å^3. It would be difficult to obtain this result using the universal program [1–3] because of the necessity of cyclic sorting of basis and reference quantities up to the 14th q_i element.

Note that the suggested algorithms considerably reduce the number of sorting procedures in the low-angle diffraction range necessary for solving the problem with the aid of Eqs. (1).

REFERENCES

1. V. P. Serykh, Kristallografiya **36**, 1013 (1991) [Sov. Phys. Crystallogr. **36**, 569 (1991)].
2. V. P. Serykh, Kristallografiya **38**, 261 (1993) [Crystallogr. Rep. **38**, 272 (1993)].
3. V. P. Serykh, Kristallografiya **39**, 353 (1994) [Crystallogr. Rep. **39**, 306 (1994)].
4. V. P. Serykh, Kristallografiya **24**, 1041 (1979) [Sov. Phys. Crystallogr. **24**, 595 (1979)].
5. Joint Committee on Powder Diffraction Standards **26**, 1010 (1976).

Translated by T. Dmitrieva

Crystallography Reports, Vol. 47, No. 3, 2002, pp. 372–378. Translated from Kristallografiya, Vol. 47, No. 3, 2002, pp. 417–423.

STRUCTURES OF INORGANIC COMPOUNDS

The $Ba_{1-x}R_xF_{2+x}$ (R = Gd–Lu) Phases with the Distorted Fluorite Structure as Products of Crystallization of Incongruent Melts in BaF_2–RF_3 Systems. II. Crystal Structures of Two New Forms of $Ba_{1-x}Yb_xF_{2+x}$ Fluorite Phases and Some Features of the Anionic Packing and the Cation Distribution

B. A. Maksimov*, Yu. B. Gubina, E. L. Belokoneva*, V. N. Molchanov*, N. B. Grigor'eva*, A. G. Vigdorchik*, E. A. Krivandina*, and B. P. Sobolev***

** Shubnikov Institute of Crystallography, Russian Academy of Sciences, Leninskiĭ pr. 59, Moscow, 117333 Russia*
e-mail: maksimov@ns.crys.ras.ru

*** Faculty of Geology, Moscow State University, Vorob'evy gory, Moscow, 119899 Russia*

Received July 19, 1999; in final form, July 9, 2001

Abstract—Two fluorite-type phases (P and F) possessing different defect structures were isolated from products of double recrystallization of a melt of the nominal composition (with respect to the charge) $Ba_{0.8}Yb_{0.2}F_{2.2}$. The P phase crystallized in the space group $Pm3m$ with $a = 6.096(1)$ Å. The structure was refined to $R = 2.19\%$ and $R_w = 2.14\%$ (142 independent reflections; λAgK_α radiation, $\sin\theta/2 \le 1.2$ Å^{-1}; 20 parameters were refined). In the primitive cubic unit cell of the P phase, two crystallographic positions are differentiated by the type of the cations occupying these positions. Thus, the position $1a$ (0, 0, 0) is occupied predominantly by Yb^{3+} cations (0.8Yb + 0.2Ba), whereas the position $3c$ (0, 1/2, 1/2) is completely occupied by Ba^{2+} cations. The F phase crystallized in the space group $Fm3m$ with $a = 6.075(1)$ Å; the structure was refined to $R = 0.69\%$ and $R_w = 0.85\%$ (72 independent reflections; λMoK_α radiation, $\sin\theta/\lambda \le 1.0$ Å^{-1}; 15 parameters were refined). In the F phase, all Yb^{3+} ions are shifted with respect to Ba^{2+} ions by 0.34 Å in the [111] direction. © *2002 MAIK "Nauka/Interperiodica".*

INTRODUCTION

Earlier, the products of crystallization from a melt of the nominal (with respect to the charge) composition $Ba_{0.8}Yb_{0.2}F_{2.2}$ were studied by X-ray diffraction methods [1], and two phases (P and F) were found. The P phase has the unit-cell parameters $a = 6.096(1)$ Å and is crystallized in the space group $Pm3m$. The F phase is crystallized in the space group $Fm3m$ with $a = 6.075(1)$ Å. It has also been noted that, although the Ba^{2+} and Yb^{3+} cations in the crystal structure of the F phase are statistically distributed over the cavities of the anionic packing, they are shifted with respect to each other along the [111] direction by 0.32 Å. Apparently, such "positional splitting" can be considered as the initial stage of ordering of the cations.

In the crystal structure of the P phase, the ordering of the cations is even more pronounced. In going from the fluorite F unit cell (the F phase) to the P unit cell (the P phase), the Ba^{2+} ions become completely ordered in the position $3c$ (0, 1/2, 1/2), and the position $1a$ (0, 0, 1) becomes occupied predominantly by ytterbium ions ($0.8Yb^{3+} + 0.2Ba^{2+}$).

In this article, we report the results of the comprehensive X-ray study of these two new forms of the $Ba_{1-x}Yb_xF_{2+x}$ fluorite-like phases and provide evidence for the reliability of the principal structure characteristics of these phases. The detailed crystallochemical analysis of the results obtained will be published elsewhere.

EXPERIMENTAL

Crystal growth was performed by the Bridgman method in an apparatus equipped with active and passive heaters. The samples of the P phase were taken from a crystal rod prepared by double crystallization. The compositions of the crystals could differ from the nominal composition by a lower Yb^{3+} content due to variations in the impurity component in two crystallization experiments. The distribution coefficient of Yb^{3+}

cations in BaF_2 was smaller than unity. Repeated crystallization was carried out with the use of the most perfect first portions of the crystal rod.

The crucible was lowered at a rate of 3.6 ± 0.1 mm/h. The crystal came out from the melting zone to the passive heater (a thermal shield). Then, the heater was turned off, and the crystals were cooled at a rate of 50–100 K/h.

The fluorinating atmosphere suppressed pyrohydrolysis in the course of growth and thus excluded contamination by oxygen. Samples for analysis were taken from crushed crystal rods obtained in several experiments. The analysis of the experimental conditions did not allow us to explain the formation of two different forms by any recorded differences in the mode crystallization.

X-ray diffraction studies. Prior to X-ray data collection, the quality of the crystals was examined by optical methods. The samples were selected under a binocular microscope with a weakly diverging polarized beam. Isometric grains of dimensions $\sim 0.5 \times 0.5 \times 0.5$ mm having no noticeable mechanical impurities and intergrowth were shaped to spheres by abrasive grinding. The sampling was hampered by stresses resulting in substantial distortions of the profiles of X-ray diffraction reflections.

Particular difficulties were encountered in the work with the *F* phase, because its Laue patterns revealed a pronounced domain structure. Thus, several similar zonal lines slightly rotated with respect to each other were observed upon prolonged expositions. Therefore, several tens of crystals were examined.

The main characteristic features of four X-ray diffraction patterns were investigated with a higher degree of precision on an automated CAD 4F diffractometer. When performing automated indexing of the X-ray diffraction reflections and searching for orientation matrices, the characteristic features of the domain structure of the samples were revealed.

These characteristic features were examined in the following way. The complete list of reflections found according to a standard procedure comprised 25 reflections. In none of the cases was the orientation matrix found by automated indexing based on the complete list of reflections obtained by this procedure. Analysis of the complete set of reflections showed that these reflections can be divided into two groups according to their intensities, namely, into intense and weak reflections, the relative intensities of reflections belonging to the same group being substantially different. Each group of reflections was unambiguously indexed within the fluorite *F* unit cell with the unit-cell parameter typical of fluorite structures. The refinement of the unit-cell parameter using the same set of high-order reflections ($25° < \vartheta < 30°$) for both domains gave the same value (6.075(1) Å). This indicated that the crystals consisted of at least two domains having identical compositions. The ratios between the domain volumes, which were evaluated based on the intensity ratios for the reflections with the same indices measured for different domains, ranged from 1 : 2 to 1 : 20. The misorientation angles for the *a*-, *b*- and *c*-axes varied from 1° to 6°. No single-domain crystals were found.

The crystal of the *F* phase with the best ratio between the domain volumes (1 : 20) was chosen for the X-ray diffraction study. The angles between the corresponding crystallographic axes of the domains were as follows: $\angle a_1–a_2 = 5.012°$, $\angle b_1–b_2 = 1.293°$, and $\angle c_1–c_2 = 0.996°$. The experimental X-ray data were collected using monochromated MoK_α radiation (graphite monochromator, $\omega/2\theta$ scanning technique, $\sin\theta/\lambda \le 1$ Å).

When designing the experiment, we took into account that reflections from different domains can partly overlap in the detector window and thus be distorted. To avoid this, the measurement of each reflection was preceded by the rotation of the crystal around the diffraction vector *H*, which was brought into coincidence with the reflection position in the equatorial plane of the diffractometer. The angle of rotation was calculated in such a way that the diffraction vector *H*' corresponding to the reflection of the second domain was also located in the equatorial plane of the diffractometer. In this case, the diffraction nodes *H* and *H*' were separated by the maximum distance with respect to the ω angle, i.e., they are best suited to the individual measurements of intensities. Following this procedure, we succeeded in separating and measuring virtually all the reflections within the total sphere of the reciprocal space with $\sin\theta/\lambda \le 1$ Å^{-1}. As a result, we collected a rather complete X-ray data set from the domain of the *F* phase characterized by the maximum volume. The analysis of the reflection profiles demonstrated that we precluded to a large degree substantial overlapping of reflections from two domains present in the *F* phase.

For the *P* phase, the X-ray data were collected according to standard procedures from crystals of satisfactory quality.

The principal characteristics of X-ray data collection and selected data on the *P* and *F* phases are given in Table 1. For the *F* phase, the rather high *R* factor for the averaging of symmetrically equivalent reflections is attributable to the fact that the crystal contained the second domain, which could lead to distortions of the intensities of some reflections in the averaged groups. In such a case, one can either exclude the reflections from the averaging, which differ sharply in intensity from other symmetrically equivalent reflections, or try to eliminate the effect of absorption by the second domain by averaging a large number of equivalent reflections. In the case of the cubic symmetry of the crystal (the Laue class *m*3*m*), the maximum multiplicity of the reflection is equal to 48, which made it possible to eliminate the effect of absorption by the second domain upon averaging the intensities. All the calculations were carried out with the use of the JANA program package [2] taking into account dispersion corrections for X-ray scattering for the ions.

Table 1. Main characteristics of the crystals and details of X-ray diffraction studies

Composition	$Ba_{0.8}Yb_{0.2}F_{2.2}$	$Ba_{0.8}Yb_{0.2}F_{2.2}$
Notation	*P* phase	*F* phase
Sp. gr.	*Pm*3*m*	*Fm*3*m*
Unit-cell parameter,* *a*(Å)	6.096(1)	6.075(1)
Number of formula units in the unit cell	4	
Crystal shape	Sphere	Sphere
Size, cm	Diameter = 0.023	Diameter = 0.025
Diffractometer	Enraf-Nonius CAD-4	
Radiation	AgK_α	MoK_α
Absorption (μR)	1.41	2.33
$(\sin\theta/\lambda)_{max}$	1.26	1.0
Range of data collection	All *h* and *k*; *l* > 0	All *hkl*
Number of measured I_{hkl}	2205	1921
Number $I_{hkl} > 3\sigma(I)$	2041	1837
Number of independent reflections	142	72
R_{int}	0.02	0.048

* The unit-cell parameters of both phases were refined based on identical sets of reflections using MoK_α radiation.

STRATEGY OF THE REFINEMENT OF STRUCTURE MODELS

The crystal structures of both phases were refined by the full-matrix least-squares method based on $|F|$ with the weights $1/\sigma^2(|F|)$. The starting model was based on the fluorite structure without considering fluorine atoms in additional positions and their deficiency in the main position 8*c*. The refinement was carried out according to the procedures that we have generally used in studies of nonstoichiometric fluorite phases [3–5].

At the first stage, the weighted mean (80% of Ba and 20% of Yb with respect to the charge) atomic scattering curve was used for the cations. The conclusions about the complete splitting of the cationic positions (*P* phase) and the partial ordering of the cations (*F* phase) were drawn based on the analysis of difference electron density maps and the results of the refinement of the corresponding structure models.

At the final stages, the occupancies of all atoms were refined independently to check the chemical composition. The occupancies of the cationic positions were calculated taking into account that the sum of the Ba and Yb atoms per formula unit should be equal to unity. The total occupancy of the anionic positions was chosen based on the requirement of the electroneutrality.

To reduce the correlation between the thermal parameters and the occupancies (q) of the atomic positions, we employed step-by-step scanning [6]. According to this procedure, a series of fixed values were assigned to the occupancies q with a step of 0.02, and all other structure parameters were refined for each q. Based on the data obtained, the reliability factors were plotted against the occupancies in the form of $R_w = f(q)$. The values of q corresponding to the minimum of this function were taken as the solutions. The errors of the determination of the occupancies were estimated based on the confidence intervals for the functions minimized. The amounts of the barium and ytterbium atoms in the formulas of the phases under study were determined with an accuracy of ±0.03 of the atomic fraction (x).

According to the results of the refinement, the compositions of both phases were close (to within the accuracy of crystallographic calculations) to the nominal (with respect to the blend) chemical composition of the solid solutions under study.

The composition of the crystal was evaluated assuming that the equation for the dependence of the unit-cell parameter of the $Ba_{1-x}Yb_xF_{2+x}$ phase on the composition is applicable to both types of the cubic lattice (regardless of the defect structure). This dependence has been found previously [7] for solid solutions brought to equilibrium by annealing. At a = 6.096(1) Å, the *P* phase contained 13.7 mol % of YbF_3. For the crystals of the *F* phase, a = 6.075(1) Å, which corresponds to 16.5 mol % of YbF_3. The compositions determined by this method differ substantially from those obtained based on the structure data. The reasons for these differences call for further investigation.

The minimum *R* factors were obtained using a mixed extinction model (type I + type II) with the Lorentz distribution of mosaic blocks. The scaling factors, the extinction parameters (G) of the crystal, and the occupancies (q) for all atoms of the structures were refined based on complete X-ray diffraction data sets. The final results of the refinement of some structure models for the *P* and *F* phases are given in Tables 2 and 3, respectively. The data on the characteristic features of the structure models were obtained in the analysis of the diagonal $(1\bar{1}0)$ sections of the difference electron density maps (Figs. 1, 2). For the phases of this type, these sections are most informative, because they show the positions of all independent atoms of the crystal structures.

PRINCIPAL STRUCTURE FEATURES OF THE PHASES

***P* phase.** In the model of the fluorite structure that was examined at the first stage, the positions 1*a* (0, 0, 0) and 3*c* (0, 1/2, 1/2) were described with the use of the mixed atomic scattering curve (0.8Ba + 0.2Yb), and the fluorine atoms were located in the position 8*g* (x, x, x) at $x \approx 0.250$. The refinement with the use of this quan-

Table 2. Results of the refinement of different structure models of the *P* phase

Sort of the atom, Wyckoff position*, parameters refined, *R* factors	Structure models			
	I	II	III	IV
(Yb, Ba), 1*a*, (0, 0, 0):				
q_{Yb}	0.20	0.20	0.20	0.20
q_{Ba}	0.05	0.05	0.05	0.05
B_{iso} (Å^2)	1.51(2)	1.63(2)	1.69(3)	1.64(3)
Ba, 3*c*, (0, 1/2, 1/2):				
q	0.75	0.75	0.75	0.75
B_{iso} (Å^2)	0.98(4)	0.95(3)	0.95(3)	0.95(3)
F_g(1), 8*g*, (*x*, *x*, *x*):				
q	1.381(7)	1.394(7)	1.419(7)	1.409(6)
x	0.228(1)	0.228(1)	0.228(1)	0.228(1)
B_{iso} (Å^2)	1.34(3)	1.28(6)	1.36(9)	2.01(9)
F_g(2), 8*g*, (*x*, *x*, *x*):				
q		0.518(9)	0.492(9)	0.509(8)
x		0.287(3)	0.287(2)	0.287(2)
B_{iso} (Å^2)		2.09(7)	1.764(7)	2.11(6)
F_e, 6*e*, (*x*, 0, 0):				
q			0.21(1)	0.19(1)
x			0.397(3)	0.397(3)
B_{iso} (Å^2)			1.96(9)	2.01(9)
F_j, 12$_j$, (1/2, *y*, *y*):				
q				0.07(1)
y				0.180(2)
B_{iso} (Å^2)				2.01(9)
F_b, 1*b*, (1/2, 1/2, 1/2):				
q				0.02(1)
B_{iso} (Å^2)				1.55(7)
R (%)	4.56	2.87	2.43	2.19
R_w (%)	4.32	2.73	2.31	2.14
Sum of q_F	1.381(7)	1.912(8)	2.121(9)	2.198(9)

* The positions occupied by F ions are labelled by subscripts according to the nomenclature recommended by the International Tables for Crystallography. In the case of several positions of the same type, the numbers 1, 2, 3, etc. are used; for example, F_g(1) and F_g(2).

titative ratio between the cations located in the positions 1*a* and 3*c* converged to high reliability factors (R = 10.8% and R_w = 11.2%). The refinement of the compositions of the cationic positions together with the occupancy and the only coordination (x) of the major position of the fluorine atom substantially reduced the R factors (R = 4.56% and R_w = 4.3%), the cations being virtually completely ordered in the structure (model I, Table 2).

The difference electron density map calculated at this stage (Fig. 1a) clearly reveals the principal features of the structural defects in the *P* phase, namely, the residual electron density in the positions 1*b* (1/2, 1/2, 1/2), 6*e* (*x*, 0, 0) at x = 0.492, 12*j* (1/2, *y*, *y*) at y = 0.165, and 8*g* (*x*, *x*, *x*) at $x \approx 0.290$ and 0.201. In addition, the map shows maxima of the positive electron density and minima of the negative electron density, which are shifted from the major position of the F atoms (indicated by a cross in Fig. 1a) along the threefold axis. The presence of these maxima and minima is attributable to the anharmonicity of thermal vibrations of the F atom, which was subtracted.

The allowance made for anharmonicity (reduced to the only non-zero C^{123} component of the third-rank tensor) resulted in the reduction of the R factors (R = 2.87% and R_w = 2.73%, model II, Table 2), the corresponding difference map being virtually cleared of the density in the vicinity of the F atom (Fig. 1b).

Table 3. Results of the refinement of different structure models of the *F* phase

Sort of the atom, Wyckoff position, parameters refined, *R* factors	Structure models				
	I	II	III	IV	V
(Ba, Yb), 4*a*, (0, 0, 0):					
q_{Ba}	0.8	0.8	0.8	0.8	0.8
q_{Yb}	0.2	0	0	0	0
B_{iso} (Å^2)	1.13(2)	1.03(2)	1.09(3)	1.04(3)	1.06(3)
Yb, 32*f*, (*x*, *x*, *x*):					
q		0.2	0.2	0.2	0.2
x		0.0309(3)	0.0309(3)	0.0309(3)	0.0309(3)
B_{iso} (Å^2)		0.95(3)	0.95(3)	0.97(3)	0.97(3)
F_c, 8*c*, (1/4, 1/4, 1/4):					
q	1.576(6)	1.647(3)	1.651(4)	1.584(4)	1.584(4)
B_{iso} (Å^2)	1.96(2)	2.09(7)	2.09(7)	2.11(6)	2.14(7)
F_i, 48*i*, (1/2, *y*, *y*):					
q			0.249(9)	0.270(9)	0.286(8)
y			0.162(3)	0.160(2)	0.158(3)
B_{iso} (Å^2)			1.96(9)	2.01(9)	2.01(9)
F_f, 32*f*, (*x*, *x*, *x*):					
q				0.230(9)	0.26(1)
x				0.206(9)	0.206(9)
B_{iso} (Å^2)				1.97(8)	1.89(7)
F_a, 4*b*, (1/2, 1/2, 1/2):					
q					0.09(1)
B_{iso} (Å^2)					3.85(2)
R (%)	3.2	1.11	0.94	0.78	0.69
Sum of q_F	1.576(6)	1.647(5)	1.900(6)	2.084(8)	2.221(9)

At the final stage of the refinement involving the above-mentioned additional positions of the F atoms, the *R* factors were reduced to *R* = 2.19% and R_w = 2.14% (model IV, Table 2). It should be noted that the sum of the F atoms per formula unit, which corresponds to the electroneutrality of the compound (2.2) was obtained only when all positions in model IV (Table 2) were taken into account.

***F* phase.** At the first stage of the refinement based on the crystal structure of fluorite as the starting model with isotropic thermal parameters, only the mixed cationic position 4*a* (80% of Ba and 20% of Yb) and the major anionic position 8*c* were taken into account. The results of this refinement are presented as model I in Table 3 (*R* = 3.2% and R_w = 3.5%). The electron density distribution calculated based on these results is shown in Fig. 2a.

As in all $Ba_{1-x}R_xF_{2+x}$ fluorite phases studied by us previously [4, 5], the major anionic position F_c in model I is to a considerable degree vacant (Table 3), and the character of the residual electron density distribution is indicative of the presence of additional F_i atoms on twofold axes in the position (1/2, *y*, *y*) at $y \approx 0.165$.

Compared to the fluorite-type structures studied previously, model I of the *F* phase has three distinguishing features, which are clearly seen in Fig. 2a. First and foremost, there is a rather powerful (~0.7 e/Å^3) peak of the residual electron density in the position 32*f* (*x*, *x*, *x*) with $x \sim 0.03$ at a distance of ~0.32 Å from the mixed cationic position.

It is reasonable to relate the latter peak to the effect of the mutual relative displacement of the Yb and Ba atoms. The displacements of all Yb atoms from the position (0, 0, 0) to the position 32*f* (*x*, *x*, *x*) with $x \sim 0.03$ resulted in the substantial reduction of the *R* factors (*R* = 1.11% and R_w = 1.22%, model II, Table 3). The inclusion of the additional anionic position F_i (1/2, *y*, *y*) with $y \approx 0.165$, which is typical of this structure type, led to a further decrease in the R factors (*R* = 0.94% and R_w = 1.12%, model III, Table 3).

The second characteristic feature is that the difference electron density maps shown in Fig. 2 have the

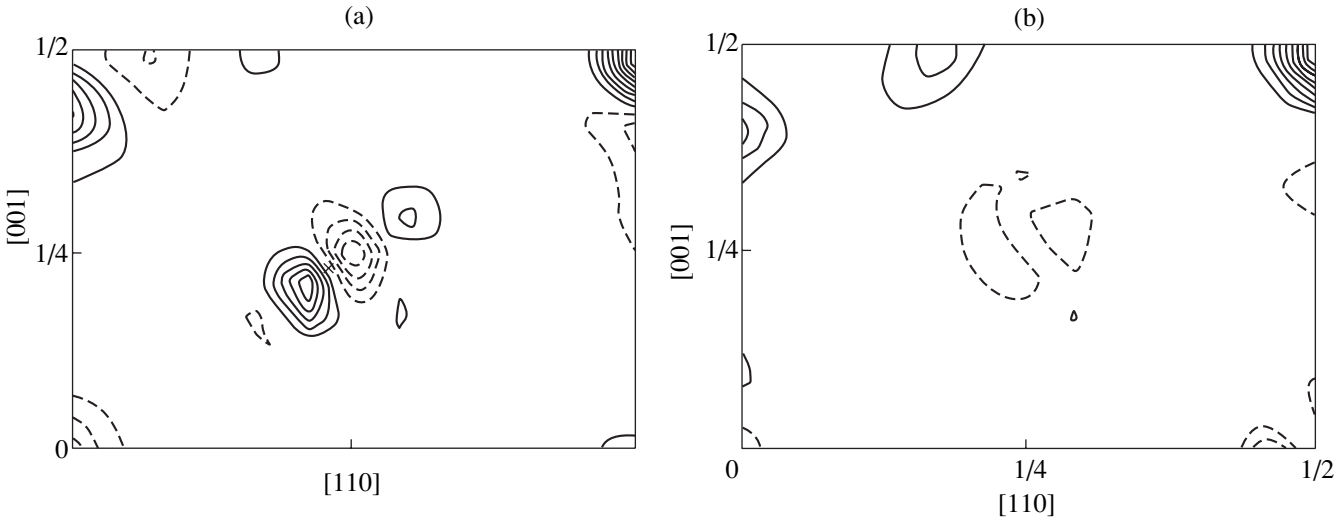

Fig. 1. Difference electron density maps for the *P* phase calculated using the structure parameters of models (a) I and (b) II (see Table 2).

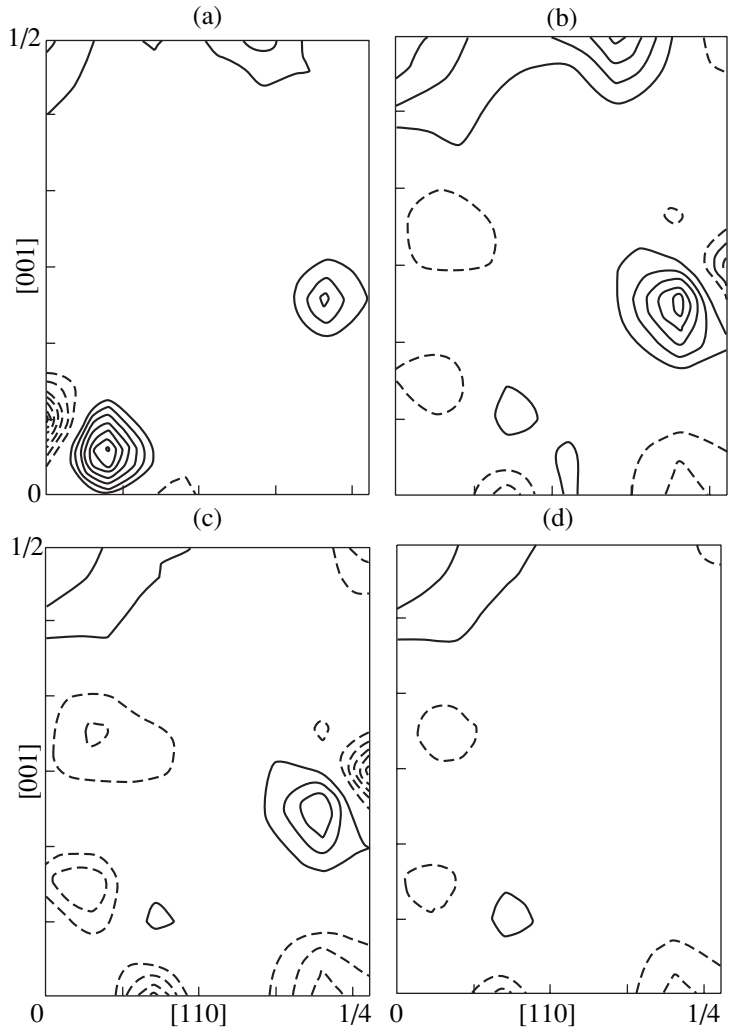

Fig. 2. Difference electron density maps for the *F* phase calculated using the structure parameters of models (a) I, (b) II, (c) III, and (d) IV (see Table 3).

residual positive electron density in the vicinity of the main position F_c (1/4, 1/4, 1/4). This density is shifted along the threefold axis toward the vertex of the cubic unit cell, i.e., toward the cationic position, rather than to the center of the cube, which is not occupied by cations, as is generally the case in analogous phases [8–10]. This residual density was taken into account in model IV (Table 3).

In addition, all electron density distributions shown in Fig. 2 have residual electron density in the centers of the unoccupied cubes of the fluorite structure. At the final stage, this additional position of the fluorine atoms was also included in the refinement of the structure parameters of the *F* phase (model V, Table 3; $R = 0.69\%$ and $R_w = 0.85\%$). The thermal vibrations of all atoms were refined isotropically.

CONCLUSIONS

The crystal structures of two new forms of the fluorite phases (*P* and *F* phases) of composition $Ba_{1-x}Yb_xF_{2+x}$ with $x = 0.20 \pm 0.03$ (based on the data of X-ray diffraction study) were established by X-ray analysis.

Among the numerous nonstoichiometric fluorite phases of composition $M_{1-x}R_xF_{2+x}$ (*M* = Ca, Sr, Ba, Cd, or Pb; *R* are rare-earth elements), the *P* phase provides the first example of the structure with the space group $Pm\bar{3}m$ different from that of CaF_2. This space group is a subgroup with respect to the higher-symmetry "fluorite" space group $Fm\bar{3}m$.

In the *F* phase, all Yb^{3+} cations are shifted with respect to the Ba^{2+} cations by 0.34 Å along the [111] direction, and the position of the "relaxed" anions (F_t) is shifted along the threefold axis toward the vertex of the cubic unit cell, i.e., toward the cationic position, rather than to the center of the cube, which is not occupied by cations, as is generally the case in analogous phases.

ACKNOWLEDGMENTS

This study was supported by the Russian Foundation for Basic Research (project no. 98-03-32805) and INTAS (project no. 97-32045).

REFERENCES

1. B. A. Maksimov, Yu. B. Gubina, E. L. Belokoneva, *et al.*, in *Proceedings of the I National Crystal Chemical Conference, Chernogolovka, 1998*, Part I, p. 133.
2. V. Petrisek, *CRYSTALLOGRAPHIC COMPUTING SYSTEM JANA 96* (Inst. of Physics, Academy of Sciences of the Czech Republic, Prague, 1996).
3. N. B. Grigor'eva, L. P. Otroshchenko, B. A. Maksimov, *et al.*, Kristallografiya **41** (4), 644 (1996) [Crystallogr. Rep. **41**, 607 (1996)].
4. L. A. Muradyan, B. A. Maksimov, V. B. Aleksandrov, *et al.*, Kristallografiya **31** (4), 661 (1986) [Sov. Phys. Crystallogr. **31**, 390 (1986)].
5. L. F. Malakhova, E. A. Zhurova, B. A. Maksimov, *et al.*, Kristallografiya **42** (2), 270 (1997) [Crystallogr. Rep. **42**, 232 (1997)].
6. T. S. Chernaya, N. N. Bydanov, L. A. Muradyan, *et al.*, Kristallografiya **33** (1), 73 (1988) [Sov. Phys. Crystallogr. **33**, 40 (1988)].
7. N. L. Tkachenko, L. S. Garashina, O. E. Izotova, *et al.*, J. Solid State Chem. **8** (3), 213 (1973).
8. A. K. Cheetham, B. T. F. Fender, D. Steele, *et al.*, Solid State Commun. **8**, 171 (1970).
9. J. P. Laval and B. Frit, J. Solid State Chem. **49**, 237 (1983).
10. L. A. Muradyan, B. A. Maksimov, and V. I. Simonov, Koord. Khim. **12** (10), 1398 (1986).

Translated by T. Safonova

Crystallography Reports, Vol. 47, No. 3, 2002, pp. 379–382. Translated from Kristallografiya, Vol. 47, No. 3, 2002, pp. 424–427.

STRUCTURES OF INORGANIC COMPOUNDS

Atomic Structure and High Anisotropy of Thermal Expansion in NiSi Single Crystals. II. Temperature-Induced Structural Changes

M. Kh. Rabadanov* and M. B. Ataev**

** Shubnikov Institute of Crystallography, Russian Academy of Sciences, Leninskiĭ pr. 59, Moscow, 117333 Russia*

e-mail: rab_mur@ns.crys.ras.ru

*** Institute of Physics, Dagestan Research Center, Russian Academy of Sciences, Makhachkala, Dagestan, Russia*

Received April 17, 2001

Abstract—X-ray diffraction analysis of the atomic structure of NiSi crystals was performed by diffraction data obtained at 295 and 418 K. The temperature-induced changes in the bond lengths and valence angles were analyzed and the high anisotropy of thermal expansion of these single crystals was interpreted in terms of crystal chemistry. *© 2002 MAIK "Nauka/Interperiodica".*

INTRODUCTION

The first part of this article [1] was dedicated to the precision structural studies of orthorhombic NiSi single crystals at 295 and 418 K. We established some relationships between the thermal parameters and the observed thermal expansion. The second part is dedicated to the crystallochemical analysis of the structure and the establishment of the relation between the atomic structure and high anisotropy of thermal expansion.

STRUCTURAL MOTIFS OF ATOMIC ARRANGEMENT

The orthorhombic MnP structure type (sp. gr. *Pnma*), to which NiSi crystals belong, can be considered pseudohexagonal and may be obtained by deformation of the NiAs structure [2]. Consider the coordination polyhedra of both atoms and their arrangement in the latter structure.

In this structure, each Si atom is surrounded by six Ni atoms forming a coordination polyhedron in the shape of a distorted trigonal [$SiNi_6$] prism. Figure 1 shows the projection of these polyhedra along the ***a***- and ***b***-axes (the fragment shown consists of three unit cells along the ***a***- and the ***b***-axes and two unit cells along the ***c***-axis). The filled and mirror-reflected empty trigonal prisms share their bases. These prisms alternate like a chessboard in the (010) plane and form chains of one-type prisms along the ***b***-axis. Numbers from *1* to *4* in Fig. 1 indicate different orientations of the filled prism related by various symmetry elements. An empty prism is shown by dashed lines. The layers of prisms *1* and *2* alternate with layers of prisms *3* and *4*. Each [$SiNi_6$]-polyhedron in the (010) plane is surrounded by four empty polyhedra. The filled prisms forming the rows along the ***b***-axis share edges, with their side faces forming corrugated planes. Since the distances between the protrusions are equal to the ***b***-parameter decreasing with an increase in the temperature [1], the corrugated planes slightly approach each other at higher temperatures.

Nickel atoms are surrounded with six silicon atoms located at the vertices of a strongly distorted octahedron. The Ni–Si bond lengths are equal to 2.279(1), 1.317(1), 2.317(1), 2.386(1), 2.399(1), and 2.399(1) Å at 295 K and 2.283(1), 2.321(1), 2.321(1), 2.390(1), 2.401(1), and 2.401(1) Å at 418 K. One of the Ni–Si bonds is considerably shorter than the other ones. The next nearest neighbors are four Ni atoms located at distances of 2.681(1)–2.685(1) Å at 295 K and 2.689(1)–2.690(1) Å at 418 K. The arrangement of the coordination octahedra of Ni atoms is shown in Fig. 2. As in [$SiNi_6$]-polyhedra, one can also distinguish four orientations of [$NiSi_6$]-octahedra indicated by numbers from *1* to *4* in Fig. 2. The structure can be represented by chains of distorted face-sharing [$NiSi_6$]-octahedra parallel to the ***a***-axis.

Considering the arrangement of atoms in the structure, one can also single out the zigzag chains of Ni atoms along the ***a***-axis with $d_{Ni–Ni}$ = 2.681(1) and 2.690(1) Å and angles of 149.72(1)° and 149.78(1)° at 295 and 418 K, respectively, the chains along the ***b***-axis with $d_{Ni–Ni}$ = 2.685(1) and 2.689(1) Å and angles of 76.67(1)° and 76.33(1)° at 295 and 418 K, respectively, and also the zigzag chains of Si atoms along the ***b***-axis with $d_{Si–Si}$ = 2.657(1) Å and an angle of 77.66(1)° at 295 K and $d_{Si–Si}$ = 2.660(1) Å and an angle of 77.32(1)° at 418 K (Fig. 3). With an increase in the temperature, the

1063-7745/02/4703-0379$22.00 © 2002 MAIK "Nauka/Interperiodica"

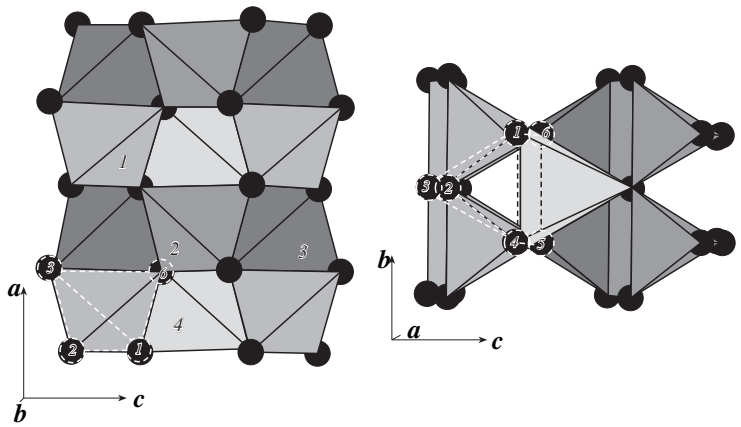

Fig. 1. Arrangement of [$SiNi_6$]-polyhedra in the NiSi structure. For explanation, see text.

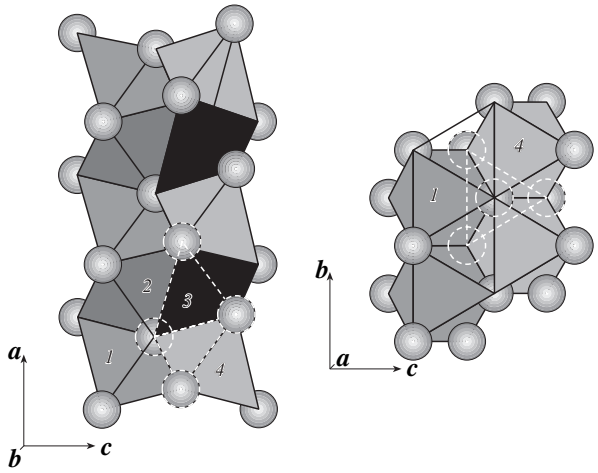

Fig. 2. Arrangement of [NiSi6]-polyhedra in the NiSi structure. For explanation, see text.

bond lengths in both Ni-chains also increase, with an almost double increase in the $d_{Ni–Ni}$ value in the chain along the ***a***-axis in comparison with its increase in the chain along the ***b***-axis. Thus, the first chain is slightly straightened, whereas the second one becomes slightly contracted. The Si chains along the ***b***-axis show insignificant increase in $d_{Si–Si}$ (by about 0.003(1) Å) and become folded with an increase in the temperature.

In addition to the Si–Si and Ni–Ni bonds formed in the above chains, the symmetry planes where all the atoms are located and which are normal to the ***b***-axis [1] also form rather strong Ni–Si bonds equal to 2.317(1) and 2.399(1) Å at 295 K and 2.321(1) and 2.401(1) Å at 418 K.

We also singled out the zigzag chains of Si atoms along the ***a***-axis characterized by considerable Si–Si distances which will be analyzed somewhat later. For comparison, we should like to indicate here that, at room temperature, the $d_{Si–Si}$ distance in a silicon crystal equals ~2.35 Å and the $d_{Ni–Ni}$ distance in a nickel crystal, ~2.49 Å.

CRYSTALLOCHEMICAL INTERPRETATION OF HIGH ANISOTROPY OF THERMAL EXPANSION AND NEGATIVE THERMAL EXPANSION ALONG THE ***b***-AXIS

To clarify the mechanism of formation of high anisotropy of thermal expansion [4], consider the bond lengths and valence angles at two of the above temperatures (we do not indicate the standard deviations because they did not exceed 0.001 Å for bond lengths and 0.01° for valence angles). Consider the geometry of the mutual arrangement of atoms in two adjacent unit cells along the ***b***-axis (for the sake of convenience, all the atoms in Fig. 4 are numbered) and in the symmetry planes (Fig. 5). It should also be indicated that, despite the considerable negative expansion of the crystal along the ***b***-axis, all the bond lengths increase with an increase in the temperature. The maximum elongation is observed for the Ni1–Ni3 bonds (from 2.681 to 2.690 Å) and Si2–Si4 bonds (from 3.197 to 3. 214 Å). The Ni3–Si4–Ni7–Si8, Si4–Ni11–Si16–Ni7, and Ni11–Si22–Ni15–Si16 parallelograms with the Ni–Si bonds can be considered as rather rigid. The valence

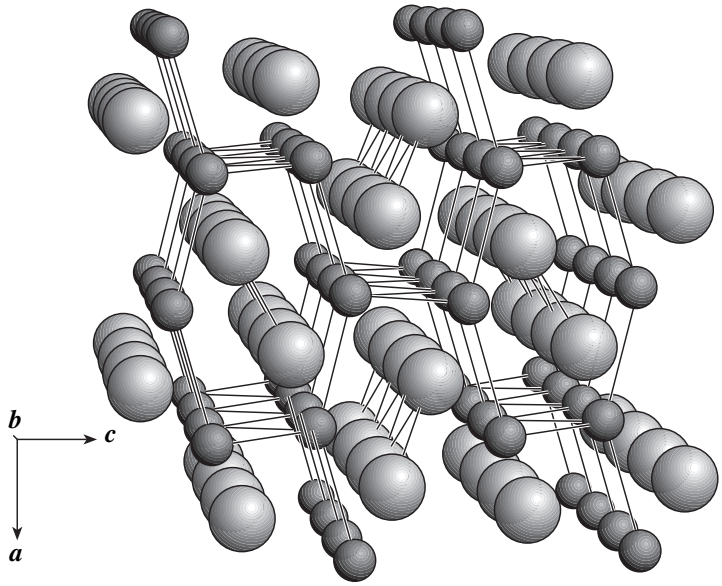

Fig. 3. Chains of Ni–Bi and Si–Si atoms in the NiSi structure. Filled and the empty circles indicate Ni and Si atoms, respectively.

angles in these parallelograms practically do not change with an increase in the temperature.

With a rise in temperature, the Ni1–Ni3–Si8 and Ni9–Ni11–Si16 and also the Ni7–Ni5–Si4 and Ni15–Ni13–Si12 triangles approach each other along the ***b***-axis, whereas the Ni1–Si2–Ni9 and Ni3–Si2–Ni11 valence angles become smaller. The Si2–Ni1–Si8 and Si2–Ni3–Si8 angles decrease only slightly; i.e., the change in the tilt of the plane of the Ni1–Si2–Ni3 triangle to the plane of the Ni1–Ni3–Si8 triangle is very small despite the fact that the Si2–Si4 and Si2–Ni7 distances increase from 3.197 and 3.507 to 3.214 and 3.525 Å, respectively. The Ni1–Si2–Ni3 and Ni9–Si2–Ni11 angles increase because of the longer Ni1–Ni3 and Ni9–Ni11 bonds. Thus, an increase in the Ni1–Ni3 bond length results in the fact that, despite the practical preservation of the angles formed by the planes of the Ni1–Ni3–Si8, Ni1–Ni3–Si2, and Si2–Ni9–Ni11 triangles, the Ni1–Si2–Ni9 and Ni3–Si2–Ni11 valence angles become smaller.

On the other hand, with an increase in the temperature, the Ni3–Si4–Ni11, Si8–Ni7–Si16, Si4–Ni11–Si12, and Ni7–Si16–Ni15 valence angles become also smaller, whereas the Ni1–Si8–Ni7 and Ni1–Ni3–Si4 angles become larger. As a result, the zigzag band of the rigid Ni3–Si4–Ni7–Si8 and Si4–Ni11–Si16–Ni7 parallelograms with the axis directed along the ***b***-axis is compressed. It is also interesting that the Ni1–Ni3–Ni7 and Ni9–Ni11–Ni15 valence angles (100.12° and 100.14° at 295 and 418 K, respectively) and the Si4–Ni7–Si6 and Si2–Ni3–Si8 valence angles (93.36° and 93.38° at 295 and 418 K, respectively) remain practically unchanged. This flattening is associated with an increased distance between the Ni1–Ni3–Si8 and the Ni7–Si4–Ni5 triangles in the plane normal to the ***b***-axis. Therefore, the more pronounced the expansion in this plane, the more pronounced the compression along the ***b***-axis should be. Experiment [4] showed that the absolute values of thermal expansion coefficients along all the three main crystallographic axes are almost equal.

Thus, an increase in the bond lengths between the atoms located in the symmetry planes results in the approach of these planes to one another and the compression of the crystal along the ***b***-axis. Therefore, it is expedient to consider the arrangement of the atoms in the symmetry planes in more detail.

Atoms of both kinds form the zigzag chains in the symmetry planes along the ***a***-axis. It should be indicated that the "teeth" of the Si-chains in the neighboring planes are aligned in the same direction (along the ***c***-axis), whereas the teeth of the Ni-chains in these planes are aligned in the opposite direction. In Si-chains, with an increase in the temperature, the angles decreased from 108.06° to 107.81°, whereas the Si–Si bond lengths increased from 3.197 to 3.214 Å. The situation in the Ni-chains is somewhat different: the bond lengths increased from 2.681 to 2.690 Å, whereas the valence angles changed insignificantly—from 149.72° to 149.78°. Thus, with an increase in the temperature, the zigzag shape of the Si chains became more pronounced, whereas the Ni-chains became more smooth.

To analyze the thermal expansion along the ***c***-axis, we have to consider the heights of the *AHG*, *BHF*, *BCF*, and *DCE* triangles "forming" the parameter *c* of the unit cell. The heights of the *AHG*, *BHF*, and *DCE* triangles are almost constant (1.5162 and 0.7015 Å at 295 K and 1.5166 and 0.7012 at 418 K). All the changes in this parameter are reduced to the change of the height of the *BCF* triangle from 1.878 to 1.894 Å. Thus, the pro-

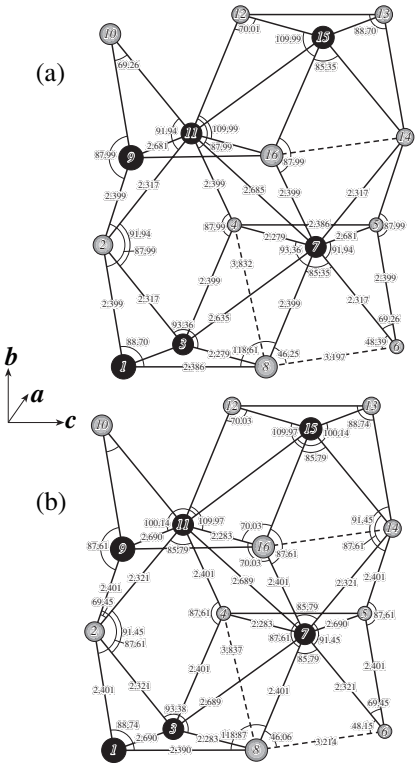

Fig. 4. Geometry of the arrangement of atoms in the NiSi structure at (a) 295 and (b) 418 K. Two unit cells along the ***b***-axis are shown. Filled and empty circles indicate Ni and Si atoms, respectively.

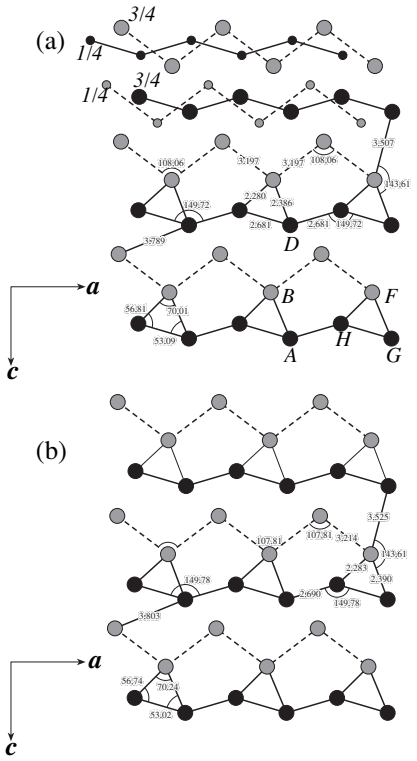

Fig. 5. Arrangement of atoms in the symmetry planes in the NiSi structure at (a) 295 K and (b) 418 K. For explanation, see text.

nounced thermal expansion observed along the ***c***-axis is associated with the more pronounced zigzag shape of the Si-chains. The analysis of the heights of the triangles forming the ***a***-parameter shows that they increase relatively uniformly (from 1.7033 and 0.8848 Å at 295 K to 1.7065 and 0.8906 Å at 418 K). Thus, the considerable thermal expansion observed along the ***a***-axis is associated with an increase in the Ni–Ni and Si–Si bond lengths in the corresponding chains.

CONCLUSIONS

Returning to Fig. 4, we see that, on the one hand, an increase in the Ni–Ni bond lengths resulting in an increase in the Ni1–Si2–Ni3 valence angle (from 69.26° to 69.45°) and a decrease in the Ni1–Si2–Ni9 and Ni3–Si4–Ni11 valence angles and, on the other hand, an increase in the Si–Si bond length resulting in an increase in the Si2–Ni3–Si4 and Si8–Ni7–Si6 bond angles (from 85.35° to 85.79°) and the Ni3–Ni7–Si6 and Si2–Ni3–Si7 valence angles (from 88.70° to 89.11°) lead to the mutual approach of the Ni1–Ni3–Si8, Si4–Ni7–Ni5, and Ni9–Ni11–Si16 triangles along the ***b***-axis. This, in turn, gives rise to the crystal compression along this axis with an increase in the temperature.

Concluding the article, we should like to emphasize that negative and zero thermal expansion is observed in many single crystals [5–8]. For a better understanding of the nature of thermal expansion, one has to perform a detailed crystallochemical analysis of all the data obtained in each case.

REFERENCES

1. M. Kh. Rabadanov and M. B. Ataev, Kristallografiya **47** (1), 31 (2002) [Crystallogr. Rep. **47**, 33 (2002)].
2. E. I. Gladyshevskiĭ, *Crystal Chemistry of Silicides and Germanides* (Metallurgiya, Moscow, 1971).
3. M. P. Shaskol'skaya, *Crystallography* (Vysshaya Shkola, Moscow, 1984).
4. S. M. Barmin and A. A. Frolov, Fiz. Tverd. Tela (Leningrad) **32** (5), 1535 (1990) [Sov. Phys. Solid State **32**, 897 (1990)].
5. S. I. Novikova, *Thermal Expansion of Solids* (Nauka, Moscow, 1974).
6. R. Roy and D. Agrawal, Nature **388** (6641), 433 (1997).
7. T. A. Mary, J. S. O. Evans, T. Vogt, and A. W. Sleight, Science **272**, 90 (1996).
8. A. U. Sheleg, E. M. Zub, L. A. Stremoukhova, and A. M. Luginets, Fiz. Tverd. Tela (St. Petersburg) **39** (6), 1038 (1997) [Phys. Solid State **39**, 932 (1997)].

Translated by L. Man

Crystallography Reports, Vol. 47, No. 3, 2002, pp. 383–389. Translated from Kristallografiya, Vol. 47, No. 3, 2002, pp. 428–434.

STRUCTURES OF INORGANIC COMPOUNDS

X-ray Diffraction Proof of Noncentrosymmetricity of the HTCS Crystals of the 1–2–3 Family

I. M. Smyt'ko

Institute of Solid State Physics, Russian Academy of Sciences, Chernogolovka, Moscow oblast, 142432 Russia

e-mail: shim@issp.ac.ru

Facultad de Ciencias, C-9 Universidad Autónoma de Madrid, Cantoblanco, Madrid E-28049, Spain

Received December 16, 1999; in final form, August 2, 2001

Abstract—X-ray diffraction and X-ray topography analysis of $Re Ba_2Cu_3O_x$ crystals (Re = Eu, Gd, Y) has demonstrated the noncentrosymmetricity of their atomic structure. It is shown that the centrosymmetricity of these crystals could not have been revealed in the previous structural studies because of their polydomain nature (the crystals consist of antiphase domains) and the use of hard MoK_α radiation. *© 2002 MAIK "Nauka/Interperiodica".*

It is commonly accepted that high-temperature superconducting crystals (HTCS) of the $Re Ba_2Cu_3O_x$ family have centrosymmetric structures. Nevertheless, a number of studies [1–3] cast doubt on this statement. In particular, it was shown [1] that highly perfect $EuBa_2Cu_3O_{x<6.5}$ single crystals grown in alundum crucibles consist of domains whose black–white X-ray topographic contrast formed in the mode of the Borrmann effect is changed to a reverse one in the transition from the $h00$ to the $h00$ reflections. The noncentrosymmetricity in this case was explained by the possible replacement of Cu atoms by Al atoms from the crucible material and the possible existence of noncentrosymmetric phases on the $EuBa_2Cu_{(3-y)}Al_yO_x$ phase diagram.

Below, we present the X-ray diffraction data indicating the noncentrosymmetricity of the $EuBa_2Cu_3O_{x<6.5}$ atomic structure and show that the $GdBa_2Cu_3O_{x<6.5}$ and $YBa_2Cu_3O_{\sim 7.0}$ crystals are also noncentrosymmetric. The results obtained lead to the assumption that not only these representatives of the 1–2–3 family are noncentrosymmetric, but also all the other members of this family are noncentrosymmetric irrespective of the rare earth atoms in their composition and the oxygen concentration.

The crystallographic characteristics of the crystals studied are listed in Table 1. The unit-cell parameters of all the crystals were determined by the least squares method using a set of 47 reflections for $YBa_2Cu_3O_{\sim 7.0}$, 45 reflections for $GdBa_2Cu_3O_{x<6.5}$, and 87 reflections for two-domain and 93 reflections for single-domain $EuBa_2Cu_3O_{x<6.5}$ crystals. These sets of reflections were recorded on a P4 Siemens complex for structural studies by scanning the reciprocal space with the use of the REFL_ARRAY procedure always preceding the conventional structural experiment and providing the determination of the unit-cell parameters and sample orientation with respect to the goniometer axes.

All the crystals were grown by the slow cooling of the melted mixture of Re_2O_3, BaO, and CuO oxides. We studied the selected black samples in the shape of rectangular plates with mirror-smooth faces and the normal to the large face coinciding with the [001] direction. The domain nature of the $EuBa_2Cu_3O_{x\le 6.5}$ samples was established from the angular-scanning topographs [4], and CuK_α radiation provided X-ray diffraction in the mode of the Borrmann effect. The topographs of various reflecting planes of sample no. 2 consisting of two large 90°-domain complexes are shown in Fig. 1. They clearly demonstrate not only the noncentrosymmetricity of this crystal, but also the direction of sublattice displacement along the [100] direction [1].

The $GdBa_2Cu_3O_x$ sample was prepared from a single crystal showing superconducting properties at ~92 K subjected to 18-h-vacuum annealing at 600°C in order to remove twins and homogenize the defects in the crystal bulk. The high quality of this sample is confirmed by the spectrum of ω-scanning on an AFC6S diffractometer (Rigaku Denki, Japan) (Fig. 2a).

The $YBa_2Cu_3O_{\sim 7.0}$ crystal had a well-developed twin structure. The temperature of the transition into the superconducting state was $T_c \approx 93$ K with the width of the transition being ~3 K.[1] Figure 2b shows the spectrum of ω-scanning of this sample. Three diffraction reflections indicate the well-developed twin structure

[1] The temperatures of the transition to the superconducting state for all the samples were determined from the temperature dependence of magnetic susceptibility. For the initial $EuBa_2Cu_3O_x$ samples and the annealed $GdBa_2Cu_3O_x$ samples, no superconductivity was revealed at all, which led to the conclusion that the oxygen content in these samples did not exceed $x \le 6.5$.

1063-7745/02/4703-0383$22.00 © 2002 MAIK "Nauka/Interperiodica"

Table 1. Crystallographic characteristics of samples studied

Sample	Single-domain $EuBa_2Cu_3O_x$	Two-domain $EuBa_2Cu_3O_x$	14-h-vacuum-annealed $GdBa_2Cu_3O_x$ at 600°C	Polytwinned $YBa_2Cu_3O_{\sim 7.0}$
Dimensions, mm^3	$0.04 \times 1.25 \times 1.25$	$0.04 \times 1.60 \times 1.10$	$0.007 \times 1.40 \times 1.25$	$0.040 \times 0.42 \times 0.30$
V, Å^3	178.19	178.08	178.19	174.36
ΔV, Å^3	0.07	0.06	0.05	0.12
a, Å	3.8969	3.8987	3.8956	3.8742
Δa, Å	0.0006	0.0006	0.0008	0.0020
b, Å	3.8954	3.8914	3.9015	3.8415
Δb, Å	0.0007	0.0009	0.0007	0.0022
c, Å	11.7384	11.7377	11.7241	11.7156
Δc, Å	0.0016	0.0017	0.0022	0.0031
α, deg	90.027	90.084	90.009	89.985
$\Delta\alpha$, deg	0.009	0.013	0.013	0.030
β, deg	90.012	90.006	89.975	90.022
$\Delta\beta$, deg	0.009	0.012	0.015	0.031
γ, deg	89.972	89.994	89.955	90.024
$\Delta\gamma$, deg	0.011	0.014	0.015	0.041
μt_0	6.11	6.12	1.10	4.28

of the sample formed during the transformation of the tetragonal unit cell into an orthorhombic one [5]. Two side reflections show the twin orientations which belong to the same twinning plane normal to the (110) reflection plane. The central peak also reflects two twin orientations, but they belong to the $(1\bar{1}0)$ twinning plane parallel to the reflecting planes. In this case, both twin components coincide in ω-scanning. The integrated intensity of the central reflection is approximately equal to the sum of the integrated intensities of the side reflections, which indicates that the volume fractions of all four twin components of the orthorhombic phase are approximately equal.

For each of the samples, we collected standard sets of X-ray diffraction reflections necessary for the determination of their atomic structure. In most of the experiments, we used copper radiation. In the case of a single-domain $EuBa_2Cu_3O_{x \le 6.5}$ crystal, we also used molybdenum radiation. The experiments with the use of CuK_α radiation were made on a P4 Siemens X-ray complex for structural studies with a rotating anode (Germany). The experiments with the use of the MoK_α radiation were made on an AFC8S apparatus with a sealed tube (Rigaku Denki, Japan). In both types of experiments, the crystal was centered with an accuracy of ±10 μm. The diameter of the primary-beam collimators was 0.5 mm. All the samples were oriented in the same way with respect to the goniometer axes; that is, the normal to the broad face coincided with the incident beam, whereas one of the (100) faces was approximately parallel to the vertical ω-axis of the goniometer.

The geometrical characteristics of the samples (Table 1) and the geometry of the experiment show that, for several orders of the $h00$, $0k0$, and $hh0$ reflections from the first three crystals, the incident beam remained within the crystal boundaries. This fact is very important because in this case we recorded only the radiation diffracted in the transmission (Laue) geometry and only from the internal parts of the samples, and moreover the diffraction from the $(hk0)$ and $(\bar{h}\bar{k}0)$ planes was recorded from the same regions of the crystal. In the case of the $YBa_2Cu_3O_{7.0}$ crystals, the specimen was "bathed" in the primary beam and, thus, the internal parts of the crystals provide the Laue diffraction, whereas the boundary regions provide the Bragg diffraction (in the reflection geometry).

The analysis described below is based on the comparison of the structure factors $F(hkl)$ and $F(\bar{h}\bar{k}\bar{l})$, which, for noncentrosymmetric structures, can be different (violation of the Friedel law). The structure factors for the samples studied are listed in Tables 2 and 3. Table 2 indicates the structure factors obtained with the use of CuK_α radiation, for which the reflecting $(hk0)$ planes are normal to the sample surface (the symmetric Laue case), and the structure factors for the $00l$-type reflections from the well-developed surfaces corresponding to the symmetric Bragg case. Since the direction of the [001] axis coincided with the normal to the broad face of the sample, the effective thickness of the crystal for all the $(hk0)$ reflections was the same (in the Borrmann diffraction, X-rays propagate along the reflecting planes). The hkl-type reflections with nonzero indices are not indicated in the tables, hence they

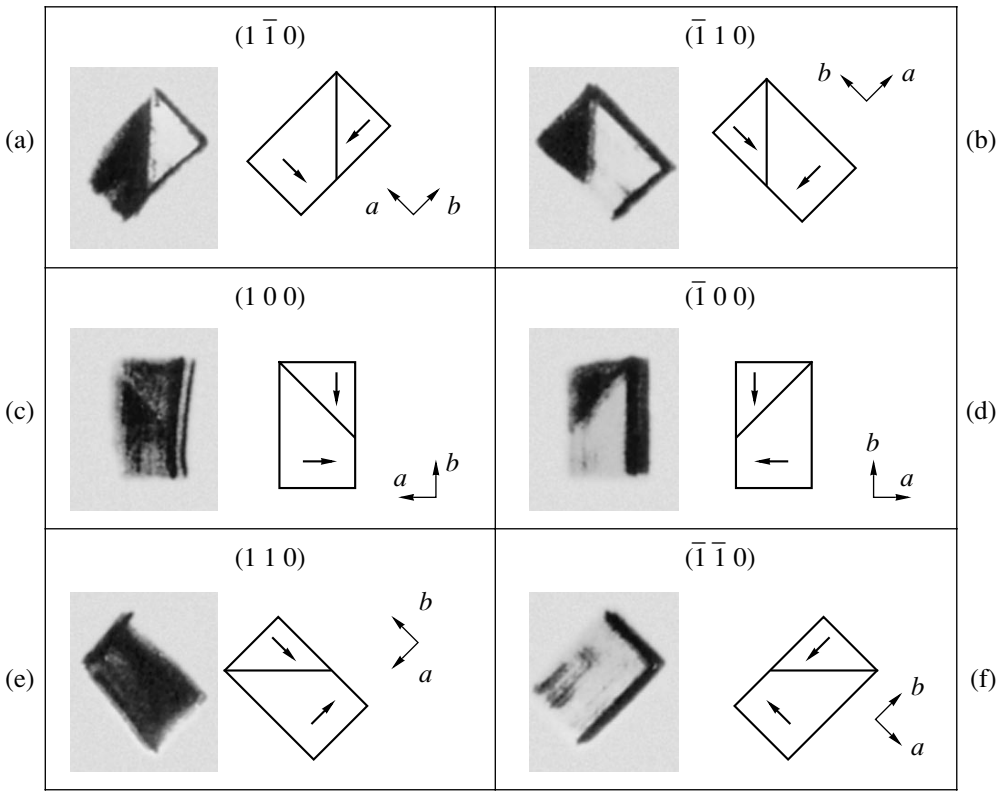

Fig. 1. Topographs of angular scanning of two-domain $EuBa_2Cu_3O_{x<6.5}$ single crystals: (a) $1\bar{1}0$, (b) $\bar{1}10$, (c) 100, (d) $\bar{1}00$, (e) 110, and (f) $\bar{1}\bar{1}0$ reflections.

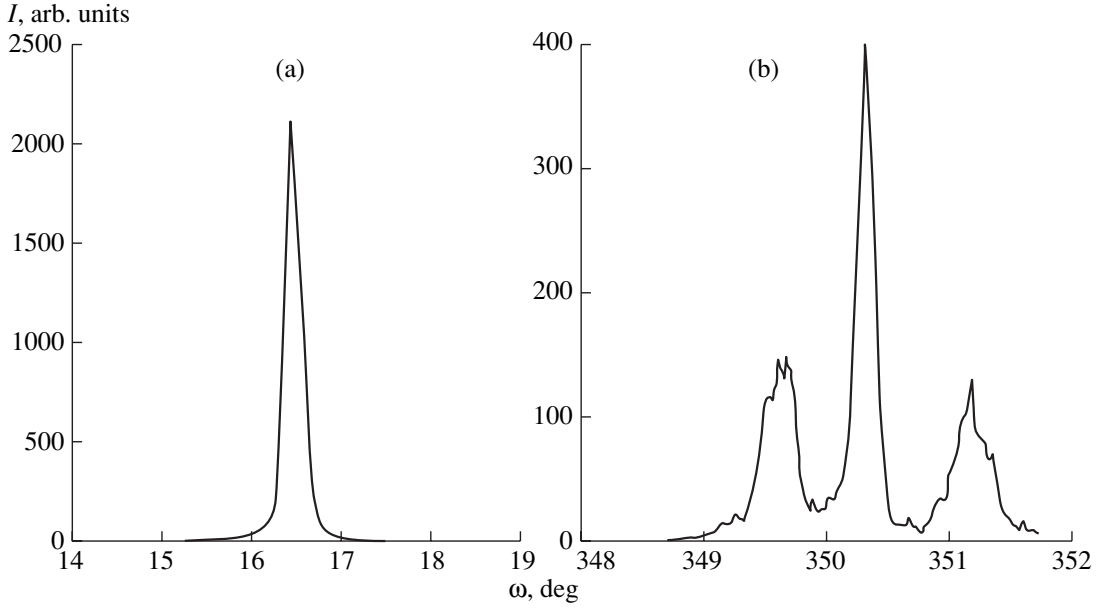

Fig. 2. Spectra of ω-scanning for a single-domain (a) $EuBa_2Cu_3O_{x<6.5}$ and (b) twinned single-domain $YBa_2Cu_3O_{\sim 7.0}$ single crystals, 110 reflection.

Table 2. Structure factors of $Re Ba_2Cu_3O_x$ crystals (CuK_α radiation)

$EuBa_2Cu_3O_x$ no.1 (single-domain sample)			$EuBa_2Cu_3O_x$ no. 2 (two-domain sample)			$GdBa_2Cu_3O_x$ (vacuum annealed at 600°C)			$YBa_2Cu_3O_{\sim 7.0}$ (twinned sample (A3))		
hkl	*F*(*hkl*)	σ, *F*(*hkl*)	*hkl*	*F*(*hkl*)	σ, *F*(*hkl*)	*hkl*	*F*(*hkl*)	σ, *F*(*hkl*)	*hkl*	*F*(*hkl*)	σ, *F*(*hkl*)
100	18.69	0.29	100	32.42	0.30	010	1065.80	16.52	100	544.37	10.27
$\bar{1}00$	299.93	1.13	$\bar{1}00$	11.76	0.18	$0\bar{1}0$	1104.49	16.76	$\bar{1}00$	482.31	9.77
200	124.91	1.47	200	131.55	1.08	020	2369.82	38.51	200	3239.68	37.97
$\bar{2}00$	1136.10	4.40	$\bar{2}00$	58.37	0.72	$0\bar{2}0$	2565.43	40.05	$\bar{2}00$	3248.12	32.13
300	8.02	0.37	300	3.30	0.11	030	759.19	25.92	300	100.48	2.81
$\bar{3}00$	45.83	1.23	$\bar{3}00$	2.67	0.08	$0\bar{3}0$	729.11	25.33	$\bar{3}00$	73.18	2.06
400	6.55	0.38	400	6.14	0.19	040	1016.44	24.85	400	59.02	2.53
$\bar{4}00$	62.96	1.86	$\bar{4}00$	3.36	0.11	$0\bar{4}0$	1053.23	25.12	$\bar{4}00$	90.85	2.30
010	201.96	0.93	010	5.10	0.12	100	680.86	13.14	010	526.49	10.44
$0\bar{1}0$	173.47	0.86	$0\bar{1}0$	40.25	0.33	$\bar{1}00$	1078.83	16.49	$0\bar{1}0$	383.03	10.16
020	685.36	3.44	020	26.09	0.47	200	1693.59	32.14	020	3918.54	35.80
$0\bar{2}0$	677.59	3.40	$0\bar{2}0$	190.96	1.28	$\bar{2}00$	3996.44	49.16	$0\bar{2}0$	3748.26	33.92
300	80.23	1.89	030	0.40	0.03	300	511.91	21.05	030	150.55	3.97
$0\bar{3}0$	58.16	1.49	$0\bar{3}0$	3.49	0.11	$\bar{3}00$	700.57	24.56	$0\bar{3}0$	124.95	3.44
110	174.36	1.10	110	180.27	0.89	110	2145.87	28.66	$1\bar{1}0$	3475.10	29.35
$\bar{1}\bar{1}0$	1326.24	3.04	$\bar{1}\bar{1}0$	54.97	0.49	$\bar{1}\bar{1}0$	2166.31	28.75	$\bar{1}10$	1683.04	21.05
220	58.24	1.41	220	60.91	1.16	220	2353.50	44.37	$2\bar{2}0$	2240.19	24.56
$\bar{2}\bar{2}0$	609.56	6.51	$\bar{2}\bar{2}0$	20.12	0.67	$\bar{2}\bar{2}0$	2425.26	44.99	$\bar{2}20$	1502.38	20.12
120	9.55	0.30	120	9.72	0.23	120	981.65	26.00	$\bar{1}20$	224.12	5.49
$\bar{1}\bar{2}0$	129.67	1.80	$\bar{1}\bar{2}0$	1.53	0.05	$\bar{1}\bar{2}0$	909.29	25.08	$1\bar{2}0$	245.92	6.00
210	15.06	0.40	210	9.60	0.23	210	938.00	25.66	$2\bar{1}0$	332.04	9.90
$\bar{2}\bar{1}0$	108.56	1.66	$\bar{2}\bar{1}0$	2.01	0.06	$\bar{2}\bar{1}0$	872.01	24.55	$\bar{2}10$	251.51	6.02
130	63.91	1.71	130	20.75	0.54	130	1236.40	33.06	$\bar{1}30$	943.32	14.58
$\bar{1}\bar{3}0$	232.84	5.40	$\bar{1}\bar{3}0$	7.31	0.22	$\bar{1}\bar{3}0$	1302.01	33.96	$1\bar{3}0$	792.86	13.67
310	13.43	0.51	310	21.22	0.53	310	1822.17	39.91	$3\bar{1}0$	825.82	13.48
$\bar{3}\bar{1}0$	255.77	5.66	$\bar{3}\bar{1}0$	9.41	0.27	$\bar{3}\bar{1}0$	1534.64	37.03	$\bar{3}10$	678.29	12.81
$00\bar{6}$	8278.00	11.84	006	1784.43	3.92	006	5658.27	58.92	006	9397.29	51.39
006	8515.89	12.02	$00\bar{6}$	1688.87	3.85	$00\bar{6}$	6279.76	61.99	$00\bar{6}$	8787.00	49.47
007	4727.24	11.77	007	1087.37	3.71	007	3412.66	49.69	007	3034.18	29.36
$00\bar{7}$	4905.29	11.97	$00\bar{7}$	1051.27	3.68	$00\bar{7}$	3607.45	51.21	$00\bar{7}$	3143.12	29.81

can be oriented inadequately because of different absorption coefficients (the Bragg–Laue geometry), which results in considerably different $F(hkl)$ and $F(\bar{h}\bar{k}\bar{l})$ structure factors.

Comparing the structure factors listed in Table 2, one can see that all the crystals studied are noncentrosymmetric. Moreover, different structure factors obtained for the coordinate directions show that the direction of the lattice displacements in a single-domain $EuBa_2Cu_3O_x$ crystal is parallel to the [100] direction, because, for the (0*k*0) reflections, the $F(0k0)/F(0\bar{k}0)$ ratio is close to unity, whereas for the (*h*00) reflections, the $F(h00)$ and $F(\bar{h}00)$ differ more than tenfold.

For a two-domain $EuBa_2Cu_3O_x$ sample, the structure factors for both (*h*00) and $(\bar{h}00)$ reflections and also for the (0*k*0) and $(0\bar{k}0)$ reflections are different. It seems that, in this case, the direction of the lattice displacement should differ from the coordinate axes of the unit cell. However, in actual fact, it is not so, which is proved by the fact that for the (*hk*0) reflections (with $h \neq 0$ and $k \neq 0$), the value of the $F(hk0)/F(\bar{h}\bar{k}0)$ ratio is lower than for the (*h*00) and (0*k*0) reflections, whereas the structure factors for the (00*l*) and $(00\bar{l})$ reflections are approximately equal. This contradiction can readily be interpreted with the aid of the topographs of angular scanning of this crystal shown in Fig. 1. It is seen that the crystal consists of two polydomain complexes of 180°-antiphase domains, for which the directions of the sublattice displacements are perpendicular (90° domains). Therefore the real change of the $F(h00)$ and $F(\bar{h}00)$ structure factors for the (*h*00) reflections leads to the formation of one domain complex whereas for the perpendicular orientation, it yields another domain complex for which the direction of the sublattice displacement also coincides with the [100] direction but is rotated by 90°. Different volumes of these domain complexes give rise to changes in the $F(0k0)/F(0\bar{k}0)$ and $F(h00)/F(\bar{h}00)$ ratios (Table 3).

The regular domains indicate a possible phase transition in the crystals of the $ReBa_2Cu_3O_x$ family. Within this interpretation of the domain structure of the 1–2–3 crystals, one can assume that their high-temperature phases are centrosymmetric, sp. gr. *P*4/*mmm*. Upon the phase transition provided by the displacement of the sublattices of different atoms along the [100] or the [110] direction, the phase symmetry is lowered to at least *Pmm*2, and the crystal acquires a domain structure.[2] Since the [100], $[\bar{1}00]$, [010], and $[0\bar{1}0]$ directions in the highly symmetric phase are equivalent, the phase transition should result in the formation of both 90° domains and antiphase 180° domains with the directions of atom displacements in the neighboring domains coinciding with the [100] and $[\bar{1}00]$ and also with the [010] and $[0\bar{1}0]$ directions. The latter statement is confirmed by the topographs of angular scanning where each 90°-domain complex has a striated contrast provided by the different intensities of the (*h*00) and $(\bar{h}00)$ reflections in the adjacent domains.

Generally speaking, the observation of the domain contrast is an accidental event; this contrast can be observed only for crystals with either very large domains, which manifest themselves in the topographs, or for crystals in which the volume of a domain of certain orientation considerably exceeds the volumes of domains of other orientations. In the general case, crystals are divided into microdomains of approximately equal volume along different directions of the sublattice displacement. Then, in the diffraction experiment at a level of macroscopically averaged values of the measured integrated characteristics for the $F(hkl)$ structure factor, the crystal looks centrosymmetric. In this connection, it is not surprising that in the conventional

Table 3. Structure factors for single-domain $EuBa_2Cu_3O_x$ crystal measured using MoK_α radiation ($\mu t_0 \approx 0.5$)

hkl	*F*(*hkl*)	σ, *F*(*hkl*)	*hkl*	*F*(*hkl*)	σ, *F*(*hkl*)
$\bar{1}00$	89.51	0.15	330	280.59	0.37
100	91.77	0.15	$\bar{3}\bar{3}0$	253.04	0.37
$\bar{2}00$	177.59	0.22	$3\bar{3}0$	255.27	0.37
200	183.98	0.22	$\bar{3}30$	282.80	0.37
$\bar{3}00$	110.55	0.30	440	231.79	0.46
300	108.48	0.29	$\bar{4}\bar{4}0$	214.91	0.46
$\bar{4}00$	164.55	0.35	$4\bar{4}0$	216.20	0.46
400	167.89	0.35	$\bar{4}40$	232.30	0.46
$0\bar{1}0$	191.90	0.15	0012	68.97	0.37
010	177.30	0.15	$00\bar{1}2$	69.09	0.37
$0\bar{2}0$	297.93	0.22	0013	225.75	0.37
020	300.37	0.22	$00\bar{1}3$	233.15	0.37
$0\bar{3}0$	159.08	0.29			
030	163.57	0.29			
$0\bar{4}0$	307.87	0.35			
040	341.19	0.35			

[2] In fact, the crystal can have an even lower symmetry, e.g., monoclinic or triclinic. However, one can state that, in this case, the monoclinicity (triclinicity) angle does not exceed several minutes, i.e., lies within the divergence angle of the incident beam.

experiments the structure of the crystals of the 1–2–3 family was recognized as being centrosymmetric. Our practice shows that most of the 1–2–3 crystals consist of finely dispersed domains. Therefore, we selected $EuBa_2Cu_3O_x$ crystals for study from several dozens of other crystals showing the "gray" contrast on topographs, which is characteristic of polydomain crystals.

A similar analysis of the $F(hk0)/F(\bar{h}\bar{k}0)$, $F(h00)/F(\bar{h}00)$, and $F(0k0)/F(0\bar{k}0)$ ratios for a $GdBa_2Cu_3O_x$ crystal leads to the conclusion that in this crystal as well the direction of the displacement of the atomic sublattices is also parallel to the [100] direction. However, in this case, the $F(h00)/F(\bar{h}00)$ ratio is considerably less than for the $EuBa_2Cu_3O_x$ crystals. This fact seems to be explained by the small thickness ($\mu t_0 \cong 1.1$) of the sample, which does not allow the complete implementation of Borrmann diffraction.

The situation with the twinned $YBa_2Cu_3O_{\sim 7.0}$ crystal is more complicated, because the crystal has not only domains but also twins. The $F(hk0)/F(\bar{h}\bar{k}0)$ ratios for this crystals exceed the $F(h00)/F(\bar{h}00)$ and $F(0k0)/F(0\bar{k}0)$ ratios, whose values are close to unity. At the same time, since, in this case, both geometries are implemented (the transmission geometry for the internal regions of the sample and the reflection geometry for the boundary regions of the sample having a certain orientation with respect to the incident beam), the intensities of the hkl and $\bar{h}\bar{k}\bar{l}$ reflections can be different, e.g., because of the different lengths of the boundaries or different structures in the near-boundary regions of the opposite faces of the sample. However, because of the rectangular shape of the sample and the orientations of the reflecting planes with respect to the crystal faces, the boundary lengths in both cases are the same. Because of the approximate equality of $F(h00)$ and $F(\bar{h}00)$ and also of $F(0k0)$ and $F(0\bar{k}0)$ (Table 2), the effect of the opposite boundaries on the diffraction intensities should also be the same. Then, the displacement of the sublattices in $YBa_2Cu_3O_7$ is directed along the [110] direction and not along the [100]. This signifies that, with the change of the oxygen concentration in $ReBa_2Cu_3O_x$ crystals, the direction of the sublattice displacement can also change.

The above-discussed microdomain nature of 1–2–3 crystals resulting in the centrosymmetricity of their macrostructure is not the only reason that did not allow the establishment of their noncentrosymmetricity in earlier studies. The other cause is the use of MoK_α radiation. Table 3 indicates the structure factors for a single-domain $EuBa_2Cu_3O_x$ crystal determined with the use of CuK_α radiation and showing the maximum discrepancies in the $F(hk0)$ and $F(\bar{h}\bar{k}0)$ structure factors listed in Table 2. The same geometry of experiment as in the case of CuK_α radiation was used. It is clearly seen that all the $F(hkl)$ and $F(\bar{h}\bar{k}\bar{l})$ structure factors are equal (within the experimental error), i.e., the crystal looks centrosymmetric.

The physical reason for such a pronounced discrepancy revealed in the experiments with the use of CuK_α and MoK_α radiations is explained by the considerable difference in their absorption coefficients, $\mu t_0 \approx 6.0$ and 0.5, respectively. In the case of MoK_α radiation, the X-ray wave field is practically not absorbed irrespective of the position of the reflecting atomic planes to this field. This results in approximately equal $F(hkl)$ and $F(\bar{h}\bar{k}\bar{l})$ structure factors. In the case of strong absorption, when the Borrmann conditions are valid the noncentrosymmetric location of the atomic planes with respect to the wave field (e.g., of the planes of rare earth atoms), the hkl reflections can be located close to the nodes of this field, which can result in its strong "photometric absorption" or, which is equivalent, in a considerable decrease in $F(hkl)$. For the $(\bar{h}\bar{k}\bar{l})$ reflections, the same planes do not necessarily coincide with the node positions, which results in a considerable increase in $F(\bar{h}\bar{k}\bar{l})$ with respect to $F(hkl)$. It is also clear that for various orders of reflection from the (hkl) plane, the mutual location of the real atomic planes and the X-ray wave field can be different. I believe that the latter fact explains the experimentally observed change in the $F(hk0)/F(\bar{h}\bar{k}0)$ ratio for various orders of reflections. This conclusion is also confirmed by the considerable change in the contrast (up to the opposite one) observed in the topographs of neighboring domains in sample no. 2 for the same $(hk0)$ reflection with the transition from CuK_α radiation to FeK_α or NiK_α radiation.

In our example, the $F(hkl)/F(\bar{h}\bar{k}\bar{l})$ ratio is equal to or even exceeds ten. At the same time, the theories developed for strongly absorbing crystals in the Laue geometry [6] yield the maximum difference in the coefficients of integrated reflection $R(hkl)/R(\bar{h}\bar{k}\bar{l})$ equal to two. I believe that these theories are somewhat incomplete, because they do not consider multicomponent crystals with several heavy atoms, for which the resonance absorption is observed for almost all the traditional X-ray radiations. This formulation of the problem depends not only on the pronounced difference in the $F(hkl)$ and $F(\bar{h}\bar{k}\bar{l})$ structure factors calculated by normalizing a large number of reflections measured on the P4 and the AFC6S complexes, but also on the black–white contrast of 90° domains on the topographs of angular scanning. According to the above estimate for the $R(hkl)$ and $R(\bar{h}\bar{k}\bar{l})$ reflections, the difference in darkening observed for adjacent domains should not exceed two, whereas the real darkening ratio on the angular-scanning topographs attains a value of several dozens.

In conclusion, we should like to indicate that our results demonstrating the noncentrosymmetricity of the

atomic structure of a number of crystals of the 1–2–3 family do not allow us to determine which of the sublattices is displaced, and by how far, from the possible center of symmetry. To determine the real atomic structure of these crystals, one has to develop X-ray analysis for dynamic X-ray diffraction and to compare the calculated structural data with the modeled results.

Thus, we obtained additional diffraction evidence of the noncentrosymmetricity of the atomic structure of $EuBa_2Cu_3O_{x<6.5}$ crystals and also showed that $GdBa_2Cu_3O_{x<6.5}$ and $YBa_2Cu_3O_{\sim 7.0}$ crystals are noncentrosymmetric. The results obtained lead to the assumption that not only the studied representatives of the 1–2–3 family, but also all the crystals of this family are noncentrosymmetric irrespective of the type of rare earth atoms and the oxygen concentration.

ACKNOWLEDGMENTS

The author is grateful to G.A. Emel'chenko and N.V. Abrosimov for supplying the crystals and to I.K. Bdikin for his help in selecting high-quality $EuBa_2Cu_3O_x$ crystals.

REFERENCES

1. I. K. Bdikin, I. M. Shmyt'ko, V. Sh. Shekhtman, *et al.*, Physica C (Amsterdam) **201**, 69 (1992).
2. V. M. Ishchuk, L. A. Kvichko, V. P. Seminozhenko, *et al.*, Pis'ma Zh. Éksp. Teor. Fiz. **49**, 341 (1989) [JETP Lett. **49**, 389 (1989)].
3. L. R. Testardi, W. G. Moulton, H. Mathias, *et al.*, Phys. Rev. B **37**, 2324 (1988).
4. V. V. Aristov, I. M. Shmy'tko, and E. V. Shulakov, Kristallografiya **21**, 151 (1976) [Sov. Phys. Crystallogr. **21**, 191 (1976)].
5. I. M. Shmyt'ko and V. Sh. Shekhtman, *The Real Structure of High-T_c Superconductors* (Springer-Verlag, Berlin, 1993), Springer Series in Materials Science, Vol. 23, p. 23.
6. Z. G. Pinsker, *Dynamical Scattering of X-rays in Crystals* (Nauka, Moscow, 1974; Springer-Verlag, Berlin, 1978).

Translated by L. Man

Crystallography Reports, Vol. 47, No. 3, 2002, pp. 390–393. Translated from Kristallografiya, Vol. 47, No. 3, 2002, pp. 435–438.

STRUCTURES OF INORGANIC COMPOUNDS

A New Centrosymmetric Modification of Synthetic Hilgardite $Pb_2[B_5O_9](OH) \cdot 0.5H_2O$

T. A. Borisova, O. V. Dimitrova, and E. L. Belokoneva

Moscow State University, Vorob'evy gory, Moscow, 119899 Russia

e-mail: tborisova@lvk.sc.msu.su

Received August 10, 2001

Abstract—A new centrosymmetric modification of Pb-hilgardite $Pb_2[B_5O_9](OH) \cdot 0.5H_2O$ is synthesized hydrothermally under conditions close to natural. This modification is intermediate between the centrosymmetric monoclinic phase studied earlier and the polar orthorhombic phase. The occupancies of the framework voids with water molecules, OH-groups, and halogen atoms are considered for all the known varieties of hilgardite. The correlation between the conditions of hilgardite formation and types of structure is established. © *2002 MAIK "Nauka/Interperiodica".*

INTRODUCTION

Lead borates are of special interest in the search for materials, since some of these compounds have pronounced nonlinear-optical properties [1, 2]. Earlier, we synthesized new nonpolar and polar modifications of Pb-hilgardites; their crystal structures were studied on single crystals [3, 4]. Below, we describe the crystal structure of a new modification of Pb-hilgardite and compare its structure with the structures of other modifications. A comparative analysis of the conditions of crystallization of Pb-hilgardites is also performed.

EXPERIMENTAL

Lead borates in the $PbO–B_2O_3–H_2O$ system were synthesized by the hydrothermal method from a solution containing alkali metal carbonates in standard autoclaves lined with fluoroplastic. The charge was a mixture of lead and boron oxides in a 1 : 1 ratio. The synthesis was performed for 20 days under pressure P = 70–100 atm at t = 250°C. Aggregates of colorless transparent prismatic crystals up to $0.625 \times 0.25 \times 0.25$ mm in size were obtained. The crystal structure was studied on a prismatic single-crystal block whose dimensions are indicated in Table 1.

The test for second-harmonic generation was made with the use of a YAG : Nd pulsed laser operating in "reflection" mode [5] and indicing the presence of the center of symmetry. The X-ray phase diagnostics were performed on a DRON-UM1 diffractometer (Co-radiation; 40 kV; 25 mA; 0.05°-step scans; the exposure time at each point was 2 s). The diffraction spectrum of the sample was close to that of monoclinic hilgardite; however, the absence of some lines indicated an intermediate phase between the monoclinic and orthorhombic hilgardite modifications.

Table 1. Crystallographic data and characteristics of the experiment

Sp. gr., Z	$P112_1/n$, 4
a, Å	11.32(1)
b, Å	6.632(1)
c, Å	11.549(8)
γ, deg	91.03(5)
V, Å^3	860(2)
F(000)	1100
d_{calcd}, g/cm^3	4.93(1)
μ, cm^{-1}	385.8
Dimensions, mm	$0.25 \times 0.125 \times 0.125$
Diffractometer	Syntex P1
Radiation	MoK_α 0.71069
Scan mode	2θ–θ
Scan speed	4 deg/min
2θ, deg and θ/λ, Å^{-1} (max)	98.75, 1.068
Number of measured reflections	2996
Number of reflections used in refinement	2370
Constraints	$F_{hkl} > 8.00\sigma(F)$
Weighting scheme	$1/[\sigma(F)^2 + 0.0020F^2]$
Number of atomic positions	18
R, R_w	0.0600, 0.0643
Scale factor (K)	0.687(3)
S	1.130

1063-7745/02/4703-0390$22.00

Table 2. Coordinates of basic atoms and thermal corrections in the $Pb_2[B_5O_9](OH) \cdot 0.5H_2O$ structure

Atoms	*x*/*a*	*y*/*b*	*z*/*c*	B^*_{eq}	Atoms	*x*/*a*	*y*/*b*	*z*/*c*	B^*_{eq}
Pb(1)	0.02351(6)	0.6616(1)	0.2248(1)	1.14(1)	O(8)	0.0795(11)	0.014(2)	0.7018(11)	1.24(3)
Pb(2)	0.31801(6)	0.0164(1)	0.02255(6)	1.22(1)	O(9)(OH)	0.5105(11)	0.166(2)	0.0684(12)	1.27(3)
O(1)	0.8229(9)	0.083(2)	0.7344(9)	0.44(3)	O(10)	0.2755(11)	0.001(2)	0.6053(11)	1.18(3)
O(2)	0.7403(10)	0.078(2)	0.1955(10)	0.86(3)	B(1)	0.9601(15)	0.174(3)	0.280(2)	0.78(3)
O(3)	0.0738(11)	0.239(2)	0.2771(11)	1.13(3)	B(2)	0.2597(15)	−0.008(3)	0.491(2)	0.73(3)
O(4)	0.2803(11)	0.229(2)	0.2391(11)	1.09(3)	B(3)	0.7276(13)	0.209(2)	0.6928(14)	1.13(3)
O(5)	0.6965(11)	0.161(2)	0.5689(12)	1.32(3)	B(4)	0.2118(15)	0.056(3)	0.7128(15)	1.13(3)
O(6)	0.1987(12)	0.149(2)	0.4306(11)	1.55(3)	B(5)	0.1842(11)	0.134(2)	0.2992(12)	1.13(3)
O(7)	0.6203(11)	0.172(2)	0.7646(11)	1.25(3)	O(11)(H_2O)	0	0	0	3.4(6)

* $B_{eq} = 1/3[B_{11}a^{*2}a^2 + \ldots + 2B_{23}b^*c^*bc\cos\alpha]$.

A set of direct- and reciprocal-lattice vectors was obtained on a Syntex P1 diffractometer, and the parameters characteristic of crystals of the hildardite family were selected for refinement by 15 reflections from the high-angular range of θ angles. On the oscillation pattern obtained on the diffractometer, the largest translation vector, **c** = 11.46 Å, was normal to the symmetry plane, which indicated the monoclinic centrosymmetric modification of hilgardite described by the sp. gr. $P112_1/n$ [3]. The characteristics of the experiment are given in Table 1. Processing of the intensities and their conversion into F^2_{hkl} were performed by the PROFIT program [6]; all further calculations were made with the use of the CSD package. An analysis of the systematic absences of reflections (00*l*: $l = 2n$ and $h + k = 2n$) confirmed the sp. gr. $P112_1/n$. At the first stage of the structure refinement, the initial coordinates were those of the framework of Pb, O, and B atoms [3]. The difference electron-density syntheses provided the localization of atoms occupying the framework voids: first, the hydroxyl groups in general positions (as in hilgardite [3]) and, then, water molecules in special positions at the centers of symmetry. The structure was refined with due regard for anomalous scattering in the isotropic approximation of thermal vibrations for Pb atoms and H_2O molecules and for that in the anisotropic approximation for all the other atoms. The pronounced absorption and its strong anisotropy were corrected at the final stage for a crystal of arbitrary shape by the DIFABS program [7]. The final refined data are listed in Table 1 and the final atomic coordinates, in Table 2.

RESULTS AND DISCUSSION

Like the hilgardite modifications studied, the boron atoms in new Pb-hilgardite have tetrahedral and trigonal coordination (Fig. 1). The interatomic distances range within 1.33–1.43 Å for the B(1)- and B(2)-triangles and 1.43–1.52 Å for the B(3)-, B(4)-, and B(5)-tetrahedra. There are $[B_5O_{11}]^{7-}$ polar chains forming $[B_5O_{10}]^{5-}$ layers that, in turn, form the $[B_5O_9]^{3-}$ framework. Large framework voids are occupied by Pb atoms, (OH) groups, and water molecules. The coordi-

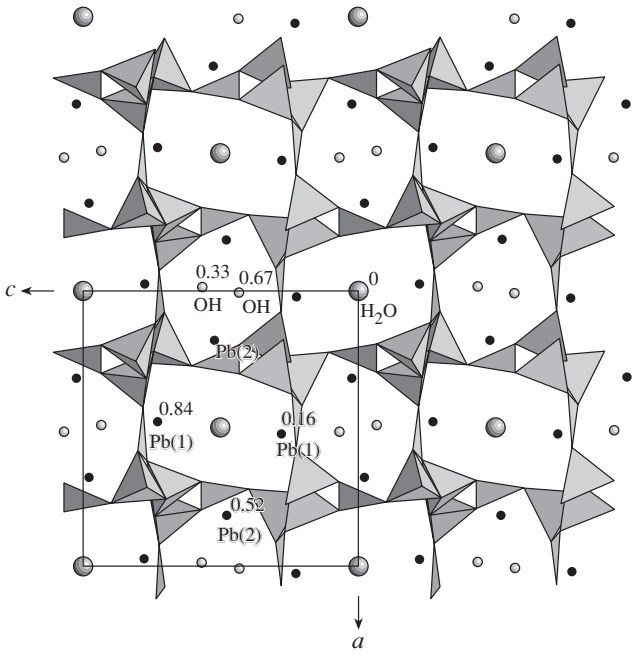

Fig. 1. The *ac* projection of the $Pb_2[B_5O_9](OH) \cdot 0.5H_2O$ crystal structure; hereafter, B atoms are shown by polyhedra; Pb atoms, OH groups, and water molecules are shown by spheres; the heights of atoms along the axis normal to the projection plane are indicated.

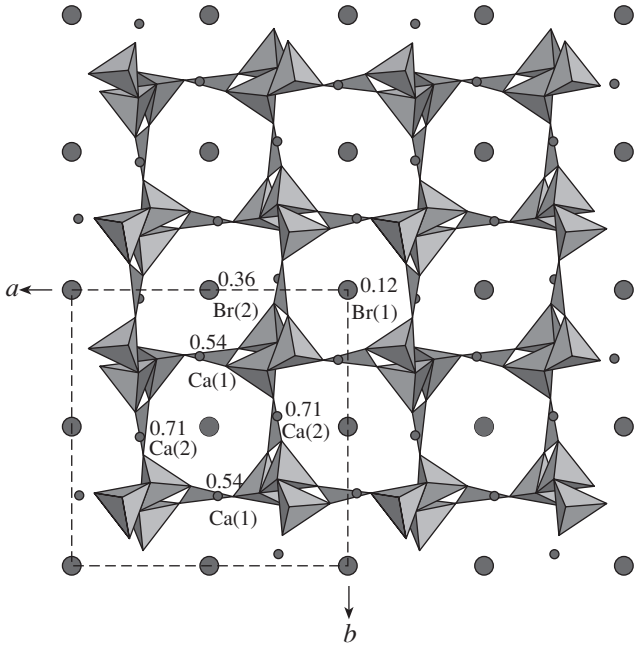

Fig. 2. The *ab* projection of the $Ca_2[B_5O_9]Br$ crystal structure; Ca and Br atoms are shown by spheres.

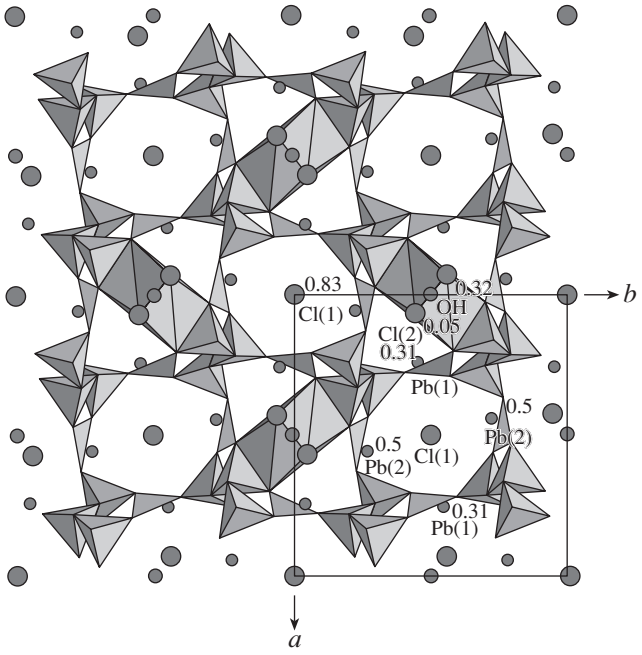

Fig. 3. The *ab* projection of the $Na_{0.5}Pb_2[B_5O_9]Cl(OH)_{0.5}$ crystal structure, Pb and Cl(1) atoms and OH groups are shown by spheres; Na atoms are depicted by their polyhedra; circles of Cl(2) atoms indicate the positions occupied by 50%.

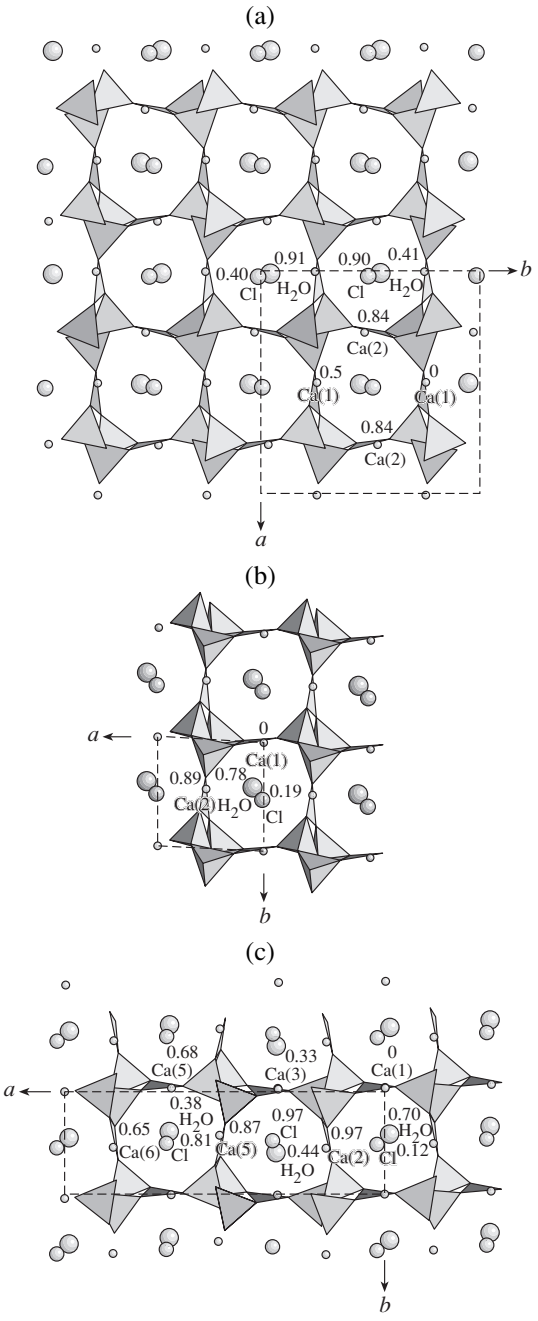

Fig. 4. The *ab* projections of the crystal structures of natural hilgardites described by the general formule $Ca_2[B_5O_9]Cl \cdot H_2O$; (a) the monoclinic polytype 2*M*; (b) the triclinic polytype 1*T*; (c) the triclinic polytype 3*T*.

nation seven-vertex or eight-vertex polyhedra of the Pb atoms are formed by O atoms located at distances of up to 3 Å. The Pb(1) atoms are surrounded with O(1), O(2), O(3), O(4), O(7), O(8), O(9), and O(10) atoms (with interatomic distances ranging within 2.37–2.93 Å); Pb(2) atoms are surrounded with O(2), O(4), O(5), O(6), O(7), and O(9) × 2 atoms (with interatomic distances ranging within 2.44–2.90 Å).

The structure framework is identical to that of the hilgardite studied earlier [3]; the arrangements of the Pb atoms and hydroxyl groups are also the same. However, the water molecules in these structures are located in

different positions in the framework voids—the general position with the coordinates $x \sim 0.03$, $y \sim 0.2$, and $z \sim 0.02$ in the hilgardite studied earlier and a special position (at the center of inversion) in the new modification (Fig. 1, Table 2). The latter feature makes the new structure similar to orthorhombic hilgardites [8], where halogen atoms occupy special positions on twofold rotation axes, sp. gr. *Pnn*2. In this case, the Br(1) atoms in the orthorhombic $Ca_2[B_5O_9]Br$ structure [8] are slightly (by 0.75 Å) displaced along the polar axis relative to the water molecules in the new modification ($z = 0$ for Br and $z = 0.12$ for H_2O) (Figs. 1, 2). The heights of the Br(2) atoms in Ca-hilgardite and of (OH) groups (additionally multiplied via the centers of inversion) in both monoclinic Pb-hilgardites are equal (Figs. 1, 2). Polar $Na_{0.5}Pb_2[B_5O_9]Cl(OH)_{0.5}$ hilgardite [4] is a somewhat more complex version of the orthorhombic phases: the Cl(1) position corresponds to the Br(1) position from [8] (Fig. 3), whereas Br(2) is changed to a more complicated filling of the framework with OH groups and Cl(2) atoms explained by the incorporation of Na atoms into the structure. The polarity of orthorhombic hilgardites and their nonlinear-optical properties are explained by the polarity of the framework and the polar arrangement of cations and halogens in the framework voids. In natural Ca-hilgardites (one monoclinic and two triclinic), the voids are statistically occupied by halogens and water molecules (Figs. 4a–4c).

CONCLUSIONS

Thus, at present, the hilgardite structure type [3] includes a number of modifications related by polytype OD-transformations. We failed to synthesize artificial analogues of natural monoclinic (sp. gr. *Aa*) and triclinic lead-hilgardites. At the same time, we synthesized polar orthorhombic and centrosymmetric monoclinic modifications that have no natural analogues.

Centrosymmetric monoclinic hilgardite [3] is stable in a pure carbonate solution and in a carbonate solution with up to 5% halides. Highly concentrated carbonate solutions with halogens allow the formation of the new centrosymmetric monoclinic modification. It can be assumed that the structural differences in the positions of the water molecules are determined by the influence of carbonate ions. In concentrated carbonate solutions of up to 20% alkali metal halides, a sodium-free orthorhombic modification is formed, whose structure is being studied. It can be stated that this modification has no OH groups—they are replaced by halogen ions. With an increase in the halogen concentration in the solution, the orthorhombic Na-modification is formed. Because of the supersaturation of the solution, the crystallization rate increases, which results in crystal nonhomogeneity and the incorporation of various cations and anions into the framework voids.

ACKNOWLEDGMENTS

The authors are grateful to S.Yu. Stefanovich for a test for nonlinear-optical properties.

REFERENCES

1. D. L. Corker and A. M. Glazer, Acta Crystallogr., Sect. B: Struct. Sci. **52**, 260 (1996).
2. E. L. Belokoneva, S. Yu. Stefanovich, T. A. Borisova, and O. V. Dimitrova, Zh. Neorg. Khim. **46** (11), 1788 (2002).
3. E. L. Belokoneva, O. V. Dimitrova, T. A. Korchemkina, and S. Yu. Stefanovich, Kristallografiya **43** (5), 864 (1998) [Crystallogr. Rep. **43**, 810 (1998)].
4. E. L. Belokoneva, T. A. Korchemkina, O. V. Dimitrova, and S. Yu. Stefanovich, Kristallografiya **45** (5), 814 (2000) [Crystallogr. Rep. **45**, 744 (2000)].
5. S. Yu. Stefanovich, in *Proceedings of the 2nd International Conference "Real Structure and Properties of Acentric Crystals"* (VNIISIMS, Aleksandrov, 1995), p. 48.
6. V. A. Strel'tsov and V. E. Zavodnik, Kristallografiya **34** (6), 1369 (1989) [Sov. Phys. Crystallogr. **34**, 824 (1989)].
7. N. Walker and D. Stuart, Acta Crystallogr., Sect. A: Found. Crystallogr. **39**, 158 (1983).
8. D. J. Lloyd, A. Levasseur, and C. Fouassier, J. Solid State Chem. **6**, 179 (1973).

Translated by T. Dmitrieva

Crystallography Reports, Vol. 47, No. 3, 2002, pp. 394–396. Translated from Kristallografiya, Vol. 47, No. 3, 2002, pp. 439–441.

STRUCTURES OF INORGANIC COMPOUNDS

Crystal Structure of Samarium Hexamolybdoaluminate $Sm[Al(OH)_6Mo_6O_{18}] \cdot 11H_2O$

G. B. Andreev*, A. M. Fedoseev*, N. A. Budantseva*, and M. Yu. Antipin**

** Institute of Physical Chemistry, Russian Academy of Sciences, Leninskiĭ pr. 31, Moscow, 117915 Russia*

e-mail: budants@ipc.rssi.ru

*** Nesmeyanov Institute of Organoelement Compounds, Russian Academy of Sciences, ul. Vavilova 28, Moscow, 119991 Russia*

Received May 29, 2001

Abstract—The structure of a new complex of samarium(III) with a hexamolybdoaluminate ion, $Sm[Al(OH)_6Mo_6O_{18}] \cdot 11H_2O$, was established by the methods of X-ray diffraction analysis. The crystallographic data are as follows: sp. gr. $Pbc2_1$, $a = 10.927(4)$ Å, $b = 11.757(5)$ Å, $c = 22.327(9)$ Å, $V = 2868(1)$ Å^3, $Z = 4$, $\rho_{calcd} = 3.040$ g/cm^3, $R = 0.084$, $R_W = 0.198$. In the $[Al(OH)_6Mo_6O_{18}]^{3-}$ anion, an Al atom is surrounded by six Mo atoms with distorted octahedral coordination. The anions are linked into chains via Sm atoms. The coordination polyhedron of a Sm atom is a tricapped trigonal prism with the vertices being occupied by two terminal oxygen atoms of two adjacent anions and seven water molecules. © *2002 MAIK "Nauka/Interperiodica".*

INTRODUCTION

The complexes of trivalent *f* elements with heteropolyanions (HPA) of the composition $XMo_6O_{24}^{n-}$, where *X* = Mo(VI) [1], Te(VI) [2], or I(VII) [3], are characterized by various structures. It was of interest to synthesize and study the complexes of trivalent *f* elements with HPA, characterized by the Andersen structure and containing six protons per HPA formula unit $Me(OH)_6Y_6O_{18}$, where *Y* = Mo and *Me* = Al, Cr, Fe, or Ni [4]. Below, we present the results of the X-ray study of a complex of trivalent samarium with the hexamolybdoaluminate ion.

EXPERIMENTAL

Square platelet-like $Sm[Al(OH)_6Mo_6O_{18}] \cdot 11H_2O$ (**I**) crystals were obtained upon storage of a $(NH_4)_3[Al(OH)_6Mo_6O_{18}] \cdot nH_2O$ (**II**) (0.01–0.02 mol/l) solution containing an equimolar amount of samarium nitrate at room temperature for several hours. Compound **II** was prepared by the method described in [5].

The X-ray diffraction data were collected on a Bruker SMART diffractometer. The X-ray data set measured at room temperature did not yield an adequately structured solution. Hence, we repeated measurements at 110 K. A total of 8104 independent reflections were measured in the 2θ range up to 60°. The absorption correction was introduced by using the SADABS program. The structure was solved by direct methods and refined by the full-matrix least-squares method with anisotropic thermal parameters for all the atoms by the SHELXTL PLUS program package. The main crystallographic data and the details of the structure refinement are given in Table 1. The atomic coordinates and the selected interatomic distances are listed in Tables 2 and 3, respectively. It should be noted that rather high *R* factors (Table 1) are, apparently, associated with the deterioration of single crystals under X-ray radiation.

Table 1. Main crystallographic parameters and details of the structure refinement

System	Orthorhombic
a, Å	10.927(4)
b, Å	11.757(5)
c, Å	22.327(9)
Sp. gr.	$Pbc2_1$
Z	4
V, Å^3	2868(1)
ρ_{calcd}, g/cm^3	2.156
Crystal dimensions, mm	$0.06 \times 0.19 \times 0.22$
Radiation (λ, Å)	MoK_α (0.71073)
Scanning mode	θ/2θ
$2\theta_{max}$, deg	60
Number of reflections	27583
Number of independent reflections	8054
R_{int}	0.090
F(000)	2429
Number of refined parameters	388
R, *wR*(F^2)	0.084, 0.198
GoF	1.062

Table 2. Atomic coordinates and equivalent thermal parameters

Atom	*x/a*	*y/b*	*z/c*	U_{eq}, Å^2
Al(1)	0.7560(5)	0.7022(4)	0.3121(3)	0.0115(9)
Sm(1)	1.25032(9)	0.67084(8)	0.51347(7)	0.0140(2)
Mo(1)	0.9967(2)	0.8056(1)	0.24174(8)	0.0123(4)
Mo(2)	0.9943(2)	0.7994(1)	0.38978(8)	0.0100(3)
Mo(3)	0.7487(2)	0.6971(1)	0.45899(8)	0.0099(3)
Mo(4)	0.5123(2)	0.6010(1)	0.38255(8)	0.0095(3)
Mo(5)	0.5225(2)	0.5994(1)	0.23432(8)	0.0125(4)
Mo(6)	0.7647(2)	0.7005(1)	0.16417(8)	0.0113(3)
O(1)	1.049(1)	0.946(1)	0.2473(7)	0.019(3)
O(2)	1.101(1)	0.737(1)	0.1982(8)	0.021(4)
O(3)	1.044(1)	0.935(1)	0.3871(8)	0.019(3)
O(4)	0.087(1)	0.729(1)	0.4381(7)	0.016(3)
O(5)	0.646(1)	0.776(1)	0.4996(7)	0.014(3)
O(6)	0.840(1)	0.626(1)	0.5082(9)	0.019(3)
O(7)	0.416(1)	0.672(1)	0.4309(8)	0.018(3)
O(8)	0.460(1)	0.470(1)	0.3769(7)	0.013(3)
O(9)	0.433(1)	0.674(1)	0.1843(9)	0.026(4)
O(10)	0.463(1)	0.467(1)	0.2363(8)	0.018(3)
O(11)	0.668(1)	0.775(1)	0.1200(8)	0.020(3)
O(12)	0.865(1)	0.632(1)	0.1179(8)	0.020(3)
O(13)	1.059(1)	0.742(1)	0.3155(9)	0.015(3)
O(14)	0.854(1)	0.828(1)	0.4399(8)	0.023(4)
O(15)	0.652(1)	0.570(1)	0.4345(8)	0.016(3)
O(16)	0.449(1)	0.661(1)	0.3084(8)	0.015(3)
O(17)	0.664(1)	0.573(1)	0.1860(8)	0.017(3)
O(18)	0.865(1)	0.829(1)	0.1874(7)	0.011(3)
O(19)	0.853(1)	0.837(1)	0.3135(9)	0.013(3)
O(20)	0.858(1)	0.654(1)	0.3759(6)	0.006(2)
O(21)	0.647(1)	0.750(1)	0.3741(7)	0.012(3)
O(22)	0.658(1)	0.569(1)	0.3107(8)	0.010(2)
O(23)	0.655(1)	0.753(1)	0.2483(7)	0.013(3)
O(24)	0.865(1)	0.651(1)	0.2512(7)	0.013(3)
O(1*W*)	1.072(1)	0.552(1)	0.5431(9)	0.032(4)
O(2*W*)	1.105(1)	0.804(1)	0.5626(8)	0.032(4)
O(3*W*)	1.274(1)	0.880(1)	0.491(1)	0.095(13)
O(4*W*)	1.430(1)	0.745(1)	0.5633(9)	0.022(3)
O(5*W*)	1.256(1)	0.638(1)	0.6268(8)	0.024(4)
O(6*W*)	1.218(1)	0.529(1)	0.4372(8)	0.032(4)
O(7*W*)	1.368(1)	0.500(1)	0.5394(8)	0.018(3)
O(8*W*)	0.598(1)	0.992(1)	0.073(1)	0.032(5)
O(9*W*)	0.809(1)	1.042(1)	0.1414(9)	0.031(4)
O(10*W*)	0.702(1)	0.353(1)	0.3299(9)	0.025(4)
O(11*W*)	0.211(1)	0.555(1)	0.314(1)	0.022(3)

Table 3. Selected interatomic distances *d*

Distance	*d*, Å	Distance	*d*, Å
Al(1)–O(19)	1.91(1)	Mo(3)–O(5)	1.71(1)
Al(1)–O(20)	1.90(2)	Mo(3)–O(6)	1.70(2)
Al(1)–O(21)	1.91(2)	Mo(3)–O(14)	1.97(2)
Al(1)–O(22)	1.90(1)	Mo(3)–O(15)	1.91(2)
Al(1)–O(23)	1.90(2)	Mo(3)–O(20)	2.26(1)
Al(1)–O(24)	1.91(2)	Mo(3)–O(21)	2.29(2)
Sm(1)–O(1*W*)	2.48(2)	Mo(4)–O(7)	1.72(2)
Sm(1)–O(2*W*)	2.48(2)	Mo(4)–O(8)	1.65(1)
Sm(1)–O(3*W*)	2.52(1)	Mo(4)–O(15)	1.95(2)
Sm(1)–O(4*W*)	2.42(2)	Mo(4)–O(16)	1.93(2)
Sm(1)–O(5*W*)	2.56(2)	Mo(4)–O(21)	2.29(1)
Sm(1)–O(6*W*)	2.40(2)	Mo(4)–O(22)	2.28(1)
Sm(1)–O(7*W*)	2.45(2)	Mo(5)–O(9)	1.72(2)
Sm(1)–O(7)	2.59(2)	Mo(5)–O(10)	1.68(1)
Sm(1)–O(4)	2.55(2)	Mo(5)–O(16)	1.98(2)
Mo(1)–O(1)	1.75(1)	Mo(5)–O(17)	1.92(2)
Mo(1)–O(2)	1.70(2)	Mo(5)–O(22)	2.28(2)
Mo(1)–O(13)	1.93(2)	Mo(5)–O(23)	2.34(1)
Mo(1)–O(18)	1.90(2)	Mo(6)–O(11)	1.68(2)
Mo(1)–O(19)	2.27(2)	Mo(6)–O(12)	1.71(2)
Mo(1)–O(24)	2.32(1)	Mo(6)–O(17)	1.92(2)
Mo(2)–O(3)	1.69(1)	Mo(6)–O(18)	1.95(1)
Mo(2)–O(4)	1.69(1)	Mo(6)–O(24)	2.30(1)
Mo(2)–O(13)	1.93(2)	Mo(6)–O(23)	2.31(2)
Mo(2)–O(14)	1.93(2)		
Mo(2)–O(19)	2.33(2)		
Mo(2)–O(20)	2.28(1)		

RESULTS AND DISCUSSION

The crystal structure of compound **I** is built by infinite chains along the [100] direction consisting of $[Al(OH)_6Mo_6O_{18}]^{3-}$-anions, Sm^{3+}-cations, and coordinated water molecules. The structure also contains molecules of crystallization water held by hydrogen bonds. The fragment of the structure of compound **I** is shown in Fig. 1.

In an $[Al(OH)_6Mo_6O_{18}]^{3-}$ anion, the Al atom is surrounded by six Mo atoms lying in the same plane. The Al–Mo distances range within 3.28(1)–3.33(1) Å. The maximum deviation of the atoms from the mean plane is 0.042(1) Å. The distances between the nearest Mo atoms range from 3.29(1) to 3.32(1) Å.

The aluminum atom is linked to the molybdenum atoms via the oxygen atoms of the hydroxy groups, forming the coordination octahedron of the aluminum atom. The O–Al–O angles differ from 90° and range

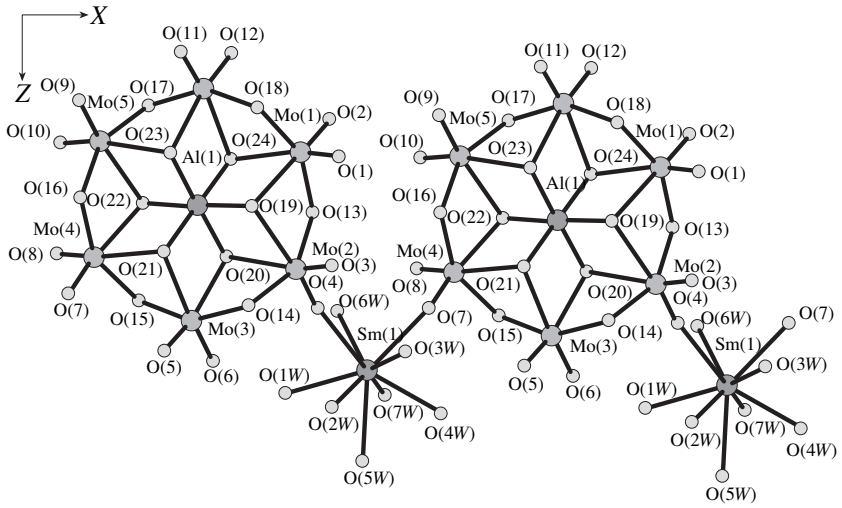

Fig. 1. Fragment of the $Sm[Al(OH)_6Mo_6O_{18}] \cdot 11H_2O$ structure projected onto the *XOZ* plane.

within 84.4(6)°–95.8(6)°. The Al–O distances are equal to 1.90(2) Å.

The coordination polyhedra of molybdenum atoms are distorted octahedra formed by three types of oxygen atoms—two terminal oxygen atoms, two bridging oxygen atoms linking the adjacent Mo atoms, and two bridging oxygen atoms linking the Mo atoms to the Al atom. Depending on the type of the oxygen atom, the Mo–O distances range within 1.65(2)–1.75(2), 1.90(2)–1.98(2), and 2.27(2)–2.34(2) Å, respectively. Each Mo-octahedron shares one edge with two adjacent MoO_6 octahedra and one AlO_6 octahedron.

Analogous anion structures were also found in the $Na_3(H_6CrMo_6O_{24}) \cdot 8H_2O$ [6], $K_6(TeMo_6O_{24}) \cdot 7H_2O$ [7], $Nd_2(TeMo_6O_{24}) \cdot 18H_2O$ [2], $(NH_4)_6(TeMo_6O_{24}) \cdot Te(OH)_6 \cdot 7H_2O$ [8] structures.

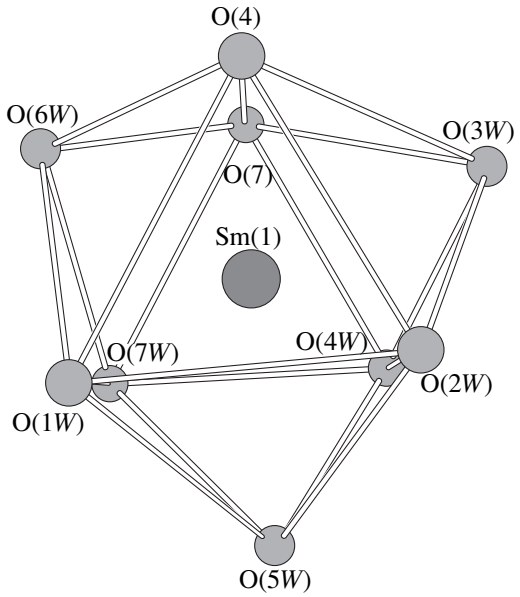

Fig. 2. Coordination polyhedron of a Sm atom in the $Sm[Al(OH)_6Mo_6O_{18}] \cdot 11H_2O$ structure.

The anions form chains connected by Sm atoms. The coordination polyhedron of a Sm atom is a tricapped trigonal prism with the vertices occupied by two terminal oxygen atoms of two adjacent anions and seven water molecules (Fig. 2). The Sm–O distances range within 2.40(2)–2.49(2) Å. The angles formed by the prism bases are 7.5°. The angles between the side faces are 58.2°, 58.3°, and 63.5°.

ACKNOWLEDGMENTS

This study was supported by the US Department of Energy (grant no. DE FG 07-ER 14940) and by the Russian Foundation for Basic Research (project no. 00-15-97359).

REFERENCES

1. A. M. Fedoseev, M. S. Grigor'ev, A. I. Yanovskiĭ, *et al.*, Dokl. Akad. Nauk SSSR **297**, 111 (1987).
2. M. S. Grigor'ev, Yu. T. Struchkov, A. M. Fedoseev, *et al.*, Zh. Neorg. Khim. **37** (11), 2507 (1992).
3. A. M. Fedoseev, M. S. Grigoriev, and N. Budantseva, J. Lumin. **87–89**, 1065 (2000).
4. M. T. Pope, *Heteropoly and Isopoly Oxometalates* (Springer-Verlag, Berlin, 1983).
5. L. C. W. Baker, G. Foster, W. Tan, *et al.*, J. Am. Chem. Soc. **77** (8), 2136 (1955).
6. A. Perloff, Inorg. Chem. **9** (9), 2228 (1970).
7. H. T. Evans, J. Am. Chem. Soc. **70** (4), 1291 (1948).
8. H. T. Evans, J. Am. Chem. Soc. **90** (12), 3275 (1968).

Translated by T. Safonova

Crystallography Reports, Vol. 47, No. 3, 2002, pp. 397–403. Translated from Kristallografiya, Vol. 47, No. 3, 2002, pp. 442–448.

STRUCTURES OF INORGANIC COMPOUNDS

Rare-Earth and Lead Mixed Anionic Oxoborates

B. F. Dzhurinskiĭ† and A. B. Ilyukhin

Kurnakov Institute of General and Inorganic Chemistry, Russian Academy of Sciences, Leninskiĭ pr. 31, Moscow, 117907 Russia

e-mail: ilyukhin@igic.ras.ru

Received February 26, 2001; in final form, July 11, 2001

Abstract—The $Nd_{4.5}Pb_{1.7}(VO_4)_{0.3}(BO_3)O_{6.42}$ (**I**), $Tb_{4.5}Pb_{1.6}(GeO_4)_{0.4}(BO_3)O_{6.02}$ (**II**), $Dy_{4.5}Pb_{1.68}(GeO_4)_{0.32}(BO_3)O_{6.28}$ (**III**), and $Ho_{8.66}(BO_3)_2(B_2O_5)O_8$ (**IV**) crystals were grown by spontaneous crystallization from flux and studied by the methods of X-ray diffraction analysis. The unit-cell parameters are a = 21.946, 21.590, 21.478, and 18.207 Å; b = 3.7881, 3.6565, 3.6333, and 3.6685 Å; c = 16.857, 16.618, 16.544, and 14.024 Å; β = 123.70°, 124.64°, 124.49°, and 119.81°; sp. gr. $C2/m$; and Z = 4, 4, 4, and 2 for **I**, **II**, **III**, and **IV**, respectively. In **I**–**III** compounds, Pb atoms, together with the atoms of group V, and Pb atoms and Ge atoms occupy the mixed positions. In structure **IV**, all the five independent Ho positions are occupied only partially. © *2002 MAIK "Nauka/Interperiodica".*

INTRODUCTION

Anhydrous rare-earth borates are of interest as luminescent and laser materials. However, simple rare-earth (RE) borates and oxoborates exhibit a limited structural variety [1]. Mixed cationic RE borates are studied in sufficient detail, whereas mixed anionic borates are studied much less. We made an attempt to synthesize RE borates with tetrahedral VO_4^{3-} or GeO_4^{4-} anions. However, in addition to tetrahedral anions, the compounds synthesized from PbO melts also contained lead.

EXPERIMENTAL

Single crystals of the compounds $Nd_{4.5}Pb_{1.7}(VO_4)_{0.3} \cdot (BO_3)O_{6.42}$ (**I**), $Tb_{4.5}Pb_{1.6}(GeO_4)_{0.4}(BO_3)O_{6.02}$ (**II**), $Dy_{4.5}Pb_{1.68}(GeO_4)_{0.32}(BO_3)O_{6.28}$ (**III**), and $Ho_{8.66}(BO_3)_2 \cdot (B_2O_5)O_8$ (**IV**) were synthesized by spontaneous crystallization from lead oxide flux containing the corresponding oxides. The compound compositions were established by the methods of X-ray diffraction analysis. Compound **I** was synthesized, and its structure was determined [2]. However, the unusual environment of one of the lead atoms and a vanadium atom gave rise to some doubts, and therefore we undertook a new structural study of compound **I**. The crystals of all the compounds synthesized have a needle-like habit. The X-ray diffraction data sets were collected on an Enraf-Nonius CAD-4 diffractometer (MoK_α radiation, graphite monochromator). The absorption correction was introduced analytically with the crystal shapes being approximated by cylinders. The structures were solved by direct methods with the use of the Fourier syntheses and the SHELXS-97 [3] and SHELXL-97 [4] program packages. The main crystallographic data and the results of the structure refinement are given in Table 1. The atomic coordinates and the equivalent (isotropic) thermal parameters are listed in Table 2. The selected interatomic distances are indicated in Table 3. In the crystal structures of compounds **I**–**III**, one of the RE atoms is disordered over two positions, *Ln*(51) and *Ln*(52). The Pb(21) and Pb(22) atoms are disordered in the similar way. The central atoms of the tetrahedral V or Ge anions statistically occupy the position in close proximity to the Pb(1) atom. The O(11) atom (the O(9) atom in [2] mistakenly located in the plane *m*) occupies its position only partly. In the structures of compounds **I**–**III**, the positions of lead atoms are unambiguously confirmed by the geometry of their environment typical of the stereochemically active lone electron pair—the low coordination numbers (3 and 4) of lead atoms and the existence of a large free zone occupied by a lone electron pair. The occupancies of the positions statistically filled with atoms were refined by the least-squares method in the isotropic approximation of thermal atomic displacements. The thermal parameters were fixed and were assumed to be the same for all the lanthanide atoms. All the lead atoms were also refined with the same thermal parameter. The thermal parameter of a vanadium (or germanium) atom was 1.5 times higher than that of lead atoms. The thermal parameter of the O(11) atom was twice as high as that of the lead atoms. The resulting occupancies of the atomic positions corresponded to the chemical formula, whose charge differed from zero by not more than +0.3 per unit cell. In the subsequent refinement, the occupancies were fixed (in order to compensate the positive charge of the chemical formula, the occupancies of the O(11) atoms were increased by 20–25%), whereas the thermal parameters were refined. The structures of compounds

† Deceased.

Table 1. Main crystallographic data and details of the X-ray diffraction study of $Nd_{4.5}Pb_{1.7}(VO_4)_{0.3}(BO_3)O_{6.42}$, $Tb_{4.5}Pb_{1.6}(GeO_4)_{0.4}(BO_3)O_{6.02}$, $Dy_{4.5}Pb_{1.68}(GeO_4)_{0.32}(BO_3)O_{6.28}$, and $Ho_{8.66}(BO_3)_2(B_2O_5)O_8$

Compound	$Nd_{4.5}Pb_{1.7}(VO_4)_{0.3} \cdot (BO_3)O_{6.42}$	$Tb_{4.5}Pb_{1.6}(GeO_4)_{0.4} \cdot (BO_3)O_{6.02}$	$Dy_{4.5}Pb_{1.68}(GeO_4)_{0.32} \cdot (BO_3)O_{6.28}$	$Ho_{8.66}(BO_3)_2(B_2O_5)O_8$
System	Monoclinic	Monoclinic	Monoclinic	Monoclinic
a, Å	21.946(3)	21.590(3)	21.478(4)	18.207(4)
b, Å	3.7881(7)	3.6565(7)	3.6333(8)	3.6685(7)
c, Å	16.857(2)	16.618(3)	16.544(2)	14.024(3)
β, deg	123.70(2)	124.64(2)	124.49(3)	119.81(2)
Sp. gr.	*C*2/*m*	*C*2/*m*	*C*2/*m*	*C*2/*m*
V, Å^3	1165.9(3)	1079.3(3)	1064.1(3)	812.8(3)
Z	4	4	4	2
ρ, g/cm^3	36.821	7.732	8.002	7.255
μ, mm^{-1}	44.393	55.087	58.573	41.714
Crystal dimensions, mm	$0.08 \times 0.01 \times 0.01$	$0.12 \times 0.02 \times 0.02$	$0.16 \times 0.03 \times 0.03$	$0.13 \times 0.04 \times 0.04$
θ_{max}, deg	40	40	40	42.5
Number of measured reflections	7146	3754	4043	3296
Number of independent reflections	3821 [*R*(*int*) = 0.0638]	3754	3672 [*R*(*int*) = 0.0768]	3222 [*R*(*int*) = 0.0681]
Number of refined parameters	94	127	127	98
*R*1, *wR*2 ($I > 2\sigma(I)$)	0.059, 0.152	0.063, 0.113	0.049, 0.129	0.062, 0.152
*R*1, *wR*2 (all reflections)	0.074, 0.158	0.075, 0.123	0.069, 0.138	0.111, 0.169
Gof	1.061	0.701	1.088	1.073

I–III were refined by the full-matrix least-squares method both in the isotropic and anisotropic approximations of thermal atomic displacements.

In [5], the structure of the $Y_{17.33}(BO_3)_4(B_2O_5)_2O_{16}$ compound (whose X-ray powder pattern is identical to our pattern of compound **IV**) was established by the Rietveld method within the sp. gr. *Cm*. An attempt to solve the structure within the sp. gr. *C*2/*m* [5] resulted in the conformation of the pyroborate group with the BOB angle equal to 180°. We managed to grow single crystals of compound **IV** suitable for X-ray diffraction study. The refinement within the sp. gr. *Cm* resulted in unrealistic thermal parameters and pronounced correlations between the positional and the thermal parameters. After the refinement within the sp. gr. *Cm* with due regard for centrosymmetric twinning, the domain ratio was 0.492(5) : 0.508(5); however, the thermal parameters of some atoms had unreasonable values. The refinement within the sp. gr. *C*2/*m* eliminated all the correlations and provided reasonable values of thermal parameters for all the atoms. The bridging O(10) atom of a pyroborate group is disordered about the center of inversion (the O(10)…O(10*a*) distance equals 0.93 Å), and the BOB angle is 142(2)°. Of all the lanthanides, the size of holmium is the closest to the size of yttrium (the ionic radii of Ho and Y at the coordination number 8 are 1.015 and 1.019 Å, respectively [6]), and the compounds including these elements are usually isostructural. Most likely, the erroneous choice of the space group in [5] is explained by the limited experimental data obtained from a polycrystal sample.

In structure **IV**, all the holmium positions are occupied only partly. The structure of compound **IV** was refined by the least-squares method, with the occupancies of the positions being refined simultaneously with the anisotropic thermal parameters of holmium atoms.

RESULTS AND DISCUSSION

Isostructural compounds **I–III** are built by six-, seven-, and eight-vertex *Ln*-polyhedra, lead-polyhedra, borate BO_3^{3-} anions, and tetrahedral VO_4^{3-} or GeO_4^{4-} anions. All the atoms, except for O(11), are located in planes *m*. In our opinion, the Nd(51) position (in the scheme of atomic numbering used in our study) in the structure of compound **I** was erroneously attributed in [2] to lead (Pb(3) in [2]), because the geometry of the

Table 2. Atomic coordinates and thermal parameters of $Nd_{4.5}Pb_{1.7}(VO_4)_{0.3}(BO_3)O_{6.42}$, $Tb_{4.5}Pb_{1.6}(GeO_4)_{0.4}(BO_3)O_{6.02}$, $Dy_{4.5}Pb_{1.68}(GeO_4)_{0.32}(BO_3)O_{6.28}$, and $Ho_{8.66}(BO_3)_2(B_2O_5)O_8$

Atom	x	y	z	U_{eq}/U_{iso}, Å^2	Occupancy
			$Nd_{4.5}Pb_{1.7}(VO_4)_{0.3}(BO_3)O_{6.42}$		
Nd(1)	0.31891(3)	1/2	0.30178(4)	0.00429(12)	1
Nd(2)	0.20576(3)	0	0.37344(4)	0.00537(12)	1
Nd(3)	0.48788(3)	1/2	0.29511(4)	0.00368(12)	1
Nd(4)	1/2	0	1/2	0.00495(15)	1
Nd(51)	0.32470(5)	0	0.11056(7)	0.00548(16)	0.33
Nd(52)	0.34189(10)	0	0.09456(13)	0.0053(3)	0.17
Pb(1)	0.15233(4)	0	0.09019(6)	0.01386(16)	0.35
V(1)*	0.1759(4)	0	0.0789(5)	0.0041(9)	0.15
Pb(21)	0.04042(9)	1/2	0.16211(15)	0.0093(3)	0.29
Pb(22)	0.05652(12)	1/2	0.1727(2)	0.0107(4)	0.21
O(1)*	0.3614(6)	1/2	0.1985(7)	0.0100(15)	1
O(2)*	0.4468(4)	1/2	0.3989(6)	0.0043(12)	1
O(3)*	0.2647(7)	0	0.2027(9)	0.018(2)	1
O(4)*	0.2121(6)	1/2	0.3045(8)	0.0111(16)	1
O(5)*	0.0803(5)	0	0.2598(7)	0.0089(15)	1
O(6)*	−0.0400(6)	1/2	0.1976(8)	0.0108(16)	1
O(7)*	0.4430(5)	0	0.5893(7)	0.0073(14)	1
O(8)*	0.3456(5)	0	0.4214(7)	0.0094(15)	1
O(9)*	0.3146(5)	0	0.5371(7)	0.0069(13)	1
O(10)*	0.1972(8)	0	0.0007(11)	0.022(2)	1
O(11)*	0.126(2)	0.398(11)	0.047(3)	0.039(9)	0.31
B(1)	0.3670(6)	0	0.5176(8)	0.0023(16)	1
			$Tb_{4.5}Pb_{1.6}(GeO_4)_{0.4}(BO_3)O_{6.02}$		
Tb(1)	0.31456(2)	1/2	0.29935(3)	0.00454(9)	1
Tb(2)	0.20468(2)	0	0.37393(3)	0.00549(10)	1
Tb(3)	0.48374(2)	1/2	0.29520(3)	0.00425(9)	1
Tb(4)	1/2	0	1/2	0.00663(12)	1
Tb(51)	0.32076(4)	0	0.11153(5)	0.00412(11)	0.33
Tb(52)	0.33892(8)	0	0.09227(10)	0.0050(2)	0.17
Pb(1)	0.14443(4)	0	0.08002(5)	0.00913(12)	0.30
Ge(1)	0.1735(2)	0	0.0761(3)	0.0136(6)	0.20
Pb(21)	0.03814(17)	1/2	0.1629(4)	0.0106(4)	0.28
Pb(22)	0.0525(2)	1/2	0.1719(5)	0.0111(5)	0.22
O(1)	0.3566(5)	1/2	0.1994(6)	0.0124(14)	1
O(2)	0.4436(4)	1/2	0.3954(5)	0.0043(10)	1
O(3)	0.2602(7)	0	0.1994(7)	0.021(2)	1
O(4)	0.2088(5)	1/2	0.3027(6)	0.0100(13)	1
O(5)	0.0795(4)	0	0.2670(6)	0.0077(11)	1
O(6)	−0.0433(5)	1/2	0.1982(6)	0.0063(11)	1
O(7)	0.4430(4)	0	0.5869(6)	0.0076(11)	1
O(8)	0.3446(5)	0	0.4205(6)	0.0095(12)	1
O(9)	0.3151(4)	0	0.5394(5)	0.0073(11)	1
O(10)	0.1970(9)	0	−0.0038(11)	0.029(3)	1
O(11)*	0.1426(13)	0.447(9)	0.0801(18)	0.025(5)	0.31
B(1)*	0.3685(6)	0	0.5169(8)	0.0058(15)	1

Table 2. (Contd.)

Atom	*x*	*y*	*z*	U_{eq}/U_{iso}, Å^2	Occupancy
		$Dy_{4.5}Pb_{1.68}(GeO_4)_{0.32}(BO_3)O_{6.28}$			
Dy(1)	0.31471(2)	1/2	0.29947(3)	0.00969(10)	1
Dy(2)	0.20525(2)	0	0.37444(3)	0.00986(10)	1
Dy(3)	0.48363(2)	1/2	0.29568(3)	0.00903(9)	1
Dy(4)	1/2	0	1/2	0.01056(12)	1
Dy(51)	0.32107(4)	0	0.11121(5)	0.01112(12)	0.35
Dy(52)	0.33915(9)	0	0.09310(12)	0.0113(2)	0.15
Pb(1)	0.14514(4)	0	0.08076(6)	0.01891(14)	0.34
Ge(1)	0.1718(3)	0	0.0779(3)	0.0170(7)	0.16
Pb(21)	0.0383(5)	1/2	0.1629(8)	0.0138(8)	0.17
Pb(22)	0.0485(2)	1/2	0.1711(4)	0.0202(6)	0.33
O(1)	0.3572(5)	1/2	0.2016(7)	0.0186(17)	1
O(2)	0.4436(4)	1/2	0.3990(6)	0.0125(13)	1
O(3)	0.2610(7)	0	0.2022(7)	0.0221(19)	1
O(4)	0.2082(5)	1/2	0.3031(7)	0.0158(14)	1
O(5)	0.0801(5)	0	0.2687(7)	0.0141(13)	1
O(6)	−0.0458(5)	1/2	0.1985(7)	0.0154(13)	1
O(7)	0.4442(4)	0	0.5877(6)	0.0108(11)	1
O(8)	0.3413(5)	0	0.4178(6)	0.0138(13)	1
O(9)	0.3143(4)	0	0.5389(6)	0.0133(13)	1
O(10)	0.1933(9)	0	−0.0047(10)	0.036(3)	1
O(11)*	0.124(5)	0.34(3)	0.049(6)	0.12(3)	0.28
B(1)*	0.3661(6)	0	0.5161(8)	0.0099(14)	1
		$Ho_{8.66}(BO_3)_2(B_2O_5)O_8$			
Ho(1)	0.34281(4)	0	0.04217(6)	0.01155(16)	0.48(1)
Ho(2)	0.37121(4)	1/2	0.27183(6)	0.01358(17)	0.48(1)
Ho(3)	0.55822(4)	0	0.27536(6)	0.01385(17)	0.48(1)
Ho(4)	0	0	0	0.0159(2)	0.241(5)
Ho(5)	0.73695(4)	0	0.59240(6)	0.01512(17)	0.48(1)
O(1)	0.2968(6)	1/2	0.0909(10)	0.0136(17)	1
O(2)	0.4848(7)	0	0.0904(12)	0.020(2)	1
O(3)	0.4201(7)	0	0.2332(11)	0.0148(18)	1
O(4)	0.6949(7)	0	0.4125(9)	0.0158(18)	1
O(5)	0.6442(7)	1/2	0.0657(10)	0.018(2)	1
O(6)	0.6291(7)	1/2	0.2273(11)	0.019(2)	1
O(7)	0.7677(7)	1/2	0.2467(11)	0.023(3)	1
O(8)	0.6413(11)	1/2	0.5676(15)	0.040(4)	1
O(9)	0.5450(16)	1/2	0.3682(14)	0.047(6)	1
O(10)*	0.4825(16)	1/2	0.462(2)	0.019(4)	0.25
B(1)*	0.6800(10)	1/2	0.1777(16)	0.016(2)	1
B(2)*	0.5629(15)	1/2	0.478(2)	0.026(4)	1

* Atoms were refined isotropically.

Table 3. Selected bond lengths (Å) in the $Nd_{4.5}Pb_{1.7}(VO_4)_{0.3}(BO_3)O_{6.42}$ (**I**), $Tb_{4.5}Pb_{1.6}(GeO_4)_{0.4}(BO_3)O_{6.02}$ (**II**), $Dy_{4.5}Pb_{1.68}(GeO_4)_{0.32}(BO_3)O_{6.28}$, and $Ho_{8.66}(BO_3)_2(B_2O_5)O_8$ structures

Atoms	**I**	**II**	**III**
	M = Nd, *A* = V	*M* = Tb, *A* = Ge	*M* = Dy, *A* = Ge
M(1)–O(2)	2.336(8)	2.293(7)	2.283(8)
M(1)–O(3) × 2	2.364(8)	2.294(6)	2.262(6)
M(1)–O(4)	2.370(10)	2.316(9)	2.322(9)
M(1)–O(1)	2.389(10)	2.302(10)	2.264(8)
M(1)–O(8) × 2	2.585(7)	2.517(6)	2.488(5)
M(2)–O(4) × 2	2.266(6)	2.207(5)	2.187(5)
M(2)–O(5)	2.324(10)	2.237(7)	2.227(8)
M(2)–O(9)	2.450(9)	2.407(7)	2.382(8)
M(2)–O(9) × 2	2.609(6)	2.510(5)	2.493(5)
M(2)–O(8)	2.706(10	2.659(9)	2.584(8)
M(3)–O(1)	2.311(10)	2.258(9)	2.237(9)
M(3)–O(6) × 2	2.356(6)	2.283(5)	2.266(5)
M(3)–O(2)	2.372(8)	2.272(7)	2.307(7)
M(3)–O(5)	2.409(9)	2.365(8)	2.354(7)
M(3)–O(7) × 2	2.531(6)	2.482(5)	2.457(5)
M(4)–O(2) × 4	2.376(5)	2.332(4)	2.295(5)
M(4)–O(7) × 2	2.434(9)	2.371(8)	2.347(7)
M(4)–O(8) × 2	2.873(10)	2.821(9)	2.867(8)
M(51)–O(1) × 2	2.260(6)	2.188(5)	2.197(5)
M(51)–O(10)	2.347(14)	2.235(16)	2.291(16)
M(51)–O(6)	2.478(10)	2.425(8)	2.364(10)
M(51)–O(10) × 2	2.517(10)	2.432(9)	2.425(8)
M(51)–O(3)	2.533(13)	2.451(12)	2.476(11)
M(52)–O(6)	2.178(11)	2.116(8)	2.066(10)
M(52)–O(10) × 2	2.318(8)	2.193(8)	2.184(7)
M(52)–O(1) × 2	2.451(7)	2.426(6)	2.426(6)
M(52)–O(10)	2.647(14)	2.526(16)	2.586(16)
M(52)–O(11) × 2	2.87(4)	3.11(4)	2.94(11)
Pb(1)–O(3)	2.119(13) 2.137(12)		2.133(11)
Pb(1)–O(10)	2.212(14)	2.241(15)	2.175(13)
Pb(1)–O(11) × 2	2.37(4)	2.02(3)	2.44(12)
A(1)–O(10)	1.625(15)	1.670(15)	1.671(13)
A(1)–O(11) × 2	1.77(4)	1.78(3)	1.50(11)
A(1)–O(3)	1.908(15)	1.829(11)	1.854(12)
Pb(21)–O(6)	2.154(10)	2.146(10)	2.193(11)
Pb(21)–O(5) × 2	2.338(6)	2.318(6)	2.321(9)
Pb(22)–O(5) × 2	2.273(6)	2.265(6)	2.264(7)
Pb(22)–O(6)	2.376(11)	2.344(10)	2.313(10)

Atoms	**IV**	Atoms	**IV**
Ho(1)–O(1) × 2	2.259(6)	Ho(1)–O(1)	2.287(11)
Ho(1)–O(2)	2.324(10)	Ho(1)–O(3)	2.325(13)
Ho(1)–O(5) × 2	2.463(8)	Ho(2)–O(1)	2.204(12)
Ho(2)–O(3) × 2	2.221(6)	Ho(2)–O(8)	2.37(2)
Ho(2)–O(10)	2.42(3)	Ho(2)–O(7) × 2	2.526(7)
Ho(2)–O(9)	2.75(3)	Ho(3)–O(2)	2.251(14)
Ho(3)–O(4)	2.265(11)	Ho(3)–O(3)	2.279(10)
Ho(3)–O(9) × 2	2.330(14)	Ho(3)–O(6) × 2	2.520(7)
Ho(4)–O(5) × 2	2.311(11)	Ho(4)–O(2) × 4	2.323(8)
Ho(4)–O(6) × 2	2.869(13)	Ho(5)–O(4) × 2	2.235(6)
Ho(5)–O(4)	2.243(11)	Ho(5)–O(7)	2.300(12)
Ho(5)–O(8) × 2	2.433(12)	Ho(5)–O(6)	2.493(13)

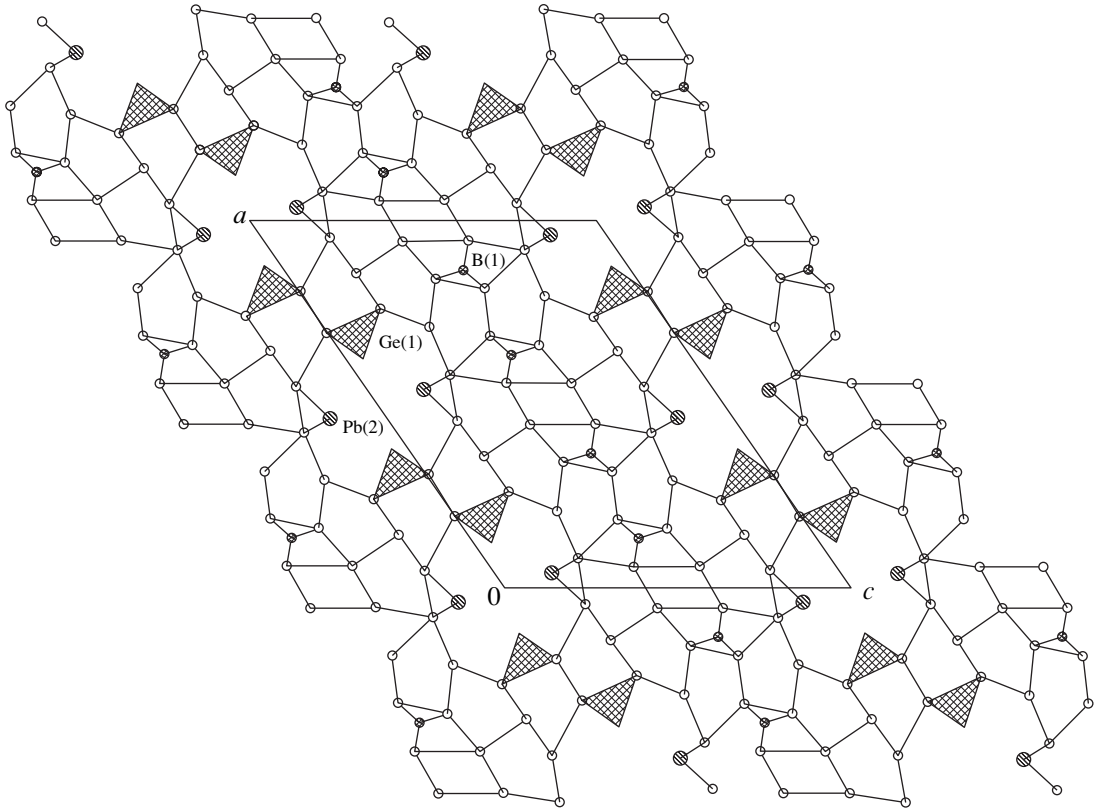

Fig. 1. Structure of compound **III** projected along the *y*-axis.

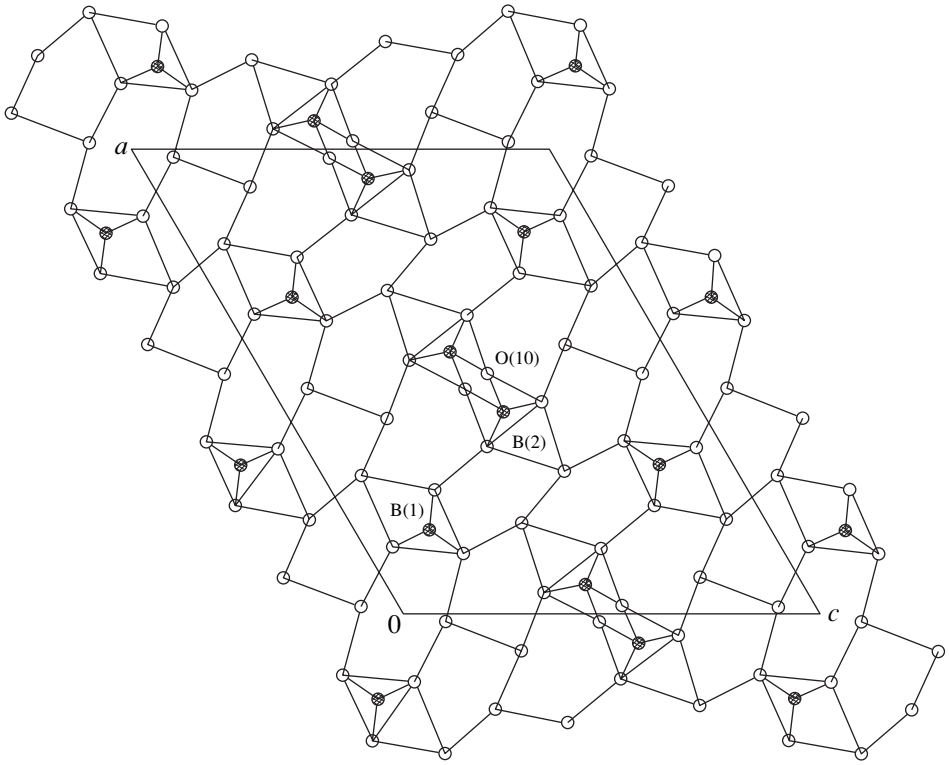

Fig. 2. Structure of compound **IV** projected along the *y*-axis.

polyhedron in this position (the coordination number 7, the Nd–O distances range within 2.26–2.53 Å) is unusual for lead but is characteristic of neodymium. This conclusion is additionally supported by the Brown calculation [7] of the local valence balance—the calculated charges for the Nd and Pb positions are 3.18 and 3.23, respectively. The coordination polyhedron of a pentavalent vanadium described in [2] as a semioctahedron (one OVO bond angle is 175° and five OVO bond angles range from 87° to 89°) seems also to be improbable. The displacement of the O(11) atom (the O(9) atom according to the numbering scheme in [2]) from the plane *m* leads to a more realistic tetrahedral coordination of the vanadium atom (the OVO angles range within 99°–115°).

The projection of the structure of compound **III** along the *y*-axis (Fig. 1) shows the GeO_4^{4-} tetrahedron in the position occupied by lead and germanium. One can clearly see large cavities toward which the lone electron pairs of lead atoms are directed.

Apparently, compounds **I**–**III** are the representatives of a large family described by the general formula $Ln_xPb_y(MO_4)_z(BO_3)O_m$. Taking into account that *M* can be either a pentavalent or a tetravalent cation and that the structure contains a partly occupied oxygen position, it is possible to expect the formation of the compounds $Ln_xPb_y(MO_4)_z(BO_3)O_m$ in which RE positions are partly replaced by the cations either with higher or lower charges.

The structure of compound **IV** is built by seven- and eight-vertex holmium polyhedra and orthopyroborate anions. All the atoms are located in the mirror symmetry planes. The occupancies of all the five crystallographically independent holmium positions are 0.96. Figure 2 shows the structure of compound **IV** projected along the *y*-axis. The framework structure has four independent oxygen atoms of the oxo groups with a tetrahedral environment of holmium atoms. Four of the five terminal oxygen atoms of borate groups also have a tetrahedral environment of three holmium and one boron atoms. The O(6) atom is involved in the bonds with four holmium atoms and one boron atom forming a trigonal bipyramid with the boron atom in the equatorial position. Even the disordered bridging O(10) atom of a pyroborate group is coordinated with a holmium atom.

As early as in the mid-1960s, the Debye patterns of the $3Ln_2O_3 \cdot B_2O_3$ compounds were indexed for all the RE elements and it was demonstrated that two morphotropic transitions took place in the series of the compounds described by the same formula—from La, Pr, and Nd (sp. gr. $P2_1/c$) to Sm–Yb ($C2/m$, $C2$, Cm; $Z = 6$) and then to Lu ($C2/m$, $C2$, Cm; $Z = 8$) [8]. However, structural studies of $3Ln_2O_3 \cdot B_2O_3$ were made only in recent years. It turned out that, in fact, the compounds have somewhat different stoichiometry. The $La_{26}(BO_3)_8O_{27}$ [9] and $Y_{17.33}(BO_3)_4(B_2O_5)_2O_{16}$ [5] compounds were studied by the methods of X-ray diffraction analysis (the latter compound is isostructural to oxoborates of Sm–Yb). The $La_{26}(BO_3)_8O_{27}$ and $Y_{17.33}(BO_3)_4(B_2O_5)O_{16}$ compounds can be written as $(3La_2O_3 \cdot B_2O_3)_4 \cdot La_2O_3$ and $(3Y_2O_3 \cdot B_2O_3)_{13.5}B_2O_3$, respectively; i.e., with a decrease in the size of the lanthanide atom the *Ln* : B ratio in $Ln_2O_3 \cdot B_2O_3$ borates is changed from 26 : 8 to 26 : 9.

In the transition from the $La_{26}(BO_3)_8O_{27}$ structure type to the $Y_{17.33}(BO_3)_4(B_2O_5)_2O_{16}$ one (which, somewhat conditionally, can be considered as a morphotropic transition), no essential changes in the RE coordination are observed (in both structures, the coordination numbers of RE are 7 and 8).

REFERENCES

1. P. A. Arsen'ev, L. M. Kovba, Kh. S. Bagdasarov, *et al.*, *Compounds of Rare-Earth Elements. Systems with Oxides of the Elements of Groups I–III* (Nauka, Moscow, 1983).
2. K. K. Palkina, N. E. Kuz'mina, B. F. Dzhurinskiĭ, *et al.*, Zh. Neorg. Khim. **43** (3), 181 (1998).
3. G. M. Sheldrick, *SHELXS97: Program for the Solution of Crystal Structures* (Univ. of Göttingen, Göttingen, 1997).
4. G. M. Sheldrick, *SHELXL97: Program for the Refinement of Crystal Structures* (Univ. of Göttingen, Göttingen, 1997).
5. J. H. Lin, S. Zhou, L. Q. Yang, *et al.*, J. Solid State Chem. **134** (1), 158 (1997).
6. R. D. Shannon, Acta Crystallogr., Sect. A: Cryst. Phys., Diffr., Theor. Gen. Crystallogr. **32**, 751 (1976).
7. I. D. Brown and D. Altermatt, Acta Crystallogr., Sect. B: Struct. Sci. **41**, 244 (1985).
8. S. F. Bertram, in *Proceedings of the Conference on Rare Earth Research* (Gordon and Breach, New York, 1964), Vol. II, p. 165.
9. J. H. Lin, S. Zhou, K. Wurst, and E. Schweda, J. Solid State Chem. **126** (2), 287 (1996).

Translated by T. Safonova

Crystallography Reports, Vol. 47, No. 3, 2002, pp. 404–407. Translated from Kristallografiya, Vol. 47, No. 3, 2002, pp. 449–452.

STRUCTURES OF INORGANIC COMPOUNDS

Average Structure of Cubic Lazurite with a Three-Dimensional Incommensurate Modulation

R. K. Rastsvetaeva*, N. B. Bolotina*, A. N. Sapozhnikov, A. A. Kashaev***, A. Schoenleber****, and G. Chapuis******

** Shubnikov Institute of Crystallography, Russian Academy of Sciences, Leninskiĭ pr. 59, Moscow, 117333 Russia*

e-mail: rast@ns.crys.ras.ru

*** Vinogradov Institute of Geochemistry, Siberian Division, Russian Academy of Sciences, ul. Favorskogo 1a, Irkutsk, 664033 Russia*

**** Irkutsk Institute of Railway Transport Engineering, ul. Chernyshevskogo 15, 664074 Irkutsk, Russia*

***** Institute of Crystallography, University of Lausanne, BSP, Lausanne, 1015 Switzerland*

Received November 8, 2001

Abstract—Three-dimensional incommensurately modulated cubic lazurite from the Malo-Bystrinskoe deposit (the Baikal region) was studied by the methods of X-ray diffraction analysis. The *a* parameter of the cubic unit cell is 9.077(1) Å. The calculations performed within the sp. gr. *P*23 ($R = 0.056$, 309 independent reflections) provided detailed information on the average structure of the mineral (the satellite reflections were ignored). © *2002 MAIK "Nauka/Interperiodica".*

INTRODUCTION

Like hauyne and noseane, lazurite of the complex composition $(Na,Ca,K)_{7–8}Si_6Al_6O_{24}(SO_4, S, Cl)_2 \cdot nH_2O$ belongs to the sodalite group. The minerals of this group are of particular interest because their X-ray diffraction patterns have, in addition to the Bragg reflections from the cubic sublattice, satellite reflections indicative of the modulation of the crystal structure. Lazurites are characterized by a wide variety of incommensurate and commensurate modulations of the structure. As a result, the symmetry of the crystal structures of various lazurite specimens change from cubic to triclinic [1–3]. In all cases, it is difficult to understand and adequately describe the character of superstructural distortions and, especially, the X-ray diffraction pattern of cubic lazurite. The intensities of the satellite reflections and the presence of high-order (up to the fourth order) satellites show that cubic lazurite is characterized by a three-dimensional incommensurate modulation with a pronounced amplitude and nontrivial wave functions. To solve the difficult problem of finding and refining the modulation parameters, it is necessary to obtain reliable information on the basis structure of cubic lazurite considered in this article.

EXPERIMENTAL

We studied cubic lazurite from the Malo-Bystrinskoe deposit (the Baikal region). The X-ray diffraction data were collected from a pale-blue poorly-faceted single crystal. The fragments of the X-ray diffraction pattern measured within the total sphere of the reciprocal space were combined into one set of the integrated intensities of 5778 main reflections of which 3688 reflections had $I > 3\sigma(I)$.

The systematic absences indicated three possible space groups of the diffraction class $m\bar{3}m$ or two space groups of the lower-symmetry diffraction class $m\bar{3}$. However, the centrosymmetric space groups *Pm*3*m* and $Pm\bar{3}$ are inconsistent with the structural model in which sulfur-tetrahedra are located at inversion centers, whereas the acentric space group *P*432 rigidly fixes the positions of the O atoms along the *z*-axis. Using the main reflections, we can describe the symmetry of cubic lazurite by the sp. gr. $P\bar{4}3m$. However, the presence of satellite reflections is indicative of a lower symmetry and requires the transition from the group $P\bar{4}3m$ to the subgroup *P*23, because some *hkl* and *khl* reflections have considerably different intensities and cannot belong to one group of equivalent reflections within the diffraction class $m\bar{3}m$ (the merging *R* factor exceeded 7%). Averaging the intensities of the equivalent reflections within the diffraction class $m\bar{3}$ ($R_{int} = 0.031$), we arrive at 309 independent reflections. It should be noted that, although the satellite reflections were ignored, the main reflections comprised the most intense but small fraction of the overall set of rather strong reflections (the total numbers of reflections, together with the satellite reflections, were 220–908 and 40–214 before and after averaging, respectively).

1063-7745/02/4703-0404$22.00 © 2002 MAIK "Nauka/Interperiodica"

All the computations were performed by the AREN and JANA crystallographic program packages [4, 5]. The atomic coordinates of cubic hauyne [6] (transformed from the sp. gr. $P\bar{4}3n$ to the sp. gr. $P23$) were used as the starting model for the refinement. The relatively high initial R factor indicated that the starting model was rather rough. The additional S(2), Na(2), and Ca positions and the mixed M(Na,Ca) position were localized from Fourier syntheses. The thermal parameter of one of the O atoms determined at this stage was twice as large as that of another oxygen atom, O(1), which provided evidence that the former position can be split. Actually, the difference electron-density synthesis contained an additional peak at a distance of 0.776(6) Å from the O atom characterized by a large thermal parameter and also four positions occupied by sulfide sulfur atoms. The refinement of the occupancies of the positions statistically occupied by O(2') and O(2") atoms and all the positions occupied by intraframework cations with due regard for the mixed occupancy of the M position reduced the R factor to 9% and 5.6% in the isotropic and anisotropic approximations, respectively. The crystallographic characteristics and the details of the X-ray diffraction study are indicated in Table 1. The atomic coordinates, thermal parameters, multiplicities, and occupancies of the positions are listed in Table 2. The interatomic distances are given in Tables 3 and 4.

Table 1. Crystallographic data and details of the X-ray diffraction experiment

Characteristic	Data and conditions
Unit-cell parameter, Å	$a = 9.077(1)$
Unit-cell volume, Å^3	$V = 747.9(3)$
Density, ρ_{calcd}, g/cm^3	2.306
Sp. gr.	$P23$
Radiation; λ (Å)	MoK_α; 0.71073
Crystal dimensions, mm	$0.30 \times 0.36 \times 0.44$
Diffractometer	Oxford Xcalibur four-circle diffractometer, κ geometry, CCD detector
$\sin\theta/\lambda$, Å^{-1}	0.11–0.72
Ranges of the indices of measured reflections	$-10 < h < 12$, $-12 < k < 10$, $-12 < l < 12$
R_{int} for equivalent reflections	0.031
$R_{e.s.d.} = \Sigma(\sigma_I)/\Sigma(I)$ upon averaging	0.0021
Total number of reflections	5778 reflections including 3688 reflections with $I > 3\sigma(I)$
Number of independent reflections	309 $I > 3\sigma(I)$
Software for diffractometer	CrysAlis RED (Version 1.167);
Programs for structural computations	AREN, JANA
Number of parameters refined	101
Extinction parameter E	0.0001112
R; R_w-factors upon anisotropic refinement	0.056; 0.046

RESULTS AND DISCUSSION

The basis structure (Fig. 1) calculated from the main reflections, with no account for the satellite reflections, is the superposition of all unit cells with their particular atomic arrangements. As a consequence, the thermal parameters of the atoms are overestimated, and the statistically occupied positions in the average structure are split. As can be seen from Tables 2 and 3, the Si and Al positions in such a structure cannot be distinguished; the position of one of the two O atoms involved in the formation of the tetrahedral framework is split into two subpositions, whereas the positions of the intraframework sulfide sulfur forms the pairs with rather short spacings between them. The sulfate sulfur atoms occupy the positions 1a and 1b with the coordinates (0 0 0) and (1/2 1/2 1/2), respectively, whereas in the structures of hauyne [6] and cubic lazurite [7] described within the sp. gr. $P\bar{4}3n$ they occupied the single (0 0 0) position. In the hauyne structure, the position of the oxygen atom involved in the environment of a sulfur atom is split. As a result, the S-tetrahedron has two statistically occurring orientations. The sulfide sulfur atoms occupy the 6i and 6f positions and are located in the same cavities as the SO_4-tetrahedra, thus competing with the sulfate sulfur atoms or their oxygen environment (Table 4).

Large Na and Ca cations occupy the positions 4e along the body diagonals of the cubic unit cell. Their polyhedra are formed not only by the O(1), O(2'), and O(2") atoms but also by the $O_{S(1)}$ and $O_{S(2)}$ atoms surrounding the sulfate sulfur atoms and the anions of S(3)–S(6) sulfide sulfur. Allowance for the statistical filling of the anionic subpositions (Table 4) reduces the coordination numbers of the cations, which is reflected in the polyhedron names in Table 3.

According to the microprobe analysis, the composition of the mineral can be written (Z = 1) as $(Na_{6.41}Ca_{1.36}K_{0.04})_{\Sigma 7.81}(Si_{6.09}Al_{5.91})_{\Sigma 12}O_{24}[(SO_4)_{1.73} \times Cl_{0.17}]_{\Sigma 1.90}$. Then, it follows that the Na/Ca ratio is inconsistent with the electroneutrality of the formula. The X-ray structure study provides a more balanced formula with some coefficients being rounded off (within the experimental error of the determination of the occupancies) and allowance for the Cl atoms detected by microprobe analysis, namely, $Na_{6.2}Ca_{1.7}(Al_6Si_6O_{24})[(SO_4)_{0.85}S^{2-}_{0.9}Cl_{0.1}]$. Since the character of incorporation of sulfur atoms into lazurite structures can hardly be determined by chemical meth-

Table 2. Atomic coordinates, multiplicities (Q), and occupancies (q) of the positions and equivalent thermal parameters

Atom	x/a	y/b	z/c	Q	q	B_{eq}, Å^2
T(1)	0.5	0.2499(1)	0	6	1	3.2(1)
T(2)	0.5	0	0.2499(1)	6	1	3.6(1)
O(1)	0.3509(3)	0.3512(3)	0.0163(5)	12	1	7.8(2)
O(2')	0.1466(3)	0.1464(3)	0.5355(3)	12	0.68(1)	4.3(1)
O(2'')	0.1508(6)	0.1521(6)	0.4502(6)	12	0.32(1)	3.2(2)
M	0.7547(3)	0.7547(3)	0.7547(3)	4	0.36(2)	5.1(3)
Ca	0.8150(3)	0.8150(3)	0.8150(3)	4	0.27(2)	5.0(3)
Na(1)	0.2585(3)	0.2585(3)	0.2585(3)	4	0.44(1)	4.4(1)
Na(2)	0.2019(5)	0.2019(5)	0.2019(5)	4	0.24(1)	3.1(2)
Na(3)	0.3253(6)	0.3253(6)	0.3253(6)	4	0.32(1)	5.7(2)
Na(4)	0.6872(5)	0.6872(5)	0.6872(5)	4	0.37(1)	6.6(2)
S(1)	0	0	0	1	0.51(1)	9.3(2)
S(2)	0.5	0.5	0.5	1	0.37(1)	8.1(2)
$O_{S(1)}$	0.8996(9)	0.8996(9)	0.8996(9)	4	0.51(1)	11.4(2)
$O_{S(2)}$	0.3930(8)	0.3930(8)	0.3930(8)	4	0.37(1)	10.4(3)
S(3)	0.1522(87)	0.5	0.5	6	0.06(1)	19.3(4)
S(4)	0.2589(30)	0	0	6	0.07(1)	8.7(7)
S(5)	0.2683(97)	0.5	0.5	6	0.03(1)	10.3(8)
S(6)	0.1471(42)	0	0	6	0.05(1)	11.6(6)

Note: $T = Si_{0.5}Al_{0.5}$; $M = Na_{0.6}Ca_{0.4}$.

Table 3. Interatomic distances (Å)

Tetrahedra					
T(1)–O(1)	1.643(3) × 2	T(2)–O(1)	1.639(2) × 2	S(1)–$O_{S(1)}$	1.578(8) × 4
O(2')	1.658(3) × 2	O(2')	1.660(3) × 2	$O_{S(1)}$–$O_{S(1)}$	2.58(1)
O(2'')	1.709(6) × 2	O(2'')	1.693(6) × 2	S(2)–$O_{S(2)}$	1.682(8) × 4
				$O_{S(2)}$–$O_{S(2)}$	2.75(1)
Nine-vertex Ca-polyhedron		Ten-vertex M-polyhedron		Seven(nine)-vertex Na-polyhedron	
Ca–S(6)	2.399(6) × 3	M–$O_{S(1)}$	2.278(9)	Na(1)–$O_{S(2)}$	2.113(8)
S(4)	2.468(8) × 3	O(2')	2.359(4) × 3	O(2'')	2.217(6) × 3
O(2')	2.585(4) × 3	O(1)	2.735(5) × 3	O(1)	2.499(5) × 3
O(1)	2.807(4) × 3	O(2'')	3.015(6) × 3	O(2')	2.896(4) × 3
		S(4)	3.151(3) × 3	S(5)	3.101(4) × 3
Ten-vertex Na-polyhedron		Nine-vertex Na-polyhedron		Nine-vertex Na-polyhedron	
Na(2)–O(2'')	2.345(7) × 3	Na(3)–S(5)	2.30(2) × 3	Na(4)–S(5)	2.44(1) × 3
O(1)	2.550(6) × 3	O(2'')	2.503(8) × 3	O(2')	2.540(6) × 3
S(6)	2.639(8) × 3	S(3)	2.7(1) × 3	S(3)	2.8(1) × 3
S(4)	2.643(7) × 3	O(1)	2.824(7) × 3	$O_{S(2)}$	2.862(9) × 3
$O_{S(2)}$	3.004(9)	O(2')	2.985(7) × 3	O(2'')	2.986(7) × 3
$O_{S(1)}$	3.04(1) × 3			O(1)	3.027(6) × 3
O(2')	3.110(5) × 3				

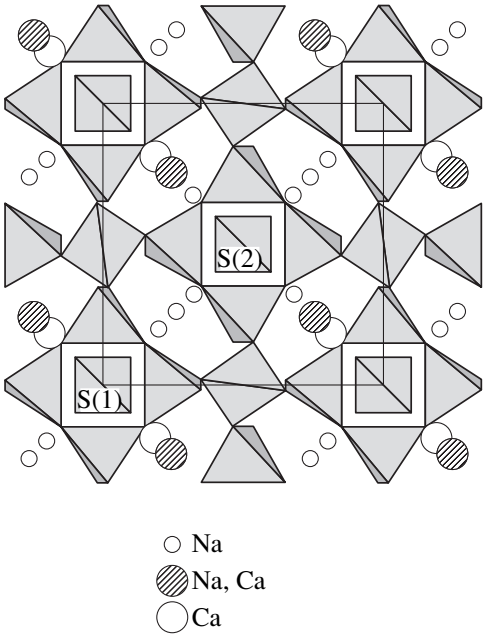

Fig. 1. Framework of the Si- and Al-tetrahedra in the average structure of cubic lazurite; the Na- and Ca-cations (circles) and the SO_4-anions (tetrahedra) are located in the framework cavities.

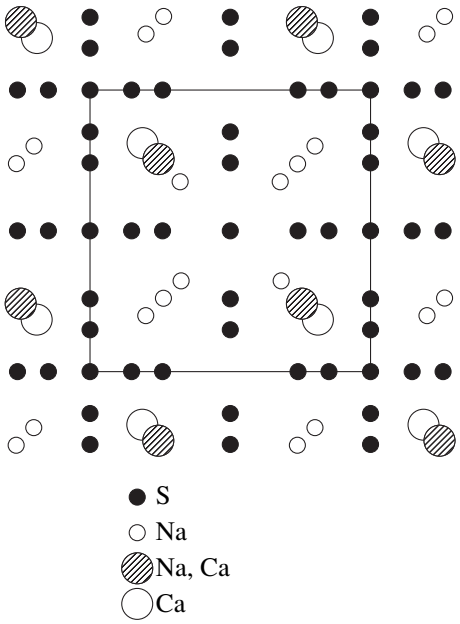

Fig. 2. Distribution of sulfide sulfur atoms around the intraframework cations.

ods, we singled out two types of sulfur atoms proceeding from crystallochemical considerations—sulfide sulfur atoms are not tetrahedrally coordinated with oxygen atoms, but are involved in the anionic environment of Na and Ca cations (Fig. 2). The differences in the Na/Ca ratio revealed in the comparison of our results with the microprobe-analysis data can be explained by their inavoidable distortions in the consideration of the modulated structure as an average model.

Table 4. Selected distances (Å) between the statistically occupied positions

Position	Distance
O(2'), O(2'')	0.777(6)
S(5), S(3)	1.1(3)
S(6), S(4)	1.01(4)
S(1), S(6)	1.33(1)
S(2), S(5)	2.10(1)
S(1), S(4)	2.35(3)
S(5), $O_{S(2)}$	1.78(5)
S(6), $O_{S(1)}$	1.36(1)
Na(1), Na(2)	0.89(1)
Na(1), Na(3)	1.05(1)
Na(2), Na(3)	1.94(1)
M, Ca	0.948(4)
M, Na(4)	1.061(6)
Ca, Na(4)	2.009(5)

Thus, we manage to solve the lazurite structure for the first time within the sp. gr. *P*23, which provided more detailed information on the mineral structure. Using these data, next we plan to examine the modulated structure with due regard for satellite reflections.

ACKNOWLEDGMENTS

This study was supported by the Russian Foundation for Basic Research, project nos. 01-05-64604, 00-02-16636, and 00-15-96633.

REFERENCES

1. A. N. Sapozhnikov, V. G. Ivanov, A. Ya. Medvedev, and L. N. Matveeva, Izv. Akad. Nauk SSSR, Neorg. Mater. **27** (4), 811 (1991).
2. V. G. Evsyunin, R. K. Rastsvetaeva, A. N. Sapozhnikov, and A. A. Kashaev, Kristallografiya **43** (6), 1057 (1998) [Crystallogr. Rep. **43**, 999 (1998)].
3. V. G. Evsyunin, A. N. Sapozhnikov, A. A. Kashaev, and R. K. Rastsvetaeva, Kristallografiya **42** (6), 1014 (1997) [Crystallogr. Rep. **42**, 938 (1997)].
4. V. I. Andrianov, Kristallografiya **32** (1), 228 (1987) [Sov. Phys. Crystallogr. **32**, 130 (1987)].
5. V. Petricek and M. Dusek, *JANA2000: The Crystallographic Computing System* (Institute of Physics, Prague, 2000).
6. V. G. Evsyunin, A. N. Sapozhnikov, R. K. Rastsvetaeva, and A. A. Kashaev, Kristallografiya **41** (4), 659 (1996) [Crystallogr. Rep. **41**, 622 (1996)].
7. I. Hassan, R. C. Peterson, and H. D. Grundy, Acta Crystallogr., Sect. C: Cryst. Struct. Commun. **41**, 827 (1985).

Translated by T. Safonova

Crystallography Reports, Vol. 47, No. 3, 2002, pp. 408–411. Translated from Kristallografiya, Vol. 47, No. 3, 2002, pp. 453–456.

STRUCTURES OF INORGANIC COMPOUNDS

Acentric Niobium-Rich Analogue of Labuntsovite-Fe: Crystal Structure and Microtwinning

K. A. Rozenberg*, R. K. Rastsvetaeva, N. V. Chukanov***, and V. V. Subbotin******

** Faculty of Geology, Moscow State University, Vorob'evy gory, Moscow, 119899 Russia*

*** Shubnikov Institute of Crystallography, Russian Academy of Sciences, Leninskiĭ pr. 59, Moscow, 117333 Russia*

e-mail: rast@ns.crys.ras.ru

**** Institute of Problems of Chemical Physics in Chernogolovka, Russian Academy of Sciences, Chernogolovka, Moscow oblast, 142432 Russia*

***** Geological Institute, Kola Research Center, Russian Academy of Sciences, ul. Fersmana 14, Apatity, Murmansk oblast, 184200 Russia*

Received July 11, 2001

Abstract—A new mineral of the labuntsovite group from Vuoriyarvi (North Karelia) was studied by the method of X-ray diffraction analysis. The unit-cell parameters are a = 14.450(6) Å, b = 13.910(6) Å, c = 7.836(4) Å, β = 117.42(1)°, V = 1398.1 Å^3, sp. gr. *Cm*. The symmetry, unit-cell parameters, splitting of the *A* position, and ordered distribution of the cations over the *B* and *C* positions of the new mineral makes it similar to the zinc-rich analogue of labuntsovite. Unlike the zinc-rich analogue, the *D* position in the new representative of the labuntsovite group is dominated by Fe atoms when the position occupancy is lower. In addition, the new representative is characterized by high occupancies of the *A* and *B* positions and the ordered distribution of the Ti and Nb atoms over two octahedral positions. In both minerals, the *A* position is split into two positions, with one of the positions in both minerals being occupied by Na and the other position being occupied by K in the new mineral and Sr in the Zn-analogue. © *2002 MAIK "Nauka/Interperiodica".*

In recent years, the minerals of the labuntsovite group have attracted interest because of their ion-exchange properties. We performed X-ray diffraction analysis on a single crystal of a new representative of this group discovered in hydrothermal paragenesis from the Vuoriyarvi carbonatite massif (North Karelia). The mineral was found in a test core of a prospecting borehole in the form of 3 mm-long brown prismatic crystals.

The chemical composition of the mineral was determined by local X-ray spectral analysis (averaging over six points). The empirical formula (with respect to 16 Si atoms), $K_{4.3–4.8}Na_{2.4–2.7}Ba_{0.7–0.9}Fe_{0.6–0.8}Mg_{0.4–0.7}Mn_{0.1–0.2} \cdot (Ti_{4.6–4.8}Nb_{3.2–3.5})[Si_4O_{12}]_4 \cdot nH_2O$, reflects the phase inhomogeneity.

The observed doubled unit-cell parameter c is indicative of lemmleinite-type twinning. To convert the experimental unit cell to a true monoclinic unit cell, we used the matrix [1 0 0 / 0 1 0 / 0 0 0.5] + [1 0 0 / 0 1 0 / –0.5 0 –0.5] used elsewhere [1]. The refined weight coefficients of the twin components are 0.53 and 0.47.

Assuming the structural similarity of the new mineral and the zinc-rich analogue of labuntsovite, we used the atomic coordinate of the latter [2] as the starting

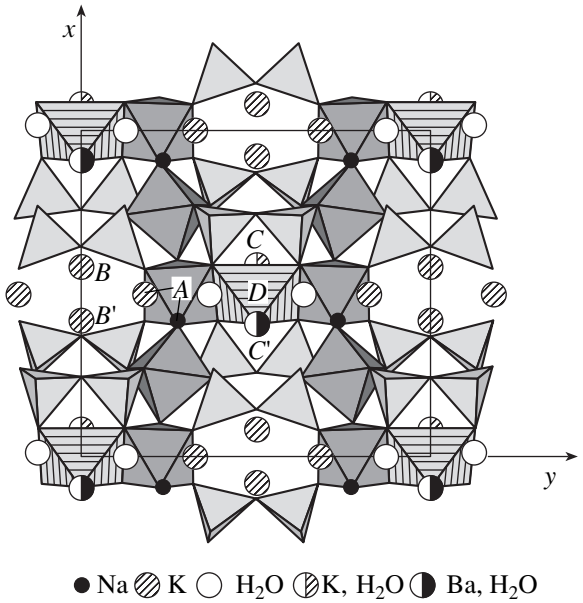

Fig. 1. Crystal structure of the mineral projected onto the (001) plane. Fe-octahedra are hatched. Circles of different types represent large cations and water molecules. The key positions are indicated by letters *A*, *B*, *C*, and *D*.

Table 1. Main characteristics of the mineral and details of the X-ray diffraction experiment

Characteristic	Data and conditions	Characteristic	Data and conditions
Parameters of the double unit cell, Å, deg	a = 14.450(6)	Crystal dimensions, mm	0.15 × 0.2 × 0.35
	b = 13.910(6)	Diffractometer	SYNTEX $P2_1$
	c = 15.672(4)	Ranges of the indices of measured reflections	$-16 < h < 14$
	β = 117.420(5)		$-14 < k < 15$
Parameters of monoclinic unit cell, Å, deg	a = 14.450(6)		$0 < l < 18$
	b = 13.910(6)	Maximum $\sin\theta/\lambda$	0.58
	c = 7.836(4)	Total number of reflections	1738
	β = 117.420(5)	Number of independent reflections	1523 $F > 4\sigma(F)$
Unit-cell volume, Å^3	V = 1398.1	R factor upon anisotropic refinement	0.066
Sp. gr.; Z	Cm; 1	Program used for refinement	AREN [3]
Radiation, Å; λ	CuK_α; 1.5418	Program used for introduction of absorption correction	DIFABS [4]
Density (calc.), g/cm^3	2.76		

Table 2. Atomic coordinates, multiplicities (Q), occupancies (q), and equivalent thermal parameters of the atoms

Position	x/a	y/b	z/c	Q	q	B_{eq}, Å^2
Ti(1)	−0.0002(1)	0.2273(1)	0.5002(1)	4	1	2.82(6)
Ti(2)	0.2518(3)	0.2516(2)	0.4943(6)	4	1	2.86(5)
Si(1)	0.2104(3)	0.1097(3)	0.7970(5)	4	1	2.3(1)
Si(2)	0.7955(3)	0.1096(2)	0.1918(4)	4	1	1.7(1)
Si(3)	0.3250(3)	0.1102(4)	0.2445(6)	4	1	2.9(1)
Si(4)	0.6843(2)	0.1104(2)	0.7492(4)	4	1	1.2(1)
Fe	0.0091(9)	0	0.513(2)	2	0.55(1)	2.9(1)
Na	0.917(1)	0.232(1)	0.006(3)	4	0.60(1)	5.5(2)
K(1)	0.5807(6)	0	0.292(1)	2	0.70(1)	7.4(1)
K(2)	0.498(1)	0.178(1)	−0.002(2)	4	0.40(1)	6.5(1)
K(3)	0.421(1)	0	0.713(2)	2	0.79(3)	8.9(2)
C(1)	0.0812(7)	0	0.322(1)	2	0.90(1)	3.4(2)
C(2)	0.9075(4)	0	0.6491(7)	2	0.81(1)	4.0(1)
O(1)	0.241(1)	0.1354(9)	0.035(2)	4	1	3.7(4)
O(2)	0.7698(5)	0.1229(7)	0.981(1)	4	1	2.1(3)
O(3)	0.2763(8)	0.1771(6)	0.737(1)	4	1	2.1(3)
O(4)	0.7285(8)	0.1884(9)	0.269(1)	4	1	2.8(3)
O(5)	0.102(1)	0.224(1)	0.380(1)	4	1	2.9(3)
O(6)	0.9024(9)	0.2278(9)	0.600(2)	4	1	3.3(4)
O(7)	0.2452(9)	0	0.790(2)	2	1	2.8(5)
O(8)	0.758(1)	0	0.221(1)	2	1	3.2(4)
O(9)	0.4174(8)	0.176(1)	0.310(2)	4	1	4.3(4)
O(10)	0.5789(7)	0.1806(6)	0.694(1)	4	1	1.6(3)
O(11)	0.272(1)	0.133(1)	0.388(1)	4	1	3.8(4)
O(12)	0.7427(6)	0.1231(7)	0.622(1)	4	1	1.7(3)
O(13)	0.369(1)	0	0.275(2)	2	1	3.0(4)
O(14)	0.643(1)	0	0.723(2)	2	1	2.1(4)
O(15)	0.0881(6)	0.1267(9)	0.681(1)	4	1	2.8(4)
O(16)	0.9206(7)	0.1151(6)	0.335(1)	4	1	1.6(3)
H_2O(2)	0.008(3)	0.123(2)	0.015(3)	4	0.73(2)	7.5(2)

Note: Ti(1) = $Ti_{0.7}Nb_{0.3}$; Ti(2) = $Ti_{0.5}Nb_{0.5}$; Fe = $Fe_{0.6}Mg_{0.4}$; K(3) = $K_{0.5}(H_3O)_{0.5}$; C(1) = $(H_2O)_{0.6}K_{0.4}$; C(2) = $(H_2O)_{0.7}Ba_{0.3}$.

Table 3. Characteristics of the coordination polyhedra

Position	Composition	Coordination number	Cation–anion distances, Å		
			minimum	maximum	average
Si(1)	4Si	4	1.55(1)	1.74(1)	1.62
Si(2)	4Si	4	1.53(1)	1.74(1)	1.64
Si(3)	4Si	4	1.50(1)	1.65(1)	1.59
Si(4)	4Si	4	1.58(1)	1.68(1)	1.64
Ti(1)	2.8Ti + 1.2Nb	6	1.90(1)	2.08(1)	1.97
Ti(2)	2Ti + 2Nb	6	1.84(1)	2.04(1)	1.96
Fe	0.66Fe + 0.44Mg	6	2.12(1)	2.18(1)	2.16
C(1)	0.72K + 1.1H_2O	11	2.86(1)	3.18(1)	3.04
C(2)	0.48Ba + 1.1H_2O	11	2.74(2)	3.31(1)	3.06
K(1)	1.4K	9	2.86(2)	3.44(1)	3.20
K(2)	1.6K	7	2.77(2)	3.15(1)	3.00
K(3)	0.79K + 0.79H_3O	9	2.86(2)	3.43(1)	3.19
Na	2.4Na	8	1.97(3)	3.08(1)	2.68

model. The structure was refined using mixed atomic scattering curves. The relatively high *R* factor is associated with the poor quality of the X-diffraction data collected from the twinned crystal.

The main characteristics of the crystal and the details of the X-ray diffraction experiment are given in Table 1. The atomic coordinates are listed in Table 2. The elemental compositions of the atomic positions and the interatomic distances are indicated in Table 3.

The mixed framework, consisting of octahedral chains of Ti-octahedra along the *a*-axis and the four-membered rings of the SiO_4-tetrahedra (Fig. 1) is common to all the minerals of the labuntsovite group. In the mineral under study, the channels parallel to the coordinate axes are occupied by Na, K, and Ba atoms, H_3O^+ ions, and water molecules. The crystallochemical formula of the mineral ($Z = 1$) can be written as $[Na_{2.4}K_{1.6}] \cdot [K_{2.2}(H_3O)_{0.8}]\{[K_{0.72}Ba_{0.48}][Fe_{0.66}Mg_{0.44}(H_2O)_{2.2}]\} \cdot [Ti_{4.8}Nb_{3.2} \cdot (OH_{5.27}O_{2.73}\}][Si_4O_{12}]_4 \cdot 2.92H_2O$, where the compositions of the key *A*, *B*, *C*, and $D(H_2O)_2$ positions in the structure channels are indicated in the first four pairs of square brackets, respectively. The cations with high values of force characteristics (Fe and Mg) occupy the sites of the *D* position where the chains approach each other at the shortest distances. In this case, their polyhedra are built up to octahedra with two additional water molecules.

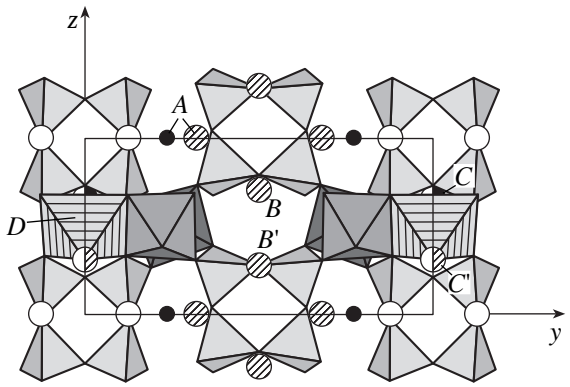

Fig. 2. Crystal structure of the mineral projected onto the (100) plane. Notation as in Fig. 1.

In the new mineral, like its Zn-analogue [2], the *A* position is split into two positions separated by a spacing of 1.73 Å. These two positions are statistically occupied by the Na and K(2) atoms, respectively (Fig. 2). The K(2) atom is located in the position occupied by an $H_2O(1)$ molecule in conventional labuntsovites. This position is shifted toward Na (like the Sr position in the Zn-analogue). The somewhat shortened Na–$H_2O(2)$ distance (1.97 Å) is explained by incomplete occupancies of both cationic and water-molecule positions.

The *B* position is occupied by K atoms and H_3O^+ ions distributed over two subpositions, $B = K(1)$ and mixed $B' = K(3)$. A similar filling of the *B* position is also observed in the analogous noncentrosymmetric Zn-dominant representative of the labuntsovite group, where one position is that of H_3O^+ and the second position is mixed (K, H_3O^+). The incorporation of oxonium ions into the mineral structure is confirmed by the presence of a weak band (ν) at 1715 cm^{-1} in the IR spectrum. According to the IR spectral data [5], the frequency of the (Ti,Nb) stretching vibration is 683 cm^{-1}, which corresponds to a relatively high occupancy of the *D* position (1.2 (Fe, Mg, Mn) atoms per unit cell). The new mineral is characterized by the ordered distribution of Ti and Nb atoms over two octahedral positions (one position is occupied mainly by Ti atoms, and the second position, by equal amounts of Ti and Nb atoms) and by selective K and Ba distribution over two *C* positions.

Thus, the symmetry, unit-cell parameters, splitting of the *A* position, and the ordered distribution of the cations over the *B* and *C* positions of the new mineral are similar to those of the zinc-rich analogue of labuntsovite. However, unlike the zinc-rich analogue, the *D* position in the new mineral is dominated by Fe atoms when its occupancy is lower. At the same time, the *A* and *B* positions in the new mineral have high occupancies, whereas Ti and Nb atoms are orderly distributed over two octahedral positions.

ACKNOWLEDGMENTS

This study was supported by the Russian Foundation for Basic Research (project no. 99-05-65035) and the Federal Program on Support of Prominent Scientists and Leading Scientific Schools, project no. 00-15-96633.

REFERENCES

1. R. K. Rastsvetaeva, R. A. Tamazyan, D. Yu. Pushcharovskiĭ, *et al.*, Kristallografiya **39**, 994 (1994) [Crystallogr. Rep. **39**, 908 (1994)].
2. K. A. Rozenberg, R. K. Rastsvetaeva, I. V. Pekov, and N. V. Chsukanov, Dokl. Akad. Nauk **383** (5), 600 (2002).
3. V. I. Andrianov, Kristallografiya **32**, 228 (1987) [Sov. Phys. Crystallogr. **32**, 130 (1987)].
4. N. Walker and D. Stuart, Acta Crystallogr., Sect. A: Found. Crystallogr. **39** (2), 158 (1983).
5. R. K. Rastsvetaeva and N. V. Chukanov, in *Proceedings of the International Symposium "Ordering in Minerals and Alloys," Rostov-on-Don, 2001*, p. 244.

Translated by T. Safonova

Crystallography Reports, Vol. 47, No. 3, 2002, pp. 412–414. Translated from Kristallografiya, Vol. 47, No. 3, 2002, pp. 457–459.

STRUCTURES OF INORGANIC COMPOUNDS

Cation Distribution in the Structure of Titanium-Containing Ludwigite

A. A. Brovkin*, I. V. Rozhdestvenskaya, and E. A. Rykova*****

** Fedorovskiĭ All-Russia Institute of Mineral Resources (VIMS), Staromonetnyĭ per. 29, Moscow, 109017 Russia*

*** Faculty of Geology, St. Petersburg State University, Universitetskaya nab. 7/9, St. Petersburg, 199164 Russia*

**** Faculty of Physics, Moscow State University, Vorob'evy gory, Moscow, 119899 Russia*

e-mail: asi@phys.msu.su

Received October 11, 2001

Abstract—The crystal structure of natural titanium-containing ludwigite has been refined. The unit-cell parameters are $a = 9.260 \pm 0.002$ Å, $b = 12.294 \pm 0.002$ Å, $c = 3.0236 \pm 0.0005$ Å, sp. gr. *Pbam*, and $R = 0.0288$. The observed cation distribution over the *M*1–*M*4 positions corresponds to the structural formula $(Mg_{0.5})(Mg_{1.0})(Mg_{0.338}Fe^{2+}_{0.162})(Fe^{3+}_{0.47}Ti^{4+}_{0.21}Mg^{2+}_{0.15}Al^{3+}_{0.10}Fe^{2+}_{0.07})(BO_3)O_2$. Highly charged titanium ions in the *M*4 position are balanced mainly with magnesium and not with divalent iron ions. © *2002 MAIK "Nauka/Interperiodica".*

The crystal structure and properties of the minerals of the ludwigite $(Mg,Fe^{2+})(Fe^{3+},Al,Sn^{4+}) \cdot (BO_3)O_2$–vonsenite $Fe^{2+}Fe^{3+}BO_3O_2$ series have been rather well studied [1–5]. The unit cell of the ludwigite structure represented in polyhedra is shown in the figure. The unit-cell parameters are $a \sim 9.2$–9.4 Å, $b \sim 12.2$–12.4 Å, and $c \sim 3.1$ Å, sp. gr. *Pbam*. The *M*1–*M*4 octahedra share horizontal edges and form columns along the short *c*-axis and in a direction forming a certain angle with the *a*-axis. The BO_3 triangles "fastening" the structure are located in trigonal channels formed by octahedra. X-ray analysis [3, 5] and Mössbauer spectroscopy [4] showed that highly charged Fe^{3+} and Al^{3+} cations are located in the *M*4 position; in isomorphous replacement of Mg atoms and Fe^{2+} cations, the latter cations mainly occupy the *M*3 cationic position. The Fe^{2+} cations start occupying (statistically) the *M*1- and *M*2-octahedra only if the ferruginosity of the ludwigite *f* exceeds 25% (*f* = FeO/(MgO + FeO), mol %). The Mössbauer spectroscopy data [4] unambiguously indicate that the degree of covalence of the Fe^{2+}–O bond in the *M*3-octahedron is higher than in the *M*1 and *M*2 positions, which is explained by their different environments: the atoms in the *M*1 and *M*2 positions are surrounded by four oxygen atoms forming the BO_3-triangle, whereas the atoms in the *M*3 position are surrounded by two oxygens (as in the *M*4 position). This study was undertaken following the discovery of ludwigites with a high TiO_2 content—from 7.3 to 15.4 wt % (asoproite)—in the Tazheran alkali massif [6]. We studied the cation distribution in the structure of ludwigite containing 8.82 wt % of TiO_2 found in this deposit. The chemical composition of ludwigite crystals kindly supplied by A.A. Kashaev was determined by V.A. Makhotko on a JXA 50A electron microanalyzer. The analysis of several crystals confirmed the chemical composition indicated earlier [6]. The degree of crystal homogeneity can be judged from the data on two analyzed crystals (Table 1). The average composition corresponds to the formula

$$(Mg_{1.97}Fe^{2+}_{0.03})(Fe^{3+}_{0.50}Fe^{2+}_{0.22}Ti_{0.21}Al_{0.10})(BO_3)O_2.$$

Table 1. Composition of ludwigite (wt %) determined from the microanalysis (JXA 50A) and chemical analysis (*x*/*a*) data [6]

Method	JXA 50A	JXA 50A		*x*/*a*, wt % [6]
Oxide	1	2	Average value	
MgO	40.46	41.61	41.04	37.39
TiO_2	8.78	8.86	8.82	7.35
Al_2O_3	2.52	2.50	2.51	1.30
FeO	28.25	27.00	9.35*	10.80
Fe_2O_3	–	–	20.78*	23.18
B_2O_3	–	–	17.50**	18.28

* In accordance with *x*/*a* [6]; the Fe^{3+}/Fe^{2+} ratio was taken to be equal to 2.

** The B_2O_3 content was estimated as the difference between 100% and the total content of all the other oxides determined on a JXA 50A microanalyzer.

Table 2. Coordinates, thermal factors, and multiplicities (*N*) of basic atoms in the ludwigite structure

Atoms	*N*	*x*/*a*	*y*/*b*	*z*/*c*	*U*(eq)*
*M*1	2	0	0	0.5	0.62(2)
*M*2	4	0.0012(7)	0.28057(5)	0.5	0.57(1)
*M*3	2	0.5	0	0	0.41(1)
*M*4	4	0.23823(4)	0.11540(3)	0	0.676(9)
B	4	0.2746(2)	0.3602(2)	0	0.59(4)
O1	4	0.3499(1)	0.4571(1)	0	0.65(3)
O2	4	0.1095(2)	0.1429(1)	0.5	0.84(3)
O3	4	0.1244(2)	0.3581(1)	0	0.72(3)
O4	4	0.3838(1)	0.0762(1)	0.5	0.95(3)
O5	4	0.3497(1)	0.2624(1)	0	0.69(3)

* The values of anisotropic thermal factors can be obtained from the authors.

X-ray diffraction analysis was performed on a ~0.15 × 0.15 × 0.2-mm crystal; the data obtained were briefly presented in [7]. Experimental data were obtained for 880 crystallographically independent nonzero reflections measured on a Syntex $P2_1$ automated diffractometer. The unit-cell parameters are $a = 9.260 \pm 0.002$ Å, $b = 12.294 \pm 0.002$ Å, $c = 3.0236 \pm 0.0005$ Å, sp. gr. *Pbam*.

The initial parameters taken from [7] were refined using the CSD complex of programs [8]. The occupancy *Q* of the *M*1–*M*4 positions was refined by a set of reflections with $\sin\theta/\lambda < 0.5$. For the *M*1–*M*3 positions, the function $f_j(\sin\theta/\lambda)$ corresponding to Mg^{2+} was used; for the *M*4 position, the function corresponding to Fe^{2+} (taken from [9]). After the introduction of the correction for absorption for a crystal of an arbitrary shape by the DIFABS program [10] and the refinement of the positional and thermal parameters over the whole set of reflections with $F(hkl) > 4\sigma_F$, the reliability factor *R* in the anisotropic approximation was 0.0288. The final values of the positional parameters of the basic atoms are given in Table 2, and the interatomic distances are listed in Table 3. The position occupancies proved to be equal: *Q*(*M*1) = 1.003(5), *Q*(*M*2) = 0.999(5), *Q*(*M*3) = 1.453(7), and *Q*(*M*4) = 0801(3).

The occupancies given above unambiguously indicate that Mg^{2+} cations are located in the *M*1 and *M*2 positions. Considering the cation distribution over the *M*3 and *M*4 positions, we assumed that the cationic *M*1–*M*4 positions are fully occupied; according to [3], the Al^{3+} cations are located in the *M*4 position. The Ti^{4+} cations were also placed in *M*4, because their valence and ionic radius were closer to Fe^{3+} than to Mg^{2+} and Fe^{2+}; the ratio $Fe^{3+}/Fe^{2+} = 2$ [6], and the number of electrons for Fe^{2+} ($Z_{Fe^{2+}}$) and Fe^{3+} ($Z_{Fe^{3+}}$) was assumed to be 24.

The content of iron cations ($C_{Fe^{2+}}$) in the *M*3 position was calculated by the obvious formula [11] $C_{Fe^{2+}}(M3) = [Q(M3)Z_{Mg^{2+}} - Z_{Mg^{2+}}]/[Z_{Fe^{2+}} - Z_{Mg^{2+}}] = [1.453 \times 10 - 10]/[24 - 10] = 0.324$; i.e., the *M*3 position is occupied by 32.4% of Fe^{2+} cations and by 67.6% of Mg^{2+} cations. The content of Fe^{2+}, Fe^{3+}, and Mg^{2+} cations in the *M*4 position was estimated in a similar way with due regard for the Ti^{4+} and Al^{3+} content. Finally, the cation distribution over the structure positions corresponds to the structural formula $(Mg_{0.5})(Mg_{1.0}) \cdot (Mg_{0.338}Fe^{2+}_{0.162})(Fe^{3+}_{0.47}Ti^{4+}_{0.21}Mg^{2+}_{0.15}Al^{3+}_{0.10}Fe^{2+}_{0.07})(BO_3)O_2$, which almost coincides with the chemical composition calculated by the electron microprobe analysis data (Table 1) and is close to the formula determined from the Mössbauer spectroscopy data, $(Mg^{2+}_{1.82}Fe^{2+}_{0.18})(Fe^{3+}_{0.46}Ti^{4+}_{0.21}Al^{3+}_{0.10}Fe^{2+}_{0.11}Mg_{0.15})_{1.03}(BO_3)O_2$ [12].

As can be seen, highly charged titanium atoms in the *M*4 position are balanced mainly by magnesium and

Table 3. Interatomic distances (*d*, Å) in natural ludwigites

Bond	*d*		Bond	*d*	
	our data	data [5]		our data	data [5]
*M*1–O1(×4)	2.120(2)	2.118(2)	*M*3–O3(×2)	2.091(3)	2.100(3)
*M*1–O2(×2)	2.029(3)	2.021(3)	*M*3–O4(×4)	2.078(2)	2.081(2)
Average value *M*1–O	2.090	2.086	Average value *M*3–O	2.082	2.087
*M*2–O2(×1)	1.967(3)	1.957(3)	*M*4–O1(×1)	2.111(3)	2.113(3)
*M*2–O3(×2)	2.120(2)	2.119(2)	*M*4–O2(×2)	1.955(2)	1.964(2)
*M*2–O4(×1)	2.069(3)	2.070(3)	*M*4–O4(×2)	2.082(2)	2.066(2)
*M*2–O5(×2)	2.129(2)	2.125(2)	*M*4–O5(×1)	2.082(3)	2.093(3)
Average value *M*2–O	2.089	2.086	Average value *M*4–O	2.048	2.044
B–O1	1.381(4)	1.379(3)	B–O3	1.392(3)	1.377(3)
B–O5	1.388(4)	1.390(2)	Average value B–O	1.387	1.382

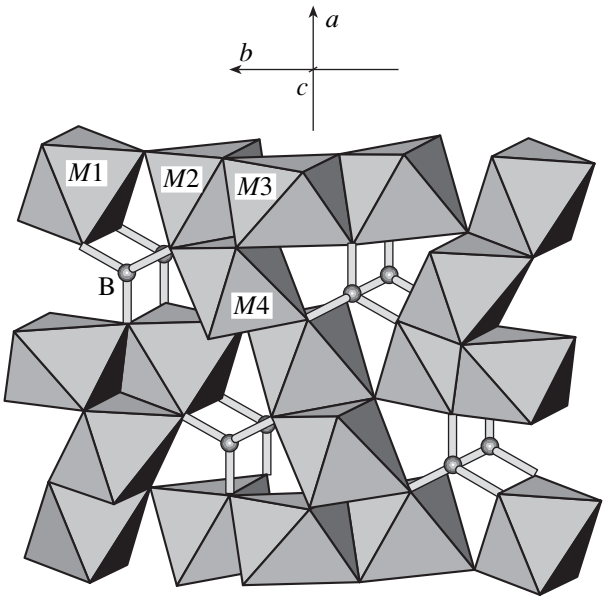

Ludwigite structure.

not divalent iron ions, which is promoted by the dimensional factor. At the average distance *M*4–O = 2.048 Å (Table 3) and with the Mg^{2+} and Fe^{2+} radii equal to 0.74 and 0.80 Å, respectively [13], the location of the Mg^{2+} cation in the *M*4 position is preferable.

In ludwigite from Krestmore described by the formula $(Mg_{0.495}Fe^{2+}_{0.005})(Mg_{0.99}Fe^{2+}_{0.01})(Mg_{0.443}Fe^{2+}_{0.557})(Fe^{3+}_{0.92}Al^{3+}_{0.08}) \cdot (BO_3)O_2$ [5] with a structure refined up to $R = 0.028$, the interatomic distances *M*3–O (Table 3) exceed the distances in the structure studied here. It is explained by a higher content of larger Fe^{2+} cations (56% of Fe^{2+} and 44% of Mg^{2+}) in this position than in ludwigite (32% of Fe^{2+} and 68% of Mg^{2+}). The *M*1–O and *M*2–O distances in both structures are equal within the experimental error ($\pm 3\sigma$), whereas the average *M*4–O distances in this position correlate with the average cation radii calculated by data [13] and are equal to 0.662 and 0.673 Å for cations in ludwigite structures from Krestmore and Tazheran massif, respectively.

ACKNOWLEDGMENTS

The authors are grateful to A.A. Kashaev for supplying the sample of titanium-containing ludwigite and to V.V. Korovushkin for the Mössbauer spectroscopy measurements made on the sample of ludwigite from Tazheran massif.

REFERENCES

1. Y. Takeuchi, T. Watanabe, and T. Ito, Acta Crystallogr. **3**, 98 (1950).
2. A. A. Brovkin, S. M. Aleksandrov, and I. Ya. Nekrasov, Rentgenogr. Miner. Syr'ya, No. 3, 16 (1963).
3. V. I. Mokeeva and S. M. Aleksandrov, Geokhimiya, No. 4, 428 (1969).
4. V. V. Kurash, V. S. Urusov, T. V. Malysheva, and S. M. Aleksandrov, Geokhimiya, No. 2, 148 (1972).
5. M. B. Irwin and R. C. Peterson, Can. Mineral. **37**, 939 (1999).
6. A. A. Konev, V. S. Lebedeva, A. A. Kashaev, and Z. F. Ushchapovskaya, Zap. Vses. Mineral. O–va., No. 2, 225 (1970).
7. A. A. Brovkin and I. V. Rozhdestvenskaya, in *Proceedings of the III All-Union Conference on Crystal Chemistry of Inorganic and Coordination Compounds* (Novosibirsk, 1983), p. 105.
8. L. G. Akselrud, Yu. N. Grin, P. Yu. Zavalii, *et al.*, in *Collected Abstracts of the XII European Crystallography Meeting* (Moscow, 1989), no. 3, p. 155.
9. *International Tables for X-ray Crystallography* (Kynoch Press, Birmingham, 1974), Vol. 4.
10. N. Wolker and D. Stuart, Acta Crystallogr., Sect. A: Found. Crystallogr. **39**, 158 (1983).
11. A. A. Brovkin, É. V. Pol'shin, V. S. Brovkina, *et al.*, Kristallografiya **23** (1), 107 (1978) [Sov. Phys. Crystallogr. **23**, 57 (1978)].
12. V. V. Korovushkin, A. A. Brovkin, E. A. Rykova, *et al.*, in *Proceedings of the II National Conference on Crystal Chemistry* (Chernogolovka, 2000), p. 84.
13. G. B. Bokiĭ, *Crystal Chemistry* (Nauka, Moscow, 1971).

Translated by T. Dmitrieva

Crystallography Reports, Vol. 47, No. 3, 2002, pp. 415–419. Translated from Kristallografiya, Vol. 47, No. 3, 2002, pp. 460–464.

STRUCTURES OF INORGANIC COMPOUNDS

Rietveld Analysis of X-ray Diffraction Pattern from β-Ta_2O_5 Oxide

L. A. Aleshina and S. V. Loginova

Petrozavodsk State University, pr. Lenina 33, Petrozavodsk, Karelia, 185640 Russia

e-mail: svlog@mainpgu. karelia.ru

Received January 20, 2000

Abstract—The structure of low-temperature β-Ta_2O_5 oxide has been studied by the method of Rietveld full-profile analysis. It is established that this oxide has an orthorhombic structure with lattice parameters a = 6.217 Å, b = 3.677 Å, and c = 7.794 Å. The atomic coordinates and thermal parameters are also determined. © *2002 MAIK "Nauka/Interperiodica".*

It is well known that transition metal oxides are widely applied in electronics, metallurgy, and optics. In particular, tantalum oxides are used in optoelectronics as optical media and dielectrics performing various important functions [1]. The low-temperature β-phase of Ta_2O_5 has low electron conductivity and is a typical dielectric. At the same time, the nature of the electronic states and atomic interactions responsible for their formation are studied insufficiently. For a better understanding of the electronic properties of tantalum oxide and more efficient use of these properties, one has to know in detail its atomic structure [2].

Unfortunately, the known data on the structure of low-temperature β-Ta_2O_5 oxide are contradictory.

Thus, the model of this oxide suggested in [3] is based on the hexagonal UO_3 structure type and is represented as a subtraction-type structure to preserve the stoichiometric composition. The hexagonal unit cell of tantalum oxide with one Ta atom has the lattice parameters a = 3.66 Å and c = 3.89 Å, sp. gr. $P\bar{3}m1$. The tantalum atom occupies the 1(a) position (0 0 0), whereas the oxygen atoms are located in the 1(b) position $\left(0\ 0\ \frac{1}{2}\right)$ and 2(d) position $\left(\frac{1}{3}\ \frac{2}{3}\ z\right)$ with z = 0.17. In order to obtain the composition $MO_{2.5}$, the distribution of oxygen vacancies was assumed to be random for the atoms in the 2(d) position. However, according to [4], the X-ray diffraction pattern of the low-temperature tantalum oxide has a number of superstructural reflections, which indicates that this phase is orthorhombic with the unit-cell parameters a = 6.18 Å, b = 3.66 Å, and c = 3.88 Å. Figures 1a and 1b show the relation between the two unit cells. In the orthorhombic unit cell, the tantalum atoms have the coordinates 1(a) (0 0 0) and 1(e) $\left(\frac{1}{2}\ \frac{1}{2}\ 0\right)$, the oxygen atoms have the coordinates 1(c) $\left(0\ 0\ \frac{1}{2}\right)$, 1($h$) $\left(\frac{1}{2}\ \frac{1}{2}\ \frac{1}{2}\right)$, 2($m$) $\left(\frac{1}{2}\ 0\ 0.83\right)$ and 2(n) $\left(\frac{1}{6}\ \frac{1}{2}\ 0.17\right)$, sp. gr. $P2/m$. The Ta_2O_5 composition is attained due to the formation of oxygen vacancies, with the main motif of the packing of oxygen and metal ions being preserved. These vacancies are randomly distributed over the lattice positions with z_1 = 0.17 and z_2 = 0.83.

The similarity of the X-ray diffraction patterns from β-Ta_2O_5 and U_3O_8 allowed one to relate the tantalum oxide structure to the U_3O_8 structure type with vacancies in the oxygen positions [5]. The oxides belonging to the U_3O_8 structure type are trigonal with the unit-cell parameters a = 6.2 Å, and c = 3.9 Å, sp. gr. $P\bar{3}$. The tantalum atoms occupy the positions 1(a) (0 0 0) and 2(d) $\left(\frac{1}{3}\ \frac{2}{3}\ z\right)$, where z = 0. The positions occupied by the oxygen atoms are 6(g) (x, y, z_1), where $x = \frac{1}{3}$, y = 0, z_1 = 0.1, and 2(d) $\left(\frac{1}{3}\ \frac{2}{3}\ z_2\right)$, where $z_2 = \frac{1}{2}$. The relation between the UO_3 and U_3O_8 unit cells is shown in Fig. 1c. In the transition from the UO_3 model to the U_3O_8 model, the positions of the tantalum and oxygen atoms remain unchanged. The only difference between the atomic arrangements in these structures is that the U_3O_8 has no oxygen atoms with the coordinates $\left(0\ 0\ \frac{1}{2}\right)$ present in the UO_3 structure. Moreover, the coordinate z for the oxygen atoms occupying the 6(g) position in the U_3O_8 model is z = 0.1, whereas in the unit cell of the UO_3 type, this coordinate is z = 0.17.

1063-7745/02/4703-0415$22.00

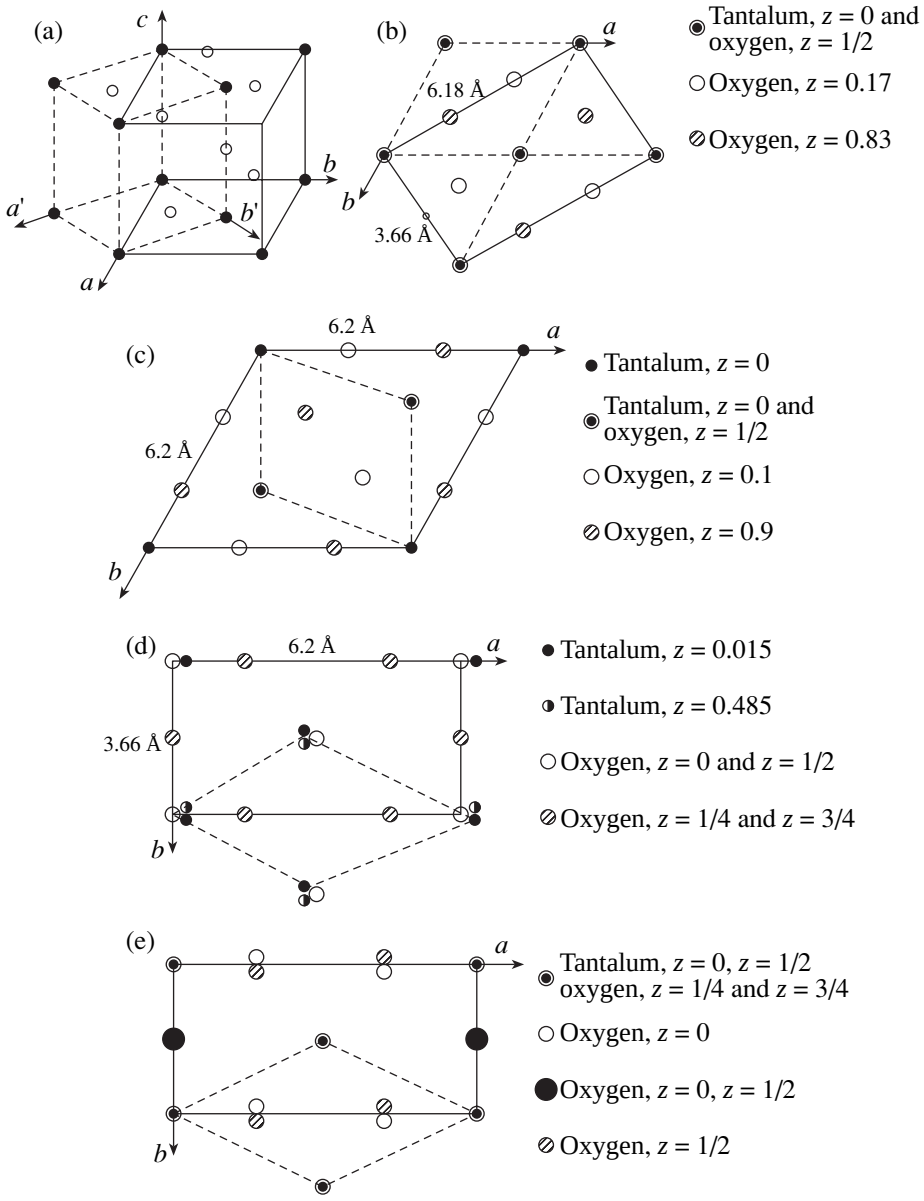

Fig. 1. (a) Spatial arrangement of atoms in the orthorhombic (solid line) and the hexagonal (dashed line) unit cells of β-Ta_2O_5 oxide and (b) the same arrangements projected onto the *ab* plane. The projections onto the *ab* plane of (c) the U_3O_8-type unit cell, (d) the unit cell considered in [6], and (e) the new unit cell (the dashed line shows the hexagonal unit cell).

According to the model suggested in [6], in the crystallized amorphous anodic oxide β-Ta_2O_5, tantalum atoms are slightly displaced from the positions characteristic of all the other above models. As a result, the unit-cell parameter along the *z*-axis is doubled. The atomic coordinates given for Ta in [6] are (α, β, γ), $\left(\alpha, -\beta, \frac{1}{2}-\gamma\right)$, (–α, –β, γ), and (–α, +β, –γ), where α = 0.04, β = 0.03, and γ = 0.015; and for O $\left(0\ \frac{1}{2}\ 0\right)$, $\left(\frac{1}{4}\ 0\ 0\right)$, $\left(\frac{3}{4}\ 0\ 0\right)$, $\left(0\ 0\ \frac{1}{4}\right)$, $\left(\frac{1}{2}\ \frac{1}{2}\ \frac{1}{4}\right)$, $\left(0\ \frac{1}{2}\ \frac{1}{2}\right)$, $\left(\frac{1}{4}\ 0\ \frac{1}{2}\right)$, $\left(\frac{3}{4}\ 0\ \frac{1}{2}\right)$, $\left(0\ 0\ \frac{3}{4}\right)$, and $\left(\frac{1}{2}\ \frac{1}{2}\ \frac{3}{4}\right)$.

Figure 1d shows the unit cell of this model projected onto the *ab* plane. The motif of the arrangement of oxygen atoms in comparison with their arrangement in the orthorhombic unit cell with $c = 3.88$ Å is changed in the following way. The oxygen atoms with the coordinates $x = \frac{1}{3}$ and $x = \frac{2}{3}$ in model [6] are displaced along the

x-axis in such a way that their coordinates become equal to $x = \frac{1}{4}$ and $x = \frac{3}{4}$, respectively. The oxygen atoms with the coordinates $\left(\frac{1}{6}\ \frac{1}{2}\ 0.17\right)$ and $\left(\frac{5}{6}\ \frac{1}{2}\ 0.83\right)$ in model [6] are displaced for a translation along the unit-cell edge into the position $\left(0\ \frac{1}{2}\ 0\right)$, so that the Ta_2O_5 composition is attained without vacancy formation.

Figure 1 shows that the motifs of the atomic arrangements in various models suggested to describe β-Ta_2O_5 are mutually related. In the transition from the UO_3 model to the U_3O_8 one, the positions of both tantalum and oxygen atoms remain unchanged. The differences between these structures reduce to the absence of an oxygen atom with the coordinates $\left(0\ 0\ \frac{1}{2}\right)$ and different values of the coordinate *z* for oxygen atoms in the positions 6(*g*) in the U_3O_8 model in comparison with this coordinate in the UO_3 model. The model suggested in [6] has different motifs of oxygen and tantalum distribution because of the considerable displacements of oxygen atoms necessary for the attainment of the stoichiometry. Tantalum atoms are displaced with respect to one another only insignificantly.

Thus, there is no unique opinion on the distribution of atoms in the lattice of the low-temperature β-Ta_2O_5 oxide. It should be indicated that models [3–5] were suggested based on the similarity of the corresponding X-ray diffraction patterns, whereas the atomic coordinates were determined only in [6]. However, the interatomic distances calculated from the coordinates determined in [6] show that the distances between the tantalum atoms in the position (α, β, γ) and the oxygen atoms in the position $\left(\frac{1}{4}\ 0\ 0\right)$ are as short as 1.31 Å, i.e., are considerably less than the sum of the atomic radii of tantalum and oxygen. Thus, data [6] cannot be recognized as reliable either.

Below, we refine the atomic coordinates in the β-Ta_2O_5 oxide by the method of Rietveld full-profile analysis (the Rietveld method) of powder diffraction patterns.

We studied the crystalline β-Ta_2O_5 powder. The X-ray diffraction patterns were obtained on an automated DRON-3.0 diffractometer (MoK_α radiation). The crystals–monochromators prepared from pyrolytic graphite were placed in both incident and reflected beams. The diffraction patterns were recorded in the automatic mode in the reflection geometry as a computer file. The X-ray diffraction pattern was scanned within the angular range 5°–70° at a step of 0.025° in the vicinity of the maxima, and at a step of 0.1° in the background region.

Table 1. Reliability factors obtained upon the refinement of four structure models

Reliability factor	Model			
	1	2	3	4
R_p^*, %	15.21	14.78	20.95	13.23
R_{pw}^{**}, %	20.10	19.50	27.18	16.47
R_f^{***}, %	6.29	10.93	8.66	7.75
R_{f2}^{****}, %	13.54	19.31	16.72	13.88

* The simple profile reliability factor.
** The weighted profile reliability factor.
***The Bragg reliability factor calculated by the moduli of structure factors.
**** The Bragg reliability factor calculated from the values of structure factors.

Table 2. Refined atomic coordinates and thermal parameters for model 4

Atom	Atomic coordinates	Thermal parameter (*B*)
2(*a*) Ta1	(0 0 0)	0.36(1)
2(*b*) Ta2	(0.5, 0.5, 0)	0.33(2)
2(*c*) O1	(0, 0.5, 0)	0.43(7)
4(*q*) O2	(0.319(5)*, –0.002(5), 0)	0.39(8)
2(*e*) O3	(0, 0, 0.25)	0.48(6)
2(*h*) O4	(0.5, 0.5, 0.25)	0.49(3)

* The figure in parentheses is within the experimental error.

The structure of the oxide was analyzed by the Rietveld method; the structure parameters were refined using the program suggested elsewhere [7].

The refinement of the profile parameters of the diffraction patterns showed that the background is best approximated by a sixth-order polynomial, whereas the profile of the X-ray diffraction pattern is best described by the Pearson function [7]. The refined data were evaluated from the values of the Bragg, simple, and weighted profile reliability factors.

In model 1 based on the hexagonal UO_3-type unit cell with the occupancy *q* of the oxygen positions, the initial *q* value for oxygen atoms in the 2(*d*) position was assumed to be 0.75; for oxygen atoms in the positions 1(*b*), it was assumed to be 1.0. Within this model, we refined the unit-cell parameters, the occupancies of the oxygen positions, and the coordinates *z* of oxygen atoms in the 2(*d*) positions. As a result, the occupancy for oxygen atoms in the 2(*d*) positions reduced to $q = 0.69$. The refinement of the coordinate $z = 0.17$ of oxygen atoms in the positions 2(*d*) yielded $z = 0.12$. The refined values of the unit-cell parameters are $a = 3.594$ Å and $c = 3.887$ Å.

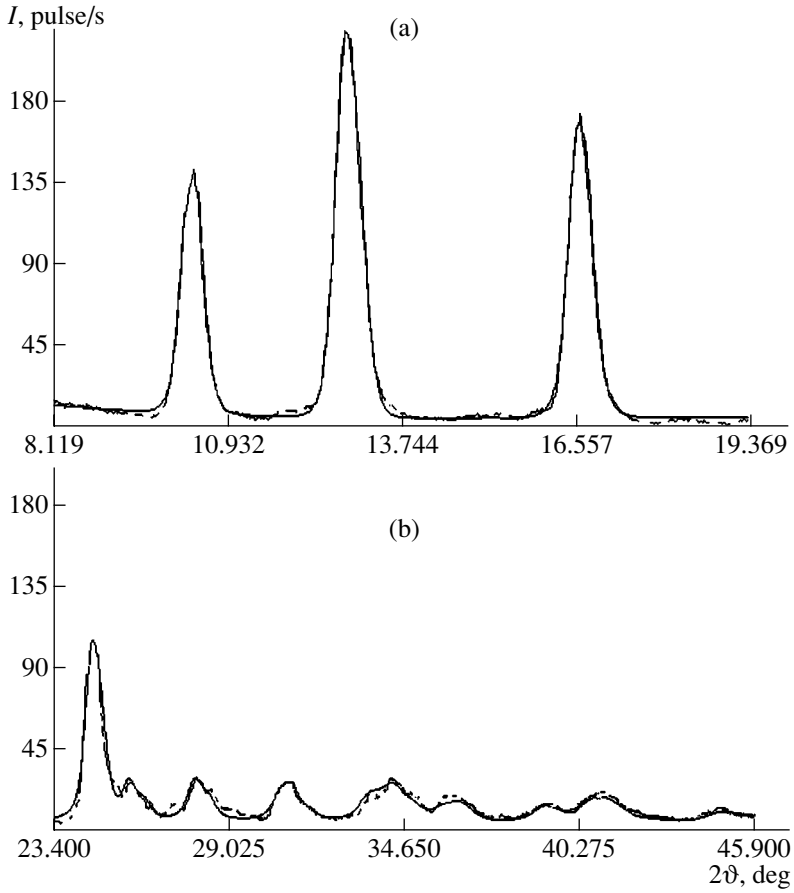

Fig. 2. Comparison of the experimental and theoretically calculated diffraction patterns in the angular ranges (a) 8°–20° and (b) 23°–46°.

The temperature factor B for tantalum atoms equals 0.156. For oxygen atoms in the positions 2(d) and 1(b), we obtained B = 0.472 and 0.466, respectively. The comparison of the experimental diffraction pattern with the diffraction pattern calculated by the refined structure parameters showed quite good agreement in the range of the main reflections. However, some weak reflections recorded on the experimental pattern were absent on the calculated one.

Model 2 suggested in [4] takes into account the additional weak reflections of the experimental diffraction pattern and is a vacancy-type model. The initial occupancies of the positions of oxygen atoms with the coordinates 2(n) $\left(\frac{1}{6}\ \frac{1}{2}\ 0.17\right)$ are q = 0.5. The refined unit-cell parameters are a = 6.225 Å, b = 3.678 Å, and c = 3.896 Å. The occupancies of the oxygen positions 2(n) upon the refinement are q = 0.231. The refined value of the z coordinate for oxygen atoms with the coordinates $\left(\frac{1}{6}\ \frac{1}{2}\ z\right)$ is z = 0.12. Such a dramatic decrease in the occupancy of oxygen positions results in nonstoichiometry, so that the composition cannot be described as $TaO_{2.5}$ any more.

When considering model 3 based on the U_3O_8-type trigonal unit cell for oxygen atoms in the positions 2(d), the initial occupancy was assumed to be equal to unity, while the occupancy of the positions 6(g) was assumed to be q = 0.92. The refinement of the unit-cell parameters yielded $a = b$ = 6.210 Å and c = 3.892 Å. The refined occupancy of oxygen positions 6(g) is q = 0.915. Thus, this model corresponds to the stoichiometry, $TaO_{2.5}$.

Using the coordinates of tantalum and oxygen atoms given in [6], we failed to determine the space group uniquely, although the oxygen subsystem was well described by the sp. gr. *Pccm*. The atomic displacements according to the law suggested in [6] did not allow us to describe the positions of Ta atoms within this space group. Assuming that the tantalum atoms have the coordinates (0 0 0), $\left(\frac{1}{2}\ \frac{1}{2}\ 0\right)$, $\left(0\ 0\ \frac{1}{2}\right)$, and $\left(\frac{1}{2}\ \frac{1}{2}\ \frac{1}{2}\right)$, we arrive at the sp. gr. *Pccm* for the β-Ta_2O_5 oxide, where oxygen atoms occupied the positions 2(c) $\left(0\ \frac{1}{2}\ 0\right)$, 4($q$) ($x\ y$ 0), 2(e) $\left(0\ 0\ \frac{1}{4}\right)$, and

2(*h*) $\left(\frac{1}{2}\ \frac{1}{2}\ \frac{1}{4}\right)$ (Fig. 1e). Thus, instead of the Ta coordinates suggested in model 4, we parametrically set the coordinates of the oxygen atoms in the positions 4(*q*). The initial values of these coordinates were taken to be the coordinates given in [6], namely, $x = \frac{1}{4} - \alpha$ and $y = -\beta$. The refined coordinates are $x = 0.319$ and $y = -0.002$. In this case, the distance between the tantalum atom with the coordinate (0 0 0) (instead of (α, β, γ)) and the oxygen atom with the coordinates (0.319, –0.002, 0) becomes equal to 1.98 Å.

The values of the profile and structural reliability factors obtained upon the refinement of all the four structure models are listed in Table 1. Their analysis shows that models 1 and 4 adequately describe the structure of the low-temperature β-Ta_2O_5 oxide. However, model 4 is somewhat more advantageous, because the lower value of the Bragg reliability factor (6.29%) for model 1 was obtained because the refinement was performed only by intense diffraction lines.

The reliability and the quality of indexing of X-ray diffraction patterns was estimated by the criterion suggested elsewhere [8],

$$M = \frac{\sin^2\vartheta_{20}}{\bar{\varepsilon}N_{20}},$$

where $\sin^2\vartheta_{20}$ is the value for the 20th line on the diffraction pattern, $\bar{\varepsilon}$ is the average error in $\sin^2\theta$, and N_{20} is the number of theoretically possible diffraction lines including the twentieth one. According to data [8], the interpretation of the results is recognized to be satisfactory only if the values of the reliability criterion *M* exceed 10. In our study, the value of *M* for model 4 was equal to 23.

Figure 2 illustrates the rather good fit of the experimental and theoretically calculated curves for model 4 (with respect to the intensities and positions of the reflections in the ranges of the intense and the weak reflections). The refined atomic coordinates and thermal parameters are listed in Table 2.

Thus, the results obtained show that the low-temperature β-Ta_2O_5 oxide is uniquely described by the sp. gr. *Pccm* and has the unit-cell parameters $a = 6.217$ Å, $b = 3.677$ Å, and $c = 7.794$ Å.

REFERENCES

1. *Optical Communication*, Ed. by I. I. Teumin (Radio i Svyaz', Moscow, 1984).
2. V. V. Bryksin and S. D. Khanin, Fiz. Tverd. Tela (St. Petersburg) **35** (8), 2266 (1993) [Phys. Solid State **35**, 1126 (1993)].
3. J. Spyridelis, P. Delavignette, and S. Amelinckx, Phys. Status Solidi **19**, 683 (1967).
4. L. D. Calvert and P. H. J. Draper, Can. J. Chem. **40**, 1943 (1962).
5. W. T. Holster, Acta Crystallogr. **19**, 196 (1956).
6. K. Lehovec, J. Less-Common Met. **7**, 397 (1964).
7. A. B. Tovbis, *Program for the Refinement of Structure Parameters by Experimental Powder Diffraction Data (the Rietveld Method), Instructions for Work with the Program* (Inst. Kristallografii Ross. Akad. Nauk, Moscow, 1994).
8. H. Lipson and H. Steeple, *Interpretation of X-ray Powder Diffraction Patterns* (MacMillan, London, 1970; Mir, Moscow, 1972).

Translated by L. Man

Crystallography Reports, Vol. 47, No. 3, 2002, pp. 420–424. Translated from Kristallografiya, Vol. 47, No. 3, 2002, pp. 465–469.

STRUCTURES OF COORDINATION COMPOUNDS

Crystal Structures of Mixed Compounds Cu(2)*Gly*(*D-Ser*)(*L-Ser*)$_2$ and Cu(2)*Gly*$_3$(*L-Ser*)

I. A. Diacon* and L. F. Chapurina**

** Institute of Applied Physics, Academy of Sciences of Moldova, Academiei 5, Chisinau, 20-28 Moldova*

*** Institute of Chemistry, Academy of Sciences of Moldova, Academiei 3, Chisinau, 20-28 Moldova*

Received December 5, 2000

Abstract—The crystal structures of mixed coordination compounds, Cu(2)*Gly*(*D-Ser*)(*L-Ser*)$_2$ (**I**) and Cu(2)*Gly*$_3$(*L-Ser*) (**II**), which contain the amino acid residues of glycine (*Gly*) and serine (*Ser*) in the 1 : 3 and 3 : 1 ratio, respectively, are studied by electron diffraction. Crystals **I** and **II** are triclinic, $Z = 1$, and space group $P1$. For **I**, $a = 8.96(2)$ Å, $b = 9.66(2)$ Å, $c = 5.07(2)$ Å, $\alpha = \beta = 90°$, and $\gamma = 92.8(3)°$. For **II**, $a = 8.37(2)$ Å, $b = 9.65(2)$ Å, $c = 5.06(2)$ Å, $\alpha = \beta = 90°$, and $\gamma = 92.8(3)°$. Compounds **I** and **II** have layered structures that are based on the Cu*Gly*(*L-Ser*) fragment. Structures **I** and **II** differ mainly in their interlayer spacing and configuration of the interlayer space. © *2002 MAIK "Nauka/Interperiodica".*

INTRODUCTION

In the crystal structures of mixed copper(II) compounds with glycine and serine, which we studied earlier in [1, 2], the *Gly* : *Ser* ratio was 1 : 1. The mixed compounds Cu(2)*Gly*(*D-Ser*)(*L-Ser*)$_2$ and Cu(2)*Gly*$_3$(*L-Ser*) differ from the above compounds in composition: the *Gly* : *Ser* ratios are 1 : 3 and 3 : 1, respectively. The structures of mixed-ligand metal complexes with different α-amino acids involved in the 1 : 1 ratio have been reported in the literature, whereas structural data on mixed compounds containing two different α-amino acids in the 1 : 3 ratio are unavailable. In this respect, our interest in the synthesis, crystal chemistry, and biological activity of these compounds is quite understandable.

The crystal structures of both compounds were determined by the electron diffraction technique using sets of reflections revealed in the electron diffraction patterns of the slanting textures. The local intensities of reflections [the 311 and 317 reflections for Cu(2)*Gly*(*D-Ser*)(*L-Ser*)$_2$ and Cu(2)*Gly*$_3$(*L-Ser*), respectively] were measured electrometrically and with a microphotometer using the method of multiple exposures [3–7].

CRYSTAL STRUCTURE OF Cu(2)*Gly*(*D-Ser*)(*L-Ser*)$_2$

The unit cell of the crystals was determined from the geometry of the reflections revealed in the electron diffraction patterns. The unit cell parameters are $a = 8.96(2)$ Å, $b = 9.66(2)$ Å, $c = 5.07(2)$ Å, $\alpha = \beta = 90°$, $\gamma = 92.8(3)°$, space group $P1$, and the number of formula units per unit cell $Z = 1$. The discrepancy factor R is equal to 14.6%. A fragment of the Cu(2)*Gly*(*D-Ser*)(*L-Ser*)$_2$ structure is shown in Fig. 1.

It is found that crystals of Cu(2)*Gly*(*D-Ser*)(*L-Ser*)$_2$ have an unusual structure. This structure is characterized by two types of complexes, namely, the mixed-ligand Cu(1)*Gly*(*L-Ser*) complexes and the binary Cu(2)(*D-Ser*)(*L-Ser*) complexes. In the Cu(1)*Gly*(*L-Ser*) complex, the amino acid residues of glycine and *L*-serine act as bidentate ligands, whereas the Cu(2)(*D-Ser*)(*L-Ser*) complex contains residues of only the serine amino acid. In both complexes, the nitrogen atoms of the amino groups are located in the *trans* positions. The coordination of copper ions in both com-

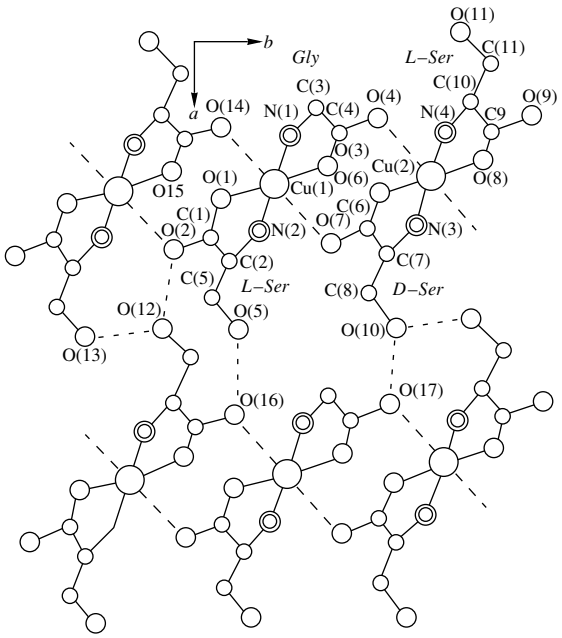

Fig. 1. A fragment of the Cu(2)*Gly*(*D-Ser*)(*L-Ser*)$_2$ crystal structure.

1063-7745/02/4703-0420$22.00 © 2002 MAIK "Nauka/Interperiodica"

plexes has the shape of an elongated octahedron. The copper ions and the amino acid residues (of glycine and serine in the former complex and serine in the latter complex) form five-membered chelate rings. The mean planes of these rings are coplanar with the carboxyl groups of the amino acid residues. The structural data obtained by the electron diffraction technique show that the serine residues in the Cu(2)(*D-Ser*)(*L-Ser*) complexes are related by the noncrystallographic center of symmetry, which coincides with the position of the Cu(2) ion. Moreover, the serine residue of the Cu(1)*Gly*(*L-Ser*) complex is related to the *D*-serine residue of the Cu(2)(*D-Ser*)(*L-Ser*) complex by the local glide-reflection plane (*b*). The Cu(1) and Cu(2) ions are also related by this plane, and their arrangement follows a rectangular centered pattern. The local symmetry is reflected in the electron diffraction patterns of the textures of Cu(2)*Gly*(*D-Ser*)(*L-Ser*)$_2$ crystals: the *hk*0 reflections with $k = 2n + 1$ have very weak intensities. At the same time, the 00*l* reflections with $l = 2n + 1$ are virtually absent in the diffraction patterns. These diffraction features indicate that the symmetry of the mutual arrangement of structural units in the Cu(2)*Gly*(*D-Ser*)(*L-Ser*)$_2$ crystals is similar to the symmetry of the space group $P2_1/b$, in which the copper ions occupy the centers of symmetry. Thus, although the crystal structure of Cu(2)*Gly*(*D-Ser*)(*L-Ser*)$_2$ consists of crystallographically independent structural units of two types, namely, Cu(1)*Gly*(*L-Ser*) and Cu(2)(*D-Ser*)(*L-Ser*), the Cu(1)*Gly*(*L-Ser*) structural unit can be considered, to a first approximation, as its independent part. For this structural unit, the coordinates of the non-hydrogen atoms are listed in Table 1 and the interatomic distances and bond angles are given in Table 2.

The packing of the complexes in the crystal is characterized by the formation of layers aligned parallel to the *bc* coordinate plane. In the layer, the shortest N⋯O contacts between the amino groups and the carboxyl oxygen atoms, which are involved in the copper coordination and belong to the neighboring complexes, lie in the range 3.19–3.25 Å. This suggests that different complexes in the layer are linked through hydrogen bonds. The Cu(1)⋯O(7) and Cu(1)⋯O(14) distances are equal to each other (2.75 Å). Short contacts between the oxygen atoms of the hydroxyl and carboxyl groups, on the one hand, and between the hydroxyl oxygens, on the other, indicate that the serine and glycine residues of the complexes of the adjacent layers are linked through hydrogen bonds: O(12)–H⋯O(2), 2.93 Å; O(5)–H⋯O(16), 2.94 Å; and O(13)–H⋯O(12)–H, 3.14 Å.

We should note one more remarkable feature of the Cu(2)*Gly*(*D-Ser*)(*L-Ser*)$_2$ structure. According to the structural data, the conformations of the glycine and serine residues differ from those in free glycine and serine. In the structure studied, the conformation of the glycine residue is virtually planar, whereas the conformation of the side radical of the serine residue is characterized by the C(1)C(2)C(5)O(5) torsion angle of –144°, which differs essentially from the corresponding torsion angle in free serine (–53°). Apparently, the torsion angle in the radical of the serine residue depends on the interactions involving the hydroxyl groups of the serine residues.

Table 1. Coordinates ($\times 10^3$) of the non-hydrogen atoms of the Cu(1)*Gly*(*L-Ser*) fragment in the Cu(2)*Gly*(*D-Ser*)(*L-Ser*)$_2$ coordination compound

Atoms	*x/a*	*y/b*	*z/c*
Cu(1)	501(3)	251(2)	249(2)
O(1)	551(7)	85(6)	442(7)
O(2)	705(7)	–85(6)	472(7)
O(3)	452(7)	416(6)	54(7)
O(4)	297(7)	586(6)	35(7)
O(5)	973(7)	116(6)	–78(7)
N(1)	345(8)	309(7)	494(8)
N(2)	656(8)	191(7)	6(8)
C(1)	659(8)	20(7)	363(8)
C(2)	745(8)	91(7)	132(8)
C(3)	255(8)	408(7)	369(8)
C(4)	343(8)	481(7)	130(8)
C(5)	863(8)	19(7)	–14(8)

Table 2. Interatomic distances (Å) and bond angles (deg) in the Cu(1)*Gly*(*L-Ser*) fragment of coordination compound **I**

Atoms	Distance	Atoms	Angle
Cu(1)–O(1)	1.95(1)	N(1)–Cu(1)–O(1)	96.4
Cu(1)–O(3)	1.95(1)	N(1)–Cu(1)–O(3)	83.8
Cu(1)–N(1)	1.97(1)	N(2)–Cu(1)–O(1)	83
Cu(1)–N(2)	1.97(1)	N(2)–Cu(1)–O(3)	96.7
N(1)–C(3)	1.44(1)	N(1)–C(3)–C(4)	110.2
C(3)–C(4)	1.59(1)	C(3)–C(4)–O(4)	119.4
C(4)–O(4)	1.22(1)	O(4)–C(4)–O(3)	127.8
C(4)–O(3)	1.26(1)	C(3)–C(4)–O(3)	112.7
C(1)–O(2)	1.24(1)	N(2)–C(2)–C(1)	110.8
C(1)–O(1)	1.25(1)	C(5)–C(2)–N(2)	121.6
C(1)–C(2)	1.54(1)	C(5)–C(2)–O(1)	121.3
C(2)–N(2)	1.43(1)	C(2)–C(5)–O(5)	107.6
C(2)–C(5)	1.49(1)	C(2)–C(1)–O(1)	113.8
C(5)–O(5)	1.37(1)	C(2)–C(1)–O(2)	121.4
		O(2)–C(1)–O(1)	124.4

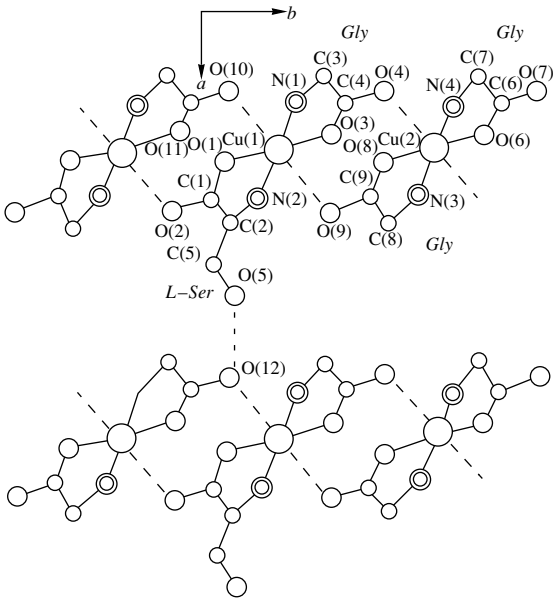

Fig. 2. A fragment of the Cu(2)*Gly*$_3$(*L-Ser*) crystal structure.

CRYSTAL STRUCTURE OF Cu(2)*Gly*$_3$(*L-Ser*)

Crystals of Cu(2)*Gly*$_3$(*L-Ser*) have the space group $P1$ and the following unit cell parameters: $a = 8.37(2)$ Å, $b = 9.65(2)$ Å, $c = 5.06(2)$ Å, $\alpha = \beta = 90°$, $\gamma = 92.8(3)°$, and the number of formula units per unit cell $Z = 1$. The discrepancy factor R is 16.7%. A fragment of the Cu(2)*Gly*$_3$(*L-Ser*) structure is shown in Fig. 2.

Similar to the structure described above, the crystal structure of Cu(2)*Gly*$_3$(*L-Ser*) is characterized by two types of complexes, namely, Cu(1)*Gly*(*L-Ser*) and Cu(2)*GlyGly*. In the former complex, the Cu(1) ion is bonded to the glycine and serine residues. In the latter complex, the Cu(2) ion is bonded to two glycine acid residues. In both complexes, the amino acid residues are situated *trans* relative to each other, as is the case in the above structure. According to the structural data, the Cu(2)*GlyGly* complex adopts a planar conformation and has a local center of symmetry that coincides with the position of the Cu(2) ion. In the structure, three glycine residues involved in the unit cell are related by the noncrystallographic glide-reflection plane (*b*) and the center of symmetry of the Cu(2)*GlyGly* complex. If the C(5)O(5) side radical of the serine residue is disregarded, complexes of two types are also related by the *b* plane. Moreover, the diffraction patterns indicate that the intensities of the *hk*0 reflections with $k = 2n + 1$ and the 00*l* reflections with $l = 2n + 1$ are negligible. Therefore, disregarding the C(5)O(5) residue of serine, we can describe the pseudosymmetry of structure **II**, like structure **I**, by the space group $P2_1/b$, in which the copper ions occupy special positions at the centers of symmetry. On this basis, the Cu(1)*Gly*(*L-Ser*) fragment can be considered, to a first approximation, as a basic structural unit that forms the Cu(2)*Gly*$_3$(*L-Ser*) structure, as is the case in the Cu(2)*Gly*(*D-Ser*)(*L-Ser*)$_2$ structure. For structure **II**, the coordinates of the non-hydrogen atoms of the Cu(1)*Gly*(*L-Ser*) fragment are listed in Table 3 and the interatomic distances and bond angles are given in Table 4.

Table 3. Coordinates ($\times 10^3$) of the non-hydrogen atoms of the Cu(1)*Gly*(*L-Ser*) fragment in the Cu(2)*Gly*$_3$(*L-Ser*) coordination compound

Atoms	*x/a*	*y/b*	*z/c*
Cu(1)	500(3)	250(2)	249(3)
O(1)	554(7)	86(6)	442(7)
O(2)	718(7)	–86(6)	469(7)
O(3)	448(7)	415(6)	55(7)
O(4)	282(7)	586(6)	34(7)
O(5)	1006(7)	116(6)	–77(7)
N(1)	332(8)	308(7)	492(8)
N(2)	664(8)	192(7)	5(8)
C(1)	669(8)	21(7)	363(8)
C(2)	761(8)	92(7)	134(8)
C(3)	238(8)	408(7)	369(8)
C(4)	332(8)	481(7)	130(8)
C(5)	887(8)	19(7)	–16(8)

Table 4. Interatomic distances (Å) and bond angles (deg) in the Cu(1)*Gly*(*L-Ser*) fragment of coordination compound II

Atoms	Distance	Atoms	Angle
Cu(1)–O(1)	1.93(1)	N(1)–Cu(1)–O(1)	96.9
Cu(1)–O(3)	1.94(1)	N(1)–Cu(1)–O(3)	83.7
Cu(1)–N(1)	1.97(1)	N(2)–Cu(1)–O(1)	83.6
Cu(1)–N(2)	1.95(1)	N(2)–Cu(1)–O(3)	95.6
N(1)–C(3)	1.42(1)	N(1)–C(3)–C(4)	110.9
C(3)–C(4)	1.59(1)	C(3)–C(4)–O(4)	119.4
C(4)–O(4)	1.22(1)	O(4)–C(4)–O(3)	127.8
C(4)–O(3)	1.26(1)	C(3)–C(4)–O(3)	112.7
C(1)–O(2)	1.25(1)	N(2)–C(2)–C(1)	110.7
C(1)–O(1)	1.24(1)	C(5)–C(2)–N(2)	121
C(1)–C(2)	1.55(1)	C(5)–C(2)–O(1)	121.4
C(2)–N(2)	1.45(1)	C(2)–C(5)–O(5)	107.3
C(2)–C(5)	1.50(1)	C(2)–C(1)–O(1)	113.7
C(5)–O(5)	1.37(1)	C(2)–C(1)–O(2)	121
		O(2)–C(1)–O(1)	125

Table 5. Crystallographic characteristics of mixed copper(II) coordination compounds containing glycine and serine in the ratios 1 : 1, 1 : 3, and 3 : 1

Compound	*a*, Å	*b*, Å	*c*, Å	α, deg	β, deg	γ, deg	Space group
I. Cu(2)*Gly*(*D-Ser*)(*L-Ser*)	8.96	9.66	5.07	90	90	92.8	*P*1
II. Cu(2)Gly_3(*L-Ser*)	8.37	9.65	5.06	90	90	92.8	*P*1
III. Cu(2)Gly_2(*D-Ser*)(*L-Ser*)	8.71	9.64	5.08	90	90	92.1	*Pb*
IV. Cu*Gly*(*L-Ser*)	8.65	9.68	5.08	90	90	92.6	$P2_1$

In crystal structure **II**, the complexes are linked into layers aligned parallel to the *bc* coordinate plane. As in structure **I**, the layers repeat with the *a* period (one layer). In the layer, the complexes are interlinked through the Cu(1)···O(9) and Cu(1)···O(10) contacts (2.74 and 2.75 Å, respectively) and the N···O distances fall in the range 3.17–3.25 Å. The O(5)–H···O(12) contacts between the oxygen atoms of the serine hydroxyl groups and the oxygen atoms of the glycine carboxyl groups of the adjacent layers are 2.37 Å. These contacts are shorter than the normal hydrogen bonds (~2.60 Å) between the hydroxyl groups and the carboxyl oxygens observed in the structures of free amino acids. This difference can stem from the inaccuracy in determining the positions of the peripheral atoms in the complexes because of the small number of structure amplitudes (317) used in the structure determination.

It was noted above that, in structure **I**, the glycinate ions adopt a planar conformation. In the serine residues, the C(1)C(2)C(5)O(5) torsion angle is identical to the corresponding angle in the serine residues in the structure of Cu(2)*Gly*(*D-Ser*)$(L\text{-}Ser)_2$.

SPECIFIC FEATURES OF THE CRYSTAL STRUCTURES Cu(2)(*D-Ser*)$(L\text{-}Ser)_2$ AND Cu(2)Gly_3(*L-Ser*)

The data obtained demonstrate that the change in the glycine : serine ratio in the compositions of the compounds described virtually does not affect the spacings *b* and *c* and the angular parameters of the unit cells. The change is observed only in the third spacing, *a*, along which the layers alternate in the structures. Thus, the change in the ratio of the amino acids results in the change of the width of layers that form the structures. In structures **I** and **II**, the layers consist both of the same fragments Cu(1)*Gly*(*L-Ser*) with close geometric and conformational characteristics and of fragments that differ in composition, namely, Cu(2)(*D-Ser*)(*L-Ser*) in structure **I** and Cu(2)*GlyGly* in structure **II**. In the layers, the copper ions are located at the sites of a rectangular centered network. The dimensions of the rectangular motifs of the networks in the *bc* layers are identical in the Cu(2)*Gly*(*D-Ser*)$(L\text{-}Ser)_2$ and Cu(2)Gly_3(*L-Ser*) compounds. These layers can be formed by the same structural fragment, Cu(1)*Gly*(*L-Ser*), through repetition of the Cu(1)(*L-Ser*) and Cu(1)*Gly* blocks of this fragment, respectively, with local symmetry operations. Thus, the crystals of Cu(2)*Gly*(*D-Ser*)$(L\text{-}Ser)_2$ and Cu(2)Gly_3(*L-Ser*) have similar structures but significantly differ in their interlayer spacing and the configuration of the interlayer space.

COMPARISON OF THE STRUCTURAL FEATURES OF MIXED COPPER(II) COMPOUNDS CONTAINING GLYCINE AND SERINE IN THE RATIOS 1 : 1, 1 : 3, AND 3 : 1

It is interesting to compare the crystal structures of the Cu*Gly*(*L-Ser*) (**IV**) and Cu(2)Gly_2(*D-Ser*)(*L-Ser*) (**III**) compounds, which have been studied and reported in [1, 2] and contain glycine and serine in the ratio 1 : 1, with the above structures of Cu(2)*Gly*(*D-Ser*)$(L\text{-}Ser)_2$ and Cu(2)Gly_3(*L-Ser*), which contain glycine and serine in the ratios 1 : 3 and 3 : 1. For convenient comparison, the crystallographic characteristics of these compounds are summarized in Table 5. We can see from this table that the parameters *b* and *c* and the angular parameters are almost identical, whereas the parameters *a*, which characterize the interlayer spacings in the structures, and the space groups of symmetry are different. Compounds **III** and **IV** crystallize in a monoclinic system, whereas compounds **I** and **II** crystallize in a triclinic system. The pseudomonoclinicity of the triclinic lattices in crystal structures **I** and **II** suggests that the symmetry of the mutual arrangement of structural units in these crystals is, on average, higher than the symmetry of the triclinic system. The Cu(2)Gly_2(*D-Ser*)(*L-Ser*) and Cu*Gly*(*L-Ser*) compounds are polytypic modifications. Like compounds **I** and **II**, they have layered structures. The main structural unit involved in the formation of the layers in all four compounds is the Cu*Gly*(*L-Ser*) fragment. In these structures, the repetition patterns of this fragment within the layer are different.

Thus, the main structural unit of all the compounds listed in Table 5 is the Cu*Gly*(*L-Ser*) fragment. However, the Cu*Gly*(*L-Ser*) fragments in compounds **I** and **II** differ structurally from similar fragments in **III** and **IV**. These compounds are similar in the main geometric characteristics but differ in the conformations of the side radicals of the serine residues.

REFERENCES

1. I. A. D'yakon, S. V. Donu, L. F. Chapurina, and A. S. Avilov, Kristallografiya **29** (2), 384 (1984) [Sov. Phys. Crystallogr. **29**, 230 (1984)].
2. I. A. D'yakon, S. V. Donu, L. F. Chapurina, and A. S. Avilov, Kristallografiya **36** (1), 219 (1991) [Sov. Phys. Crystallogr. **36**, 126 (1991)].
3. B. K. Vainshtein, *Structure Analysis by Electron Diffraction* (Akad. Nauk SSSR, Moscow, 1956; Pergamon, Oxford, 1964).
4. B. B. Zvyagin, *Electron Diffraction Analysis of Clay Minerals* (Nauka, Moscow, 1964; Plenum, New York, 1967).
5. B. B. Zvyagin, Z. V. Vrublevskaya, A. P. Zhukhlistov, *et al.*, *High-Voltage Electron Diffraction in Research of Layered Materials* (Nauka, Moscow, 1979).
6. A. S. Avilov, R. M. Imamov, and S. A. Semiletov, Prib. Tekh. Éksp., No. 3, 214 (1976).
7. A. S. Avilov, Kristallografiya **21** (6), 1117 (1976) [Sov. Phys. Crystallogr. **21**, 646 (1976)].

Translated by I. Polyakova

Crystallography Reports, Vol. 47, No. 3, 2002, pp. 425–427. From Kristallografiya, Vol. 47, No. 3, 2002, pp. 470–472.

STRUCTURES OF COORDINATION COMPOUNDS

Crystal Structure of Tris(methylcyclopentadienyl) Tetrahydrofuranatosamarium*

Taiqi Liu**

Changchun Institute of Applied Chemistry, Chinese Academy of Sciences, Changchun, 130022 China

e-mail: liut@mailer.uni-marburg.de; FAX: 49-(0)6421-2828916

Received September 10, 2001

Abstract—The first crystal structure of tris(methylcyclopentadienyl) tetrahydrofuranato (*THF*) lanthanide complexes, $(CH_3Cp)_3Sm \cdot THF$, is determined. The complex crystallizes from mixed solvents of tetrahydrofuran and hexane as a monomer in the orthorhombic space group $Pc2_1n$ with the unit cell parameters a = 9.135(2) Å, b = 13.263(2) Å, c = 16.176(3) Å, and Z = 4. © *2002 MAIK "Nauka/Interperiodica".*

INTRODUCTION

Up to now, a series of molecular structures of tris(cyclopentadienyl) lanthanide and tris(methylcyclopentadienyl) lanthanide complexes have been reported. From these results, we can see that the molecular structure of these compounds substantially depends on both the substituent in the cyclopentadienyl ring and the coordinated solvent and that the tris(cyclopentadienyl) lanthanide complexes are polymeric compounds [1–4]. However, the tris(methylcyclopentadienyl) lanthanide complexes are tetrameric complexes [5–8], and the structure of solvent coordinated complexes $Cp_3Ln \cdot THF$ (*Ln* is a lanthanide element) is a monomer [9–13]. An interesting question is how does the molecular structure of $(CH_3Cp)_3Ln \cdot THF$ compare with its non-solvent coordinated compound. Here, we report the molecular structure of $(CH_3Cp)_3Sm \cdot THF$.

EXPERIMENTAL

Since the complexes described below are extremely air- and moisture-sensitive, all the experiments were conducted under pure argon by Schlenk techniques. Tetrahydrofuran and hexane were distilled from sodium benzophenone ketyl before use. The $(CH_3Cp)_3Sm$ complex was prepared by the same method as was used to synthesize $(CH_3Cp)_3Nd$ [5]. Analysis for metals was carried out by direct complexometric titration. Mass spectrometric measurements were performed on a VG-Quattro mass spectrometer at T = 200°C and EV = 70 eV. Isotopes refer to ^{12}C, ^{1}H, ^{16}O, and ^{152}Sm.

Preparation of $(CH_3Cp)_3Sm \cdot THF$. $(CH_3Cp)_3Sm$ (2 g, 5 mmol) and *THF* (20 mmol) were added to a 100-ml flask. The reaction mixture was allowed to stir for 48 h at a temperature of 60°C. The solvent was removed and an ether–hexane (10 : 1) mixture was added to the solution to form a saturation solution. The solution was cooled to –15°C, and a yellow crystal was produced. The yield was 78%.

Anal. calcd. (%): Sm, 32.7. Found (%): Sm, 32.5. MS (m/z): 389 $[(CH_3Cp)_3Sm]^+$, 310 $[(CH_3Cp)_2Sm]^+$, 231 $[(CH_3Cp)Sm]^+$, 79 $[CH_3Cp]^+$.

X-ray structure analysis of $(CH_3Cp)_3Sm \cdot THF$. A single crystal ($0.29 \times 0.60 \times 0.52$ in size) was sealed in a glass capillary with nitrogen as an inner gas. The structure was solved by the heavy atom method, and the

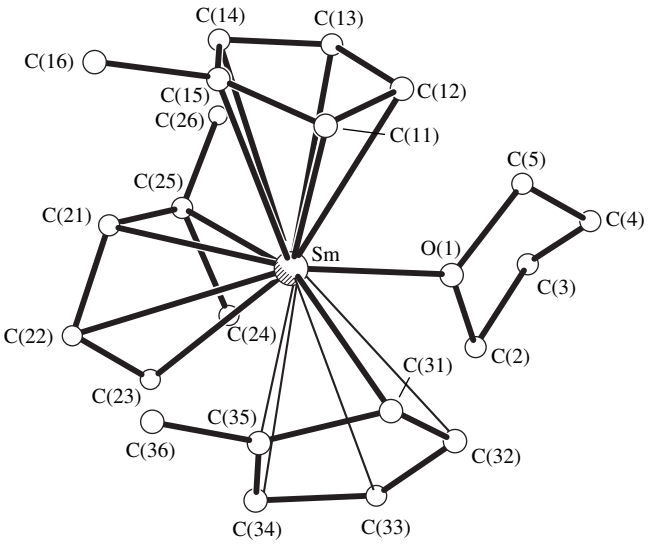

A perspective view of the molecular structure of $(CH_3Cp)_3Sm \cdot THF$.

* This article was submitted by the author in English.

** Corresponding address: Department of Chemistry and Materials Science Center, Institute of Physical Chemistry, Nuclear Chemistry, and Macromolecular Chemistry, Philipps University Marburg, Hans-Meerwein-Strasse, D-35032 Marburg, Germany.

Table 1. Atomic coordinates ($\times 10^4$) and equivalent isotropic thermal parameters ($Å^2 \times 10^3$)

Atom	*x*	*y*	*z*	*U**
Sm	1321(1)	1881(5)	6680(1)	92(1)
O(1)	−295(13)	1906(21)	7892(8)	131(2)
C(2)	−1455(27)	2698(22)	8112(22)	339(2)
C(3)	−2542(23)	2176(19)	8627(16)	219(2)
C(4)	−1730(22)	1345(16)	9005(13)	135(2)
C(5)	−703(23)	1059(16)	8391(13)	131(2)
C(11)	3795(21)	622(16)	6892(11)	99(2)
C(12)	2738(19)	345(14)	7449(13)	93(2)
C(13)	1580(19)	−102(15)	6975(11)	94(2)
C(14)	1807(25)	−123(22)	6213(15)	181(2)
C(15)	3204(21)	271(17)	6185(12)	116(2)
C(16)	3654(25)	242(22)	5404(13)	198(2)
C(21)	43(21)	1502(15)	5272(11)	123(2)
C(22)	539(26)	2460(18)	4973(18)	212(2)
C(23)	−482(23)	2933(19)	5558(14)	143(2)
C(24)	−1475(22)	2304(18)	6119(16)	155(2)
C(25)	−1030(22)	1301(16)	5768(15)	130(2)
C(26)	−1554(26)	380(20)	5993(21)	259(2)
C(31)	3722(21)	2973(16)	7316(12)	116(2)
C(32)	2556(25)	3275(19)	7790(17)	167(2)
C(33)	1625(19)	3867(15)	7349(12)	99(2)
C(34)	2176(20)	3866(15)	6526(12)	96(2)
C(35)	3407(20)	3235(18)	6484(12)	114(2)
C(36)	4578(26)	3091(23)	5928(16)	248(2)

* Equivalent isotropic *U* defined as one-third of the trace of the orthogonalized U_{ij} tensor.

coordinates of the hydrogen atoms were added according to the theoretical model. The atomic coordinates and isotropic thermal parameters are listed in Table 1. The data collection, crystal data, and refinement parameters for the $(CH_3Cp)_3Sm \cdot THF$ compound are presented in Table 2. Selected bond lengths and angles are given in Table 3. A perspective view of the molecular structure of $(CH_3Cp)_3Sm \cdot THF$ is shown in the figure. Crystallographic data are deposited in the Cambridge Crystallographic Database Center (deposition number CCDC168188).

RESULTS AND DISCUSSION

The X-ray structure analysis shows that the $(CH_3Cp)_3Sm \cdot THF$ crystals has a monomeric structure,

Table 2. Crystal data of the $(CH_3Cp)_3Sm \cdot THF$ compound

Formula	$(CH_3Cp)_3Sm \cdot THF$
Molecular weight	459.8
Space group	$Pc_{21}n$
Unit cell parameters:	
a, Å	9.135(2)
b, Å	13.263(2)
c, Å	16.176(3)
V, $Å^3$	2025.36(6)
Z	4
D_{calcd}, g/cm^3	1.32
Radiation	MoK_α (0.71069 Å)
Reflections for lattice parameters, deg	25
θ range for lattice parameters, deg	5.31–9.65
F(000)	796
μ, cm^{-1}	29.4
Data collection	
Diffractometer	Nicolet R3 M/E
Scan mode	ω–2θ
Scan range 2θ, deg	2–50
h	0–16
k	0–16
l	0–20
R_{int}	0.034
No. of reflections measured	2198
No. of unique reflections	2025
Reflections for $I > 3\sigma(I)$	1130
Intensity decay	2.0%
Standard reflections	3/100
Refinement	
R	0.0469
R_w	0.0456
S	1.03097
No. of parameters refined	217
$\Delta\rho_{min}$, e $Å^{-3}$	−0.4908
$\Delta\rho_{max}$, e $Å^{-3}$	0.0443

which is similar to those of $Cp_3Ln \cdot THF$ [9–13]. The structure of $Cp_3Ln \cdot THF$ differs significantly from that of $[(CH_3Cp)_3Ln]_4$ (*Ln* = La, Yb, Nd, Ce). The coordination mode of penta rings of $[(CH_3Cp)_3Ln]_4$ with the central metals are $\eta^1 : \eta^5$. However, the coordination mode of penta rings of $(CH_3Cp)_3Sm \cdot THF$ is η^5. In $(CH_3Cp)_3Sm \cdot THF$, three penta rings and *THF* are

Table 3. Selected bond lengths (Å) and bond angles (deg)

Selected bond lengths			
Sm–O(1)	2.507(13)	Sm–C (ring *1*, av.)	2.785(22)
Sm–C (ring *1*, av.)	2.819(23)	Sm–C (ring *3*, av.)	2.792(22)
C–C (ring *2*, av.)	1.378(29)	C–C (ring *2*, av.)	1.460(32)
C–C (ring *3*, av.)	1.418(30)	Sm–*Cp*(1)	2.517(1)
Sm–*Cp*(2)	2.537(10)	Sm–*Cp*(3)	2.519(1)
Selected bond angles			
O(1)–Sm–*Cp*(1)	105.9(10)	O(1)–Sm–*Cp*(2)	102.9(4)
O(1)–Sm–*Cp*(3)	92.4(9)	*Cp*(1)–Sm–*Cp*(2)	116.0(1)
Cp(2)–Sm–*Cp*(3)	119.9(1)	*Cp*(1)–Sm–*Cp*(3)	118.5(1)

coordinated to the central metal to form a tetrahedral geometry. The angles *Cp*(1)–Sm–*Cp*(2) (*Cp* denotes the centrodes of the cyclopentadienyl rings), *Cp*(2)–Sm–*Cp*(3), *Cp*(1)–Sm–*Cp*(3), O(1)–Sm-*Cp*(1), O(1)–Sm–*Cp*(2), and O(1)–Sm–*Cp*(3) in $(CH_3Cp)_3Sm \cdot THF$ are equal to 116.0(1)°, 115.9(1)°, 118.5(1)°, 105.9(10)°, 102.9(4)°, and 92.4(9)°, respectively. The average η^5-C–Sm distance is 2.799(22) Å.

ACKNOWLEDGMENTS

This work was supported by the National Science Foundation of China.

REFERENCES

1. C. H. Wong, T. Lee, and Y. Lee, Acta Crystallogr., Sect. B: Struct. Crystallogr. Cryst. Chem. **25**, 2580 (1969).
2. J. L. Atwood and K. D. Smith, J. Am. Chem. Soc. **95**, 1488 (1973).
3. W. Hinrichs, D. Melzer, M. Rehwoldt, *et al.*, J. Organomet. Chem. **251**, 299 (1983).
4. S. H. Eggers, J. Kopf, and R. D. Fisher, Organometallics **5**, 383 (1986).
5. J. H. Burns, W. H. Baldwin, and F. H. Fink, Inorg. Chem. **13**, 1916 (1974).
6. A. Hammel, W. Schwarz, and J. Weidlein, J. Organomet. Chem. **363**, C29 (1989).
7. S. D. Stults, R. A. Andersen, and A. Zalkin, Organometallics **9**, 115 (1990).
8. Z. Xie, F. E. Nafa, and C. Qian, J. Organomet. Chem. **414**, C12 (1991).
9. Z. Wu, X. Yu, X. Zhou, and J. Chen, Polyhedron **13**, 379 (1994).
10. R. D. Rogers, J. L. Atwood, A. Emad, *et al.*, J. Organomet. Chem. **216**, 383 (1981).
11. Y. Fan, P. Lu, Z. Jin, *et al.*, Sci. Scin., Ser. B **27**, 993 (1984).
12. C. Z. Ni, D. L. Deng, and C. T. Qian, Inorg. Chim. Acta **110**, L7 (1985).
13. R. D. Rogers, R. V. Bynum, and J. L. Atwood, J. Organomet. Chem. **192**, 65 (1980).

Crystallography Reports, Vol. 47, No. 3, 2002, pp. 428–432. Translated from Kristallografiya, Vol. 47, No. 3, 2002, pp. 473–477.

STRUCTURES OF ORGANIC COMPOUNDS

X-ray Mapping in Heterocyclic Design: VII. Diffraction Study of the Structure of *N*-Pyridoneacetic Acid and the Product of Its Intramolecular Dehydration

V. B. Rybakov, E. V. Babaev, and V. V. Chernyshev

Faculty of Chemistry, Moscow State University, Vorob'evy gory, Moscow, 119899 Russia

e-mail: rybakov@biocryst.phys.msu.su

Received July 25, 2001

Abstract—The structure of pyridoneacetic acid $C_7H_7N_1O_3$ (**I**) is determined by the single-crystal X-ray diffraction technique. The crystals of **I** are monoclinic, a = 7.4502(15) Å, b = 10.006(6) Å, c = 9.960(3) Å, β = 109.96(2)°, Z = 4, and space group $P2_1/c$. The structure of pyridoneacetic acid is solved by the direct method and refined by the least-squares procedure in the anisotropic approximation to R = 0.0387. The structure of the product of its intramolecular dehydration, $C_7H_6N_1O_2B_1F_4$ (**II**), is determined by the grid search procedure and refined by the Reitveld method (R_p = 0.045, R_{wp} = 0.58, R_e = 0.026, and χ^2 = 4.69). The crystals of **II** are monoclinic, a = 10.4979(3) Å, b = 11.4467(3) Å, c = 7.6027(1) Å, β = 100.83(2)°, Z = 4, and space group $P2_1/n$. The system of two conjugated heterocycles is planar. © *2002 MAIK "Nauka/Interperiodica"*.

INTRODUCTION

This study continues our structural investigations of heterocyclic compounds that are able to enter readily into reactions of ring transformation [1–12]. In this paper, we concentrate on the structural study of pyridoneacetic acid, $C_7H_7N_1O_3$ (**I**), and the product of its intramolecular dehydration (cyclization), namely, 2-oxo-2,3-dihydrooxazolo[1,2-*a*]pyridinium tetrafluoroborate, $C_7H_6N_1O_2B_1F_4$ (**II**). There are no data on the structures of **I** and **II** in the Cambridge Structural Database [13]. Pyridoneacetic acid **I** was synthesized by alkylation of pyridone with chloracetic acid in the presence of an alkali. The cyclization of pyridone **I** into the oxazolopyridinium salt **II** was achieved by its treatment with acetic anhydride and the following careful addition of tetrafluoroboric acid

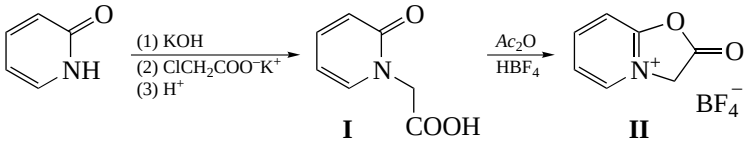

EXPERIMENTAL

The unit cell parameters of **I** ($C_7H_7NO_3$) were determined and refined using 25 reflections in the range 14° ≤ θ ≤ 16° on an Enraf–Nonius CAD4 automated diffractometer [14] (λMoK_α, graphite monochromator). Crystals **I** are monoclinic, a = 7.4502(15) Å, b = 10.006(6) Å, c = 9.960(3) Å, β = 109.96(2)°, V = 697.9(5) Å^3, d_{calcd} = 1.457 g/cm^3, μ(λMo) = 0.116 mm^{-1}, Z = 4, and space group $P2_1/c$. A set of 1745 reflections with $I \geq 2\sigma(I)$ was collected from a crystal no larger than 0.48 × 0.48 × 0.06 mm in size in the range 2.98° ≤ θ ≤ 28.97° on the same diffractometer (ω scan mode) at room temperature. The primary processing of the set of diffraction data was performed with the WinGX98 program package [15]. The structure was solved by the direct method and refined by the least-squares procedure in the anisotropic approximation using the SHELX97 program package [16]. All the hydrogen atoms of the molecule were located from the electron-density difference synthesis and refined in the isotropic approximation. The final discrepancy factors are R_1 = 0.0387 and wR_2 = 0.0793. The residual electron density lies between $\Delta\rho_{max}$ = 0.124 and $\Delta\rho_{min}$ = –0.132 e/Å^3. The atomic coordinates and thermal parameters are listed in Table 1.

The diffraction experiment for $C_7H_6N_1O_2B_1F_4$ (**II**) was performed on an XRD7 automated powder diffractometer (Seifert-FPM, Freiburg) (λCuK_α, Ni filter) in

1063-7745/02/4703-0428$22.00

Table 1. Atomic coordinates ($\times 10^4$) and isotropic thermal parameters ($Å^2 \times 10^3$) for molecule **I**

Atom	*x*	*y*	*z*	U_{eq}/U_{iso}
N(1)	6745(2)	1982(1)	502(1)	34(1)
C(2)	6691(2)	955(1)	1403(1)	34(1)
O(2)	5112(1)	701(1)	1553(1)	42(1)
C(3)	8427(2)	281(2)	2085(2)	46(1)
C(4)	10050(3)	636(2)	1854(2)	57(1)
C(5)	10030(3)	1702(2)	937(2)	61(1)
C(6)	8396(3)	2349(2)	288(2)	49(1)
C(7)	4980(2)	2696(2)	−217(2)	38(1)
C(8)	4411(2)	3690(1)	706(1)	33(1)
O(81)	2943(2)	4305(1)	226(1)	55(1)
O(82)	5628(2)	3828(1)	2001(1)	41(1)
H(3)	8440(20)	−421(19)	2727(19)	56(5)
H(4)	11190(30)	100(20)	2324(19)	63(5)
H(5)	11170(30)	1910(20)	760(20)	78(6)
H(6)	8190(30)	3100(20)	−370(20)	73(6)
H(7*A*)	3960(20)	2079(16)	−588(15)	38(4)
H(7*B*)	5130(20)	3178(18)	−1010(20)	60(5)
H(82)	5090(30)	4480(20)	2460(20)	80(6)

Table 2. Atomic coordinates ($\times 10^4$) and isotropic thermal parameters ($Å^2$) for molecule **II**

Atom	*x*	*y*	*z*	B_{iso}
N(1)	9(7)	2021(8)	8178(11)	1.56(7)
C(2)	1313(10)	1858(9)	8553(16)	1.56
C(3)	1830(8)	715(9)	8354(14)	1.56
C(4)	942(11)	−153(8)	7795(13)	1.56
C(5)	−401(10)	83(8)	7412(13)	1.56
C(6)	−883(10)	1182(10)	7607(14)	1.56
C(7)	−282(10)	3240(10)	8468(12)	1.56
C(8)	1095(12)	3721(7)	9063(14)	1.56
O(2)	2001(6)	2839(6)	9089(8)	1.56
O(8)	1417(6)	4710(5)	9476(8)	1.56
B	961(17)	3254(15)	3844(24)	3.7(5)
F(1)	1134(8)	4387(5)	3513(10)	2.78(8)
F(2)	966(9)	2664(5)	2345(7)	2.78
F(3)	1927(6)	2763(5)	4970(8)	2.78
F(4)	−101(6)	3003(6)	4395(9)	2.78
H(3)	2697(71)	596(66)	8610(82)	4.0
H(4)	1254(75)	−915(56)	7655(96)	4.0
H(5)	−991(77)	−543(60)	7033(85)	4.0
H(6)	−1779(70)	1333(71)	7369(96)	4.0
H(7*A*)	−786(69)	3358(66)	9425(90)	4.0
H(7*B*)	−729(71)	3638(60)	7401(78)	4.0

0.02° steps. Compound **II** is very unstable and tends to undergo self-condensation. Because of the high hygroscopicity and instability of compound **II**, the powder to be studied was placed in a cell inside a dry box filled with argon and then was isolated from the atmospheric moisture with a thin polyester film. The unit cell parameters were determined with the ITO indexing program [17] in the range of angles $12° \le 2\theta \le 150°$ and indices

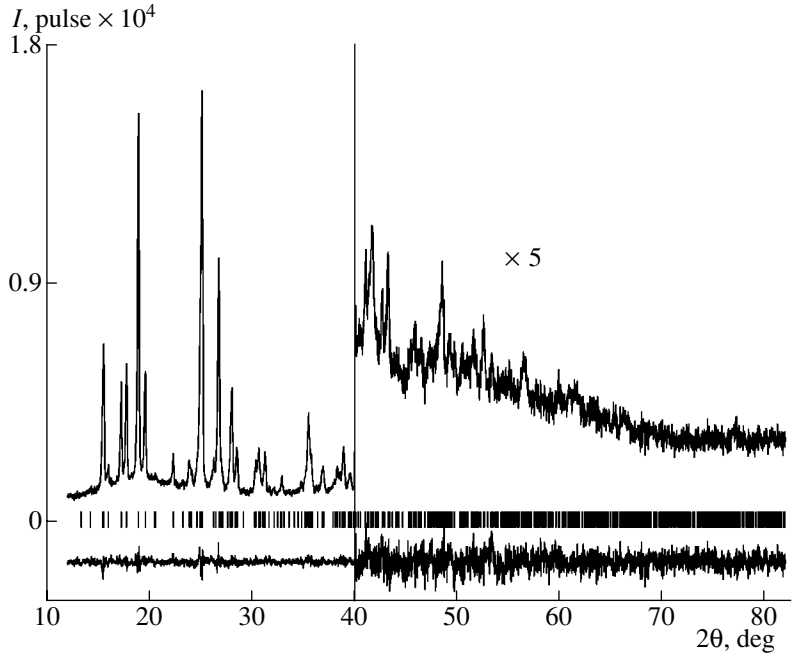

Fig. 1. Experimental and difference (Reitveld refinement) spectra for **II**.

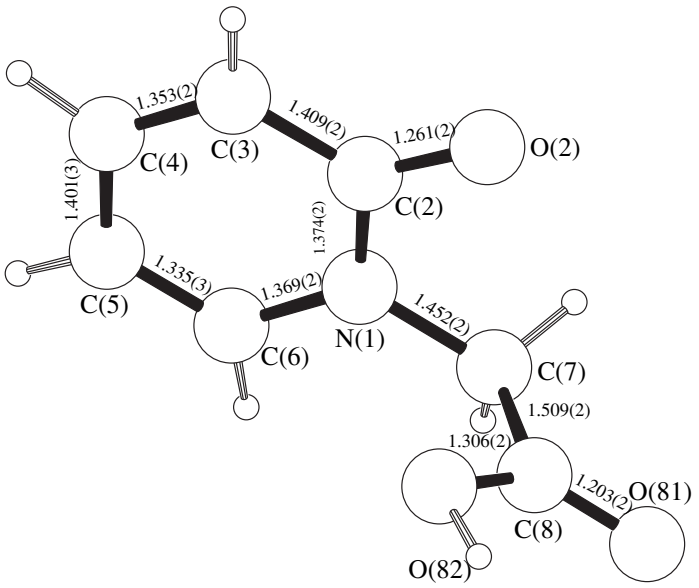

Fig. 2. Molecular structure, atomic numbering, and interatomic distances in **I**.

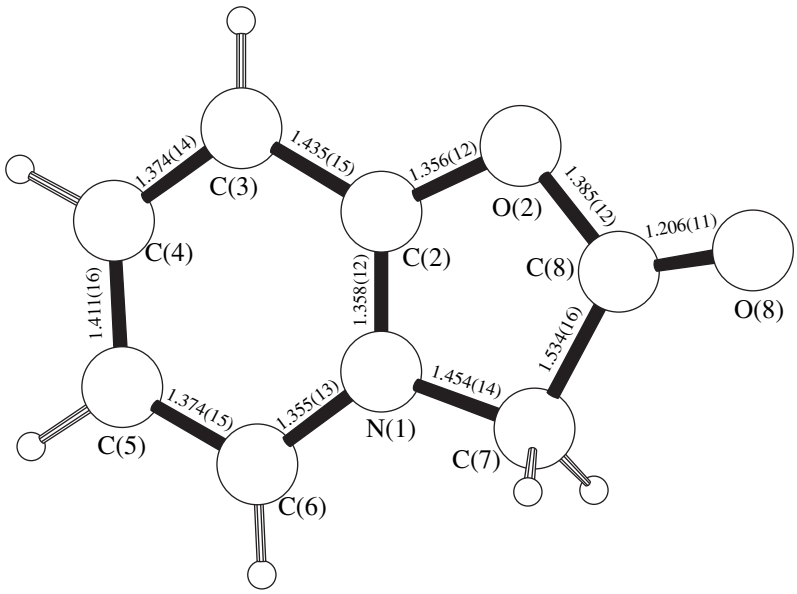

Fig. 3. Molecular structure, atomic numbering, and interatomic distances in **II**.

$0 \le h \le 6$; $0 \le k \le 7$; and $-5 \le l \le 5$. The space group was determined from the systematic absences of reflections. Crystals **II** are monoclinic, $a = 10.4979(3)$ Å, $b = 11.4467(3)$ Å, $c = 7.6027(1)$ Å, $\beta = 100.83(3)°$, $V = 897.3(1)$ Å^3, $d_{calcd} = 1.6502$ g/cm^3, $\mu(\lambda Cu) = 15.369$ cm^{-1}, $Z = 4$, and space group $P2_1/n$.

The data of the NMR spectroscopic study of **II** were used as preliminary structural data. The initial geometrical model of the molecule was constructed using semiempirical and empirical methods with the MOPAC 6.0 [18] and PCMODEL [19] programs. The structure was solved according to the grid search procedure [20] based on the given molecular fragments. The full-profile refinement of the structure was performed by the Reitveld method with the MRIA program [21]. The pseudo-Voigt function was used as a profile function, and the background was approximated by the Chebyshev polynomials of the fifth order. The texture parameters were refined within the March–Dollase model [22] in the [010] direction. In the refinement, the thermal parameters of the non-hydrogen atoms of the cation were averaged. The thermal parameters of the fluorine atoms of the anion were also averaged. The final parameters of the refinement had the following values:

Table 3. Parameters of interatomic contacts [24] in **I**

D–H	*d*(*D*–H)	*d*(*D*···*A*)	*d*(H···*A*)	ω*DHA*	*A*	Symmetry code
C(7)–H(7*A*)	0.95(2)	2.643(2)	2.44(2)	92(1)	O(2)	(*x*, *y*, *z*)
C(3)–H(3)	0.95(2)	3.322(2)	2.60(2)	134(1)	O(81)	(1 – *x*, *y* – 1/2, 1/2 – *z*)
C(4)–H(4)	0.98(2)	3.315(2)	2.80(2)	114(1)	O(81)	(*x* + 1, 1/2 – *y*, *z* + 1/2)
C(4)–H(4)	0.98(2)	3.526(2)	2.57(2)	166(2)	O(82)	(2 – *x*, *y* – 1/2, 1/2 – *z*)
C(5)–H(5)	0.95(2)	3.612(3)	2.87(2)	136(2)	O(81)	(*x* + 1, *y*, *z*)
C(6)–H(6)	0.97(2)	3.481(3)	2.75(2)	132(2)	O(81)	(1 – *x*, 1 – *y*, –*z*)
C(7)–H(7*B*)	0.96(2)	3.377(3)	2.87(2)	114(1)	O(81)	(1 – *x*, 1 – *y*, –*z*)
C(7)–H(7*B*)	0.96(2)	3.626(2)	2.67(2)	172(2)	O(2)	(*x*, 1/2 – *y*, *z* – 1/2)
C(7)–H(7*B*)	0.96(2)	3.339(2)	2.93(2)	107(1)	O(82)	(*x*, 1/2 – *y*, *z* – 1/2)
O(82)–H(82)	0.96(2)	2.535(2)	1.61(2)	162(2)	O(2)	(1 – *x*, *y* + 1/2, 1/2 – *z*)

Note: *D* is a donor atom, *A* is an acceptor atom, and H is a hydrogen atom (the *d* distances and ω angles are given in Å and degrees, respectively).

Table 4. Parameters of interatomic contacts [24] in **II**

D–H	*d*(*D*–H)	*d*(*D*···*A*)	*d*(H···*A*)	ω*DHA*	*A*	Symmetry code
C(7)–H(7*B*)	0.97(6)	3.15(1)	2.60(7)	116(4)	F(4)	(*x*, *y*, *z*)
C(6)–H(6)	0.94(7)	3.49(1)	2.88(7)	124(6)	O(8)	(*x* – 1/2, 1/2 – *y*, *z* – 1/2)
C(6)–H(6)	0.94(7)	3.33(1)	2.75(7)	121(5)	O(2)	(*x* – 1/2, 1/2 – *y*, *z* – 1/2)
C(6)–H(6)	0.94(7)	3.53(1)	2.63(8)	162(6)	F(1)	(*x* – 1/2, 1/2 – *y*, *z* + 1/2)
C(6)–H(6)	0.94(7)	3.40(1)	2.80(8)	122(6)	F(3)	(*x* – 1/2, 1/2 – *y*, *z* + 1/2)
C(7)–H(7*A*)	0.99(8)	3.53(1)	2.82(8)	129(5)	F(3)	(*x* – 1/2, 1/2 – *y*, *z* + 1/2)
C(5)–H(5)	0.96(7)	3.21(1)	2.47(7)	134(5)	F(2)	(–*x*, –*y*, 1 – *z*)
C(4)–H(4)	0.95(7)	3.69(1)	2.98(7)	133(5)	F(4)	(–*x*, –*y*, 1 – *z*)
C(3)–H(3)	0.91(7)	3.29(1)	2.87(7)	110(5)	O(8)	(1/2 – *x*, *y* – 1/2, 3/2 + *z*)
C(3)–H(3)	0.91(7)	3.26(1)	2.68(7)	123(5)	F(1)	(1/2 – *x*, *y* – 1/2, 3/2 + *z*)
C(4)–H(4)	0.95(7)	3.49(1)	2.81(7)	129(5)	F(3)	(1/2 – *x*, *y* – 1/2, 3/2 + *z*)
C(4)–H(4)	0.95(7)	3.63(1)	2.84(8)	142(5)	O(2)	(1/2 – *x*, *y* – 1/2, 3/2 + *z*)
C(3)–H(3)	0.91(7)	3.49(1)	2.78(7)	136(6)	F(4)	(*x* + 1/2, 1/2 – *y*, *z* + 1/2)
C(7)–H(7*A*)	0.99(8)	3.17(1)	2.50(8)	126(5)	O(8)	(–*x*, 1 – *y*, 2 – *z*)
C(7)–H(7*A*)	0.99(8)	3.06(1)	2.72(6)	101(4)	F(2)	(*x*, *y*, 1 + *z*)
C(7)–H(7*B*)	0.97(6)	3.15(1)	2.38(7)	136(5)	F(1)	(–*x*, 1 – *y*, 1 – *z*)

Note: *D* is a donor atom, *A* is an acceptor atom, and H is a hydrogen atom (the *d* distances and ω angles are given in Å and degrees, respectively).

$R_p = 0.045$, $R_{wp} = 0.58$, $R_e = 0.026$, and $\chi^2 = 4.69$, where $R_p = \Sigma|I_o - I_c|/\Sigma I_o$, $R_{wp} = \Sigma w|I_o - I_c|/\Sigma w I_o$, $R_e = \Sigma\sigma I_o/\Sigma I_o$, I_o is the observed intensity, and I_c is the calculated intensity. The observed and difference X-ray diffraction patterns are shown in Fig. 1. The atomic coordinates and isotropic thermal parameters are listed in Table 2.

The molecular structures of **I** and **II** with the atomic numberings are shown in Figs. 2 and 3, respectively. The drawings were obtained with the PLUTON96 program [23].

RESULTS AND DISCUSSION

Earlier, we studied the structures of the *N*-substituted pyridones-2 containing the phenacyl [3] and *para*-nitrophenacyl [8] groups at the nitrogen atom. The structure of the pyridine fragment in molecule **I** is similar to those in the pyridones studied earlier. The O(2) and C(7) atoms lie in the plane of the heterocycle. In the pyridine fragment (Fig. 2), formally single and double bonds alternate to form the quasi-diene structural fragment C(3)=C(4)–C(5)=C(6). The C(2)–N(1)–C(7)–C(8) tor-

sion angle is equal to 77.2(2)°, which rules out the formation of the O(2)···H(82)–O(82) intramolecular hydrogen bond. A similar molecular structure is observed in 1,2-dihydro-2-imino-1-carboxymethylpyridine [5], in which the planes of the carboxyl group and the pyridine ring form a dihedral angle of 80.81(5)°. In crystal structure **I**, a network of intermolecular hydrogen bonds is observed. The parameters of the hydrogen bonds are listed in Table 3.

The heterocyclic cation **II** has a planar structure. The largest atomic deviation from the plane of the bicyclic fragment is 0.01 Å. The O(8) atom lies in this plane. It is interesting to reveal structural changes that accompany the **I** ⟶ **II** cyclization. As was noted above, the bond lengths in the six-membered ring of molecule **I** alternate. Upon cyclization, the diene-like structure is retained but the bond alternation becomes less pronounced (due to the stronger bond delocalization in the cation). At the same time, upon cyclization, the carbonyl fragment of the amide group loses the double-bond character. Most likely, this indicates significant charge localization at the nitrogen atom of the cation.

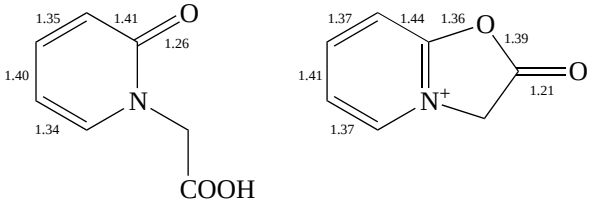

The aforementioned specific structural feature of cation **II** suggests that no aromatization occurs in the bicyclic fragment formed from the monocycle. A system of intermolecular contacts involving the hydrogen, oxygen, and fluorine atoms is formed in crystal structure **II** (Table 4). These contacts were calculated using the PARST95 program [24]. The mean B–F bond length in the tetrahedral anion is 1.321(19) Å.

ACKNOWLEDGMENTS

We are grateful to Professor E. Kemnitz (Humboldt Universität, Berlin), who kindly allowed us to perform the diffractometric experiment.

The synthetic part of this study was supported by the Russian Foundation for Basic Research, project no. 99-03-33076. We also acknowledge the support of this Foundation in the payment of the license for using the Cambridge Structural Database, project no. 99-07-90133.

REFERENCES

1. E. V. Babaev, A. V. Efimov, S. G. Zhukov, and V. B. Rybakov, Khim. Geterotsikl. Soedin., No. 7, 983 (1998).
2. E. V. Babaev, S. V. Bozhenko, D. A. Maiboroda, *et al.*, Bull. Soc. Chim. Belg. **106** (11), 631 (1997).
3. S. G. Zhukov, V. B. Rybakov, E. V. Babaev, *et al.*, Acta Crystallogr., Sect. C: Cryst. Struct. Commun. **53**, 1909 (1997).
4. E. V. Babaev, S. V. Bozhenko, S. G. Zhukov, and V. B. Rybakov, Khim. Geterotsikl. Soedin., No. 8, 1105 (1997).
5. V. B. Rybakov, S. G. Zhukov, E. V. Babaev, *et al.*, Kristallografiya **44**, 1067 (1999) [Crystallogr. Rep. **44**, 997 (1999)].
6. V. B. Rybakov, S. G. Zhukov, E. V. Babaev, *et al.*, Kristallografiya **45**, 108 (2000) [Crystallogr. Rep. **45**, 103 (2000)].
7. V. B. Rybakov, S. G. Zhukov, E. V. Babaev, *et al.*, Kristallografiya **45**, 292 (2000) [Crystallogr. Rep. **45**, 261 (2000)].
8. E. V. Babaev, V. B. Rybakov, S. G. Zhukov, and I. A. Orlova, Khim. Geterotsikl. Soedin., No. 4, 542 (1999).
9. S. G. Zhukov, E. V. Babaev, V. V. Chernyshev, *et al.*, Z. Kristallogr. **215**, 306 (2000).
10. V. B. Rybakov, S. G. Zhukov, K. Yu. Pasichnichenko, and E. V. Babaev, Koordin. Khim. **26** (9), 714 (2000).
11. V. B. Rybakov, S. G. Zhukov, E. V. Babaev, and E. J. Sonneveld, Kristallografiya **46** (3), 435 (2001) [Crystallogr. Rep. **46**, 385 (2001)].
12. V. B. Rybakov, S. I. Troyanov, E. V. Babaev, *et al.*, Kristallografiya **46** (6), 1069 (2001) [Crystallogr. Rep. **46**, 986 (2001)].
13. F. H. Allen and O. Kennard, Chem. Design Automat. News **8** (1), 31 (1993).
14. *Enraf–Nonius CAD4 Software: Version 5.0* (Enraf–Nonius, Delft, The Netherlands, 1989).
15. L. J. Farrugia, *WinGX98: X-ray Crystallographic Programs for Windows* (Univ. of Glasgow, Glasgow, 1998).
16. G. M. Sheldrick, *SHELX97: Program for the Solution and Refinement of Crystal Structures* (Univ. of Göttingen, Göttingen, 1997).
17. J. W. Visser, J. Appl. Crystallogr. **2**, 89 (1969).
18. J. J. P. Stewart, *MOPAC 6.0. QCPE Program No. 455* (Indiana Univ., Department of Chemistry, Bloomington, 1990).
19. *PCMODEL 7.0. Molecular Modeling Software for the Windows95/NT* (Sarena Software, Bloomington, 1999).
20. V. V. Chernyshev and Y. Schenk, Z. Kristallogr. **213**, 1 (1998).
21. V. B. Zlokazov and V. V. Chernyshev, J. Appl. Crystallogr. **25**, 447 (1992).
22. W. A. Dollase, J. Appl. Crystallogr. **19**, 267 (1986).
23. A. L. Spek, *PLUTON96: Molecular Graphics Program* (Univ. of Utrecht, The Netherlands, 1996).
24. M. Nardelli, J. Appl. Crystallogr. **28**, 659 (1995).

Translated by I. Polyakova

Crystallography Reports, Vol. 47, No. 3, 2002, pp. 433–442. Translated from Kristallografiya, Vol. 47, No. 3, 2002, pp. 478–487.

STRUCTURES OF ORGANIC COMPOUNDS

X-ray Crystal Structure of the Complex of Enniatin *B* with KNCS

N. E. Zhukhlistova

Shubnikov Institute of Crystallography, Russian Academy of Sciences, Leninskiĭ pr. 59, Moscow, 117333 Russia

e-mail: nez@ns.crys.ras.ru

Received November 6, 2001

Abstract—The crystal structure of the complex of enniatin *B*, *cyclo*[–(*L-MeVal-D-Hyi*)$_3$–] ($C_{33}H_{57}N_3O_9$), with KNCS is determined by X-ray diffraction [CuK_α radiation, $R = 0.0594$ for 7925 reflections with $I > 2\sigma(I)$]. The crystals belong to the space group $P3$, $a = 24.448(5)$ Å, $c = 23.578(5)$ Å, $V = 12277(9)$ Å^3, and $Z = 6$. The unit cell contains 12 symmetrically independent molecules of the antibiotic, which are located on crystallographic threefold axes. The K^+ ions are located on the threefold axes and are coordinated by the carbonyl oxygen atoms of the hydroxy acid or amino acid residues of the enniatin molecules to form prisms, twisted prisms, and antiprisms. All the independent enniatin molecules retain the principal conformational features revealed earlier in the structures of enniatin *B* and its complexes. © *2002 MAIK "Nauka/Interperiodica".*

INTRODUCTION

Antibiotics of the enniatin series, whose depsipeptide rings consist of alternating amino acid and hydroxy acid residues, belong to membrane-active compounds. Their physiological function is to induce transport of alkali and alkaline-earth ions through biological membranes. Earlier [1], it was demonstrated that the functioning of these antibiotics is governed to a large extent by conformational factors. Studies of the structure of these antibiotics both in the free state and in complexes with metals are of importance for the understanding of the mechanism of their action. The structures of enniatin *B* and its analogues were investigated in solutions by using calculation methods [2, 3] and in crystals by X-ray diffraction [4–8]. In addition to the 1 : 1 complexes of enniatin *B* with K^+ ions, the 2 : 1 and 3 : 1 sandwich complexes were also found in solutions. The former sandwich complex contains only the amide carbonyl groups as the ligands, whereas the latter complex involves both the amide and ester ligands [9]. The sandwich structure of the 2 : 1 complex of enniatin *B* with KI has been established using X-ray diffraction [7]. In the crystal structure of this complex, the amide oxygen atoms of two independent molecules of the antibiotic face each other and the K^+ cation is located between these molecules. The coordination environment of the K^+ ion is a distorted trigonal prism formed by the amide oxygen atoms of both independent molecules. In the crystal structure of the complex of an analogue of enniatin *B*, beauvericin (*Bv*), with barium picrate (Ba*Pic*$_2$) [10] of composition $(Bv \cdot Pic_3 \cdot \mathrm{Ba} \cdot Bv)^+ \cdot Pic^-$, each *Bv* molecule is coordinated to the adjacent Ba^{2+} ion through three amide oxygen atoms. The *Bv* molecules present the same side (the amide oxygen atoms) to each other, and three *Pic*$^-$ anions are located between the Ba^{2+} cations. That is to say, the beauvericin molecule encloses the cationic–anionic complex as a whole into a "capsule." The results obtained gave a better insight into the mechanism of the transmembrane transport of metal ions with antibiotics of the enniatin series. This transport can occur with the help of carrier molecules or proceed through relay-race ion transfer or through a continuous channel formed by stacks of the enniatin molecules [11]. The crystal structure of the 1 : 1 complex of enniatin *B* with KNCS was determined by X-ray diffraction analysis as a continuation of studies on the membrane-active antibiotic enniatin. The crystals of the complex were grown from methanol.

EXPERIMENTAL

Single crystals of the complex of enniatin *B* with KNCS were grown at the Shemyakin–Ovchinnikov Institute of Bioorganic Chemistry of the Russian Academy of Sciences. The crystals belong to the space group $P3$, $a = 24.448(7)$ Å, $c = 23.718(7)$ Å, $V = 12277(9)$ Å^3, $Z = 6$, and $\rho_{calcd} = 1.196$ g/cm^3. The intensities of reflections were measured on a Syntex $P2_1$ four-circle diffractometer (CuK_α radiation, graphite monochromator, $\theta_{max} = 52.6°$, $\theta/2\theta$ scan mode). A total of 8606 reflections were measured, of which 7925 reflections were with $I > 2\sigma(I)$. The application of the standard direct method to the solution of the structure containing more than 200 independent non-hydrogen atoms proved to be inefficient. Initially, the positions of the K atoms were revealed on threefold axes. Then, the partial structure

1063-7745/02/4703-0433$22.00 © 2002 MAIK "Nauka/Interperiodica"

Table 1. Coordinates and thermal parameters of the independent atoms in the crystal structure of the complex of enniatin *B* with KNCS

Atom	*x*/*a*	*y*/*b*	*z*/*c*	U_{eq}
		Molecule 1		
N(1)	−0.1591(4)	−0.1013(4)	0.6139(3)	0.050(2)
C(1*A*)	−0.1702(5)	−0.0491(5)	0.6004(5)	0.050(3)
C(1')	−0.1100(5)	0.0140(5)	0.6110(5)	0.047(3)
O(1)	−0.0758(3)	0.0250(3)	0.6498(3)	0.057(2)
C(1)	−0.1751(7)	−0.1264(7)	0.6719(5)	0.084(4)
C(1*B*)	−0.2283(5)	−0.0534(6)	0.6262(6)	0.075(4)
C(1*G*1)	−0.2862(6)	−0.1132(6)	0.6044(7)	0.093(4)
C(1*G*2)	−0.2351(7)	0.0059(7)	0.6130(8)	0.112(6)
O(2')	−0.1007(3)	0.0571(3)	0.5744(5)	0.061(2)
C(2*A*)	−0.0484(5)	0.1233(5)	0.5819(6)	0.069(3)
C(2')	0.0106(5)	0.1223(5)	0.5774(5)	0.058(3)
O(2)	0.0750(4)	−0.0221(4)	0.5371(4)	0.066(2)
C(2*B*)	−0.0562(7)	0.1614(7)	0.5323(10)	0.123(7)
C(2*G*1)	−0.0099(9)	0.2301(8)	0.5493(14)	0.236(17)
C(2*G*2)	−0.1191(9)	0.1591(10)	0.5348(10)	0.143(7)
		Molecule 2		
N(1)	0.1053(4)	−0.0568(4)	0.3286(3)	0.049(2)
C(1*A*)	0.1548(5)	0.0052(5)	0.3442(5)	0.057(3)
C(1')	0.1346(5)	0.0541(5)	0.3304(5)	0.050(3)
O(1)	0.1030(3)	0.0525(4)	0.2907(3)	0.058(2)
C(1)	0.1045(6)	−0.0837(5)	0.2738(5)	0.068(3)
C(1*B*)	0.2180(6)	0.0242(6)	0.3150(6)	0.072(3)
C(1*G*1)	0.2443(6)	−0.0155(6)	0.3400(8)	0.099(5)
C(1*G*2)	0.2648(6)	0.0930(6)	0.3214(9)	0.105(6)
O(2')	0.1589(3)	0.1018(4)	0.3690(3)	0.060(2)
C(2*A*)	0.1508(5)	0.1549(5)	0.3581(6)	0.065(3)
C(2')	0.0784(5)	0.1342(6)	0.3625(5)	0.053(3)
O(2)	0.0484(4)	0.0972(4)	0.3978(4)	0.066(2)
C(2*B*)	0.1868(8)	0.2071(12)	0.3952(15)	0.196(13)
C(2*G*1)	0.2583(8)	0.2200(13)	0.4019(13)	0.217(16)
C(2*G*2)	0.1660(10)	0.2096(15)	0.4396(8)	0.219(18)
		Molecule 3		
N(1)	−0.0989(4)	0.0609(4)	0.1165(4)	0.049(2)
C(1*A*)	−0.0474(6)	0.1220(5)	0.1014(5)	0.061(3)
C(1')	0.0151(6)	0.1251(5)	0.1118(5)	0.057(3)
O(1)	0.0273(4)	0.1006(4)	0.1513(3)	0.066(2)
C(1)	−0.1310(7)	0.0450(7)	0.1691(6)	0.089(4)
C(1*B*)	−0.0483(6)	0.1768(6)	0.1341(7)	0.086(4)
C(1*G*1)	−0.1072(9)	0.1804(9)	0.1126(10)	0.150(10)
C(1*G*2)	0.0085(14)	0.2411(8)	0.1177(12)	0.219(17)
O(2')	0.0580(4)	0.1580(4)	0.0732(4)	0.074(2)
C(2*A*)	0.1217(5)	0.1709(5)	0.0807(5)	0.062(3)
C(2')	−0.1096(5)	0.0124(5)	0.0777(4)	0.049(3)
O(2)	−0.0228(4)	−0.0949(4)	0.0388(4)	0.077(3)
C(2*B*)	0.1596(8)	0.2113(8)	0.0262(8)	0.108(6)
C(2*G*1)	0.2286(7)	0.2244(7)	0.0314(7)	0.100(5)
C(2*G*2)	0.1523(10)	0.2755(8)	0.0311(9)	0.145(9)

Table 1. (Contd.)

Atom	*x*/*a*	*y*/*b*	*z*/*c*	U_{eq}
		Molecule 4		
N(1)	−0.0426(5)	−0.1589(4)	0.8302(4)	0.059(2)
C(1*A*)	0.0204(5)	−0.1407(5)	0.8470(5)	0.057(3)
C(1')	0.0664(5)	−0.0728(5)	0.8288(5)	0.051(3)
O(1)	0.0599(3)	−0.0447(3)	0.7899(3)	0.056(2)
C(1)	−0.0684(8)	−0.1872(8)	0.7727(6)	0.101(5)
C(1*B*)	0.0434(7)	−0.1857(7)	0.8291(7)	0.099(5)
C(1*G*1)	0.0033(8)	−0.2520(7)	0.8523(10)	0.118(6)
C(1*G*2)	0.1130(8)	−0.1611(8)	0.8392(10)	0.120(6)
O(2')	−0.1589(3)	−0.1137(4)	0.8651(3)	0.060(2)
C(2*A*)	−0.1428(5)	−0.1638(5)	0.8506(7)	0.076(4)
C(2')	−0.0726(5)	−0.1362(5)	0.8589(6)	0.060(3)
O(2)	−0.0450(4)	−0.0983(4)	0.8991(4)	0.075(2)
C(2*B*)	−0.1782(9)	−0.2173(8)	0.8951(16)	0.208(15)
C(2*G*1)	−0.1561(17)	−0.2524(16)	0.9080(3)	0.620(6)
C(2*G*2)	−0.2521(7)	−0.2456(7)	0.8828(16)	0.260(2)
		Molecule 5		
N(1)	0.5681(4)	0.3928(3)	0.3048(3)	0.040(2)
C(1*A*)	0.5128(4)	0.3297(5)	0.3177(5)	0.054(3)
C(1')	0.5328(4)	0.2805(4)	0.3090(5)	0.042(2)
O(1)	0.5631(3)	0.2794(3)	0.2692(3)	0.053(2)
C(1)	0.5751(5)	0.4241(6)	0.2509(5)	0.069(3)
C(1*B*)	0.4532(5)	0.3169(6)	0.2877(5)	0.071(3)
C(1*G*1)	0.4299(6)	0.3608(6)	0.3095(8)	0.090(5)
C(1*G*2)	0.3998(5)	0.2445(6)	0.2958(7)	0.096(5)
O(2')	0.7284(3)	0.4921(3)	0.3494(3)	0.050(2)
C(2*A*)	0.6659(5)	0.4853(5)	0.3424(5)	0.052(3)
C(2')	0.6173(4)	0.4152(5)	0.3448(5)	0.048(3)
O(2)	0.6151(4)	0.3817(4)	0.3810(3)	0.063(2)
C(2*B*)	0.6572(5)	0.5184(6)	0.3948(5)	0.060(3)
C(2*G*1)	0.5884(6)	0.5096(8)	0.3941(7)	0.097(5)
C(2*G*2)	0.7034(7)	0.5868(6)	0.3966(3)	0.082(4)
		Molecule 6		
N(1)	0.5038(3)	0.2622(4)	0.0878(3)	0.045(2)
C(1*A*)	0.5105(5)	0.3245(5)	0.0753(5)	0.054(3)
C(1')	0.5761(5)	0.3747(4)	0.0848(4)	0.046(2)
O(1)	0.6092(3)	0.3793(3)	0.1245(3)	0.062(2)
C(1)	0.4813(7)	0.2330(6)	0.1399(6)	0.083(4)
C(1*B*)	0.4597(7)	0.3343(7)	0.1042(6)	0.088(4)
C(1*G*1)	0.3944(6)	0.2863(8)	0.0833(10)	0.132(7)
C(1*G*2)	0.4711(8)	0.4027(7)	0.0884(13)	0.175(11)
O(2')	0.5942(4)	0.4197(4)	0.0447(4)	0.080(2)
C(2*A*)	0.6593(6)	0.4791(5)	0.0525(6)	0.075(4)
C(2')	0.7112(5)	0.4657(5)	0.0545(5)	0.048(3)
O(2)	0.7114(4)	0.4320(4)	0.0150(3)	0.072(2)
C(2*B*)	0.6594(8)	0.5167(6)	−0.0031(9)	0.117(6)
C(2*G*1)	0.7188(8)	0.5857(6)	0.0113(11)	0.152(9)
C(2*G*2)	0.6053(8)	0.5207(9)	−0.0156(9)	0.138(7)

Table 1. (Contd.)

Atom	*x*/*a*	*y*/*b*	*z*/*c*	U_{eq}
		Molecule 7		
N(1)	0.5091(4)	0.2236(4)	0.8029(3)	0.047(2)
C(1*A*)	0.5268(6)	0.1753(5)	0.8170(5)	0.062(3)
C(1')	0.5939(5)	0.1983(5)	0.8088(4)	0.045(2)
O(1)	0.6251(3)	0.2324(3)	0.7681(3)	0.050(2)
C(1)	0.4820(6)	0.2258(6)	0.7475(5)	0.070(3)
C(1*B*)	0.4794(6)	0.1125(5)	0.7851(6)	0.072(4)
C(1*G*1)	0.4153(6)	0.0826(6)	0.8002(8)	0.102(5)
C(1*G*2)	0.5054(7)	0.0641(6)	0.7892(8)	0.104(5)
O(2')	0.5605(3)	0.3823(3)	0.8474(3)	0.050(2)
C(2*A*)	0.5079(5)	0.3217(5)	0.8379(5)	0.051(3)
C(2')	0.5301(5)	0.2711(4)	0.8409(5)	0.047(3)
O(2)	0.5642(4)	0.2759(3)	0.8795(3)	0.061(2)
C(2*B*)	0.4637(5)	0.3091(6)	0.8888(7)	0.077(3)
C(2*G*1)	0.4058(6)	0.2428(6)	0.8848(7)	0.094(4)
C(2*G*2)	0.4408(7)	0.3546(7)	0.8906(8)	0.114(6)
		Molecule 8		
N(1)	0.8298(4)	0.4296(4)	0.5915(4)	0.050(2)
C(1*A*)	0.8347(5)	0.3779(5)	0.5745(5)	0.064(3)
C(1')	0.7763(4)	0.3169(5)	0.5884(5)	0.045(2)
O(1)	0.7430(4)	0.3093(4)	0.6281(3)	0.066(2)
C(1)	0.8493(6)	0.4558(6)	0.6483(5)	0.076(3)
C(1*B*)	0.8960(5)	0.3784(6)	0.5988(6)	0.072(3)
C(1*G*1)	0.9562(7)	0.4378(9)	0.5744(10)	0.142(8)
C(1*G*2)	0.9007(7)	0.3224(8)	0.5806(9)	0.125(6)
O(2')	0.7649(4)	0.2698(4)	0.5524(3)	0.064(2)
C(2*A*)	0.7134(5)	0.2067(5)	0.5672(5)	0.054(3)
C(2')	0.6497(5)	0.2072(5)	0.5588(4)	0.050(3)
O(2)	0.6450(4)	0.2358(4)	0.5191(3)	0.063(2)
C(2*B*)	0.7209(6)	0.1637(6)	0.5305(6)	0.077(4)
C(2*G*1)	0.7130(11)	0.1709(10)	0.4734(8)	0.135(7)
C(2*G*2)	0.6812(8)	0.0941(7)	0.5466(8)	0.111(5)
		Molecule 9		
N(1)	0.1740(4)	0.6112(4)	0.2515(4)	0.060(2)
C(1*A*)	0.1636(4)	0.5485(4)	0.2685(5)	0.052(3)
C(1')	0.2200(5)	0.5412(5)	0.2550(5)	0.056(3)
O(1)	0.2542(4)	0.5676(3)	0.2148(3)	0.062(2)
C(1)	0.1579(6)	0.6202(6)	0.1960(5)	0.073(3)
C(1*B*)	0.1005(7)	0.4904(7)	0.2475(9)	0.114(6)
C(1*G*1)	0.0488(7)	0.5025(11)	0.2732(9)	0.148(8)
C(1*G*2)	0.0908(7)	0.4296(7)	0.2656(13)	0.184(13)
O(2')	0.2762(3)	0.7719(3)	0.2905(4)	0.065(2)
C(2*A*)	0.2131(6)	0.7245(5)	0.2793(6)	0.067(3)
C(2')	0.2101(5)	0.6570(5)	0.2883(5)	0.058(3)
O(2)	0.2356(4)	0.6509(4)	0.3271(4)	0.076(2)
C(2*B*)	0.1723(6)	0.7280(6)	0.3282(7)	0.093(4)
C(2*G*1)	0.1034(8)	0.6746(8)	0.3292(9)	0.124(6)
C(2*G*2)	0.1762(9)	0.7968(9)	0.3172(12)	0.170(11)

Table 1. (Contd.)

Atom	*x*/*a*	*y*/*b*	*z*/*c*	U_{eq}
		Molecule 10		
N(1)	0.1692(4)	0.5806(4)	0.5214(4)	0.063(3)
C(1*A*)	0.1758(5)	0.6404(5)	0.4992(6)	0.067(3)
C(1')	0.2345(6)	0.6957(5)	0.5256(6)	0.066(3)
O(1)	0.2659(4)	0.6966(4)	0.5622(4)	0.075(2)
C(1)	0.1451(7)	0.5609(7)	0.5773(6)	0.092(4)
C(1*B*)	0.1148(6)	0.6459(7)	0.5009(10)	0.123(7)
C(1*G*1)	0.0952(11)	0.6597(15)	0.5506(10)	0.188(13)
C(1*G*2)	0.0612(6)	0.5844(8)	0.4684(8)	0.108(5)
O(2')	0.2523(4)	0.4958(4)	0.4950(4)	0.074(2)
C(2*A*)	0.1929(6)	0.4923(6)	0.5094(7)	0.085(4)
C(2')	0.2015(6)	0.5559(6)	0.4944(6)	0.069(4)
O(2)	0.2361(4)	0.5856(5)	0.4510(4)	0.095(3)
C(2*B*)	0.1447(8)	0.4385(10)	0.4752(13)	0.159(9)
C(2*G*1)	0.0767(11)	0.4314(11)	0.4797(16)	0.222(16)
C(2*G*2)	0.1379(8)	0.3792(8)	0.4917(13)	0.194(13)
		Molecule 11		
N(1)	0.4917(4)	0.7637(4)	0.7428(4)	0.057(2)
C(1*A*)	0.4857(5)	0.8197(5)	0.7582(6)	0.063(3)
C(1')	0.4154(5)	0.8002(5)	0.7469(5)	0.055(3)
O(1)	0.3840(3)	0.7702(4)	0.7061(3)	0.062(2)
C(1)	0.5140(6)	0.7572(6)	0.6884(5)	0.074(3)
C(1*B*)	0.5310(6)	0.8799(6)	0.7252(6)	0.079(4)
C(1*G*1)	0.5959(6)	0.8966(7)	0.7463(7)	0.097(4)
C(1*G*2)	0.5185(8)	0.9326(6)	0.7376(8)	0.106(5)
O(2')	0.4279(4)	0.6042(4)	0.7874(3)	0.069(2)
C(2*A*)	0.4825(6)	0.6632(6)	0.7809(5)	0.072(3)
C(2')	0.4653(4)	0.7144(5)	0.7813(4)	0.048(3)
O(2)	0.4319(4)	0.7174(4)	0.8202(3)	0.070(2)
C(2*B*)	0.5210(7)	0.6717(7)	0.8368(8)	0.115(6)
C(2*G*1)	0.5810(9)	0.7393(8)	0.8371(13)	0.195(14)
C(2*G*2)	0.5329(9)	0.6190(9)	0.8476(10)	0.152(8)
		Molecule 12		
N(1)	0.2293(5)	0.5031(4)	1.0381(4)	0.060(2)
C(1*A*)	0.1770(5)	0.5182(6)	1.0210(5)	0.069(3)
C(1')	0.1989(6)	0.5862(6)	1.0354(6)	0.065(3)
O(1)	0.2294(4)	0.6146(4)	1.0750(4)	0.074(2)
C(1)	0.2257(7)	0.4734(7)	1.0920(6)	0.096(4)
C(1*B*)	0.1176(8)	0.4737(7)	1.0551(9)	0.122(6)
C(1*G*1)	0.0915(11)	0.4066(10)	1.0293(11)	0.164(9)
C(1*G*2)	0.0660(7)	0.4834(8)	1.0526(9)	0.121(6)
O(2')	0.3923(4)	0.5672(5)	0.9980(3)	0.078(3)
C(2*A*)	0.3318(7)	0.5140(6)	1.0101(7)	0.086(4)
C(2')	0.2809(7)	0.5332(7)	1.0012(7)	0.084(4)
O(2)	0.2831(4)	0.5680(4)	0.9648(4)	0.079(3)
C(2*B*)	0.3137(13)	0.4552(15)	0.9727(17)	0.206(15)
C(2*G*1)	0.3603(12)	0.4274(10)	0.9910(13)	0.200(12)
C(2*G*2)	0.3226(16)	0.4758(13)	0.9227(10)	0.195(15)

Table 1. (Contd.)

Atom	*x*/*a*	*y*/*b*	*z*/*c*	U_{eq}
		Molecule 12		
K(1)	0	0	0.7188(2)	0.053(1)
K(2)	0	0	0.4682(2)	0.047(1)
K(3)	0	0	0.2181(2)	0.049(1)
K(4)	0	0	0.9668(2)	0.049(1)
K(5)	0.6667	0.3333	0.4484(2)	0.048(1)
K(6)	0.6667	0.3333	0.1947(2)	0.046(1)
K(7)	0.6667	0.3333	0.9434(2)	0.048(1)
K(8)	0.6667	0.3333	0.6946(2)	0.046(1)
K(9)	0.3333	0.6667	0.1414(2)	0.055(1)
K(10)	0.3333	0.6667	0.3862(2)	0.047(1)
K(11)	0.3333	0.6667	0.6333(2)	0.057(1)
K(12)	0.3333	0.6667	0.8892(2)	0.053(1)
S(1)	0.9215(2)	0.6171(2)	0.7213(2)	0.128(2)
C(1)	0.8772(8)	0.6336(10)	0.6987(9)	0.144(8)
N(1)	0.8438(9)	0.6585(13)	0.6799(10)	0.248(13)
S(2)	0.9524(4)	0.3767(5)	0.1532(5)	0.220(3)
C(2)	0.9192(12)	0.3241(11)	0.2138(11)	0.107(9)
N(2)	0.9110(9)	0.3023(8)	0.2347(6)	0.060(4)
S(3)	0.2788(6)	0.9400(5)	0.6970(6)	0.309(5)
C(3)	0.3460(16)	0.9444(17)	0.6787(14)	0.201(15)
N(3)	0.3638(13)	0.9323(11)	0.6614(11)	0.189(11)
S(4)	0.2900(6)	0.3594(6)	0.1599(5)	0.307(5)
C(4)	0.2570(2)	0.2943(14)	0.2014(11)	0.270(2)
N(4)	0.2604(10)	0.2781(10)	0.2314(12)	0.178(10)

Table 2. Distances (Å) between the K^+ ions and the O atoms involved in the coordination polyhedra

Bond	Length	Bond	Length	Bond	Length
K(1)–O(1)_1	2.760(8)	K(5)–O(2)_5	2.653(7)	K(9)–O(1)_12[3]	2.707(9)
K(1)–O(1)_4	2.790(8)	K(5)–O(2)_8	2.742(8)	K(9)–O(1)_9	2.819(8)
K(2)–O(2)_2	2.651(9)	K(6)–O(1)_6	2.755(8)	K(10)–O(2)_9	2.627(8)
K(2)–O(2)_1	2.705(8)	K(6)–O(1)_5	2.818(7)	K(10)–O(2)_10	2.689(8)
K(3)–O(1)_3	2.714(8)	K(7)–O(2)_7	2.652(8)	K(11)–O(1)_10	2.701(9)
K(3)–O(1)_2	2.780(8)	K(7)–O(2)_6[2]	2.695(9)	K(11)–O(1)_11	2.792(9)
K(4)–O(2)_4	2.631(8)	K(8)–O(1)_8	2.723(8)	K(12)–O(2)_11	2.653(8)
K(4)–O(2)_3[1]	2.705(9)	K(8)–O(1)_7	2.767(7)	K(12)–O(2)_12	2.753(9)

Note: The figures following the notations of the oxygen atoms correspond to the order numbers of the molecules. The superscripts 1, 2, and 3 correspond to the symmetry codes: $-y, x-y, z+1$; $x, y, z+1$; and $x, y, z-1$.

expansion (TEXP) procedure included in the SHELX97 program package [12] was employed and difference electron density syntheses were calculated. The atomic positions of 12 independent molecules (a total of 192 independent atoms) were located in a step-by-step manner. At this stage, the structural model was refined to $R = 0.25$. No further decrease in the R factor was achieved, the rhodanide ions were not revealed, and certain geometric parameters had unreasonable values. The unsatisfactory results obtained at this stage were attributed to possible microtwinning. Hence, the structure was refined taking into account merohedral

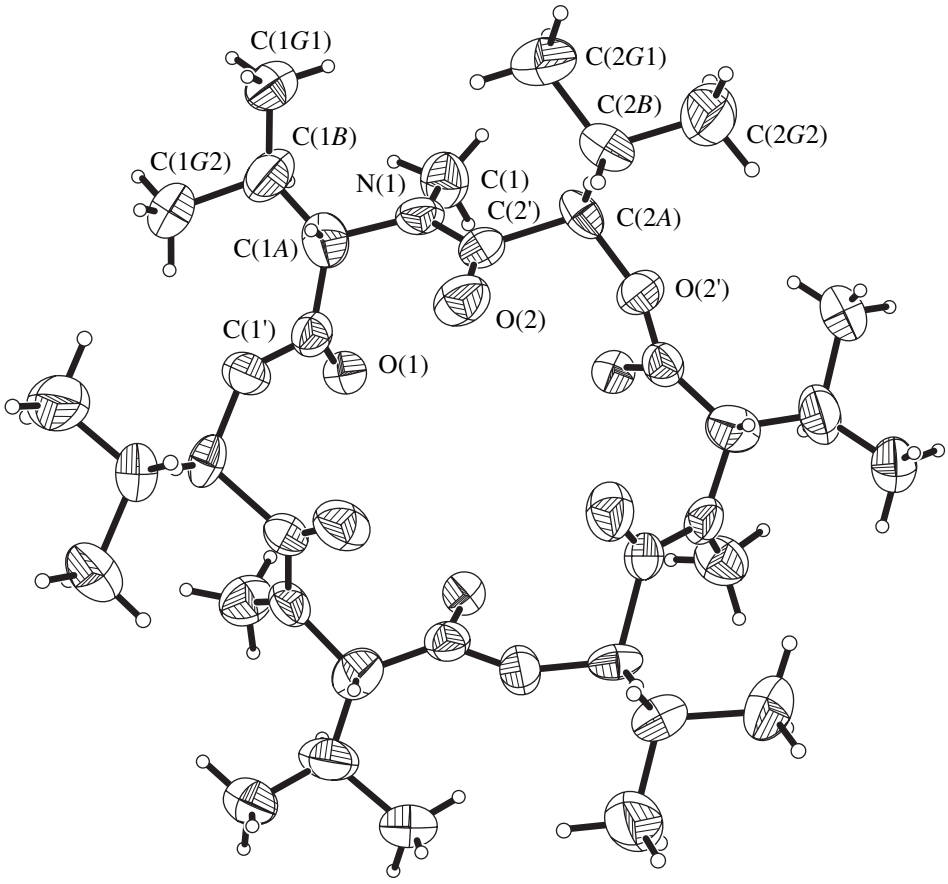

Fig. 1. Conformation of one of 12 symmetrically independent molecules of enniatin *B*.

(or pseudomeroheral) twinning with the use of the SHELX97 program package [12]. In this case, the reciprocal lattices of the twin domains are identical and the *hkl* indices for two components are related to each other by a matrix describing the mutual orientation of the blocks. Several possible models of twinning were

Table 3. Conformational parameters of 12 crystallographically independent molecules of enniatin *B* in the complex with KNCS

Molecule	φ		Ψ		ω		χ^1		χ^2	
	MeVal	*Hyi*	*MeVal*	*Hyi*	*MeVal*	*Hyi*	*MeVal*	*Hyi*	*MeVal*	*Hyi*
1	−73.6(11)	65.5(13)	142.8(9)	−138.1(10)	173.7(9)	−166.6(9)	−61.5(14)	168.6(16)	176.5(12)	59.7(19)
2	−71.4(11)	67.4(12)	146.3(9)	−146.3(10)	172.5(9)	−167.8(9)	−70.5(13)	45(3)	167.6(12)	−86(3)
3	−74.1(11)	66.1(12)	142.7(9)	−138.3(10)	173.3(9)	−164.9(9)	−68.3(16)	−177.9(12)	178.6(16)	60.9(14)
4	−75.0(12)	71.2(13)	148.4(9)	−154.1(10)	177.4(9)	−167.7(11)	−59.7(16)	−153(5)	171.1(14)	66(2)
5	−71.2(11)	64.1(11)	140.3(8)	−137.0(8)	171.2(8)	−164.0(8)	−67.0(13)	−175.9(10)	170.6(10)	63.6(11)
6	−65.8(11)	59.4(14)	141.0(9)	−142.2(10)	173.4(9)	−165.1(10)	−62.3(15)	167.0(13)	179.7(13)	46.7(18)
7	−71.9(11)	69.0(11)	142.1(9)	−137.3(9)	167.0(8)	−171.3(8)	−64.6(14)	−177.2(11)	168.7(10)	63.6(14)
8	−75.3(11)	71.2(10)	150.3(9)	−149.3(9)	172.3(8)	−169.0(9)	−63.3(15)	−64.4(16)	179.6(12)	167.5(12)
9	−78.9(11)	69.6(12)	148.8(9)	−141.2(10)	173.7(9)	−168.9(8)	−59.0(16)	−171.8(13)	−178.8(17)	67.9(14)
10	−85.9(12)	64.5(14)	169.0(9)	−152.4(10)	−176.4(10)	−173.5(11)	78(2)	−174(2)	−54.4(19)	66(2)
11	−74.6(11)	64.8(13)	141.1(9)	−136.3(10)	171.1(10)	−162.8(9)	−67.6(13)	−174.9(16)	174.0(12)	55.0(19)
12	−71.8(11)	72.2(14)	147.7(9)	−146.6(11)	170.3(10)	−172.4(9)	−72.3(16)	79(3)	167.1(14)	−51(3)

Note: The conformational parameters φ, Ψ, ω, χ^1, and χ^2 correspond to the torsion angles C(*j*'–1)–N(*j*)[O(*j*')]–C(*j*A)–C(*j*'), N(*j*)[O(*j*')]–C(*j*A)–C(*j*')–O(*j*'+1)[N(*j*+1)], C(*j*A)–C(*j*')–N(*j*+1)[O(*j*'+1)]–C[(*j*+1)*A*], N(*j*)[O(*j*')]–C(*j*A)–C(*j*B)–C(*j*G1), and N(*j*)[O(*j*')]–C(*j*A)–C(*j*B)–(*j*G2), where *j* is the number of the residue.

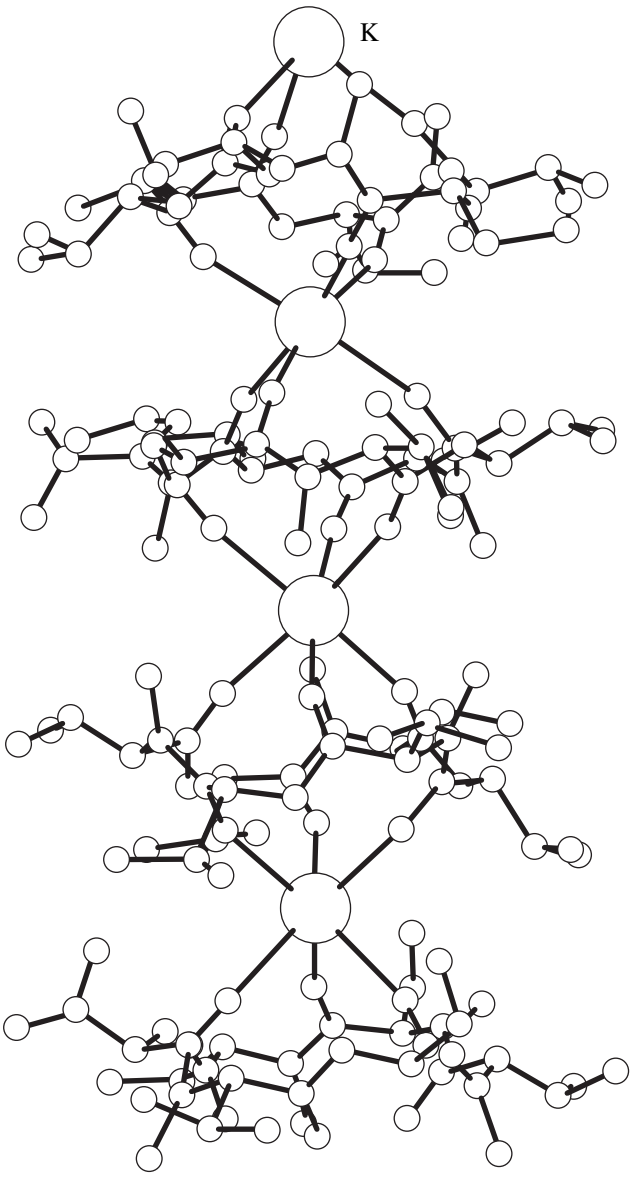

Fig. 2. Fragment of the crystal structure including four independent enniatin molecules and the K^+ ions located along the threefold axis.

examined. It was found that the twin components of the crystal are related to each other by a twofold axis whose direction coincides with the crystallographic threefold axis. In the course of the structure refinement taking into account twinning, the atomic positions of four rhodanide groups were determined and the geometric parameters of the molecules were improved. A total of 204 non-hydrogen atoms were located and refined anisotropically. The positions of the hydrogen atoms of the enniatin molecules were calculated from geometric considerations and refined using the riding model. The thermal parameters of the H atoms were taken equal to $1.2U_{eq}$ of the atoms to which the corresponding H atoms are attached. The final *R* factors were 0.0643 and 0.0594 for all the reflections used in the calculations and 7925 reflections with $I > 2\sigma(I)$, respectively. The atomic coordinates and the equivalent thermal parameters are given in Table 1.

RESULTS AND DISCUSSION

The trigonal unit cell of the complex of enniatin *B* with KNCS contains 12 crystallographically independent enniatin molecules. One of these molecules is shown in Fig. 1. Each enniatin molecule has a molecular threefold axis and is located on one of the three crystallographic threefold axes (four independent molecules along each axis) so that the molecular axis coincides with the crystallographic axis. As a result, the enniatin molecules are packed in infinite stacks along these axes. The K^+ ions are located on the threefold axes between the enniatin molecules (Fig. 2). In each stack, the carbonyl oxygen atoms of the amide or ester groups of the enniatin molecules face each other. The coordination polyhedra of the K^+ ions are formed by the carbonyl oxygen atoms, all of which belong to either the hydroxy acid residues or the amino acid residues of the enniatin molecules. These polyhedra can be in the form of regular trigonal prisms, distorted prisms, and antiprisms. The oxygen atoms of the ester groups form antiprisms about the K(1), K(3), K(6), and K(8) ions or distorted antiprisms about the K(9) and K(11) ions. The oxygen atoms of the amide groups form regular trigonal prisms about the K(7) and K(12) ions and twisted prisms about the remaining K(2), K(4), K(5), and K(10) ions. The K··O distances in the coordination polyhedra are given in Table 2. The substantial differences in the K··O distances (2.627–2.819 Å) are attributable to twinning. However, it should be noted that the average bond length between the K^+ ions and the oxygen atoms of the ester groups (2.760 Å) is substantially larger than the average bond length between K^+ and the O atoms of the amide groups (2.680 Å). Apparently, this difference results from the fact that the *N*-methylamide groups and the O atoms of the ester groups are located on the same side of the molecular plane. In the 2 : 1 sandwich complex of enniatin *B* with KI [7], in which the coordination environments about the K^+ ions are formed by the oxygen atoms of the amide groups, the average K··O distance (2.69 Å) is close to that found in this study.

In the crystal, the stacks are composed of K^+ ions intervening between the enniatin molecules and are arranged in a hexagonal fashion (Fig. 3). The K^+ ions and, consequently, the enniatin molecules in the stacks are located at different heights along the *c*-axis. The molecular stack located on the [2/3, 1/3, *z*] axis is shifted along the *c*-axis with respect to the initial stack (located on the threefold axis passing through the origin of coordinates) to the smallest extent (0.567 Å), whereas the corresponding shift of the molecular stack located on the [1/3, 2/3, *z*] axis is 2.029 Å. The hydro-

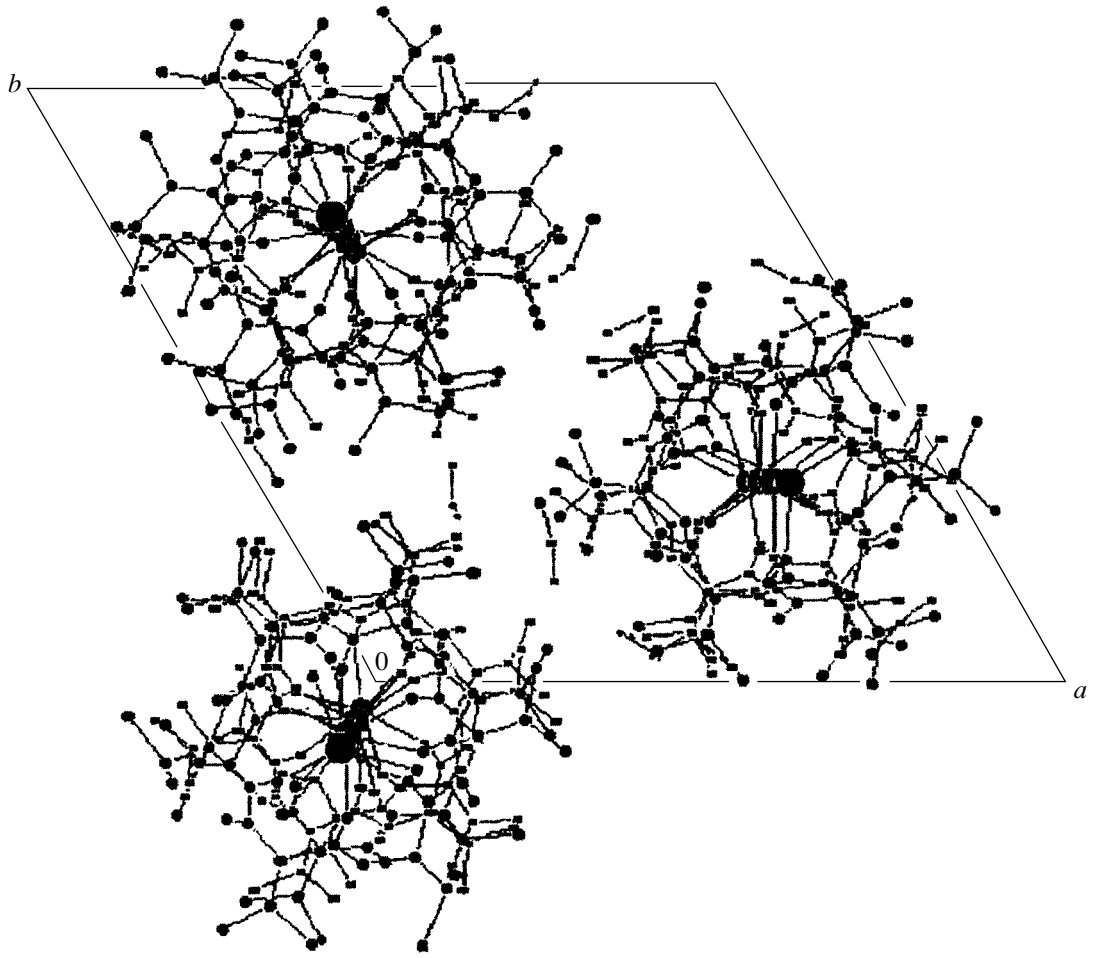

Fig. 3. Crystal structure of the 1 : 1 complex of enniatin *B* with KNCS.

phobic environment of the molecular complex (the molecular stack) is formed by the side radicals and the *N*-methylamide groups of the amino acid residues. The existence of the molecular stacks in this crystal structure is indirect evidence in favor of one of the mechanisms of ion transport through biological membranes, which were proposed earlier in [11], namely, ion transfer through the channel formed by the enniatin molecules packed in stacks. Thus, the carbonyl O atoms of two adjacent enniatin molecules form polyhedra that are occupied by the metal ion as it moves along the channel. Hence, the transport of the cation is accompanied by the formation of intermediate sandwich complexes. It is these two stages of ion transfer through the channel that were revealed in the structure under study (the formation of the coordination polyhedra about the K^+ ions by the oxygen atoms of the ester or amide groups). It has been suggested [11] that the size of the molecular cavity is large enough for the K^+ ion to pass through it. An analogous model in support of the location of the K atom in the cavity of the enniatin molecule was proposed earlier in [13] from an analysis of the Patterson function. The study of the molecular structure of enniatin *B* in the free state [8] demonstrated that the molecular cavity can be occupied by a water molecule that is comparable in size to the K^+ ion.

The rhodanide anions are located between the molecular stacks at two heights along the *c*-axis. The adjacent rhodanide anions are separated by a distance of approximately one-half of the unit cell parameter *c* and are located at nearly the same height as the K^+ ions whose coordination spheres are formed by the carbonyl oxygen atoms of the amino acid residues.

All 12 independent molecules of enniatin *B* in the structure under consideration adopt conformations that are similar to one another and to those observed earlier in the complexes of enniatin *B* with KI [7] and with Na and Ni [5]. All the molecules are characterized both by alternating upward and downward orientations of the carbonyl groups with respect to the main ring and by the pseudoequatorial arrangement of the side radicals of valine and by hydroxyisovaleryl. Although the major conformational features of the independent enniatin molecules are retained, the conformational parameters of the residues differ substantially. The conformational angles of the molecules are given in Table 3. The

N-methylamide and ester groups have *trans* structures. The largest deviations of the ω angle from 180° are observed in the *N*-methylamide group of the seventh molecule (13.0°) and in the ester group of the eleventh molecule (17.2°). Most of the χ angles are close to 60° and 180°, the H atoms at the C(*A*) and C(*B*) atoms being in almost *trans* orientations. The exceptions are molecules 2, 8, and 12, in which the χ angles for the side radicals of the hydroxy acid residues differ substantially from the standard values, and molecule 10, in which the C(*A*)H–C(*B*)H fragment of the amino acid residue adopts the *gauche* configuration (Table 3). These deviations from the standard geometry are due, apparently, to steric hindrances upon the complex formation.

The bond lengths and angles have values typical of depsipeptide rings [4–8]. The rms bond-length and bond-angle deviations range within 0.012–0.020 Å (0.016–0.040 Å for the side radicals) and 0.8°–3.0°, respectively. As was expected, the largest rms deviations are observed for the bond lengths and angles in the side radicals, which is in agreement with the large thermal parameters of the atoms in these groups. The average bond lengths are as follows: N–C', 1.359 Å; N–C(*A*), 1.470 Å; N–C, 1.451 Å; O'–C', 1.332 Å; O'–C(*A*), 1.451 Å; C(*A*)–C', 1.522 Å; C'–O, 1.214 Å; C(*A*)–C(*B*), 1.54 Å; and C(*B*)–C(*G*), 1.52 Å. The bond lengths and angles in the NCS groups vary over a wide range (the S–C and C–N bond lengths range from 1.43 to 1.83 Å and from 0.68 to 1.32 Å, respectively, and the N–C–S bond angles are in the range 145°–170°). This scatter in the bond lengths and angles results is, apparently, attributable to the difficulties associated with the location of the atoms of the rhodanide groups due to the twinning and large thermal parameters of the atoms.

ACKNOWLEDGMENTS

I would like to thank Yu.V. Nekrasov for his help in collecting the X-ray diffraction data.

REFERENCES

1. M. M. Shemyakin, Yu. A. Ovchinnikov, V. T. Ivanov, *et al.*, Biochem. Biophys. Res. Commun. **29**, 834 (1967).
2. Yu. A. Ovchinnikov and V. T. Ivanov, *Conformational States and Biological Activity of Cyclic Peptides. Tetrahedron Report* (Pergamon, Oxford, 1976), p. 1.
3. Yu. A. Ovchinnikov and V. T. Ivanov, *The Proteins* (Academic, New York, 1982, 3rd ed.), p. 307.
4. N. E. Zhukhlistova, G. N. Tishchenko, and K. M. Polyakov, Kristallografiya **27** (2), 288 (1982) [Sov. Phys. Crystallogr. **27**, 176 (1982)].
5. N. E. Zhukhlistova and G. N. Tishchenko, Kristallografiya **26** (6), 1232 (1981) [Sov. Phys. Crystallogr. **26**, 700 (1981)].
6. N. E. Zhukhlistova, G. N. Tishchenko, V. I. Andrianov, and P. Main, Kristallografiya **40** (3), 532 (1995) [Crystallogr. Rep. **40**, 486 (1995)].
7. N. E. Zhukhlistova, G. N. Tishchenko, L. Refaat, and M. M. Vul'fson, Kristallografiya **43** (1), 50 (1998) [Crystallogr. Rep. **43**, 45 (1998)].
8. N. E. Zhukhlistova, G. N. Tishchenko, I. V. Tolstykh, and V. A. Zenkova, Kristallografiya **44** (1), 12 (1999) [Crystallogr. Rep. **44**, 8 (1999)].
9. Yu. A. Ovchinnikov, FEBS Lett. **44**, 1 (1974).
10. J. A. Hamilton, L. K. Steinrauf, and B. Braden, Biochem. Biophys. Res. Commun. **64**, 151 (1975).
11. G. N. Tishchenko and B. K. Vainshtein, in *Crystals: Growth, Structure, and Properties (On the Occasion of the Fiftieth Anniversary of the Institute of Crystallography)* (Inst. Kristallografii, Moscow, 1992), p. 96.
12. G. M. Sheldrick, *SHELX97: Program for the Solution and Refinement of Crystal Structures* (Univ. of Göttingen, Göttingen, 1997).
13. M. Dobler, J. D. Dunitz, and J. Kraewski, J. Mol. Biol. **42**, 603 (1969).

Translated by T. Safonova

Crystallography Reports, Vol. 47, No. 3, 2002, pp. 443–448. Translated from Kristallografiya, Vol. 47, No. 3, 2002, pp. 488–493.

STRUCTURES OF ORGANIC COMPOUNDS

Clathrate Formation of Gossypol: The Structure of the Complex of Gossypol with Tropolone

S. A. Talipov*, B. T. Ibragimov*, Y. Ohashi, J. Harada**, and M. I. Saleh*****

** Institute of Bioorganic Chemistry, Tashkent, Uzbekistan*

e-mail: ckrystal@uzsci.net

*** Department of Chemistry, Tokyo Institute of Technology, O-okayama, Mesuro-ku, Tokyo, 152-8550 Japan*

**** School of Chemical Sciences, Malaysian University of Science, 11800 USM, Penang, Malaysia*

Received January 30, 2001

Abstract—The clathrate of gossypol with tropolone is prepared for the first time and studied by X-ray diffraction. The structure is determined and refined using 7307 reflections (Siemens SMART/CCD diffractometer). The crystals are monoclinic, $C_{30}H_{30}O_8 \cdot 2C_7H_6O_2$, a = 35.5892(1) Å, b = 12.8893(2) Å, c = 18.5910(2) Å, β = 118.54(3)°, Z = 8, space group $C2/c$, and R = 0.058. Each gossypol molecule is linked to two tropolone molecules through hydrogen bonds. The host (gossypol) and guest (tropolone) molecules form separate bilayers that are parallel to the *bc* plane and alternate along the *a*-axis. © *2002 MAIK "Nauka/Interperiodica".*

INTRODUCTION

All the known host–guest complexes of gossypol (more than 100) were prepared by crystallization of gossypol from specific solvents that became guest components [1–5]. For practical needs, it is reasonable to synthesize gossypol complexes with compounds that are solid under standard conditions. For example, preparation of gossypol clathrates with crystalline medicinals offers considerable promise. Usually, in order to prepare such clathrates, one chooses a solvent suitable for both the host and the guest, dissolves the components, and carries out their cocrystallization. However, the desired complex is not necessarily formed in this procedure, because gossypol has a pronounced tendency to form clathrates with molecules of almost all the solvents used. In the case of tropolone (2-hydroxy-2,4,6-cycloheptatrien-1-one), $C_7H_6O_2$, a non-benzenoid aromatic compound [6, 7], which is solid under standard conditions, the cocrystallization of two components [gossypol (**I**) and tropolone (**II**)] from dichloromethane led to the expected result: the host–guest (1 : 2) complex between gossypol and tropolone was obtained.

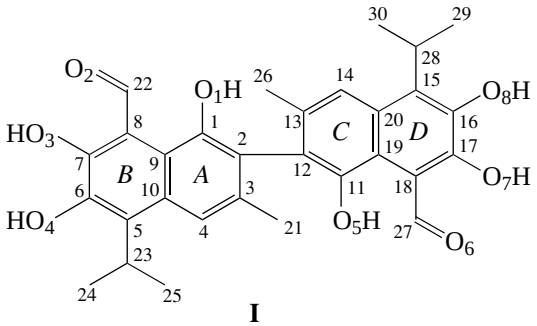

I

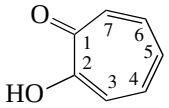

II

EXPERIMENTAL

Dark yellow single crystals of the gossypol : tropolone complex with the melting point in the range 167–168°C were prepared by slow evaporation from a mixture of solutions containing tropolone (25 mg) in dichloromethane (2 ml) and gossypol (50 mg) in dichloromethane (2 ml) for 8 h at 30°C.

The crystallographic parameters of the single crystals were determined and refined using 8192 reflections on a Siemens SMART/CCD diffractometer. The crystals are monoclinic, $C_{30}H_{30}O_8 \cdot 2C_7H_6O_2$, a = 35.5892(1) Å, b = 12.8893(2) Å, c = 18.5910(2) Å, β = 118.54(3)°, M_r = 762.78, V = 7492.09(14) Å^3, Z = 8, ρ_{calcd} = 1.353 g/cm^3, and space group $C2/c$.

1063-7745/02/4703-0443$22.00 © 2002 MAIK "Nauka/Interperiodica"

Table 1. Coordinates ($\times 10^4$) and isotropic thermal parameters ($Å^2 \times 10^3$) of the non-hydrogen atoms in the structure of the 1 : 2 complex of gossypol with tropolone

Atoms	*x*/*a*	*y*/*b*	*z*/*c*	U_{eq}	Atoms	*x*/*a*	*y*/*b*	*z*/*c*	U_{eq}
C(1)	3645(1)	8022(1)	−370(1)	16(1)	O(8)	3564(1)	3398(1)	−3941(1)	29(1)
C(2)	3405(1)	7902(1)	−1213(1)	16(1)	O(1*A*)	4114(1)	9487(2)	−1171(1)	30(1)
C(3)	3117(1)	8691(1)	−1685(1)	19(1)	O(2*A*)	3931(1)	11295(2)	−946(1)	35(1)
C(4)	3085(1)	9574(1)	−1300(1)	19(1)	C(1*A*)	4332(1)	9772(2)	−440(2)	21(1)
C(5)	3268(1)	10656(1)	−72(1)	19(1)	C(2*A*)	4239(1)	10831(2)	−270(2)	24(1)
C(6)	3462(1)	10710(1)	767(1)	20(1)	C(3*A*)	4411(2)	11392(4)	443(3)	27(1)
C(7)	3745(1)	9919(1)	1261(1)	20(1)	C(4*A*)	4736(1)	11098(3)	1213(3)	30(1)
C(8)	3841(1)	9049(1)	933(1)	18(1)	C(5*A*)	4958(1)	10187(2)	1470(2)	32(1)
C(9)	3611(1)	8921(1)	47(1)	16(1)	C(6*A*)	4911(1)	9296(2)	988(2)	28(1)
C(10)	3324(1)	9721(1)	−441(1)	17(1)	C(7*A*)	4643(1)	9118(2)	174(2)	25(1)
C(11)	3629(1)	6937(1)	−2112(1)	16(1)	O(1*B*)	4473(1)	6545(2)	−350(1)	31(1)
C(12)	3428(1)	6924(1)	−1628(1)	17(1)	O(2*B*)	4875(1)	6626(2)	−1151(2)	47(1)
C(13)	3220(1)	6007(1)	−1583(1)	20(1)	C(1*B*)	4482(1)	5678(3)	−669(2)	20(1)
C(14)	3198(1)	5173(1)	−2065(1)	20(1)	C(2*B*)	4722(1)	5690(3)	−1124(2)	27(1)
C(15)	3337(1)	4286(1)	−3097(1)	19(1)	C(3*B*)	4798(1)	4900(3)	−1521(2)	39(1)
C(16)	3571(1)	4258(1)	−3506(1)	21(1)	C(4*B*)	4669(4)	3837(7)	−1644(7)	47(4)
C(17)	3827(1)	5109(2)	−3489(1)	23(1)	C(5*B*)	4408(3)	3430(6)	−1382(6)	37(3)
C(18)	3860(1)	6019(1)	−3049(1)	20(1)	C(6*B*)	4233(1)	3815(3)	−886(2)	35(1)
C(19)	3630(1)	6062(1)	−2581(1)	16(1)	C(7*B*)	4264(1)	4797(2)	−584(2)	28(1)
C(20)	3386(1)	5178(1)	−2587(1)	17(1)	O(1*A*')	4418(2)	8523(5)	−825(4)	29(2)
C(21)	2836(1)	8553(2)	−2595(1)	25(1)	O(2*A*')	4886(2)	8276(6)	722(5)	37(2)
C(22)	4177(1)	8372(1)	1512(1)	22(1)	C(1*A*')	4448(3)	9311(7)	−393(6)	24(2)
C(23)	2977(1)	11536(2)	−597(1)	24(1)	C(2*A*')	4720(4)	9228(7)	490(8)	23(3)
C(24)	3176(1)	12622(2)	−344(1)	30(1)	C(3*A*')	4842(4)	9967(8)	1090(7)	29(2)
C(25)	2540(1)	11452(2)	−633(2)	33(1)	C(4*A*')	4698(8)	10997(12)	1010(12)	56(9)
C(26)	3012(1)	5933(2)	−1041(2)	34(1)	C(5*A*')	4422(7)	11516(17)	309(8)	32(6)
C(27)	4152(1)	6800(2)	−3056(1)	27(1)	C(6*A*')	4185(4)	11136(9)	−484(8)	25(3)
C(28)	3029(1)	3411(2)	−3195(1)	24(1)	C(7*A*')	4196(3)	10198(7)	−800(6)	27(2)
C(29)	2723(1)	3162(2)	−4101(1)	35(1)	O(1*B*')	4203(1)	5599(4)	−364(3)	33(1)
C(30)	3261(1)	2440(2)	−2722(2)	41(1)	O(2*B*')	4023(2)	3753(4)	−765(3)	42(1)
O(1)	3916(1)	7243(1)	97(1)	20(1)	C(1*B*')	4385(2)	5249(6)	−738(4)	20(1)
O(2)	4340(1)	8477(1)	2270(1)	29(1)	C(2*B*')	4299(2)	4174(6)	−982(5)	30(2)
O(3)	3920(1)	10102(1)	2072(1)	29(1)	C(3*B*')	4440(9)	3458(16)	−1344(17)	61(9)
O(4)	3395(1)	11533(1)	1155(1)	27(1)	C(4*B*')	4703(10)	3831(19)	−1652(19)	56(9)
O(5)	3828(1)	7817(1)	−2170(1)	22(1)	C(5*B*')	4940(3)	4692(6)	−1627(5)	38(2)
O(6)	4345(1)	6712(1)	−3465(1)	37(1)	C(6*B*')	4912(2)	5627(5)	−1272(4)	32(2)
O(7)	4034(1)	4972(1)	−3930(1)	35(1)	C(7*B*')	4672(2)	5864(5)	−899(4)	24(2)

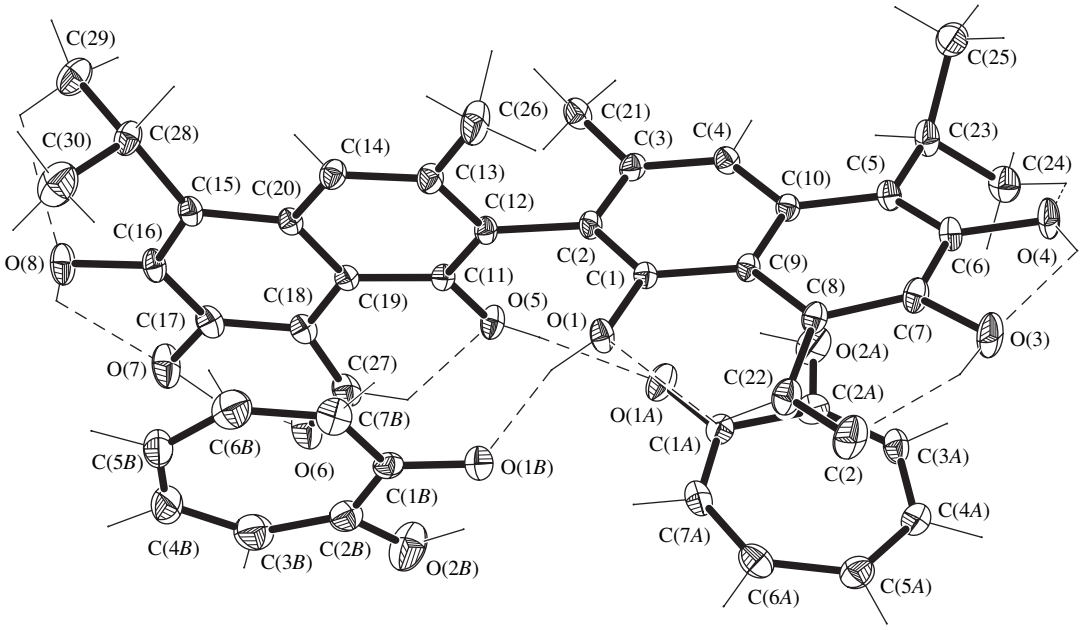

Fig. 1. Structures of the gossypol and tropolone molecules (for clarity, only the dominant orientations of the guest molecules are shown).

An experimental set of 26957 reflections (MoK_α radiation, sharp-focused tube, graphite monochromator) was collected at 100(2) K in a complete reciprocal-space sphere and consisted of three runs with the φ angles equal to 0°, 88°, and 180°. The exposure time was 30 s per frame, and the ω step was 0.3°. The crystal-to-detector distance was 4 cm, and the swing angle of the detector was –35°. For each run, the coverage was ~99%. Crystal decomposition was controlled by measuring 30 frames at the beginning and the end of data collection. For a crystal $0.25 \times 0.25 \times 0.25$ mm in size, the absorption coefficient μ was equal to 0.098 mm^{-1}, $F(000) = 1888$, the θ range was 1.30°–28.39°, and the index ranges were $-47 \le h \le 44$, $-16 \le k \le 17$, and $-16 \le l \le 24$. Correction for absorption was introduced with the SADABS programs [8].

A set of 7307 observed reflections that was used in calculations was obtained after averaging the equivalent reflections (9282 unique reflections, $R_{int} = 0.038$) and disregarding the weak reflections [$I < 2\sigma(I)$]. The structure was solved by the direct method with the SHELXS86 program package [9] and refined by the full-matrix least-squares procedure in the anisotropic approximation using the SHELXL93 program package [10]. The hydrogen atoms of the gossypol molecules were located from the difference Fourier synthesis. Because of the disorder of tropolone molecules, their hydrogen atoms were positioned geometrically. The H atoms of the gossypol molecule and of the hydroxyl groups of the tropolone molecules were refined isotropically, and the remaining hydrogen atoms of tropolone were refined according to the riding model. The final discrepancy factor was $R = 0.058$ ($\Delta\rho_{max} = 1.160$ eÅ^{-3} and $\Delta\rho_{min} = -1.862$ eÅ^{-3}). The coordinates of the nonhydrogen atoms are listed in Table 1. The molecular structure of the complex and the atomic numbering are shown in Fig. 1. The molecular graphics was performed with the XP program in the SHELXTLPLUS software package [11].

RESULTS AND DISCUSSION

Like other crystal modifications of gossypol, the gossypol molecule in the complex studied has an aldehyde tautomeric form [12, 13], which is characterized by a large number of O–H···O and C–H···O intramolecular hydrogen bonds (Table 2) [12]. The C(24)–H···O(4) [C(29)–H···O(8)] hydrogen bond is responsible for the orientation of the isopropyl group with the H(23) [H(28)] hydrogen atom facing the H(4) [H(14)]

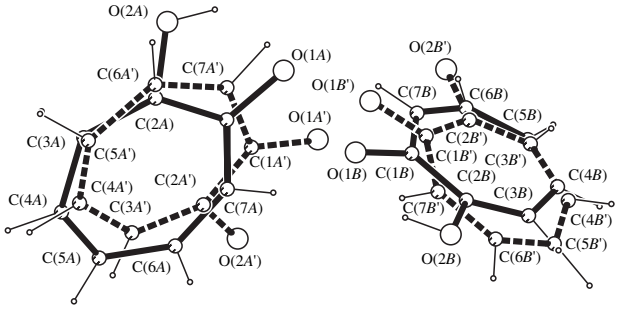

Fig. 2. Mutual orientation of the guest molecules (the dominant orientations of molecules *A* and *B* are shown by solid lines).

Table 2. Hydrogen bonds in the structure of the 1 : 2 complex of gossypol with tropolone

D–*H*···*A* hydrogen bond	Intramolecular bonds			
	D···*A*, Å	*D*–H, Å	H···*A*, Å	*D*–H···*A*, deg
Gossypol				
O(3)–H···O(2)	2.497(2)	0.86(3)	1.69(3)	151(3)
O(4)–H···O(3)	2.600(2)	0.81(3)	2.12(3)	118(3)
C(22)–H···O(1)	2.750(2)	0.98(3)	2.14(2)	118(2)
C(24)–H24A···O(4)	2.875(3)	1.05(4)	2.30(2)	113(2)
O(7)–H···O(6)	2.468(2)	0.91(3)	1.50(3)	158(3)
O(8)–H···O(7)	2.623(3)	0.89(3)	2.08(3)	118(2)
C(27)–H···O(5)	2.753(2)	0.96(3)	2.10(2)	125(2)
C(29)–H29A···O(8)	2.879(3)	1.03(4)	2.33(3)	112(2)
Tropolone*				
O(2*A*)–H···O(1*A*)	2.509(4)	0.82(4)	1.88(4)	133(4)
O(2*B*)–H···O(1*B*)	2.511(4)	0.89(4)	1.89(4)	126(4)

O–H···O hydrogen bond	Intermolecular bonds				
	symmetry code	O···O, Å	O–C, Å	H···O, Å	O–H···O, deg
O(5)–H···O(1*A*)		2.704(2)	0.78(3)	1.96(3)	160(3)
O(5)–H···O(1*A*')		2.544(7)	0.78(3)	1.90(3)	140(3)
O(1)–H···O1*B*		2.646(3)	0.91(3)	1.76(3)	163(3)
O(1)–H···O(1*B*')		2.665(5)	0.91(3)	1.88(3)	143(3)
O(8)–H···O(1)	$x, 1-y, -0.5+z$	2.756(2)	0.89(3)	2.05(3)	135(2)
O(4)–H···O(5)	$x, 2-y, 0.5+z$	2.861(2)	0.81(3)	2.15(3)	147(3)

* The data are given only for the dominant positions of the tropolone molecules.

atom. The O(4)–H···O(3) [O(8)–H···O(7)] and O(3)–H···O(2) [O(7)–H···O(6)] hydrogen bonds close the five-membered and six-membered rings, respectively (Fig. 1). The C(1)–C(10) and C(11)–C(20) naphthyl nuclei are planar, and the dihedral angle between their rms planes is 80.59(7)°.

In the crystal, each tropolone molecule is disordered over two positions. The site occupancies of the dominant positions are 0.79 and 0.67 for molecules *A* and *B*, respectively (Fig. 2). In both tropolone molecules, the O(1*A*) [O(1*B*)] carbonyl atoms are involved in hydrogen bonds with the gossypol molecules [O(1)–H··· O(1*A*) and O(5)–H···O(1*B*), Table 2] and the hydroxyl groups participate in intramolecular hydrogen bonds. The rms planes of the naphthyl nuclei and the tropolone molecules are almost parallel (the angle between the C(1)–C(10) nucleus and molecule *A* is 9.4°, and the angle between the C(11)–C(20) nucleus and molecule *B* is 8.5°). Analysis of the arrangement of the disordered guest molecules reveals that the symmetry of the gossypol : tropolone associate is disturbed because of the different arrangement of the dominant orientations with respect to the corresponding naphthyl nucleus. For example, the hydroxyl group in molecule *B* is directed toward the neighboring aldehyde group of the gossypol molecule, whereas the hydroxyl group in molecule *A* is antiparallel to the aldehyde group of the other half of the gossypol molecule (Fig. 1). This associate would be symmetric either for a combination of the preferred orientation of molecule *A* and the minor orientation of molecule *B* or for the reverse combination. Thus, an individual supramolecular associate is asymmetric and this asymetry is more energetically favorable, since the tropolone molecules in this associate are held not only by the hydrogen bonds but also by the dipole–dipole interactions. This conclusion is supported by the following short interatomic contacts between the naphthyl nuclei and the corresponding tropolone molecules: C(1*A*)···C(9), 3.29 Å; C(6*A*)···C(22), 3.41 Å; C(2*A*)···C(10), 3.43 Å; C(1*B*)···C(11), 3.36 Å; and O(2*B*)···C(27), 3.24 Å.

In the crystal, the gossypol molecules are linked by the O(8)–H···O(1) and O(4)–H···O(5) hydrogen bonds (Table 2). Both hydroxyl groups [O(1)–H and O(5)–H] act as proton acceptors, which is uncommon for gossypol crystals [4, 5]. Each gossypol molecule is linked to

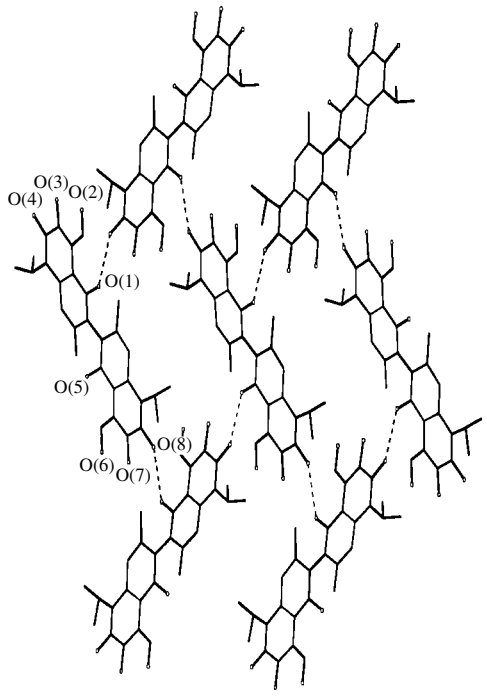

Fig. 3. A monolayer consisting of the gossypol molecules.

four molecules (Fig. 3) that are related to the reference molecule by the glide-reflection planes. This results in the formation of an infinite monolayer that is aligned parallel to the *bc* plane and has inequivalent surfaces. The surface of the monolayer that faces the guest molecules is more hydrophilic, and, on this side of the layer, the gossypol molecules are bonded to the guest molecules. The guest molecules are linked by weak dipole–dipole interactions (the interplanar spacing is ~3.50 Å) into specific bilayers that lie between the gossypol monolayers (Fig. 4). The other surface is more hydrophobic and is in contact with a similar surface of the neighboring inversion-related layer. The contacts between the layers are characterized by the C(29)···C(29) (3.40 Å) and C(25)···C(25) (3.68 Å) van der Waals interactions. The interactions between the monolayers of the gossypol molecules result in the formation of an infinite bilayer.

Thus, in the crystal structure, the host (gossypol) and guest (tropolone) molecules form separate bilayers that are aligned parallel to the *bc* plane and alternate along the *a*-axis. Note that this mode of association of the host molecules with one another and with the guest molecules is observed for the first time.

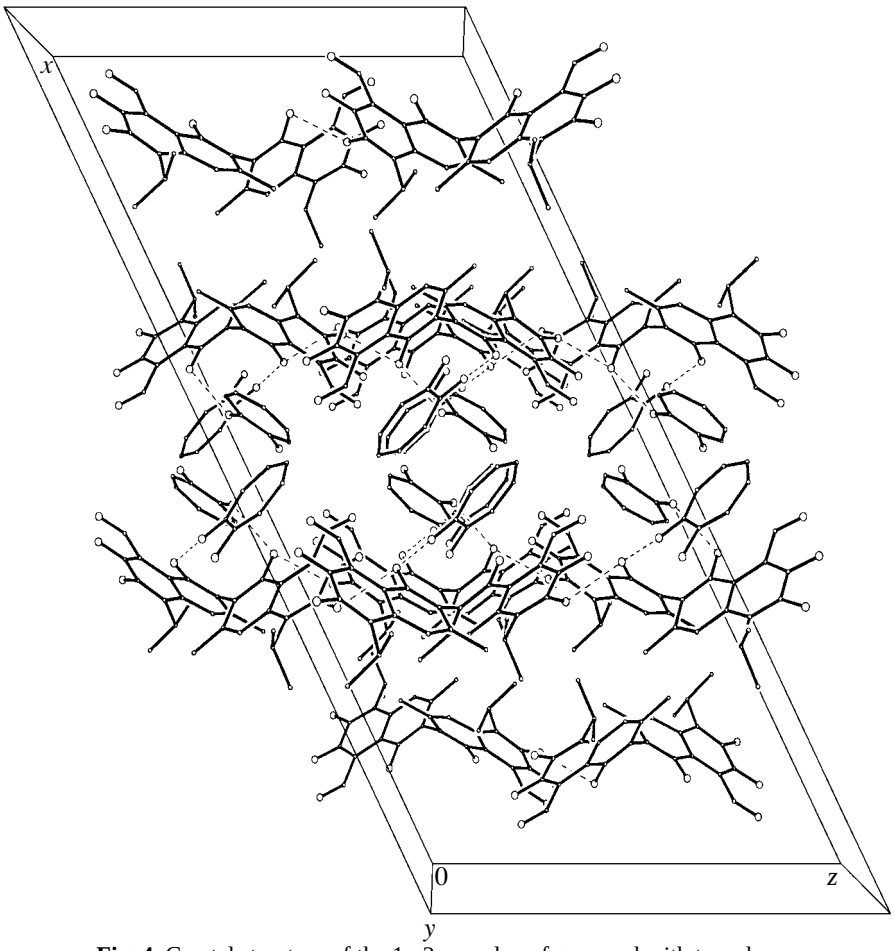

Fig. 4. Crystal structure of the 1 : 2 complex of gossypol with tropolone.

ACKNOWLEDGMENTS

S.A. Talipov and B.T. Ibragimov acknowledge the support of the Foundation for Basic Research of the State Committee for Science and Technology, contract no. 4/99. We also acknowledge the support of the Russian Foundation for Basic Research in the payment of the license for using the Cambridge Structural Database, project no. 99-07-90133.

REFERENCES

1. A. L. Markman and V. P. Rzhekhin, *Gossypol and Its Derivatives* (Pishchevaya Promyshlennost', Moscow, 1965).
2. B. T. Ibragimov, S. A. Talipov, and P. M. Zorky, Supramol. Chem. **3**, 147 (1994).
3. B. T. Ibragimov and S. A. Talipov, Mol. Cryst. Liq. Cryst. **276**, 305 (1996).
4. M. Gdaniec, B. T. Ibragimov, and S. A. Talipov, in *Comprehensive Supramolecular Chemistry*, Vol. 6: *Solid State Supramolecular Chemistry: Crystal Engineering*, Ed. by D. D. MacNicol, F. Toda, and R. Bishop (Pergamon, New York, 1996), p. 117.
5. B. T. Ibragimov and S. A. Talipov, Zh. Strukt. Khim. **40**, 849 (1999).
6. J. Dewar, Nature (London) **155**, 50 (1945).
7. H. Shumanouchi and Y. Sasada, Acta Crystallogr. Sect. B: Struct. Crystallogr. Cryst. Chem. **29**, 81 (1973).
8. G. M. Sheldrick, *SADABS: Program for the Empirical Absorption Correction of Area Detector Data* (Univ. of Göttingen, Göttingen, 1996).
9. G. M. Sheldrick, Acta Crystallogr., Sect. A: Found. Crystallogr. **46**, 467 (1990).
10. G. M. Sheldrick, *SHELXL93: Program for the Refinement of Crystal Structures* (Univ. of Göttingen, Göttingen, 1993).
11. *Siemens XP: Molecular Graphics Program. Version 5.03* (Siemens Analytical X-ray Instruments Ins., Madison, Wisconsin, 1994).
12. B. T. Ibragimov, Z. G. Tiljakov, K. M. Beketov, and S. A. Talipov, J. Inclusion Phenom. Mol. Recognit. Chem. **27**, 99 (1997).
13. F. G. Kamaev, N. I. Baram, A. I. Ismailov, *et al.*, Izv. Akad. Nauk SSSR, Ser. Khim., 1003 (1989).

Translated by I. Polyakova

Crystallography Reports, Vol. 47, No. 3, 2002, pp. 449–451. From Kristallografiya, Vol. 47, No. 3, 2002, pp. 494–496.

STRUCTURES OF ORGANIC COMPOUNDS

Crystal Structure Analysis of 4-Phenylquinolin-2-(1*H*)-one*

Rajnikant[a], V. K. Gupta[a], M. B. Deshmukh[b], B. Varghese[c], and Dinesh[a]**

[a] *X-ray Crystallography Laboratory, Post-Graduate Department of Physics, University of Jammu, Jammu Tawi, 180006 India*

[b] *Department of Chemistry, Shivaji University, Kolhapur, 416004 Maharashtra, India*

[c] *Regional Sophisticated Instrumentation Center, Indian Institute of Technology, Chennai, 600036 India*

e-mail: rajni_kant_verma@hotmail.com

Received January 15, 2001; in final form, March 12, 2001

Abstract—The crystal structure of 4-phenylquinolin-2-(1*H*)-one ($C_{15}H_{11}NO$) is determined by X-ray diffraction. The compound crystallizes in the orthorhombic crystal system (space group *Pbca*) with the unit cell parameters $a = 7.382(2)$ Å, $b = 21.795(3)$ Å, $c = 14.066(5)$ Å, and $Z = 8$. The structure is solved by direct methods and refined to an *R*-value of 0.0398 for 1360 observed reflections [$F_0 > 4\sigma(F_0)$]. The quinoline moiety and the substituted phenyl ring are nearly planar. The dihedral angle between these two moieties is 64.65(6)°. The crystal structure is stabilized by two intermolecular N–H···O and C–H···O interactions.© *2002 MAIK "Nauka/Interperiodica".*

INTRODUCTION

Alkaloids containing a quinoline moiety are of considerable interest due to their biological properties [1–3]. Quinoline derivatives possess high antibacterial, antiarrhythmic, and antihypertensive activities [4, 5].

EXPERIMENTAL

4-Phenylquinolin-2-(1*H*)-one was synthesized by adding a mixture of aniline (0.1 mol) and ethyl benzoyl acetate (0.1 mol) in dioxane (50 ml) in a round bottomed flask, heated with reflux condenser for three or four hours on an oil bath, cooled, and neutralized with sodium carbonate. The separated oil was extracted in chloroform. Removal of the solvent under vacuum gave heavy oil, which was distilled under reduced pressure. A mixture of benzoylacetanilide (0.1 mol) and concentrated sulfuric acid (20 ml) was heated on an oil bath with stirring at 70–80°C for 30 min and at 100°C for 1 h, then cooled, and poured in ice water (500 ml) with continuous stirring. The resultant solid was filtered off and recrystallized from ethanol. The reaction mechanism is shown in Fig. 1 [6].

Three-dimensional intensity data for pale yellow needle-shaped crystals of 4-phenylquinolin-2-(1*H*)-one (the melting point is 553 K) were collected on an Enraf–Nonius CAD4 diffractometer (MoK_α radiation, $\lambda = 0.71073$ Å, $\omega/2\theta$ scan mode). The unit cell parameters were obtained from a least-squares fit of the setting angle of 25 reflections in the range of $7.96° < \theta < 13.21°$. A total of 1987 reflections were found to be unique ($-8 \le h \le 0$, $0 \le k \le 25$, $0 \le l \le 16$), and 1360 reflections were observed [$F_0 > 4\sigma(F_0)$]. Two standard reflections ($\bar{2}60$ and $\bar{1}110$) measured every 100 reflections showed no significant variation in the intensity data. The reflection data were corrected for Lorentz and polarization effects. Absorption and extinction corrections were not applied.

The structure has been solved by using the SHELXS97 program [7]. All the non-hydrogen atoms of the molecule were located from the *E*-map. The full-

* This article was submitted by the authors in English.

** Author for correspondence.

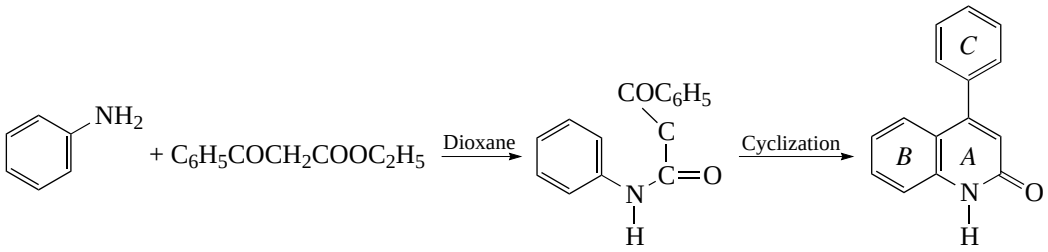

Fig. 1. Scheme of the chemical reaction.

1063-7745/02/4703-0449$22.00 © 2002 MAIK "Nauka/Interperiodica"

Table 1. Crystal data and structure refinement details

Crystal habit	Pale yellow needles
Empirical formula	$C_{15}H_{11}NO$
Molecular weight	221.25
Temperature	293(2) K
Wavelength	0.71073
Crystal system, space group	Orthorhombic, *Pbca*
Unit cell parameters:	a = 7.382(2) Å, b = 21.795(3) Å, c = 14.066(5) Å, $\alpha = \beta = \gamma = 90°$
Volume	2263.1(11) Å^3
Z, density (calcd)	8, 1.299 g/cm^3
Absorption coefficient	0.082 mm^{-1}
F(000)	928
Crystal size	0.45 × 0.14 × 0.04 mm
θ range for data collection	2.36°–24.98°
Index ranges	$-8 \le h \le 0$, $0 \le k \le 25$, $0 \le l \le 16$
Reflections collected/unique	1987/1987
Maximum and minimum transmission	0.99 and 0.95
Refinement method	Full-matrix least-squares on F^2
Data/restraints/parameters	1987/0/155
Goodness-of-fit on F^2	1.106
Final R factors [$F_0 > 2\sigma(F_0)$]	R_1 = 0.0398, wR_2 = 0.0830
R factors (all data)	R_1 = 0.0744, wR_2 = 0.1073
Residual (maximum and minimum) electron densities	0.162 and –0.133 e Å^{-3}

Table 2. Atomic coordinates and equivalent isotropic thermal parameters (Å^2) for non-hydrogen atoms (e.s.d.'s are given in parentheses)

Atom	x	y	z	U^*_{eq}
N(1)	0.2087(2)	0.4601(1)	0.0169(1)	0.044(1)
O(1)	–0.0035(2)	0.4426(1)	–0.0961(1)	0.059(1)
C(2)	0.1446(3)	0.4281(1)	–0.0588(2)	0.045(1)
C(3)	0.2570(3)	0.3786(1)	–0.0919(2)	0.046(1)
C(4)	0.4189(3)	0.3648(1)	–0.0515(2)	0.041(1)
C(5)	0.6441(3)	0.3890(1)	0.0779(2)	0.050(1)
C(6)	0.6941(3)	0.4245(1)	0.1540(2)	0.057(1)
C(7)	0.5847(3)	0.4729(1)	0.1833(2)	0.054(1)
C(8)	0.4256(3)	0.4852(1)	0.1371(1)	0.044(1)
C(9)	0.3720(3)	0.4486(1)	0.0612(1)	0.038(1)
C(10)	0.4811(3)	0.4003(1)	0.0292(1)	0.039(1)
C(11)	0.5317(3)	0.3136(1)	–0.0897(1)	0.041(1)
C(12)	0.4692(3)	0.2539(1)	–0.0868(2)	0.053(1)
C(13)	0.5720(3)	0.2065(1)	–0.1235(2)	0.061(1)
C(14)	0.7370(3)	0.2183(1)	–0.1647(2)	0.058(1)
C(15)	0.8008(3)	0.2775(1)	–0.1679(2)	0.058(1)
C(16)	0.6998(3)	0.3249(1)	–0.1303(2)	0.051(1)

* $U_{eq} = (1/3)\sum_i \sum_j U_{ij} a^*_i a^*_j (a_i, a_j)$.

Table 3. Bond lengths (Å) and bond angles (deg) for non-hydrogen atoms of the quinoline moiety (e.s.d.'s are given in parentheses)

N(1)–C(2)	1.358(3)	C(7)–C(8)	1.369(3)
N(1)–C(9)	1.380(3)	C(8)–C(9)	1.390(3)
O(1)–C(2)	1.253(3)	C(9)–C(10)	1.400(3)
C(2)–C(3)	1.438(3)	C(5)–C(6)	1.371(4)
C(3)–C(4)	1.357(3)	C(5)–C(10)	1.406(3)
C(4)–C(10)	1.448(3)	C(6)–C(7)	1.391(3)
C(4)–C(11)	1.492(3)		
C(2)–N(1)–C(9)	124.4(2)	C(8)–C(9)–C(10)	121.0(2)
N(1)–C(2)–O(1)	120.2(2)	N(1)–C(9)–C(10)	119.6(2)
O(1)–C(2)–C(3)	123.8(2)	C(5)–C(10)–C(9)	117.9(2)
N(1)–C(2)–C(3)	116.0(2)	C(4)–C(10)–C(9)	118.1(2)
C(2)–C(3)–C(4)	122.6(2)	C(4)–C(10)–C(5)	124.0(2)
C(3)–C(4)–C(11)	120.4(2)	C(4)–C(11)–C(16)	120.9(2)
C(3)–C(4)–C(10)	119.3(2)	C(4)–C(11)–C(12)	120.5(2)
C(10)–C(4)–C(11)	120.3(2)	N(1)–C(9)–C(8)	119.4(1)
C(6)–C(5)–C(10)	120.8(2)	C(5)–C(6)–C(7)	120.2(2)
C(6)–C(7)–C(8)	120.4(2)	C(7)–C(8)–C(9)	119.8(2)

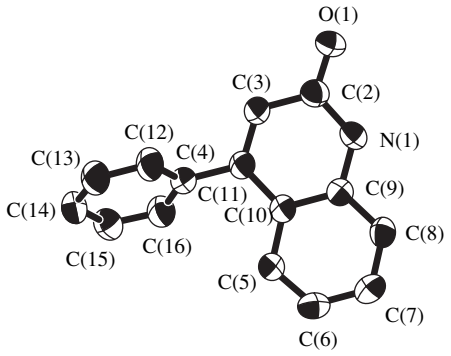

Fig. 2. A general view of the molecule with the atomic numbering.

matrix least-squares refinement of the structure has been carried out using the SHELXL97 program [8]. The positional and thermal parameters of the non-hydrogen atoms were refined isotropically. Out of 11 hydrogen atoms, the hydrogen atom attached to the nitrogen atom was located from the difference Fourier map. Its positional and isotropic temperature factors were refined and the remaining hydrogen atoms were fixed stereochemically. Few cycles of the refinement with anisotropic thermal parameters for the non-hydrogen atoms resulted into the final *R*-factor of 0.0398 with $wR(F^2) = 0.0830$. The maximum and minimum residual electron densities were equal to 0.16 and –0.13 $eÅ^{-3}$, respectively. The atomic scattering factors were taken from the *International Tables for Crystallography* (1992, Vol. C: Tables 4.2.6.8 and 6.1.1.4). The crystallographic data are listed in Table 1.

RESULTS AND DISCUSSION

The final atomic coordinates and equivalent isotropic displacement parameters for all the non-hydrogen atoms are listed in Table 2. The bond lengths and bond angles of the quinoline moiety are presented in Table 3. The chemical reaction is illustrated in Fig. 1. The general view of the molecule with the atomic numbering (thermal ellipsoid is drawn at a 50% probability) is shown in Fig. 2 [9]. The geometric calculations were performed using the PARST program [10].

The bond lengths agree well with the values reported in the literature for some analogous structures containing quinoline moieties [11–15]. The mean bond lengths C(sp^2)–N 1.369(3) Å are quite close to their theoretical values [16]. Both rings (*A* and *B*) of the quinoline moiety adopt almost planar conformations with average torsion angles of 1.2(3)° and 1.0(3)°, respectively. The phenyl ring (*C*) also exists in a planar conformation with an average torsion angle of 0.6(4)° and shows a dihedral angle of 64.65(6)° with the quinoline moiety. The O(1) atom of the ketone group deviates from the *A* plane by 0.026(1) Å. The crystal structure is stabilized by two intermolecular interactions [N(1)···O(1), 2.834 Å; H(1)···O(1), 1.98 Å; N(1)–H(1)···O(1), 176°; and symmetry code: $x, -y + 1, -z$ and C(16)···O(1), 3.407 Å; H(16)···O(1), 2.57 Å; C(16)–H(16)···O(1), 150°; and symmetry code: $x + 1, y, z$].

ACKNOWLEDGMENTS

Dinesh acknowledges the support of the University of Jammu, Government of India, for research funding under the University Scholarship Program.

REFERENCES

1. D. Zacharias and J. P. Glusker, Acta Crystallogr., Sect. C: Cryst. Struct. Commun. **44**, 1656 (1988).
2. D. H. Hua, Y. Chen, H.-S. Sin, *et al.*, J. Org. Chem. **62**, 6888 (1997).
3. S. W. Newell, E. M. Perchellet, J. B. Ladesich, *et al.*, Int. J. Oncol. **12**, 433 (1998).
4. G. Jones, *Chemistry of Heterocyclic Compounds: I. Quinolines*, Ed. by G. Jones (Wiley, Chichester, 1977), Vol. 32, p. 93.
5. F. S. Yates, *Comprehensive Heterocyclic Chemistry*, Ed. by A. R. Katrizky and C. W. Rees (Pergamon, New York, 1984), Vol. 2, p. 511.
6. M. B. Deshmukh, private communication (Shivaji Univ., Kohapur, India, 1999).
7. G. M. Sheldrick, *SHELXS97: Program for the Solution of Crystal Structures* (Univ. of Göttingen, Göttingen, 1997).
8. G. M. Sheldrick, *SHELXL97: Program for the Refinement of Crystal Structures* (Univ. of Göttingen, Göttingen, 1997).
9. M. N. Burnett and C. K. Johnson, *ORTEP-III: Report ORNL-5138* (Oak Ridge National Laboratory, Tennessee, 1996).
10. M. Nardelli, Comput. Chem. **7**, 95 (1983).
11. G. Giorgi, A. Cappelli, M. Anzini, and S. Vomero, Acta Crystallogr., Sect. C: Cryst. Struct. Commun. **54**, 1127 (1998).
12. Y. K. Yan, N. K. Goh, and L. E. Khod, Acta Crystallogr., Sect. C: Cryst. Struct. Commun. **54**, 1322 (1998).
13. B. J. Prince and M. M. Turnbull, Acta Crystallogr., Sect. C: Cryst. Struct. Commun. **54**, 1178 (1998).
14. D. H. Hua, Y. Chen, H.-S. Sin, *et al.*, Acta Crystallogr., Sect. C: Cryst. Struct. Commun. **55**, 1698 (1999).
15. J. Lokaj, V. Kettmann, V. Machacer, and A. Halama, Acta Crystallogr., Sect. C: Cryst. Struct. Commun. **55**, 1101 (1999).
16. L. E. Sutton, *Tables of Interatomic Distances and Configuration in Molecules and Ions* (The Chemical Society, London, 1965), Chemical Society (Great Britain), Spec. Publ., No. 18.

Crystallography Reports, Vol. 47, No. 3, 2002, pp. 452–466. Translated from Kristallografiya, Vol. 47, No. 3, 2002, pp. 497–513.

REVIEW.
CRYSTAL CHEMISTRY

Systematics of Minerals in the Class of Nonmetals

G. B. Bokij†

Institute of Geology of Ore Deposits, Petrography, Mineralogy, and Geochemistry, Russian Academy of Sciences, Staromonetnyĭ per. 35, Moscow, 109017 Russia

e-mail: furm@rsa.crystal.msk.su

Received January 18, 2001

Abstract—At present, the systematics of minerals is still far from satisfactory. There are no two monographs or reference books on mineralogy based on the same systematics. Only the Berzelius concept formulated at the beginning of the 19th century, according to which the minerals are recognized to be natural chemical compounds, is the commonly accepted statement. All authors use only one additional section with a taxon for minerals consisting of metals only, whereas none of these authors uses a special section with minerals consisting of nonmetal chemical elements only. The present article is dedicated to just these minerals. © *2002 MAIK "Nauka/Interperiodica".*

LIST OF CONTENTS

1. INTRODUCTION

We consider a class of minerals whose chemical composition has no metals and consists only of nonmetal elements. Earlier, we developed the systematics of minerals in the silicate and oxide classes [1, 2]. We also considered some general problems of mineral classification and suggested using the decimal symbols for their description. This classification was based on the Periodic System of chemical elements. The same principles and symbols are also used in this study. The development of an essentially new science—crystal chemistry—in the 20th century led to the creation of a rather rigorous classification of chemical compounds, including minerals, using the taxa lower than the taxon *class.*[1]

At the beginning of the 19th century (mainly in the period 1814–1824), J. Berzelius extended his concept of the electrochemical nature of compounds to minerals [3, 4]. He divided all the chemical elements into two groups—electronegative nonmetals and electropositive metals—and assumed that every chemical compound (including minerals) consists of two parts—positive and negative. He also suggested classifying minerals

† Deceased.

[1] Hereafter, the taxa of the suggested classification are printed in italic.

according to their chemical composition instead of their physical properties (specific weight, color, hardness, etc.) and combining them into groups according to the electronegative elements (O, S, …) or complex anions (OH, SO_4, etc.).

Berzelius' works were reviewed in detail by Solov'ev and Korennoĭ [5], who also referred the reader to the Russian translations of Berzelius' articles regularly published in *Gornyĭ Zhurnal* in the period from 1828 to 1832.

In Berzelius' time, only about 300 minerals (now their number is about 4000) and about 60 chemical elements were known, of which Si, Th, Ce, and Se were discovered by Berzelius himself. Berzelius and his followers continued combining the minerals possessing the same anions in groups, because it was noticed that minerals having the same anion and several different cations have more similar properties than the minerals with the same cation and different anions. This resulted in the use of taxa that are intermediate between the *kingdom of minerals* and *mineral species*, in particular, mineral *classes*. However, the level of chemistry in that time was insufficient for creating rigorous a classification of minerals and, moreover, for enumerating minerals within individual groups. Even the Periodic System had not been discovered as yet (Mendeleev, 1869).

In this article, the terms "mineral" and "mineral species" and also the terms "systematics" and "classification" are used as synonyms. Only crystalline substances are considered as objects of mineralogical classification. Other objects, such as amorphous, metamict, liquid (with the exception of mercury), and gaseous states of natural substances, which should have been considered as the objects of mineralogy [6], are not considered in this article. Earlier, in order to avoid the confusion in the mineral systematics, I suggested calling these substances "mineraloids."

2. MODERN STATE OF MINERAL CLASSIFICATION

One can judge the modern state of mineralogical classification by comparing the first two taxa for the kingdom of minerals suggested by various authors (Table 1).

Inconsistency in the division and the taxa used in modern mineralogical classifications suggested by different authors is really amazing. In each new monograph or reference work, a new classification negating the previous one is suggested without any explanations.

How many years is the modern mineralogical classification behind the biological one?

Since the last Berzelius publication (1824), no breakthrough has been made in mineral systematics, so that mineralogical classification is behind the biological one by about 175 years. The principles of mineral systematics considered in this article were stated in detail in my earlier publication [1]. The names of the minerals are given in accordance with handbook [7].

3. DEFINITION OF NOTIONS "METALS" AND "NONMETALS" FOR CHEMICAL ELEMENTS

Upon the discovery of the Periodic Law by Mendeleev in 1869, it became possible to consider the notions "metal" and "nonmetal" at a higher level. It is well known that among the chemical elements there are typical metals (Cu, Au, Fe) and typical nonmetals (O, S, halogens), but the boundary between them and properties determined by them are still an open question.

Thus, the latest edition of the Chemical Encyclopedia [8] has no entry "nonmetals" at all. The notion "metals" is defined, first and foremost, by a number of specific properties of the corresponding elemental substances, e.g., by high electrical conductivity and thermal capacity, the ability to reflect light waves (luster), plasticity, and ductility. At present, one of the most important characteristics of metals is considered to be the negative thermal coefficient of electric conductivity [8]. Of course, all these properties are not the properties of the chemical elements themselves but of the elemental substances which, while in the crystalline state, can be minerals.

At the same time, it was indicated [8] that an element can be attributed either to metals or nonmetals only upon the consideration of the physical properties of the corresponding elemental substance and the chemical properties of the element. In this connection, we should like to indicate that the metals from the neighboring groups of the Periodic Table can have the same valence in compounds and can crystallize as elemental substances within the same structure type. Unlike metals, nonmetals from the neighboring groups always show different valences in the compounds and the structures of the corresponding elemental substances.

All the elemental substances in the crystalline state have atomic structures, which, to a large extent, determine their physical properties. Therefore, when defining the notion of a metal, one has also to take into account the crystal structure. As a rule, the structures of metals under normal conditions are characterized by rather high symmetries and high coordination numbers (c.n.) of atoms equal to or higher than eight, whereas the structures of crystalline nonmetals under normal conditions are characterized by lower symmetries and coordination numbers of atoms (2–4) and usually obey the Hume–Rothery rule, c.n. = $8 - N$, where N is the number of the group of the element in the Periodic Table [however, for boron (from group 3), it equals either 6 or 4 instead of 5].

It was indicated [8] that the boundary between metals and nonmetals in the Periodic Table established on the basis of the physical properties of elemental substances lies along the diagonal from B to At (dashed line in Table 2). It is also indicated [8] that Ge is usually considered as a nonmetal and Sb as a semimetal. The *z*-

Table 1. The first two divisions (taxa) in the classification of minerals suggested by different authors

Author (year)	First division	Second division
A.A. Godovikov (1979)	2 kingdoms	6 types
A.S. Povarennykh (1966)	4 types	23 classes
A.G. Bulakh *et al*. (1955)	4 types	20 classes
A.A. Godovikov (1975)	5 types	16 classes
A.G. Betekhtin (1950)	6 divisions	18 classes
A.A. Godovikov (1997)	7 types and quasi-types	21 subtypes and quasi-subtypes
E.S. Dana (1937)	8 without names	24 without name
A.G. Bulakh (1999)	9 types	30 classes
H. Schtrunz (1978)	9 classes	39 orders
E.I. Semenov (1991)	9 classes	57 subclasses
A.N. Winchell and H. Winchell (1953)	10 without names	19 without name
H. Schtrunz and E. Nikel (1997)	10 classes	–
I. Kostov (1971)	12 classes	23 *A*, *B*, *C* …
K. Herblatt and K. Klein (1982)	13 without names	24 without names
I. Kostov (1993)	13 classes	37 without names
E.I. Semenov (1981)	18 classes	118 subclasses
New mineralogy by Dana (1997)	22 without names	78 classes
A.M. Clark (1993)	32 without names	–
G.B. Bokij (1997)	7 subkingdoms	21 types

boundary established in our study [1] (solid line in Table 2) divides the elemental substances into metals (whose structures under normal conditions are characterized by the coordination number eight and higher) and nonmetals with coordination numbers six or less. In our case, both Ge and Sb are consistent with this boundary. The above form of the Periodic Table is most convenient for fixing the *z*-boundary. As is well known, the forms of the Periodic Table are very diverse. Thus, Trifonov, who considered this problem, indicates that the number of variants of the Periodic Table exceeds 300 [9].

The *z*-boundary in the Periodic Table established from the analysis of the atomic structures of the elemental substances is confirmed by the analysis of the electronegativities of chemical elements, the notion closer to the notion of a chemical element than to the notion of an elemental substance.

The term *electronegativity* was suggested in 1932 by Pauling [10], who studied problems of chemical bonding. The electronegativity of an atom is determined by the energy of attraction of a valence electron to the nucleus. Pauling's book *The Nature of the Chemical Bond and the Structure of Molecules and Crystals* [11] reflects numerous aspects of the problem.

There are numerous methods for determining electronegativity of atoms, but the results obtained by these methods are often inconsistent. Table 3 indicates the electronegativities of chemical elements below their symbol according to [12] or [13]. The first study [12] yields the data for various valence states of some elements and shows that electronegativity increases with an increase in the element valence. In [12], several electronegativity values are indicated for some complex ions. The data listed in [13] seem to be given for neutral elements. In [13], hydrogen is located in subgroup I*A* and its electronegativity equals 2.1. Therefore, in Table 3, it is in the same place, whereas the first upper position corresponding to subgroup VII*B* is occupied by OH^- with the electronegativity value 4.3 (according to [12]). The existence of the *z*-boundary is confirmed by the fact that on the right of this boundary, nonmetals show a tendency to decrease in electronegativity down the subgroup, whereas on the left, metals show a tendency to increase in electronegativity.

The main and additional *classes* of the mineral species are defined in accordance with the established *z*-boundary between the metals and nonmetals in the Periodic Table.

4. TAXON *CLASS*

The taxon *class* is very important for mineral species, because, in most of the cases, concrete minerals can be related to classes based on the data of the chemical analysis, whereas their relation to lower taxa requires knowledge of their atomic structures.

Table 2. Periodic system of chemical elements

	I*A*	II*A*	III*A*	IV*A*	V*A*	VI*A*	VII*A*		VIII*A*		I*B*	II*B*	III*B*	IV*B*	V*B*	VI*B*	VII*B*	VIII*B*
1																	H	He
2	Li	Be											B	C	N	O	F	Ne
3	Na	Mg											Al	Si	P	S	Cl	Ar
4	K	Ca	Sc	Ti	V	Cr	Mn	Fe	Co	Ni	Cu	Zn	Ga	Ge	As	Se	Br	Kr
5	Rb	Sr	Y	Zr	Nb	Mo	Tc	Ru	Rh	Pd	Ag	Cd	In	Sn	Sb	Te	I	Xe
6	Cs	Ba	La	Hf	Ta	W	Re	Os	Ir	Pt	Au	Hg	Tl	Pb	Bi	Po	At	Rn
7	Fr	Ra	Ac	Ku	Ns													
				Ce	Pr	Nd	Pm	Sm	Eu	Gd	Tb	Dy	Ho	Er	Tm	Yb	Lu	
				Th	Pa	U	Np	Pu	Am	Cm	Bk	Cf	Es	Fm	Md	No	Lr	

Table 3. Electronegativity—the ability of atoms to attach electrons

H																	OH
2.1																	4.3
Li	Be											B	C	N	O	F	
1.0	1.5											2.0	2.5	3.0	3.5	4.0	
Na	Mg											Al	Si	P	S	Cl	
0.9	1.2											1.5	1.8	2.1	2.5	3.0	
K	Ca	Sc	Ti	V	Cr	Mn	Fe	Co	Ni	Cu	Zn	Ga	Ge	As	Se	Br	
0.8	1.0	1.3	1.5	1.6	1.6	1.5	1.8	1.8	1.8	1.9	1.6	1.6	1.8	2.0	2.4	2.8	
Rb	Sr	Y	Zr	Nb	Mo	Tc	Ru	Rh	Pd	Ag	Cd	In	Sn	Sb	Te	I	
0.8	1.0	1.2	1.4	1.6	1.8	1.9	2.2	2.2	2.2	1.9	1.7	1.7	1.8	1.9	2.1	2.5	
Cs	Ba	La	Hf	Ta	W	Re	Os	Ir	Pt	Au	Hg	Tl	Pb	Bi	Po	At	
0.7	0.9	1.1	1.3	1.5	1.7	1.9	2.2	2.2	2.2	2.4	1.9	1.8	1.8	1.9	2.0	2.2	
Fr	Ra	Ac	Th	Pa	U												
0.7	0.9	1.1	1.3	1.5	1.9												

Berzelius and his successors believed that the chemical formula of a mineral can always be represented by cations and anions. The only exception is a group of metals. Such minerals as Cu, Au, and Fe were known long before Berzelius. In particular, the native metals were considered as one of the four constituent parts of the kingdom of minerals—salts and acid substances, earth substances (in particular, clay), combustible minerals (sulfur, diamond), and metal substances (copper, gold, etc.). A *class* is used as the first or the second taxon in most suggested systems of minerals (Table 1). In the zoological classification, *class* is the fourth taxon. Higher taxa are *subkingdom*, *phylum*, and *subphylum*. Therefore, we suggest using the taxon *class* also in the fourth place of the mineralogical classification.

Despite the complete chaos in the mineralogical classification, we see that, beginning from the second half of the 19th century, mineralogists in the whole world were influenced by Berzelius' works and based their classifications on the chemical compositions of minerals.

It is expedient to compare the mineralogical classification with the biological classifications, e.g., with the zoological one created by C. Linnaeus in 1735, because they are the most developed ones and, what is very important, are the same in the whole world. The objects classified in biology exist irrespective of the human activity, and most of the classifications widely used in the 20th century were developed for industrial objects (e.g., the classification of spare parts of automobiles).

Earlier [1], we made an attempt to enumerate all the mineral *classes*. Of course, the rigorous enumeration of all the classes can be made only upon the creation of a complete systematics of all known mineral species (about 4000). The number of *classes* is about 50. Thus, on average, each *class* should contain about 80 minerals. However, some *classes* comprise a much larger number of minerals; e.g., we considered 839 silicates [1] and 428 oxides [2]. There are *classes* containing only several (from one to five) mineral species. We started our studies with *classes* containing the largest number of species.

Indeed, minerals containing cations and anions are most widespread in nature, and, therefore, the minerals comprising most of the *classes* also consist of cations and anions. These are the major *classes*. The modern mineralogical classification also includes an additional *class* (or a lower taxon) of minerals consisting only of metals. In recent years, the systematics of minerals within the *class* of metals and intermetallic compounds was repeatedly published [14, 15]. We suggest separating into an additional *class* the minerals consisting only of nonmetals. This class was never considered in any other modern mineralogical classification.

5. DECIMAL SYMBOLS OF TAXA IN THE SYSTEMATICS OF MINERALS

The first numeral in a decimal symbol of each of the major *classes* coincides with the number of the group of the anion (nonmetal element) in the Periodic Table which can be located in groups from 3 to 8. Since numeral 1 and 2 have not been used, they can denote two additional *classes* (of metals and nonmetals) in the first place of the decimal symbol of a mineral. Thus, the *class* of metals is denoted by the symbol 1100/, and the *class* of nonmetals, by the symbol 2100/, where a slash separates the taxon *class* from lower taxa.

All the nonmetals are located to the right of the *z*-boundary, whereas all the metals are on the left of this boundary (Table 2). Not all of the elements located on the right of the *z*-boundary are encountered in minerals.

These are, first of all, the noble gases, polonium, and astatine. Negatively charged hydrogen H^- is never encountered in minerals, but an important hydroxyl OH^- ion is often found in minerals, and, since its electronegativity is higher than the electronegativity of F^-, it is located in the first place in subgroup VII*B* (Table 3).

Metals in the symbols of minerals in the *class* of nonmetals are indicated only if they substitute (in small amounts) a certain nonmetal.

Nonmetal atoms in this *class* can be, first, isolated anions, second, play the part of cations (which is characteristic of heavy nonmetals), and, third, form complex anions, e.g., NO_3^- or SO_4^{2-}.

It follows from the above that our mineralogical classification is based on 19 chemical elements forming the series B–C–Si–Ge–Sn–N–P–As–Sb–Bi–O–S–Se–Te–H(OH)–F–Cl–Br–I, hereafter called a preference series, in which each preceding element is more preferable than the succeeding one.

For this series, the taxa are characterized by minerals containing only one nonmetal element (oxides, sulfides, etc.) or consisting of two or more taxon-determining chemical elements (nitrates, sulfates) with one of them being the prevalent element. Thus, for $NaNO_3$ and $CaSO_4$, the prevalent element is oxygen. If a mineral contains an equal number of different nonmetals, the preferred nonmetal is the one which is closer to the beginning of the preference series. Thus, in poyarkovite Hg_3OCl, the preferred nonmetal is oxygen and, therefore, this mineral is related to the *class* of oxides and there to the division (in this case the *order*) in which the mineral composition is determined by oxygen and nonmetal atoms from group VII*B* of the Periodic Table. In some instances, the number of preferred atoms in the mineral can be lower than that of other nonmetals. In such instances, a special stipulation is always made.

Class 2100/ (nonmetals) is divided into *subclasses* and *orders* over the subgroups of the Periodic Table. The corresponding numerical indices are indicated immediately after a slash. Thus, *order* 2100/31 signifies that the preferred chemical element is located in the first place in subgroup III*B*; i.e., in the case under consideration, this element is boron. *Orders* /41 and /42 of *subclass* /4 are determined by the elements C and Si located in the first and second places in subgroup IV*B* of the Periodic Table, etc.

If a mineral is an elemental substance, the third and fourth numerals (corresponding to *suborder* and *family*) in their symbols are zeroes. If a mineral also contains some other chemical elements, the third and fourth numerals of the symbol correspond, as a rule, to the numbers of the corresponding groups in the Periodic Table and the positions of the elements in these groups.

Only 13 elements of the total 19 nonmetal elements form *orders* containing minerals. These *orders* belong to four *subclasses*—/3, /4, /5, and /6, which include 13 *orders*—/31-B, /41-C, /42-Si, /43-Ge, /44-Sn, /52-P, /53-As, /54-Sb, /55-Bi, /61-O, /62-S, /63-Se, and /64-Te.

The further division is described below in the sequence of occurrence of these *orders*.

6. THREE VARIANTS OF CRYSTALLOCHEMICAL RELATIONSHIPS OF NONMETAL ELEMENTS IN CHEMICAL COMPOUNDS

Nonmetal elements in chemical compounds can be either monatomic ions or form complex cations and anions consisting of two or more elements. If such elements form a complex cation, e.g., NH_4^+, then the classification of suborders and families in the *class* of nonmetals ignores this cation and it is considered along with other cations in other classes. An NH_4^+ ion is used in all the classifications as an analogue of alkali cations. Therefore, the compounds of the $(NH_4)_2SiF_6$ type (cryptohalite) is considered together with malladrite ($NaSiF_6$) in the corresponding *class* and not in *class* 2100/.

There is no rule determining the order of elements in the formulas of complex ions in chemistry. Thus, the central atom of an ammonium ion is written in the first place, then the peripheral atoms follow, whereas in the formula of an oxonium ion (H_3O^+), the order is reversed. We suggest writing the central atom of a com-

plex ion always in the first place as is usually done for most of the ions such as NO_3^-, As O_3^-, SO_4^{2-}, SiO_4^{4-}, etc.

The number of complex anions considerably exceeds the number of complex cations. We write them in the formulas immediately after the element determining the *order*. Their symbol is written in the same order and determined by the central atom. The complex ions are followed by single ions (prevalent in number or preferred if the numbers of the additional elements are equal).

In numerous mineralogical studies, the minerals containing complex anions are related to the divisions determined by these anions, i.e., are considered together with the metal-containing minerals. Thus, eulytite $Bi_4(SiO_4)_3$ is considered as an orthosilicate. This is associated with the fact that heavy nonmetals in compounds containing light nonmetals (as is well known, possessing pronounced electronegativity) play the part of electropositive elements, e.g., Sn and Bi in SnO_2 and BiOCl and $Bi(AsO_4)$, respectively. In some instances, these nonmetals can form solid solutions with metals, e.g., varlamoffite $(Sn,Fe)(O,OH)_2$. In this concrete case, we consider it to be a variety of cassiterite (SnO_2), because Sn and O are the prevalent elements and both minerals have tetragonal unit cells with close parameters.

7. SYMBOLS OF TAXA LOWER THAN *CLASSES*

Now, proceed to the description of *subclasses* and *orders*.

First of all, we should like to review the decimal symbols of mineral species lower than the symbol of a *class*, i.e., indicated after a slash in the class index.

The first numeral determining the *subclass* corresponds to the number of the group of the chemical element used to characterize this taxon. The second numeral determining the *order* corresponds to the position of this element in the group in the downward direction. If a *class* is determined by one element from the Periodic Table, the third numeral of the symbol determining the *suborder* is zero. If a *class* is determined by two elements, then the *suborder* is determined by the number of the group of the second element in the Periodic Table. The fourth index corresponding to the taxon *family* indicates the type of the chemical formula beginning with numeral 1, then 2, etc. if the given *suborder* consists of many *families* or characterizes the position of the element in the corresponding group if the number of *families* is small. The fifth index determining the *genus* usually indicates the structure type. The last index characterizing *mineral species* is indicated by numerals from 1 to 10 in accordance with the numbers of crystal systems from cubic to triclinic. This system is broken only in those rare occasions where the number of lower taxa exceeds ten.

Table 4 lists the first three numerals for all the *subclasses* of *class* 2100/. In two cases, it includes the numeral 9 to emphasize the fact that the characteristic of this taxon is inconsistent with the Periodic Table (as is well known, the Periodic Table has only eight groups with the maximum number of elements in some groups being six). Numeral 9 in the first place upon the slash, i.e., in the *subclass* symbol, denotes hydrates, the taxon in the third place in *subclass* /559 is determined by a complex anion instead of a chemical element.

The last three numerals in the decimal symbols for each concrete *subclass* are indicated in the following tables.

8. *SUBCLASS* 2100/3

8.1. Order 2100/31

This *order* contains only two minerals. Their chemical compositions include, in addition to boron, O and OH. Their symbols, in accordance with additional preferred elements, are indicated by numerals 6 and 7. These minerals are cubic metaborite BO(OH) (sp. gr. *P*43), 2100/316111 and triclinic sassolite $B(OH)_3$ (sp. gr. *P*1), 2100/317111. There are some indications that bornitride BN also occurs in nature, i.e., is a mineral, and therefore can be located in the first place in this *order*. However, it is not even mentioned in other monographs and reference books on mineralogy.

Boron does not occur as an elemental substance in nature. There exist some more minerals consisting only of nonmetal elements, with boron being a preferred element. These are, e.g., larderellite $(NH_4)[B_5O_6(OH)_4]$, ammonioborite $(NH_4)_2[B_{10}O_{16}] \cdot 5H_2O$, etc., but in these minerals, two nonmetal elements form an ammonium cation, which is a complete analogue of alkali metals in chemical compounds. These minerals are considered in the *class* of borates together with borgite $NaB_5O_6(OH)_4 \cdot 3H_2O$ and other similar minerals.

9. *SUBCLASS* 2100/4

9.1. Order 2100/41

The preferred chemical element in this *order* is carbon. The *suborders* and *families* are determined by the presence of additional nonmetals. Carbon itself is contained in many minerals that are elemental substances. Since this *suborder* and *family* contain no additional anions, the third and the fourth numerals of the symbol are zeroes.

Thus, *suborder* 2100/410 is represented by minerals consisting of native carbon.

Table 5 lists the main representatives of native carbon which differ from one another by their structure types, i.e., by *genera*.

In the 1980s, a new form of carbon consisting of spherical molecules of 60 atoms was discovered. This carbon modification, with molecules in the shape of a

Table 4. *Subclasses*, *orders*, and *suborders* in *class* of nonmetals 2100/

Symbols of *subclasses* and *orders*	Chemical elements or atomic groups determining *suborders*	Symbols of taxa lower than *order*
/31	B and O; B and OH	/316; /317
/41	C; C–C; C and N; C and O	/410; /414; /415; /416
/42	Si and N; Si and O	/425; /426
/43	Ge and O	/436
/44	Sn and Sb; Sn and O; Sn and S; Sn and OH	/440; /445; /446; /447
/51	N	There are no minerals
/52	P	/520
/53	As; As and Sb (Bi); As and O	/530; /535; /536
/53	Sb; Sb and As; Sb and O (Se, Te)	/540; /545; /546
/55	Bi; Bi and O; Bi and (OH); Bi and *XYn*	/550; /556; /557; /559
/61	O and Se; O and Te	/6163; /6164
/62	S	/620
/63	Se	/630
/64	Te	/640
/9	Hydrates	/941; /961

ball, are called fullerenes. In 1992, native fullerenes were discovered in the specimens of high-carbon shungite. However, usually fullerenes are not mentioned in the reference books on mineralogy. Lately, fullerenes consisting of larger molecules, in particular of C_{70}, were discovered.

The structure of crystalline fullerene C_{60} is a cubic close packing of spherical C_{60} molecules. However, because of the low symmetry of the molecules, the structure symmetry is lowered to *Fm*3 (instead of *Fm*3*m*). The molecules in fullerene C_{70} are elongated ellipsoids of rotation, and the C_{70} structure is a hexagonal close packing.

Order 2100/41 includes *suborder* /414 characterized by C–C bonds, with C atoms always forming additional C–H bonds. The crystal structures of the representatives of this *suborder* are built, as a rule, by molecules of the corresponding compositions. If, in addition to the C–C and C–H bonds, a compound is also characterized by the presence of a nonmetal element from subgroups V*B* (N), VI*B* (O), or VII*B*, the compound is related to the *suborder* with symbol /415, /416, or /417, respectively.

Order /41 includes an enormous number (several million) of artificially synthesized organic compounds, with most of them having C–C and C–H bonds. If such compounds contain only C and H, the symbol of their *suborder* is /414.

There are only a few natural minerals with compositions analogous to synthesized organic compounds, and none of them was known to Berzelius.

Since the C/H ratios in these minerals are different, then, strictly speaking, they cannot be related even to one *family*. In Table 6, these minerals are grouped into *suborders* in accordance with the presence of additional (other than C and H) elements. The last mineral in *suborder* /414 is evenkite, a mineral of the paraffin series characterized by a chain structure. The *families* in this *suborder* are enumerated depending on the number of carbon atoms in molecular formulas of the corresponding compounds. Thus, this family comprises minerals–hydrocarbons with the same number of carbon atoms in their molecules. No minerals possessing, in addition to C–C and C–H bonds, C–*X* bonds (where *X* is a halogen) have been discovered as yet. In addition to C–C bonds, organic compounds often have bonds between carbon and nonmetal atoms from other groups of the Periodic Table. The presence of the latter bonds determines the third numeral of this *suborder*.

An exhaustive classification of all the organic compounds was beyond the scope of this study. We made an attempt to distribute only the minerals over the lower taxa, and, because their number is rather small, they could be classified using the decimal system (Table 6).

The chemical composition of the minerals urea and acetamide show the absence of C–C bonds. Carbon atoms in their formulas are bound to three or four atoms of other chemical elements, respectively. However, as an exception, these compounds are also considered in all the reference books on organic chemistry.

The last mineral in Table 6 could have been flagstaffite $C_{10}H_{18}(OH)_2 \cdot H_2O$, the only hydrate among the organic minerals. Its symbol /419111 includes numeral 9 characteristic of hydrates from other divisions of mineralogy, which shows that this index is not associated with the Periodic Table.

Table 5. Natural carbon modifications

Symbol of *genus*	Symbol of *species*	Mineral	System, sp. gr.
/41001	/410011	Diamond	Cubic, *Fd*3*m*
/41002	/410021	Lonsdaleite	Hexagonal, $P6_3mc$
/41003	/410031	Chaoite	Hexagonal, *P*6/*mmm*
/41004	/410041	Graphite-2*H*	Hexagonal, $P6_3/mmc$
/41005	/410051	Graphite-3*R*	Trigonal, *R*3*m*
/41006	/410061	Fullerene C_{60}	Cubic, *Fm*3
/41007	/410071	Fullerene C_{70}	Hexagonal, $P6_3mmc$

9.2. Order 2100/42

In the previous sections, we considered minerals–organic compounds, i.e., minerals with C–C and C–H bonds. We suggested using a special index in the third place after the *class* (*suborder*) that would correspond to the subgroup of an additional nonmetal of the Periodic Table.

Of course, in this case, numeral 2 remains free, because subgroup II*B* of the Periodic Table has no nonmetals. Therefore, numeral 2 in the index of *order* and *family* can be used for silicon, because it is the second element in group IV*B*, i.e., for minerals containing C and Si. Then, the *suborder* and the *family* would have symbol /4241.

There exist several natural minerals described by the chemical formula CSi containing only two elements. Since the chemical and the mineralogical literature ignores the notion of a preferred chemical element, the order of writing the elements is reversed, i.e., SiC. We are not going to change this tradition and consider the corresponding family not within *order* /41 but within *order* /42, so that the symbol of this family, /4241, exactly corresponds to the composition SiC. In this case, the first family is, in fact, native silicon.

9.2.1. *Family* /4200. Silicon is crystallized in the cubic system (sp. gr. *Fd*3*m*) and is isostructural to diamond. Its symbol is 2100/420011. I believe that native silicon may also occur on the Moon.

Table 7 lists the minerals of the composition SiC or the so-called group of carborundum. Their polytypes have different structures. Here, we encounter the case of polytypism. The problem of whether each polymorphic modification is an individual mineral species or whether they all should be considered within one species is widely discussed, and there is still no unique opinion on this problem. Both standpoints have their pros and cons. The polymorphic types have different symmetries, i.e., belong not only to different *species* but also to different *genera*. An important fact is that they all have the same chemical composition. Earlier, in our book on the systematics of mineral *species* ([1], p. 114), we made an attempt to attribute individual symbols to all of the polymorphous modifications. However, the idea that polytypism is a property of the minerals of one *species* (i.e., that its taxon should be lower than *species*) should also be taken into account. In this case, we suggest considering polytypes not as *species* but as *varieties* of one *species*. As a rule, the researcher is interested in the whole set of polytypes and not only in one of them, and, therefore, in the search systems, which are an inherent part of any classification, each symbol should contain the whole information on all of the polytypes of the given *species*.

It is also possible to use an intermediate variant—to combine some polytype modifications into large groups, e.g., into crystal systems.

The results of such an attempt are given in Table 7.

There is only one cubic polytype, whereas other crystal systems can contain several polytypes.

Sometimes, the formula of the polytype modification of moissanite is written as 3*C*. Then, the group of carborundum consists of eight polytype modifications of one *species.* Of course, it is possible to attribute an individual number to each modification (by changing the last numeral in their symbol). The problem of symbols for polytypes should be discussed at the international level.

9.2.2. *Suborder* /425. This *suborder* includes two N-containing minerals—hexagonal nierite Si_3N_4, sp. gr. *P*31*c* occurring only in meteorites, symbol /425111 and orthorhombic sinoite Si_2N_2O, sp. gr. $Cmc2_1$, symbol /425121.

No mineral containing, in addition to Si, some other elements of subgroup V*B* (P, As, Sb, or Bi) was revealed in *order* /42. It would be reasonable to relate to this *order* also eulytite $Si_3Bi_4O_{12}$, however it contains a SiO_4 anion, and, therefore, its formula should be written as $Bi_4[SiO_4]_3$. As was indicated above, the minerals containing complex anions would be considered separately, therefore this mineral would be considered later. In some mineralogical studies, this mineral is related to orthosilicates, because Bi often plays the role of a cation. Our classification suggests dividing metals and nonmetals at a very early stage, because such a division is the further development of the Berzelius idea underlying our classification.

9.2.3. *Suborder* /426. In this *suborder*, Si is combined with nonmetals from subgroup VI*B* of the Peri-

Table 6. Minerals–organic compounds

Suborder	*Family*	*Genus*	*Species*	Formula and name	System, sp. gr.
/414	/4141	/41411	/414111	$C_{13}H_{10}$ kratochvilite	Orthorhombic, *Pnma*
	/4142	/41421	/414211	$C_{14}H_{10}$ ravatite	Monoclinic, $P2_1$
	/4143	/41431	/414311	$C_{18}H_{18}$ phylloretine	Orthorhombic, *Pnna*
	/4144	/41441	/414411	$C_{15}H_{24}$ simonellite	Orthorhombic, *Pnaa*
		/41442	/414421	$C_{19}H_{34}$ fichtelite	Monoclinic, $P2_1$
	/4145	/41451	/414511	$C_{20}H_{34}$ hartite	Triclinic, *P*1
		/41452	/414531	$C_{20}H_{36}$ dinite	Orthorhombic, $P2_12_12_1$
	/4146	/41461	/414611	$C_{22}H_{14}$ idrialite	Orthorhombic, *B*-cell
	/4147	/41471	/414711	$C_{24}H_{12}$ karpatite	Monoclinic, $P2_1c$
		/41472	/414721	$C_{24}H_{50}$ evenkite	Monoclinic, $P2_1/a$
/415	/4151	/41511	/415111	$C(NH_2)_2O$ urea	Tetragonal, $P42_1$
	/4152	/41521	/415211	CH_3CONH_2 acetamide	Hexagonal, *R*3*c*
	/4153	/41531	/415311	$C_5H_4N_4O_3$ uricite	Monoclinic, $P2_1/c$
	/4154	/41541	/415411	$C_5H_3(NH_2)N_4O$ guanine	Monoclinic, $P2_1/c$
	/4155	/41551	/415511	$C_6H_4(CO)_2NH$ kladnoite	Monoclinic, $P2_1/c$
/416	/4162	/41621	/416211	$C_{14}H_8O_2$ hoelite	Monoclinic, $P2_1/c$
	/4163	/41631	/416311	$C_{17}H_{14}O_8$ or $C_{19}H_{14}O_8$ graebeite	Monoclinic
	/4164	/41641	/416411	$C_{20}H_{32}O_2$ refikite	Orthorhombic, $P2_12_12$

odic Table. Minerals are known only for compounds of silicon with oxygen of the composition SiO_2 (Table 8). They all belong to *family* /4261.

The synthetic mineral keatite has a framework similar to that of quartz. Its structure is often compared with the structures of other SiO_2 modifications, and, therefore, we placed keatite into Table 8; since it belongs to the same space group as cristobalite, we related both these minerals to the same *genus*. The symmetry of keatite is the same as of α-cristobalite, but the unit-cell parameters are different: a = 7.46 Å and c = 8.61 Å for keatite and a = 4.97 Å and c = 6.93 Å for cristobalite.

Similar to minerals considered earlier, coesite possesses a framework structure, but it is different from the structure of the quartz group and similar to that of feldspars.

Melanophlogite is a clathrate with the "host" being the zeolite framework of SiO_2 composition and the "guests," the molecules of N_2, CH_4, CO_2, etc. We believe that the clathrates should be classified by the structure of the host, and, therefore, this mineral is considered along with the other SiO_2 modifications. This standpoint is also used in a number of mineralogical reference books.

Sometimes, the formulas of clathrates includes both hosts and guests, but these compounds are considered together with the corresponding oxides. Thus, Libau [16] writes the formula of melanophlogite as $46SiO_2 \cdot 8(N_2, CH_4, CO_2)$. He also mentions the dodecasil 1H $34SiO_2 \cdot 5N_2[(C_2H_5)_2NH(C_5NH_{11},C_6NH_{13})]$ and some other compounds.

A specific case is presented by stishovite possessing not a framework but a coordination structure, a very rare one, in which silicon has c.n. = 6. Stishovite is isostructural to rutile TiO_2.

Many mineralogists believe that various modifications of SiO_2 are silicates and consider them along with other silicates, which is erroneous, because, in addition to SiO_n, silicates always contain metal atoms (see their definition in our earlier study [1], p. 39). Chemically, these compounds are not oxides but salts of silicic acids.

Order /42 includes no minerals with nonmetals other than silicon and oxygen.

9.3. Order 2100/43

This *order* includes Ge and its compounds with nonmetals. Germanium never occurs in nature as an elemental substance. The only mineral of this *order* is argutite GeO_2, sp. gr. $P4_2/mnm$ possessing the rutile structure. Its symbol is /436111.

9.4. Order 2100/44

This *order* includes Sn and its compounds with nonmetals. Native tin is encountered in nature in the form β-Sn, usually called white tin. Its symbol is /440011.

Table 7. Group of carborundum SiC

Genus	*Species*	Name	System, sp. gr.
/42411	/424111	Carborundum (moissanite)	Cubic, *F*43*m*
/42412	/424121	α-2*H*, 4*H*, 5*H*, 6*H*	Hexagonal, $P6_3mc$
/42413	/424131	Carborundum 10*R*, 15*R*, 33*R*	Trigonal, *R*3*m*

White tin is tetragonal, sp. gr. $I4_1/amd$. Among the tin compounds with nonmetals, there are minerals containing antimony, oxygen, and sulfur (Table 9), which complete the *order* /44.

10. *SUBCLASS* 2100/5

10.1. Order 2100/51

There are no minerals without metals and with nitrogen as a preferred element in this *order.*

10.2. Order 2100/52

There are no minerals without metals and with a phosphorus as a preferred element in this *order.* However, one mineral of this *order* is encountered in meteorites—it is the cubic modification of white phosphorus with symbol /520011.

10.3. Order 2100/53

In nature, arsenic is encountered in two modifications. The more widespread one is the rhombohedral modification, sp. gr. *R*3*m*, with symbol /530011. In mineralogy, it is simply called arsenic. The second, the orthorhombic modification, sp. gr. *Acam*, has a special mineralogical name—arsenolamprite with symbol /530021. This modification is isostructural to black phosphorus.

Among the compounds of this *order*, mineralogical books often indicate the mineral stibarsen AsSb isostructural to rhombohedral As and Sb. However, it should rather be considered as a solid solution of arsenic and antimony and can hardly be considered as an individual mineral *species*.

The real mineral *species* with arsenic as the preferred element are the compounds of As with the elements from subgroups V*B* and VI*B* of the Periodic Table.

There are only a few mineral *species* which include, in addition to As, some other elements of subgroup V*B* (i.e., Sb and Bi). There are only three minerals formed by As and Sb. These are laphamite $As_2(Sb,S)_3$ with symbol /535411, monoclinic getchellite $AsSbS_3$ with the sp. gr. $P2_1/a$, symbol /535421, and a structure similar to the monoclinic structure of As_2S_3, sp. gr. $P2_1/n$, but a double unit-cell parameter *c*, and, finally, paakkontnite $AsSb_2S_2$ with symbol /535431.

Several minerals are characterized by the simultaneous presence of As and Bi. In these minerals, bismuth plays the role of a metal, and, therefore, they are considered in *order* /55 in the division that includes bismuth minerals with complex anions (see below).

The minerals including As and the elements of subgroup VI*B* are indicated in Table 10.

10.4. Order 2100/54

Antimony as an elemental substance is encountered in nature in the form of the mineral antimony. It is crystallized in the rhombohedral system, sp. gr. *R*3*m*, and is described by symbol /540011.

The mineralogical textbooks mention one more mineral with the composition close to pure antimony—paradocrasite $Sb_2(Sb,As)_2$ crystallizing in the monoclinic system—which, therefore, cannot be considered as a solid solution of antimony and arsenic. It is attributed to symbol /545411.

Table 8. Silicon oxides

Genus	*Species*	Name of mineral	System, sp. gr.
/42611	/426111	β-cristobalite	Cubic, *Fm*3*m*
/42612	/426121	β-trydimite	Hexagonal, $P6_3/mmc$
/42613	/426131	β-quartz	Hexagonal, $P6_222$
/42614	/426141	α-quartz	Trigonal, $P3_121$
/42615	/426151	α-cristobalite	Tetragonal, $P4_12_12$
–	/426152	Keatite	Tetragonal, $P4_12_12$
/42616	/426161	α-trydimite	Orthorhombic, $C222_1$
/42617	/426171	Coesite	Monoclinic, *C*2/*c*
/42618	/426181	Melanophlogite	Cubic, $P4_232$
/42619	/426191	Stishovite	Tetragonal, $P4_2/mnm$

Table 9. Compounds of tin with other nonmetals

Family	*Genus*	*Species*	Name and formula	System, sp. gr.
/4454	/44541	/445411	Stistaite SnSb	Trigonal, *R*3*m*
/4461	/44611	/446111	Romarchite SnO	Tetragonal, *P*4/*mmm*
	/44612	/446121	Cassiterite SnO_2	Tetragonal, *P*4/*nmm*
	/44613	/446131	Hydroromarchite $Sn_3O_2(OH)_2$	Tetragonal, *P*4/*mnc*
/4462	/44621	/446211	Herzenbergite SnS	Orthorhombic, *Pbnm*
	/44622	/446221	Berndtite SnS_2	Trigonal, *P*3*m*1
	/44623	/446231	Ottemannite Sn_2S_3	Orthorhombic, *Pnam*
/4471	/44711	/447111	Abhurite $Sn_3O(OH)_2Cl_2$	Trigonal, *R*32/*m*

Table 10. Compounds of arsenic with nonmetals of subgroup VI*B* of the Periodic Table

Family	*Genus*	*Species*	Name and formula	System, sp. gr.
/5361	/53611	/536111	Arsenolite As_2O_3	Cubic, *Fd*3*m*
	/53612	/536121	Claudetite As_2O_3	Monoclinic, $P2_1/n$
/5362	/53621	/536211	Realgar AsS	Monoclinic, $P2_1/n$
	/53622	/536221	Pararealgar AsS	Monoclinic, $P2_1/c$
	/53623	/536231	Orpiment As_2S_3	Monoclinic, $P2_1/n$
	/53624	/536241	Duranusite As_4S	Orthorhombic
	/53625	/536251	Dimorphite As_4S_3	Orthorhombic, *Pnma*
	/53626	/536261	Uzonite As_4S_5	Monoclinic, $P2_1/m$
	/53627	/536271	Alacranite As_8S_3	Monoclinic, *C*2/*c*
	/53628	/536281	Wakabayashilite $(As, Sb)_{11}S_{18}$	Monoclinic, $P2_1/n$

A mineral including both stibium and bismuth is bismutostibiconite $(Sb^{5+},Fe^{3+})_2BiO_7$, which is isostructural to stibiconite crystallizing in the cubic sp. gr. *Fd*3*m* (Table 11). Its symbol is /545511.

Antimony in *order* /54 is encountered mainly in the form of compounds with elements of subgroup VI*B* of the Periodic Table (Table 11).

There is mention of some other forms of antimonite in the literature—metastibnite and gorobstedite $(Sb,Bi)_2S_3$, but these are noncrystalline forms (i.e., according to the nomenclature used here, are not minerals but mineraloids).

10.5. Order 2100/55

Bismuth as an elemental substance is encountered in nature and has the same structure type as As and Sb (trigonal sp. gr. *R*3*m*). Its symbol is /550011.

Among the compounds of this *order*, bismuth is encountered mainly in combination with the elements of subgroup VI*B* of the Periodic Table.

Table 12 lists the minerals containing bismuth and oxygen.

Table 13 indicates the minerals including bismuth and also sulfur, selenium, and tellurium. The *families* are chosen in accordance with their Bi/*X* ratios, i.e., Bi*X*, Bi_2X_3, and Bi_3X_4 or Bi_4X_3, Bi_6X_5, Bi_7X_3, and Bi_2X_6. Such a choice of *family* allows us to keep the minerals which are related to individual *genera* (structure types) close together.

10.5.1. *Suborder* /557. The only mineral of this *suborder* is gananite BiF_3 (cubic sp. gr. *P*43*m*) with symbol /557211.

As was mentioned above, in a number of Bi-containing minerals, some light nonmetals form complex anions. These minerals are also included in *order* /55.

In the mineralogical literature, these minerals are distributed over classes in accordance with these complex anions. In other words, they are classified together with the minerals containing a complex anion and metals, which is inconsistent with our system because we consider Bi as a nonmetal. These minerals are listed in Table 14. Since in our system the numerals usually determine the position of a chemical element in the Periodic Table, the minerals listed in Table 14 should be considered in a different way in order to define the anionic group as a whole. We suggest using numeral 9 in the index of the *suborder*, which cannot characterize any group in the Periodic Table. The mineral roosevelttite is isostructural to monazite $CePO_4$.

Table 11. Compounds of antimony with nonmetals of subgroup VI*B*

Family	*Genus*	*Species*	Name	Formula	System, sp. gr.
/5461	/54611	/546111	Senarmontite	Sb_2O_3	Cubic, *Fd*3*m*
	/54612	/546121	Valentinite	Sb_2O_3	Orthorhombic, *Pccn*
	/54613	/546131	Cervantite	$Sb^{5+}Sb^{3+}O_4$	Orthorhombic, $Pbn2_1$
	/54614	/546141	Kermesite	$SbOS_2$	Triclinic, *P*1
	/54615	/546151	Stibiconite	$Sb_2^{5+}Sb^{3+}O_6(OH)$	Cubic, *Fd*3*m*
	/54616	/546161	Onoratoite	$Sb_8O_{11}Cl_2$	Triclinic, *P*1
/5462	/54621	/546211	Antimonite (stibnite)	Sb_2S_3	Orthorhombic, *Pbnm*
/5463	/54631	/546311	Antimonselite	Sb_2Se_3	Orthorhombic, *Pbnm*
/5464	/54641	/546411	Tellurantimony	Sb_2Te_3	Trigonal, *R*3*m*

Table 12. Compounds of bismuth with oxygen and other nonmetals

Family	*Genus*	*Species*	Name	Formula	System, sp. gr.
/5561	/55611	/556111	Sillenite	γ-Bi_2O_3	Cubic, *I*23
	/55612	/556121	Sphaerobismite	β-Bi_2O_3	Tetragonal, $P4_22_12$
	/55613	/556131	Bismite	α-Bi_2O_3	Monoclinic, $P2_1/c$
	/55614	/556141	Russelite	$(Bi_2,W)O_3$	Tetragonal, *I*42*d*
	/55615	/556151	Daubreeite	BiO(OH, Cl)	Tetragonal, *P*4/*nm*
		/556152	Zavaritskite	BiOF	Tetragonal, *P*4/*nm*
		/556153	Bismoklite	BiOCl	Tetragonal, *P*4/*nm*

11. *SUBCLASS* 2100/6

11.1. Order 2100/61

The preferred element in this *order*, and especially in the compounds of heavy elements from subgroup VI*B*, is oxygen. In the mineralogical literature, these compounds are considered as oxides, and oxygen in their formulas is written in the second place. Below, we shall follow this tradition.

Thus, the minerals in this *order* are selenolite SeO_2 (sp. gr. $P4_2cb$) with symbol 2100/616311, paratellurite TeO_2 (tetragonal sp. gr. $P4_12_12$) with symbol 2100/616411, and tellurite TeO_2 (orthorhombic sp. gr. *Pbca*) with symbol 2100/616421.

Among the oxygen compounds with the elements of subgroup VII*B*, there is only one mineral containing O and H—ice. Ice H_2O (hexagonal sp. gr. $P6_3mc$) has symbol 2100/617111. Below –80°C, its second modification is observed (cubic sp. gr. *Fd*3*m*).

11.2. Order 2100/62

In this *order*, there are three elemental substances—three mineral modifications of sulfur consisting of S_8 molecules—orthorhombic α-S (sp. gr. *Fddd*) with symbol 2100/620011, monoclinic β-S (sp. gr. $P2_1/c$) with symbol 2100/620021, and monoclinic γ-S (sp. gr. $P2/c$) with symbol 2100/620031.

Among the sulfur compounds with other nonmetals, there are only those in which the preferred element is not sulfur but some other element (As, Sb, and Bi). Like Se and Te, they are included in Tables 10, 11, and 13.

11.3. Order 2100/63

The elemental substance in this *order* is trigonal Se (sp. gr. $P3_121$) with symbol 2100/630011.

Only those selenium compounds with other elements are known in which the preferred element is not Se but some other element.

11.4. Order 2100/64

The elemental substance in this *order* is trigonal Te (sp. gr. $P3_121$), symbol 2100/640011.

In this case as well, only those Te compounds with other elements are encountered in which the preferred element is not Te but some other element.

12. *SUBCLASS* 2100/7

This *subclass* consists of five *orders*—/71, /72, /73, /74, and /75. However, none of these *orders* includes a mineral having the form of an elemental substance. All the elemental substances of these elements are encountered in nature either in the gaseous or the liquid state.

Table 13. Compounds of bismuth with S, Se, and Te

Family	*Genus*	*Species*	Name	Formula	System, sp. gr.
/5562	/55621	/556211	Nevskite	BiSe	Trigonal, *P*3*m*
		/556212	Tsumoite	BiTe	
/5563	/55631	/556331	Ingodite	Bi_2TeS	
		/556312	Sulfotsumoite	Bi_3Te_2S	
	/55632	/556321	Bismuthinite	Bi_2S_3	Orthorhombic, *Pbn*
		/556322	Guanajuatite	$Bi_2(Se, S)_3$	
	/55633	/556391	Csiklovaite	$Bi_2(S, Se)_2Te$	Trigonal, *R*3*m*
		/556332	Paraguanajuatite	$Bi_2(Se, S)_3Bi_2$	
		/556333	Skippenite	$Bi_2Se_2(Te, S)$	
		/556334	Tetradymite	Bi_3Te_2S	
		/556335	Kawazulite	$Bi_2(Te, Se, S)_3$	
		/556335	Tellurobismuthite	Bi_2Te_3	
/5564	/55641	/556411	Rucklidgeite	$(Bi, Pb)_3Te_4$	
	/55642	/556421	Ikunolite	Bi_4S_3	
		/556422	Laitakarite	Bi_4Se_2S	
		/556423	Pilsenite	Bi_4Te_3	
		/556424	Joseite-A	Bi_4TeS_2	
		/556425	Joseite-B	Bi_4Te_2S	
/5565	/55651	/556511	Baksanite	$Bi_6Te_2S_3$	
/5566	/55661	/556611	Hedleyite	Bi_7Te_3	
/5567	/55671	/556711	Smirnite	$Bi_2Te^{4+}O_5$	Orthorhombic

Table 14. Compounds of bismuth with complex anions

Family	*Genus*	*Species*	Name	Formula	System, sp. gr.
/5594	/55941	/559411	Bismutite	$Bi_2[CO_3]O_2$	Tetragonal, *I*4/*m*
	/55942	/559421	Eulitite	$Bi_4[SiO_4]_3$	Cubic, *I*43*d*
/5595	/55951	/559511	Smrkovecite	$Bi_2[PO_4]O(OH)$	Monoclinic
	/55952	/559521	Petitjeanite	$Bi_3[PO_4]_2O(OH)$	Triclinic, *P*1
	/55953	/559531	Tetrarooseveltite	β-$Bi[AsO_4]$	Tetragonal, $I4_1/a$
	/55954	/559541	Rooseveltite	$Bi[AsO_4]$	Monoclinic, $P2_1/n$
	/55955	/559551	Atelestite	$Bi_2[AsO_4]O(OH)$	Monoclinic, $P2_1/m$
	/55956	/559561	Preizingerite	$Bi_3[AsO_4]_2O(OH)$	Triclinic, *P*1
	/55957	/559571	Arsenobismite	$Bi_2[AsO_4](OH)_3$	Orthorhombic
	/55961	/559611	Cannonite	$Bi_2[SO_4](OH)_2$	Monoclinic, $P2_1/c$
/5596	/55962	/559621	Pingguite	$Bi_6[TeO_4]_2O_5$	Orthorhombic

Even the heaviest element, iodine, artificially synthesized in the crystalline state, evaporates already at room temperature.

Since halogens are the last elements of the preference series, they cannot play the part of preferred elements.

In accordance with the Berzelius recommendations, our classification is based on nonmetals (electronegative elements). Hydrogen, hydroxyl, and halogens are present in the minerals related to *class* 2100 which are built only by nonmetals (i.e., do not contain metals), but the preferred elements are those located before these

nonmetals in the preference series. The examples are daubreeite BiOCl, sassolite $B(OH)_3$, etc.

Moreover, as was indicated above, in some minerals containing only nonmetal chemical elements, some of them form complex cations. These are, first of all, ammonium ions. The examples are cryptohalite $(NH_4)_2SiF_6$, ammonium chloride $(NH_4)Cl$, etc. In the classification, this complex cation is taken into account along with alkali metals and is located after these metals (Li, Na, K, Rb, Cs, and NH_4).

Polonium, astatatine, and all noble (inert) gases do not occur as individual elements in minerals.

13. *SUBCLASS* 2100/9. HYDRATES

Class of oxides 6100/ includes numerous hydrates, which we related to *subclass* 6100/9. At the same time, there are only two hydrates in *class* 2100/.

These are an extremely rare mineral—flagstaffite $C_{10}H_{18}(OH)_2 \cdot H_2O$ (orthorhombic sp. gr. *Fdd*2) which is an organic compound. Its symbol is 2100/941111. The second mineral of this *subclass* is coguandite $Sb_6O_8(SO_4) \cdot H_2O$. Its symbol is 2100/961111.

14. CONCLUSION

Considering the minerals of the *class* of oxides in [2], we wrote a special chapter entitled "Oxides and Hydroxides from the Class of Nonmetals" (comprising about thirty minerals). Earlier, these minerals were related to oxides in all the courses of mineralogy. Therefore, the reader who did not find these minerals in class of oxides 6100/ should not think that they were omitted by mistake. Therefore, these minerals were assigned the decimal symbols in which *class* symbol 2100/ is followed by the indices of the *subclass* and the *order* corresponding to oxygen atoms (e.g., in Tables 35 and 36 in [2]). Now that the systematics of class of nonmetals 2100/ is completed, we substituted these symbols with new ones. The order of the indices of taxa lower than *class* was considered above in this article.

APPENDIX

List of minerals with the indication of the table or the section of its appearance

Abhurite, Table 9
Acetamide, Table 6
Alacranite, Table 10
Antimonite, Table 11
Antimonselite, Table 11
Antimony, Sect. 10.4
Argutite, Sect. 9.3
Arsenic, Sect. 10.3
Arsenobismite, Table 14
Arsenolamprite, Sect. 10.3
Arsenolite, Table 10
Atelestite, Table 14
Baksanite, Table 13
Berndtite, Table 9
Bismite, Table 12
Bismoklite, Table 12
Bismuth, Sect. 10.5
Bismuthinite, Table 13
Bismutite, Table 14
Bismutostibiconite, Sect. 10.4
Bornitride, Sect. 8.1
Cannonite, Table 14
Carborundum, Table 7
Cassiterite, Table 9
Cervantite, Table 11
Chaoite, Table 5
Claudetite, Table 10
Coesite, Table 8
Coguandite, Sect. 13
α- and β-cristobalite, Table 8
Csiklovaite, Table 13
Daubreeite, Table 12
Diamond, Table 5
Dimorphite, Table 10
Dinite, Table 6
Dodecasil, Sect. 9.2.3
Duranusite, Table 10
Evenkite, Table 6
Eulytite, Table 14
Fichtelite, Table 6
Flagstaffite, Sects. 9.1 and 13
Fullerene C_{60} and C_{70}, Table 5
Gananite, Sect. 10.5.1
Gerzenbergite, Table 9
Getchellite, Sect. 10.3
Graebeite, Table 6
Graphite, Table 5
Guanajuatite, Table 13
Guanine, Table 6
Hartite, Table 6
Hedleyite, Table 13
Herzenbergite, Table 9
Hoelite, Table 6
Hydroromarchite, Table 9
Ice, Sect. 11.1
Idrialite, Table 6
Ikunolite, Table 13
Ingodite, Table 13
Joseite, Table 13
Karpatite, Table 6
Kawazulite, Table 13
Keatite, Table 8
Kermesite, Table 11

Kladnoite, Table 6
Kratochvilite, Table 6
Laitakarite, Table 13
Laphamite, Sect. 10.3
Lonsdaleite, Table 5
Melanophlogite, Table 8
Metaborite, Sect. 8.1
Moissanite, Table 7
Nevskite, Table 13
Nierite, Sect. 9.2.2
Onoratoite, Table 11
Orpiment, Table 10
Ottemannite, Table 9
Paakkontnite, Sect. 10.3
Paraguanajuatite, Table 13
Paradocrasite, Sect. 10.4
Pararealgar, Table 10
Paratellurite, Sect. 11.1
Petitjeanite, Table 14
Phosphorus, Sect. 10.2
Phylloretine, Table 6
Pilsenite, Table 13
Pingguite, Table 14
Preigingerite, Table 14
α- and β-quartz, Table 8
Ravatite, Table 6
Realgar, Table 10
Refikite, Table 6
Romarchite, Table 9
Rooseveltite, Table 14
Rucklidgeite, Table 13
Russellite, Table 12
Sassolite, Sect 8.1
Selenium, Sect. 11.3
Selenolite, Sect. 11.1
Senarmontite, Table 11
Silicon, Sect. 9.2.1
Sillenite, Table 12
Simonellite, Table 6
Sinoite, Sect. 9.2.2
Skippenite, Table 13
Smirnite, Table 13
Smrkovecite, Table 14
Sphaerobismite, Table 12
Stibarsen, Sect. 10.3
Stibiconite, Table 11
Stibnite, Table 11
Stishovite, Table 8
Stistaite, Table 9
Sulphotsumoite, Table 13
α-, β-, and γ-sulfur, Sect. 11.2
Tellurantimony, Table 11
Tellurium, Sect. 11.4
Tellurite, Sect. 11.1
Tellurobismuthite, Table 13
Tetradymite, Table 13
Tetraroosevelitite, Table 14
Tin, Sect. 9.4
α- and β-tridymite, Table 8
Tsumoite, Table 13
Urea, Table 6
Uricite, Table 6
Uzonite, Table 10
Valentinite, Table 11
Varlamoffite, Sect. 6
Wakabayashilite, Table 10
Zavaritskite, Table 12

REFERENCES

1. G. B. Bokij, *Systematics of Natural Silicates*, in *Advances in Science and Technology. Series "Crystal Chemistry"* (VINITI, Moscow, 1997), Vol. 31.
2. G. B. Bokij, *Systematics of Natural Oxides*, in *Advances in Science and Technology. Series "Crystal Chemistry"* (VINITI, Moscow, 2000), Vol. 32.
3. J. J. Berzelius, Ann. Phys. (Leipzig) **48**, 326 (1814).
4. J. J. Berzelius, Pogg. Ann. **12**, 1 (1824).
5. Yu. I. Solov'ev and V. I. Korennoĭ, *Jacob Berzelius* (Nauka, Moscow, 1980).
6. A. G. Betekhtin, *Mineralogy* (Gos. Izd. Geolog. Lit., Moscow, 1950).
7. M. Fleischer, *Glossary of Mineral Species* (Mineralogical Record Inc., Tucson, 1987; Mir, Moscow, 1990).
8. *Chemical Encyclopedia* (Nauchnoe Izd. Bol'shaya Ross. Entsiklopediya, Moscow, 1992), Vol. 3, p. 95.
9. D. N. Trifonov, *Periodic System of Elements: History in Tables* (Mosk. Pravlenie Vsesoyuz. Khim. O–va im. D.I. Mendeleeva, Moscow, 1992).
10. L. Pauling, J. Am. Chem. Soc. **54**, 3570 (1932).
11. L. Pauling, *The Nature of the Chemical Bond and the Structure of Molecules and Crystals* (Cornell Univ. Press, Ithaca, 1960).
12. S. S. Batsanov, *Electronegativity of Elements and Chemical Bond* (Sib. Otd. Akad. Nauk SSSR, Novosibirsk, 1962).
13. E. Parthé, *Elements of Inorganic Structural Chemistry* (Poge Druck, Leipzig, 1990; Mir, Moscow, 1993).
14. G. B. Bokij, Mineral. Zh. **8** (3), 83 (1986).
15. M. I. Novgorodova, *Crystal Chemistry of Native Metals and Natural Intermetallic Compounds. Advances in Science and Technology. Ser. Crystal Chemistry* (VINITI, Moscow, 1994), Vol. 29.
16. F. Liebau, *Structural Chemistry of Silicates: Structure, Bonding, and Classification* (Springer-Verlag, New York, 1985; Mir, Moscow, 1988).

Translated by L. Man

Crystallography Reports, Vol. 47, No. 3, 2002, pp. 467–470. Translated from Kristallografiya, Vol. 47, No. 3, 2002, pp. 514–517.

PHASE TRANSITIONS

Balanced and Unbalanced Domain Walls in $Pb_3(PO_4)_2$

V. A. Nepochatenko

Bila Tserkva State Agrarian University, Bila Tserkva, 09117 Ukraine

e-mail: aaa@btsau.kiev.ua

Received May 16, 2001

Abstract—The equations of domain walls in the vicinity of a phase transition are obtained from the condition of the deformation balance at phase boundaries and domain walls for a ferroelastic lead orthophosphate crystal. All domain walls can be divided into three groups, in accordance with the conditions of their formation—balanced, conventionally balanced, and unbalanced domain walls. The structure of staggered domain walls is suggested. © *2002 MAIK "Nauka/Interperiodica".*

The method of calculating orientations of domain walls in ferroelastics was proposed in [1]. However, it fails to explain the whole variety of domain structures, in particular, the formation of staggered domain walls and the changes in domain structure preceding a phase transition. The influence of the type of phase transition on the formation of a domain structure in various groups of ferroelastics is studied insufficiently [2]. Therefore, it is expedient to examine the conditions of the formation of domain structure in a "pure" improper ferroelastic $Pb_3(PO_4)_2$ undergoing the first-order phase transition $R\bar{3}m \longrightarrow C2/c$.

The formation of a domain structure requires the maintenance of the balance of deformations at both the interface between the two phases and at the domain walls. Below, we analyze the conditions of such a balance in three stages—the balance at phase boundaries, the balance at a domain wall, and finally, the balance of deformations at the phase boundaries and the domain wall formed by these boundaries.

The method of calculating the orientations of phase boundaries in $Pb_3(PO_4)_2$ based on the matching of the crystal lattices of two different phases was suggested in [3]. It is shown that there are six different orientations of phase boundaries with each pair forming two close orientational states. According to the chosen crystallographic setting (the *X*-axis coincides with the *c*-axis, the *Y*-axis, with the *b*-axis), the equations of these two phase boundaries with respect to the coordinate system of the β-phase are

$$X - eY + dZ = 0, \quad (1)$$

$$X + eY + dZ = 0, \quad (2)$$

whereas the equation with respect to the coordinate system of the α-phase are

$$X' - nY' + kZ' = 0, \quad (3)$$

$$X' + nY' + kZ' = 0, \quad (4)$$

where $e = 1.1759$, $d = 0.1164$, $n = 1.1679$, and $k = 0.11675$.

Knowing the equations of the plane in two coordinate systems, one can determine the matrix of the transition (rotation) from one coordinate system to another [4]. We designate these matrixes in accordance with the orientational state they represent. The calculations are made in the coordinate system of the β-phase. Let the orientation states formed by phase boundaries (1) and (2) be C_1 and C_1', respectively. Then, the corresponding rotation matrices for the coordinate system are

$$C_1 = \begin{pmatrix} C_{11} & C_{12} & C_{13} \\ C_{21} & C_{22} & C_{23} \\ C_{31} & C_{32} & C_{33} \end{pmatrix}, \quad C_1' = \begin{pmatrix} C_{11} & -C_{12} & C_{13} \\ -C_{21} & C_{22} & -C_{23} \\ C_{31} & -C_{32} & C_{33} \end{pmatrix},$$

where

$$C_{11} = 9.999943 \times 10^{-1}, \quad C_{12} = 3.351618 \times 10^{-3},$$

$$C_{13} = 1.456987 \times 10^{-4}, \quad C_{21} = -3.351534 \times 10^{-3},$$

$$C_{22} = 9.999942 \times 10^{-1}, \quad C_{23} = -5.627930 \times 10^{-4},$$

$$C_{31} = -1.475741 \times 10^{-4}, \quad C_{32} = 5.623016 \times 10^{-4},$$

$$C_{33} = 9.999998 \times 10^{-1}.$$

Hereafter, all the values were rounded off to the sixth decimal place, but the calculations were performed to the 16th decimal place. If the absolute value was less than 1.0×10^{-15}, it was taken to be zero.

The rotation matrixes for four other orientation states, C_2, C_2', C_3, C_3', can be obtained by the formulas $C_2 = B_1C_1$, $C_2' = B_1C_1'$, $C_3 = B_2C_1$, $C_3' = B_2C_1'$, where B_1 is the rotation matrix for the coordinate system rotat-

Equations of domain walls

Adjacent orientational states	No.	Balanced domain walls	Conventionally balanced domain walls	Unbalanced domain walls
C_1–C_1'	1	$Y = 0$		
	2		$X - 0.013753Z = 0$	
C_1–C_2'	3	$X + 1.732051Y - 0.449109Z = 0$		
	4		$X - 0.577350Y = 0$	
C_1'–C_2	5	$X - 0.577350Y = 0$		
	6		$X + 1.732051Y - 0.445109Z = 0$	
C_1–C_2	7			$X + 1.718970Y - 0.445503Z = 0$
	8			$X - 0.581743Y = 0$
C_1'–C_2'	9			$X + 1.745281Y - 0.449109Z = 0$
	10			$X - 0.572973Y = 0$
C_2–C_2'	11	$X + 0.577350Y = 0$		
	12		$X - 1.732051Y - 0.027505Z = 0$	

ing about the Z-axis in the β phase through the angle $\alpha = 120°$, and B_2, the matrix of rotation through the angle $\alpha = -120°$.

The intersection of any pair of orientation states in the vicinity of a phase transition should result in a formation of an interface. Two variants are possible—the formation of a domain wall or a new orientational state separating the two initial ones.

Consider the first variant and analyze the possible orientations of the domain walls. The method of calculation suggested here is almost identical to that used in [1] except that we used the tensor of thermal expansion instead of the tensor of spontaneous deformation. Our method is based on the assumption that the deformations at domain walls must be compatible; i.e., the lengths of a vector **r** chosen at a domain wall in two adjacent orientational systems are equal. Proceed to the analysis of the change of the vector **r** caused by a jump-like change in crystal parameters (a first-order phase transition). For the β-phase, we have $r^2 = x^2 + y^2 + z^2$. For the first orientational state (the α-phase), $r_1^2 = x_1^2 + y_1^2 + z_1^2$ and

$$x_1 = (1 + a_{11})x + a_{12}y + a_{13}z,$$
$$y_1 = a_{21}x + (1 + a_{22})y + a_{23}z,$$
$$z_1 = a_{31}x + a_{32}y + (1 + a_{33})z,$$
$$a_{ij} = C_{ik}C_{jl}e_{kl},$$

where C_{ij} are the components of the transformation matrix for the given orientational state and e_{kl} are the components of the tensor of thermal expansion.

The e_{11}, e_{22}, and e_{33} values were calculated from the dilatometric data [5]; the estimated e_{13} value was determined from the equation $e_{13}^s/e_{11}^s = -\tan\theta$ [1] with the use of the data from [6].

The value of $r_2^2 = x_2^2 + y_2^2 + z_2^2$ for the second orientation state was determined in the same way. Equating r_1^2 and r_2^2, we arrive at the second-order equation

$$A_{11}x^2 + A_{22}y^2 + A_{33}z^2 + 2A_{12}xy + 2A_{13}xz + 2A_{23}yz = 0, \quad (5)$$

which corresponds, provided that $\det\{A_{ij}\} = 0$, to the equation of two intersecting planes

$$(x + By + Dz)(x + Ny + Kz) = 0.$$

Since in a first-order phase transition, the domain walls are nucleated at the sites of intersection of the phase boundaries, the domain wall and the phase boundaries should be intersected along the same straight line, otherwise the condition for the deforma-

tion balance would be violated. According to [4], three planes,

$$A_1x + B_1y + C_1z + D_1 = 0,$$

$$A_2x + B_2y + C_2z + D_2 = 0,$$

$$A_3x + B_3y + C_3z + D_3 = 0$$

are intersected along the same straight line if

$$\det S = \begin{vmatrix} A_1 & B_1 & C_1 \\ A_2 & B_2 & C_2 \\ A_3 & B_3 & C_3 \end{vmatrix} = 0. \quad (6)$$

The above arguments allow one to obtain the equations for domain walls for various combinations of adjacent orientational states C_1, C_2, C_1', C_2'. We analyzed condition (6) for each domain wall and tabulated the results obtained (see table).

The equations of domain walls can be classified in the following way: *balanced domain walls* for which conditions (5) and (6) are fulfilled; *conventionally balanced domain walls* for which condition (5) is fulfilled but condition (6) is not; and *unbalanced domain walls* for which $\det\{A_{ij}\} = -4.6 \times 10^{-10}$ (for balanced domain walls $\det\{A_{ij}\} = 8.7 \times 10^{-22}$; i.e., it had a value close but not equal to zero. Such domain walls can be formed only at small deformations. It should be mentioned that condition (6) for domain wall no. 7 is very sensitive to the value of e_{13} (to the 14th decimal place). This condition is fulfilled at $e_{13} = 7.56269834025012 \times 10^{-4}$. Since the estimated e_{13} value (9.8×10^{-4}) is close to the calculated one, it was used for the final analysis.

The equations of domain walls separating the orientational states C_1–C_3, C_1–C_3', C_1'–C_3, C_1'–C_3', C_2–C_3, C_2–C_3', C_2'–C_3, C_2'–C_3' can be obtained by applying to the equations of domain walls (see table) the operation of the rotation of the coordinate system about the Z-axis through the angle $\alpha = \pm 120°$.

Since the conditions of the balance of deformations at domain walls and between the phase boundaries and the domain walls are fulfilled, the domain walls are formed in a phase transition. The conventionally balanced walls can be formed because of domain restructuring (in the absence of phase boundaries). The unbalanced domain walls are formed because of mechanical stresses.

Now, analyze in detail the equations of domain walls and compare them with the experimental results.

The balanced domain walls (nos. 3, 5 in table) are observed along the symmetry elements of the β-phase that are absent in the adjacent domains (the "lost" symmetry elements), which is consistent with the experimental data [7].

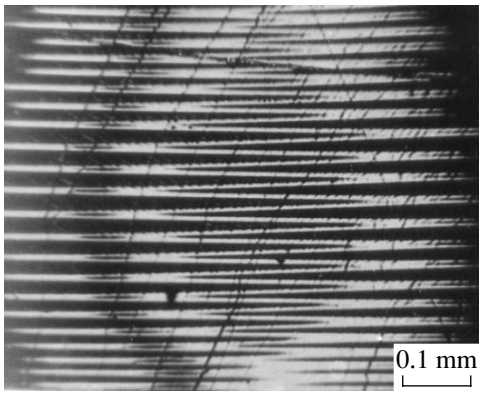

Staggered (Z'-type) domain wall; the (001) plane, $T = 25°C$.

The balanced (nos. 1, 11) and conventionally balanced (nos. 2, 12) domain walls are arranged along the symmetry elements of the β-phase that are not lost in the phase transition. These walls have not been observed experimentally. Their identification is hindered by the fact that they separate very close orientational systems; moreover, their orientation coincides with the orientation of the balanced domain walls separating the systems C_2–C_3', C_2'–C_3, C_1'–C_3, C_1–C_3'. The conventionally balanced domain walls (nos. 4, 6) have not been observed experimentally. It is most probable that their formation is forbidden by the structure of the W and W' domain walls.

Unbalanced domain walls nos. 8 and 10 are arranged symmetrically at a small angle φ to balanced walls no. 5 and walls similar to domain (7, 9)–3, respectively. The angle φ increases with an increase in spontaneous deformation and attains a value of ~2° at room temperature.

The analysis shows that the staggered Z'-domain structure (see figure) consists of unbalanced domain walls nos. 7 and 9. The angle between the traces of these domain walls on the (001) plane at the temperature of the phase transition is $\beta = 2\varphi = 0.376°$. Assuming that this angle is proportional to the spontaneous deformation, then, at room temperature, $\beta = 3.4°$ (the experimental value is ~4°). The staggered structure of the Z-type domain wall formed by walls nos. 8 and 10 is similar.

Domain restructuring preceding the phase transition occurs in the presence of unbalanced or conventionally balanced domain walls.

Thus, the first-order phase transition in a pure improper ferroelastic is accompanied by the rotation of the crystallographic axes due to lattice mismatch of the two phases. Thus, each possible orientational state [8, 9] can have two close orientations depending on the phase boundary forming this state. In addition to balanced domain walls, unbalanced domain walls are also formed whose orientation does not coincide with the

symmetry elements inherent in the initial phase. The restructuring of the domains is associated mainly with these domain walls.

REFERENCES

1. J. Sapriel, Phys. Rev. B **12** (11), 5128 (1975).
2. L. A. Shuvalov, Izv. Akad. Nauk SSSR, Ser. Fiz. **43** (8), 1554 (1979).
3. E. F. Dudnik and V. A. Nepochatenko, Kristallografiya **25**, 984 (1980) [Sov. Phys. Crystallogr. **25**, 564 (1980)].
4. G. A. Korn and T. M. Korn, *Mathematical Handbook for Scientists and Engineers* (McGraw-Hill, New York, 1968; Nauka, Moscow, 1974).
5. J. C. Toledano, Mater. Res. Bull. **10** (2), 103 (1975).
6. C. Joffrin, J. P. Benoit, L. Deschamps, and M. Lambert, J. Phys. (Paris) **38** (2), 205 (1977).
7. M. Chabin, J. P. Ildefonse, and F. Gilletta, Ferroelectrics **13**, 333 (1976).
8. K. Aizu, J. Phys. Soc. Jpn. **27** (2), 387 (1969).
9. V. Janovec, Ferroelectrics **12**, 43 (1976).

Translated by A. Zalesskiĭ

Crystallography Reports, Vol. 47, No. 3, 2002, pp. 471–474. Translated from Kristallografiya, Vol. 47, No. 3, 2002, pp. 518–521.

REAL STRUCTURE OF CRYSTALS

Diffuse Scattering from Crystals with Point Defects

N. M. Andrushevsky*, B. M. Shchedrin*, L. F. Malakhova, and V. I. Simonov***

**Faculty of Computational Mathematics and Cybernetics, Moscow State University, Leninskie gory, Moscow, 119992 Russia*

e-mail: nandrush@cs.msu.su

***Shubnikov Institute of Crystallography, Russian Academy of Sciences, Leninskiĭ pr. 59, Moscow, 117333 Russia*

Received July 11, 2001

Abstract—The analytical expressions for calculating the intensities of X-ray diffuse scattering from a crystal of finite dimensions and monatomic substitutional, interstitial, or vacancy-type point defects have been derived. The method for the determination of the three-dimensional structure by experimental diffuse-scattering data from crystals with point defects having various concentrations is discussed and corresponding numerical algorithms are suggested. © *2002 MAIK "Nauka/Interperiodica".*

Since the time of the discovery of diffuse scattering, the use of this effect for determining the characteristics of defects in crystals has attracted the attention of researchers. Thus, Krivoglaz cites more than 717 publications to the effect in his famous monograph on diffuse scattering [1]. The sections dedicated to diffuse scattering are also included in some other books [2, 3]. In recent years, interest in diffuse scattering has continuously increased for several reasons. The main one is that the character and structure of defects in crystals essentially influence many of the physical properties of crystals and are very important for the establishment of regular relationships between the structure and properties of crystals. The second reason for analyzing diffuse scattering is the fact that, today, the methods of classical structure analysis (based on the consideration of the intensities of Bragg reflections) are so accurate that the results of the study are essentially dependent on the real structure of the sample. And, finally, recent progress in science and, first and foremost, the creation of new sources of X-ray synchrotron radiation, position-sensitive detectors, and powerful computers have made the use of diffuse scattering more accessible and reliable.

However, there is no direct method of extracting information on defects in crystals from the distribution of diffuse-scattering intensity. Like the early stages of classical structure analysis, the interpretation of diffuse-scattering data is based on the trial and error method. A researcher constructs the models of defects, then, using these models, calculates diffuse scattering and compares the results obtained with the experimental diffuse-scattering data. The availability of powerful computers stimulates the use of the Monte Carlo method—the exhaustion of all the possible parameters of defects and their distribution in the crystal space [4]. Numerous examples of the extraction of information on defects in crystals from diffuse-scattering data can be found elsewhere [5–7]. Once the model of a defect is established, one can apply the well-known algorithms and programs for its refinement by the least squares method using the known experimental diffuse-scattering data [8].

The great variety of defects in crystals does not allow the creation of a unique approach and a general algorithm for the interpretation of diffuse-scattering data for all types of defects. Therefore, various approaches are developed for each type of defect that take account of the specific features and the nature of these defects.

Below, we consider crystals only with point (monatomic) defects of vacancy-, substitution-, and interstitial-types. It is assumed that the structure of the mother crystal without defects is known and that a formed point defect gives rise to the displacements of the atoms from their positions only within the first coordination sphere. It is also assumed that the displacements of atoms located at longer distances from the defect are infinitesimal, the unit-cell parameters are constant, all the unit cells with defects have the same spatial structure, and that the defects are distributed over the crystal arbitrarily. Then, the problem is formulated as the determination of the spatial structure of the unit cells with defects from the experimental data on diffuse scattering.

Consider a crystal of finite dimensions in the shape of a parallelepiped consisting of $N = N_1N_2N_3$ unit cells of which M unit cells have some defects in the regular structure—the point defects. Introduce the following notation: $J_d = \{\mathbf{m}_1, \mathbf{m}_2, \ldots, \mathbf{m}_M\}$ is the set of integer-valued coordinates of the unit cells with defects and $J_u = \{\mathbf{k}_1, \mathbf{k}_2, \ldots, \mathbf{k}_{N-M}\}$ is the set of coordinates of the unit cells without defects. Obviously, $J_i = J_d \cup J_u = \{\mathbf{n}_1, \mathbf{n}_2, \ldots, \mathbf{n}_N\}$ are the coordinates of all the unit cells of the crystal irrespec-

1063-7745/02/4703-0471$22.00

tive of the presence or absence of defects. Now, let $\rho_d(\mathbf{r})$ and $\rho_u(\mathbf{r})$ be the atomic electron densities in the unit cells with and without defects, respectively, and $F_d(\mathbf{h})$ and $F_u(\mathbf{h})$ be the corresponding structure factors. The electron density of a crystal of finite dimensions can be obtained as the convolution of $\rho_d(\mathbf{r})$ and $\rho_u(\mathbf{r})$ with δ-lattices of the sets J_d and J_u [9], i.e., as $\rho(\mathbf{r}) = \rho(\mathbf{r}, J_d) + \rho(\mathbf{r}, J_u)$. Using the well-known theorem on Fourier transform of the convolution of the functions [10], we arrive at the structure factor of the electron density of the crystal in the form

$$F(\mathbf{h}) = F_d(\mathbf{h})D_d(\mathbf{h}) + F_u(\mathbf{h})D_u(\mathbf{h}). \quad (1)$$

The diffuse-scattering intensity is

$$\begin{aligned} I_{dif}(\mathbf{h}) &= |F(\mathbf{h})|^2 = |F_d(\mathbf{h})|^2 L_d(\mathbf{h}) \\ &+ F_d(\mathbf{h})F_u^*(\mathbf{h})D_d(\mathbf{h})D_u^*(\mathbf{h}) \\ &+ F_d^*(\mathbf{h})F_u(\mathbf{h})D_d^*(\mathbf{h})D_u(\mathbf{h}) + |F_u(\mathbf{h})|^2 L_u(\mathbf{h}), \end{aligned} \quad (2)$$

where

$$L_d(\mathbf{h}) = |D_d(\mathbf{h})|^2, \quad L_u(\mathbf{h}) = |D_u(\mathbf{h})|^2.$$

Hereafter, the asterisk denotes the complex-conjugate quantity. The functions

$$D_d(\mathbf{h}) = \sum_{\mathbf{m} \in J_d} \exp[-i2\pi(\mathbf{h}, \mathbf{m})],$$

$$D_u(\mathbf{h}) = \sum_{\mathbf{k} \in J_u} \exp[-i2\pi(\mathbf{h}, \mathbf{k})]$$

are in fact the Fourier transforms (structure factors) of the δ-lattices determined by the sets J_d and J_u, respectively. Equation (2) is the natural generalization of the expression for the intensity scattered from an ideal crystal of finite dimensions for which

$$F(\mathbf{h}) = F_u(\mathbf{h})D_i(\mathbf{h}), \quad I(\mathbf{h}) = |F_u(\mathbf{h})|^2 L_i(\mathbf{h}),$$

where

$$D_i(\mathbf{h}) = \sum_{\mathbf{n} \in J_i} \exp[-i2\pi(\mathbf{h}, \mathbf{n})]$$

is the Fourier transform (structure factor) of an ideal δ-lattice and

$$L_i(\mathbf{h}) = |D_i(\mathbf{h})|^2 = \prod_{j=1}^{3} \left(\frac{\sin(\pi h_j N_j)}{\sin(\pi h_j)} \right)^2$$

is the Laue interference function. As is well known [11], the functions $D_i(\mathbf{h})$ and $L_i(\mathbf{h})$ possess a number of remarkable properties. Consider the most important ones.

The functions $D_i(\mathbf{h})$ and $L_i(\mathbf{h})$ are periodic,

$$D_i(\mathbf{h}) = D_i(\mathbf{h} + \mathbf{q}), \quad L_i(\mathbf{h}) = L_i(\mathbf{h} + \mathbf{q}),$$

where $\mathbf{q}$ are the reciprocal-space vectors with integer-valued coordinates (the Bragg points).

In all the Bragg points, these functions have the constant values

$$D_i(\mathbf{q}) = N, \quad L_i(\mathbf{q}) = N^2. \quad (3)$$

At the reciprocal-space points outside the Bragg ones, we have

$$D_i(\mathbf{h} \neq \mathbf{q})/D_i(\mathbf{q}) \approx 1/N, \quad L_i(\mathbf{h} \neq \mathbf{q})/L_i(\mathbf{q}) \approx 1/N^2. \quad (4)$$

Thus, almost the whole integrated scattering intensity is concentrated in the Bragg points

$$\sum_{\mathbf{q}} I(\mathbf{q}) \approx \int I(\mathbf{h}) d\mathbf{h}.$$

Because of the above properties, the experimental intensities form a rigorously discrete set of $\{I(\mathbf{q})\}$ values measured at the reciprocal-space points with the integer-valued coordinates. As is well known, this information is quite sufficient for the construction of the synthesis of the electron-density convolution in one unit cell (the so-called Patterson function). The methods of interpretation of the Patterson function have been developed in the classical structure analysis [12].

Now, proceed to the analysis of the analytical expression of the diffuse-scattering intensity from crystals containing point defects. The functions $D_d(\mathbf{h})$, $L_d(\mathbf{h})$ and $D_u(\mathbf{h})$, $L_u(\mathbf{h})$ possess similar properties,

$$\begin{aligned} D_d(\mathbf{h}) &= D_d(\mathbf{h} + \mathbf{q}), \quad L_d(\mathbf{h}) = L_d(\mathbf{h} + \mathbf{q}), \\ D_u(\mathbf{h}) &= D_u(\mathbf{h} + \mathbf{q}), \quad L_u(\mathbf{h}) = L_u(\mathbf{h} + \mathbf{q}), \\ D_d(\mathbf{q}) &= M, \quad L_d(\mathbf{q}) = M^2, \\ D_u(\mathbf{q}) &= N - M, \quad L_u(\mathbf{q}) = (N - M)^2. \end{aligned} \quad (5)$$

However, there are also some essential differences, namely:

$$\begin{aligned} D_d(\mathbf{h} \neq \mathbf{q})/D_d(\mathbf{q}) &\neq (\approx) 1/M, \\ L_d(\mathbf{h} \neq \mathbf{q})/L_d(\mathbf{q}) &\neq (\approx) 1/M^2, \\ D_u(\mathbf{h} \neq \mathbf{q})/D_u(\mathbf{q}) &\neq (\approx) 1/(N - M), \\ L_u(\mathbf{h} \neq \mathbf{q})/L_u(\mathbf{q}) &\neq (\approx) 1/(N - M)^2, \end{aligned} \quad (6)$$

$$\sum_{\mathbf{q}} I(\mathbf{q}) \neq \int I(\mathbf{h}) d\mathbf{h}. \quad (7)$$

Relationships (6) and (7) reflect the fact that the diffuse-scattering intensity is distributed over the whole reciprocal space, whereas the character of the intensity distribution depends on the distribution of defect-containing unit cells over the crystal.

The interpretation of diffuse-scattering data consists in the following. Since it is impossible to construct a sufficiently representative synthesis of the Patterson function (the convolution of the electron density of the whole crystal) because of the insufficient resolution of the experimental data, the problem of the interpretation of such syntheses becomes even more difficult. The use of Eq. (2) for numerical modeling and the comparison of the models with the experimental data is very time-consuming (the Monte Carlo method [4]). The use of a priori known functions of the statistical distribution of the distances between the unit cells with defects or the microdomains of such unit cells (in the case of their random uniform distribution) allows one to considerably reduce the number of unknown parameters and to solve the problem by one of the known methods [7]. However, the result thus obtained can be essentially dependent on the form of the predicted distributions, whose adequate selection is an independent problem.

A more promising approach seems to be the solution of the general problem of determining the structure of a crystal with defects in several stages. At the first stage, one has to determine the spatial structure of the unit cells with point defects. At the second stage, one determines the characteristics of the spatial distribution of unit cells with defects.

With this aim, we have to write the formulas for the analytical calculation of the diffuse-scattering intensities in a more constructive way by using the technique of the compensation of the electron density to the electron density of an ideal crystal of finite dimensions. The electron density $\rho_d(\mathbf{r})$ of the unit cell with a defect can be represented in the following equivalent form:

$$\rho_d(\mathbf{r}) \equiv \rho_u(\mathbf{r}) + \hat{\rho}_d(\mathbf{r}),$$

where

$$\hat{\rho}(\mathbf{r}) = \rho_d(\mathbf{r}) - \rho_u(\mathbf{r}) \quad (8)$$

is the corrected electron density of the unit cell with a defect (with the "compensating subtraction"). Then, the total electron density of the crystal is the sum of the corrected electron density of all the unit cells with defects and the electron density of an ideal crystal

$$\rho(\mathbf{r}) = \hat{\rho}(\mathbf{r}, J_d) + \rho(\mathbf{r}, J_i).$$

Then, the structure factor of the electron density of the whole crystal is

$$F(\mathbf{h}) = \hat{F}_d(\mathbf{h})D_d(\mathbf{h}) + F_u(\mathbf{h})D_i(\mathbf{h}),$$

where, in accordance with Eq. (8),

$$\hat{F}_d(\mathbf{h}) = F_d(\mathbf{h}) - F_u(\mathbf{h}). \quad (9)$$

Now, the diffuse-scattering intensity can be written as

$$I_{dif}(\mathbf{h}) = \left|\hat{F}_d(\mathbf{h})\right|^2 L_d(\mathbf{h}) + \hat{F}_d(\mathbf{h})F_u^*(\mathbf{h})D_d(\mathbf{h})D_i^*(\mathbf{h}) \quad (10)$$
$$+ \hat{F}_d^*(\mathbf{h})F_u(\mathbf{h})D_d^*(\mathbf{h})D_i(\mathbf{h}) + \left|F_u(\mathbf{h})\right|^2 L_i(\mathbf{h}).$$

Equation (10) has a number of advantages over Eq. (2).

Based on Eqs. (3) and (5), the intensities at the Bragg points acquire a simpler form

$$I(q) = N^2\Big[c^2|F_d|^2 + 2c(1-c)(A_dA_u + B_dB_u) + (1-c)^2|F_u|^2\Big], \quad (11)$$

where $c = M/N$ is the concentration of the unit cells with defects and $F_d(\mathbf{q}) = A_d(\mathbf{q}) + iB_d(\mathbf{q})$ and $F_u(\mathbf{q}) = A_u(\mathbf{q}) + iB_u(\mathbf{q})$ are the structure factors of the electron densities in the unit cells with and without defects, respectively.

Equation (11) reflects the fact that the intensities of the Bragg reflections are independent of the character of the distribution of the unit cells with defects over the crystal; they depend only on the concentration of these unit cells. The expression in brackets in Eq. (11) is, in fact, the structure factor (Fourier transform) of the generalized Patterson function,

$$P(\mathbf{r}) = c^2[\rho_d(\mathbf{r}) \otimes \rho_d(\mathbf{r})] + 2c(1-c)[\rho_d(\mathbf{r}) \otimes \rho_u(\mathbf{r})] + (1-c)^2[\rho_u(\mathbf{r}) \otimes \rho_u(\mathbf{r})], \quad (12)$$

obtained as a result of the convolution of the function in the form of the combination of two electron densities with weights $\rho(\mathbf{r}) = c\rho_d(\mathbf{r}) + (1-c)\rho_u(\mathbf{r})$.

The expediency of using the intensities of Bragg reflections for determining the atomic structure of the unit cells with point defects depends on their concentration.

It follows from Eq. (11) that the contribution to the intensities of the Bragg reflections that comes from the unit cells with defects at $c > 0.7$ exceeds the total contribution from the unit cells without defects and their "correlation contribution." Therefore, the generalized Patterson syntheses described by Eq. (12) clearly reveal the images of the atomic structure of the unit cell with a defect. Thus, for the crystal structure of the composition $K(D_{0.95}, H_{0.05})_2[PO_4]$, we have

$$I(\mathbf{q}) = N^2\Big[0.9025|F_d|^2 + 0.095(A_dA_u + B_dB_u) + 0.0025|F_u|^2\Big]$$

and, therefore, the synthesis of the generalized Patterson function consists of three components,

$$P(\mathbf{r}) = 0.9025P_d(\mathbf{r}) + 0.095P_{du}(\mathbf{r}) + 0.0025P_u(\mathbf{r}). \quad (13)$$

In this case, the superposition analysis of Patterson function (13) readily localizes the hydrogen and deuterium atoms, because in the case of the replacement of hydrogen by deuterium, the displacements of all the other atoms are insignificant and cannot substantially change the vector system of interatomic distances. Then, one has to refine the positions of all the atoms in the unit cell with a defect by the least squares method with the use of Eq. (11) for the parametric modeling.

In the concentration range $0.3 < c < 0.7$, Eq. (11) has no dominating term, which considerably hinders the analysis of the Patterson function. If the suggested model of the spatial structure is correct, then it can be refined by the least squares method.

At defect concentrations $c < 0.3$, the refinement of the atomic parameters for the unit cell with a defect can fail even if the spatial model is correct. In this case, one has to consider diffuse-scattering intensities outside the Bragg points.

According to (4), at the reciprocal-space points outside the Bragg ones, the functions $D_i(\mathbf{h})$ and $L_i(\mathbf{h})$ have infinitesimal values. Therefore, ignoring the three last terms in Eq. (10), we arrive at an approximate expression for the diffuse scattering intensity:

$$I_{dif}(\mathbf{h} \neq \mathbf{q}) \cong \left|\hat{F}_d(\mathbf{h})\right|^2 L_d(\mathbf{h}). \quad (14)$$

It should be emphasized that, unlike Eq. (10), formula (14) uses the effective structure factor described by Eq. (9). The property of periodicity possessed by the function $L_d(\mathbf{h})$ allows one to ignore, at the first stage, the influence of the defect distribution over the crystal space. Thus, we can use the following expression:

$$\frac{I_{dif}(\mathbf{h}+\mathbf{q})}{I_{dif}(\mathbf{h})} \cong \frac{\left|\hat{F}_d(\mathbf{h}+\mathbf{q})\right|^2 L_d(\mathbf{h}+\mathbf{q})}{\left|\hat{F}_d(\mathbf{h})\right|^2 L_d(\mathbf{h})} = \frac{\left|\hat{F}_d(\mathbf{h}+\mathbf{q})\right|^2}{\left|\hat{F}_d(\mathbf{h})\right|^2}. \quad (15)$$

Then, we can create a file of the experimental $\frac{I^e_{dif}(\mathbf{h}+\mathbf{q})}{I^e_{dif}(\mathbf{h})}$ values and use Eq. (15) in the functional of the least squares procedure to refine the atomic-structure parameters in the unit cell with point defects.

Based on the analytical formula for the diffuse-scattering intensity derived above and its analysis, we suggested the algorithms for the determination of the nature of defects in the unit cell depending on their concentration in the crystal. Thus, it is shown that the problem of determining the spatial structure of the unit cells with substitutional or interstitial atoms or vacancies (point defects) can now be solved by the methods of classical structure analysis, including the study of the generalized Patterson function and the refinement of the atomic structure of the unit cell with a point defect by the least squares method.

The method for the determination of the $L_d(\mathbf{h})$ function characterizing the distribution of defects in the crystal space is an independent problem and will be considered in our next publication.

ACKNOWLEDGMENTS

This study was supported by the Russian Foundation for Basic Research, project no. 00-02-17557 and the Federal Program on Support of Prominent Scientists and Leading Scientific Schools, project no. 00-15-96663.

REFERENCES

1. M. A. Krivoglaz, *Diffuse Scattering of X-rays and Neutrons by Fluctuation Irregularities in Real Crystals* (Naukova Dumka, Kiev, 1984).
2. A. Guinier, *Théorie et technique de la radiocristallographie* (Dunod, Paris, 1956; Fizmatgiz, Moscow, 1961).
3. V. I. Iveronova and G. P. Revkevich, *Theory of X-ray Scattering* (Mosk. Gos. Univ., Moscow, 1972).
4. T. R. Welberry, Th. Proffen, and M. Bown, Acta Crystallogr., Sect. A: Foundam. Crystallogr. **54**, 661 (1998).
5. F. Frey, Acta Crystallogr., Sect. B: Struct. Sci. **51**, 592 (1995).
6. R. B. Neder, F. Frey, and H. Schulz, Acta Crystallogr., Sect. A: Found. Crystallogr. **46**, 799 (1990).
7. R. B. Neder, F. Frey, and H. Schulz, Acta Crystallogr., Sect. A: Found. Crystallogr. **46**, 792 (1990).
8. S. Hull and C. C. Wilson, J. Solid State Chem. **100**, 101 (1992).
9. B. K. Vainshtein, *Diffraction of X-rays by Chain Molecules* (Akad. Nauk SSSR, Moscow, 1963; Elsevier, Amsterdam, 1966).
10. E. C. Titchmarsh, *Introduction to the Theory of Fourier Integrals* (Clarendon, Oxford, 1937; Gostekhizdat, Moscow, 1948).
11. A. I. Kitaĭgorodsky, *X-ray Structure Analysis* (Gostekhizdat, Moscow, 1950).
12. M. Buerger, *Vector Space and Its Application in Crystal-Structure Investigation* (Wiley, New York, 1959; Inostrannaya Literatura, Moscow, 1961).

Translated by L. Man

Crystallography Reports, Vol. 47, No. 3, 2002, pp. 475–479. Translated from Kristallografiya, Vol. 47, No. 3, 2002, pp. 522–526.

REAL STRUCTURE OF CRYSTALS

Statistical Characteristics of Inhomogeneities of Dislocation Networks

E. I. Gutorov

Lebedev Physical Institute, Russian Academy of Sciences, Leninskiĭ pr. 53, Moscow, 117924 Russia

Received April 25, 2001

Abstract—The distribution functions of segment lengths of dislocation networks of different origin have been analyzed using numerous experimental data. It was found that the experimental histograms are well described by the functions of the type $f^n(x) = n(nx)^{n-1}/(n-1)e^{-nx}$, where $x = l/\langle l\rangle$, l is a length of a segment of the dislocation network, $\langle l\rangle$ is its average value, and n is the number of dislocation glide systems active during the formation of the dislocation network. The most widespread dislocation networks are described by the functions $f_n(x)$, where $n = 5$. It is shown that the value of n can be determined from the type of the function $f_n(x)$. © *2002 MAIK "Nauka/Interperiodica".*

INTRODUCTION

The widespread use of epitaxy and vacuum deposition of substances in micro- and optoelectronics, along with the creation of inhomogeneous diffusion and implanted layers of micron and submicron thicknesses and areas on the same substrates, inevitably gives rise to the formation of regions of microheterogeneous plasticity and thus also stresses in electrooptic devices and integrated circuits. When relaxing, these stresses lead to the formation of various structural defects and, first of all, large dislocation networks [1–20]. The geometrical structure of dislocation networks was extensively studied [10–12]. However, no statistical analysis of the inhomogeneities of their structure has been performed as yet. At the same time, the inhomogeneities of dislocation networks give rise to the formation of local uncompensated internal stresses, which, finally, may change the electrical and the optical properties of active layers [3–5]. Below, the statistical characteristics of dislocation networks are determined by analyzing a great number of experimental data.

RESULTS OF THE STATISTICAL ANALYSIS AND DISCUSSION

We studied the statistics of the distribution of the lengths of segments l between the nodes of the dislocation networks. For each dislocation network micrograph, the measured values of l were reduced to the dimensionless lengths x using the formula

$$x_j = l_j\langle l\rangle^{-1}, \quad (1)$$

where j is the number of the segment and $\langle l\rangle$ is the average segment length in the sampling. The calculated x values in accordance with their frequencies were classified to construct the histograms for all the seventeen cases indicated in Table 1.

The statistical data on the distribution of the segment lengths for all the crystals are listed in Table 2. Analyzing these data and the corresponding 17 histograms, we drew the following conclusions. Each histogram has only one maximum corresponding to the most probable range of segment lengths: $(0.7–0.8)\langle l\rangle$. On all the histograms, the number of short segments rapidly increases, whereas the distribution of long segments decreases much more slowly.

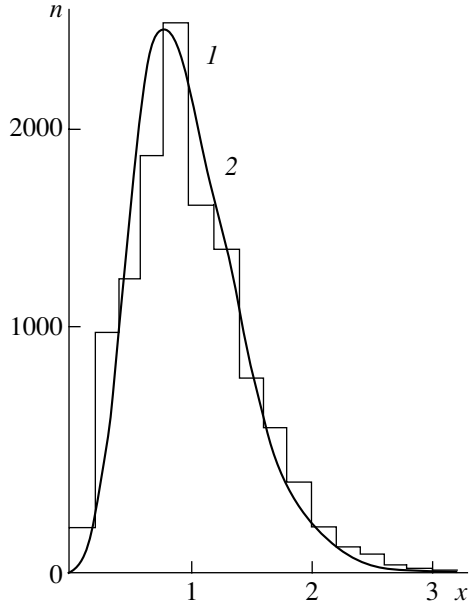

Fig. 1. (*1*) Total histogram of the distribution of reduced lengths of dislocation segments and (*2*) the corresponding approximation by the F_5-function.

1063-7745/02/4703-0475$22.00 © 2002 MAIK "Nauka/Interperiodica"

Table 1. Crystallographic and technological parameters of studied crystals

1	2	3	4	5	6	7	8	9	10	11	12	13	14	15	16	17	18
Crystal	Au	Si + P	Si + P^+		Si + B^+	Ge	CaAsSb	GaAsP		InGaAsP	MgO	Zn		CdS		Te	Ti
Reference	[4]	–	[7]	[9]	[8]	[11]	–	[13]	[14]	[15]	[16]	[17]	[18]	–	[19]	–	[20]
Symmetry	Cubic											Hexagonal					
Lattice type	f.c.c.	Diamond					Sphalerite				NaCl	h.c.p.		Wurtzite		h.c.p. with a screw axis	
Group of periodic system	I	IV					III, V				II, VI	II		II, VI		VI	
Nature of chemical bond	Metallic	Covalent					Covalent–ionic				Ionic	Metallic		Covalent		Metallic	
Melting point, °C	1063	1410				937	500				2825	420		1405		449	1658
Orientation	[001]	[111]		[001]	[111]	[111]	[001] [111]	[001]	[113A]	[111]	[110]	[0001]				[$10\bar{1}0$]	
Technological process	Sintering	Diffusion	Ion implantation			Stretching	Liquid phase epitaxy				Stretching	Ultrasonic vibration	Rolling	Electron irradiation	Uniaxial compression		Extrusion
Dislocation density, cm^{-2}	10^{11}	$\approx 10^9$											$\approx 10^{10}$				$\approx 10^9$
Dislocation type	Screw	Edge				73°-dislocations	60°-dislocations				Screw					Edge	Screw
Geometry of the dislocation network	Rectangular	Complex	Hexagonal	Rectangular	Hexagonal	Rectangular	Rectangular		Complex	Rectangular	Hexagonal					Complex	Hexagonal
Average length of segments, nm	18	180	278	792	424	175	171	504	226	368	160	215	91.2	110	700	144	293
Atomic weight	197	28.08				~73	~144.64				40.3	65.37		144.46		~128	~48
Illuminated volume of the crystal, $cm^3 \times 10^{12}$	7.7×10^{-3}	20	4.2	12	4.46	7.4	1.0	1.0	7	1.3	1.2	5.2×10^{-1}	2.6×10^{-1}	1.0	2	5.3	2

Table 2. Frequencies of reduced lengths of dislocation segments for studied crystals

1	2	3	4	5	6	7	8	9	10	11	12	13	14	15	16	17
x_j	Frequencies of reduced lengths of dislocation segments, n_j													$\Sigma n_j = N_j$	$N_j/11843$	α
	Au	Si + P	Si + P^+	Si + B^+	Ge	A^3B^5	MgO	Zn(17)	Zn(18)	CdS	CdS(18)	Te	Ti			
0–0.19	0	77	17	0	0	95	0	0	0	0	0	13	0	205	0.01731	0.01731
0.2–0.39	0	385	71	3	7	443	4	0	5	32	24	37	22	1033	0.08722	0.10453
0.4–0.59	18	550	48	19	8	400	0	30	12	70	34	34	31	1254	0.10588	0.21041
0.6–0.79	61	748	136	26	63	483	57	39	11	70	40	33	6	1773	0.1497	0.36011
0.8–0.99	174	792	257	53	60	481	97	164	85	62	28	22	57	2332	0.1969	0.55701
1.0–1.19	84	737	122	35	36	290	0	96	42	49	20	15	38	1564	0.1321	0.68911
1.2–1.39	88	561	165	44	33	254	37	48	8	49	23	6	57	1373	0.11593	0.80504
1.4–1.59	33	440	83	19	21	166	18	10	0	10	15	4	7	826	0.069776	0.87479
1.6–1.79	28	297	35	1	4	197	0	6	14	6	14	2	19	623	0.052605	0.9274
1.8–1.99	11	165	22	3	5	129	2	0	7	6	12	10	10	382	0.03226	0.9596
2.0–2.19	13	60	5	0	3	88	0	0	4	2	11	2	10	199	0.0168	0.9764
2.2–2.39	1	10	4	0	0	82	0	0	0	3	7	3	4	114	0.009626	0.9861
2.4–2.59	2	11	1	0	1	53	2	0	5	2	8	0	4	89	0.007515	0.9936
2.6–2.79	0	0	1	0	0	17	0	0	3	0	0	3	1	25	0.0022111	0.9957
2.8–2.99	0	0	0	0	2	17	0	0	0	0	0	1	0	20	0.001689	0.9974
3.0–3.19	0	0	0	0	0	8	0	0	0	0	0	1	0	9	0.0007599	0.99815
3.2–3.39	0	0	0	0	0	4	0	0	3	0	0	0	0	7	0.0005911	0.9987
3.4–3.59	0	0	0	0	0	2	0	0	0	0	0	0	0	2	0.0001689	0.9989
3.6–3.79	0	0	0	0	0	3	0	0	0	0	0	0	0	3	0.0002533	0.99916
3.8–3.99	0	0	0	0	0	1	0	0	0	0	0	2	0	3	0.0002533	0.99942
4.0–4.19	0	0	0	0	0	5	0	0	0	0	0	0	0	5	0.0004222	0.99984
4.2–4.39	0	0	0	0	0	2	0	0	0	0	0	0	0	2	0.0001689	1.00
Total	513	4833	958	203	203	3220	243	393	199	364	236	188	266	11843	1.00	–

The dislocation networks have different geometries for different crystals, plane indices, and methods of layer application. It is explained by the nature of relaxation of stresses formed during the deposition of surface layers described in numerous monographs. Below, we make an attempt to reveal some general characteristics inherent in all the networks.

The analysis of the images of dislocation networks shows that all the dislocation networks are topologically irregular and inhomogeneous. Although some fragments are almost periodic, e.g., in PbS/PbTe [2], Si + P^+ [7], and in zinc [15], the common feature of all the dislocation networks is the statistical distribution for all the main parameters of dislocation networks (segment lengths, the angles between these segments at the nodes) irrespective of the bond type, the system of the crystal, and the technological process during which these networks are formed. The theory of dislocation structures states that for any complicated stress state the existence of only five glide systems is sufficient to pro-

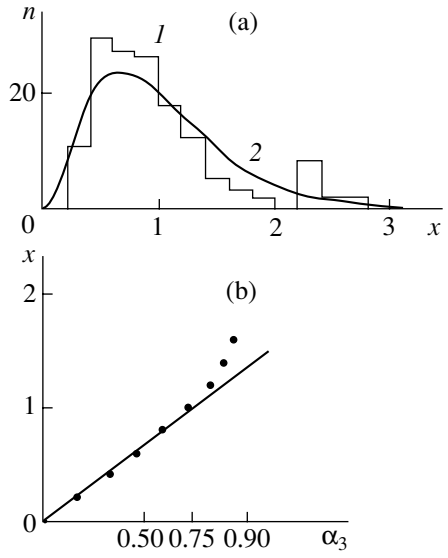

Fig. 2. (a) (*1*) Histogram of the distribution of the reduced lengths of dislocation segments in Te and the corresponding approximation by (*2*) the F_3-function and (b) the probabilistic line.

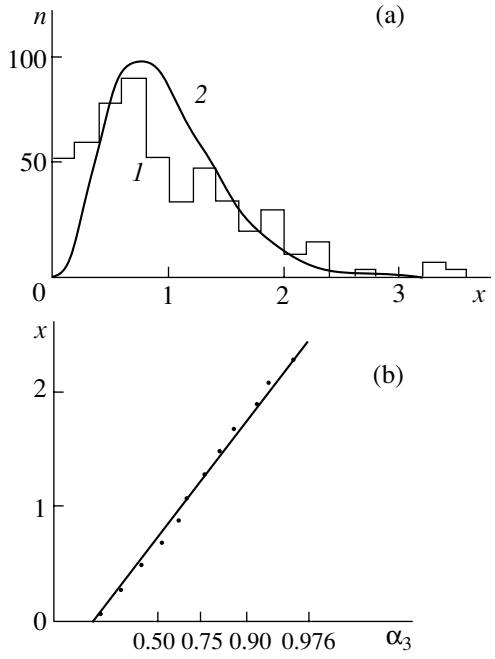

Fig. 3. (*1*) Histogram of the distribution of the reduced lengths of dislocation segments in GaAlSb/GaSb(100) epitaxial films, (*2*) its approximation by the F_4-function (a) and (b) the probabilistic line.

vide any deformation. Thus, we can assume that the probability density of the segment-length distribution obeys the following law:

$$F(x) = \frac{5^5}{4}x^4 l^{-5x}. \quad (2)$$

Distribution (2) has the maximum at the point $x = 0.8$. Comparing the total experimental distribution and the distribution calculated by Eq. (2) (Fig. 1), we see their good agreement. Thus, the statistical characteristics of the ensemble of segment lengths (which is, in fact, a mixture of various dislocation structures) may be described by the effect of five equivalent glide systems. If the number of active glide systems at the heteroboundary is less than five, the distribution of segment lengths in the dislocation network can be compared with the following formula used for calculation:

$$Fn(x) = \frac{n(nx)^{n-1}}{(n-1)}l^{-nx}, \quad (3)$$

where n is the number of the active glide systems.

Thus, it becomes possible to analyze the specific features of generation of dislocations in different glide systems by considering the deviation of the experimental length distribution from that given by Eq. (3).

The latter assumption was verified experimentally on the dislocation networks formed in plastically deformed Te and at the boundary of the GaSb/GaAlSb(100) heterostructure obtained by the method of the liquid phase epitaxy.

In accordance with the experimental conditions (Table 1), three glide systems were active in Te and four glide systems, in GaAlSb film. The corresponding histograms and the probabilistic lines in Figs. 2 and 3 are qualitatively described by the F_3- and F_4-distributions, respectively.

ACKNOWLEDGMENTS

The author is grateful to A.A. Alekseev, V.L. Indenbom†, V.I. Nikitenko, and Yu.M. Popov for their interest in this study.

REFERENCES

1. M. G. Mil'vidskiĭ and V. B. Osvenskiĭ, *Structural Defects in Epitaxial Semiconductor Layers* (Metallurgiya, Moscow, 1985).
2. Yu. A. Tkhorik and L. S. Khazan, *Plastic Deformation and Misfit Dislocations in Heteroepitaxial Structures* (Naukova Dumka, Kiev, 1983).
3. G. Z. Nemtsev, A. I. Pekarev, Yu. D. Chistyakov, *et al.*, Zarubezh. Élektron. Tekh., No. 11, 3 (1981).
4. T. Shober and R. W. Balluffi, Philos. Mag. **21** (169), 109 (1970).
5. H. F. Matare, *Defect Electronics in Semiconductors* (Wiley, New York, 1971; Mir, Moscow, 1974).
6. M. Z. Joshi, C. H. Ma, and J. Makris, J. Appl. Phys. **38** (2), 725 (1967).
7. G. V. Akulova and L. A. Koledov, in *Proceedings of X All-Union Conference on Electron Microscopy* (Tashkent, 1976), Vol. 1, p. 124.

† Deceased.

8. V. V. Kalinin, N. N. Gerasimenko, and S. S. Stenin, Fiz. Tverd. Tela (Leningrad) **18** (9), 2803 (1976) [Sov. Phys. Solid State **18**, 1637 (1976)].
9. M. P. A. Viegers, S. W. Bulle-Lienwma, and W. J. Bartels, Physica B (Amsterdam) **116**, 612 (1983).
10. V. L. Indenbom and G. N. Dubnova, Fiz. Tverd. Tela (Leningrad) **9** (4), 1171 (1967) [Sov. Phys. Solid State **9**, 915 (1967)].
11. M. M. Myshlyaev, M. Kh. Khannanov, and I. I. Khodos, Izv. Akad. Nauk SSSR, Ser. Fiz. **38** (11), 2389 (1974).
12. J. P. Hirth and J. Lothe, *Theory of Dislocations* (McGraw-Hill, New York, 1967; Atomizdat, Moscow, 1972).
13. S. S. Ahearn and C. Laird, J. Mater. Sci. **12** (4), 699 (1977).
14. S. Mader and A. E. Blakesle, IBM J. Res. Dev. **19** (2), 151 (1975).
15. Yu. B. Bolkhovityanov, Yu. D. Vaulin, A. K. Gutakovskiĭ, *et al.*, Izv. Akad. Nauk SSSR, Ser. Fiz. **44** (6), 1238 (1980).
16. R. J. Stokes and C. H. Li, Discuss. Faraday Soc. **38**, 233 (1964).
17. G. M. Zinenkova and N. A. Tyapunina, Fiz. Met. Metalloved. **28** (4), 637 (1969).
18. S. Amelinckx, *The Direct Observation of Dislocations* (Academic, New York, 1964; Mir, Moscow, 1968), Solid State Physics, Suppl. 6.
19. Ju. A. Osipyan, V. F. Petrenko, and G. K. Strukova, Phys. Status Solidi A **57**, 477 (1980).
20. S. P. Agrawal, Metall. Trans. **5**, 2415 (1974).

Translated by V. Semenov

Crystallography Reports, Vol. 47, No. 3, 2002, pp. 480–483. Translated from Kristallografiya, Vol. 47, No. 3, 2002, pp. 527–530.

PHYSICAL PROPERTIES OF CRYSTALS

Anisotropic Optical Properties of Crystals with the Ca-Gallogermanate Structure

A. F. Konstantinova*, K. A. Kaldybaev, Z. B. Perekalina*, and V. P. Orekhova***

** Shubnikov Institute of Crystallography, Russian Academy of Sciences, Leninskiĭ pr. 59, Moscow, 117333 Russia*

e-mail: afkonst@usa.net

*** Issyk-Kul State University, ul. 1 Maya 32, Karakol, 722360 Kyrgyzstan*

Received June 15, 2001

Abstract—The optical properties of inactivated and activated crystals with the structure of Ca-gallogermanate have been studied. The components of the gyration pseudotensor for $Sr_3Ga_2Ge_4O_{14}$ crystals are determined. In the ultraviolet range of the spectra of all the crystals studied, the bands of circular and linear dichroism and the anomalous behavior of the linear birefringence are observed irrespective of the activating dopant. The formation of these bands is not associated with the electron transitions of doping ions and can be caused by structural defects formed in the growth process. © *2002 MAIK "Nauka/Interperiodica".*

Crystals with Ca-gallogermanate structure possess a unique combination of physical properties—luminescent, lasing, optical (including nonlinear), elastic, dielectric, piezoelectric, etc. [1–4]. All these crystals are related to the trigonal–trapezohedral class 32 (sp. gr. D_3^2–$P321$) and have only one molecule in the unit cell [4, 5]. The generation of the stimulated radiation first observed in Nd^{3+}-doped $La_3Ga_5SiO_{14}$ crystals [1] gave an impetus to complex studies of these inactivated and activated crystals.

We studied the optical properties of inactivated $La_3Ga_5SiO_{14}$, $La_3Ga_5GeO_{14}$, $La_3Ga_{5.5}Nb_{0.5}O_{14}$, $La_3Ga_{5.5}Ta_{0.5}O_{14}$, $Ca_3Ga_2Ge_4O_{14}$, and $Sr_3Ga_2Ge_4O_{14}$ crystals [6, 7] and measured the dispersion dependences of the absorption and linear-dichroism ($\Delta\kappa$) coefficients (Fig. 1) and also the refractive and birefringence (δn) indices (Fig. 2). Figures 1 and 2 show that, in the ultraviolet range of the spectrum, the dispersion curves $\Delta\kappa(\lambda)$ and $\delta n(\lambda)$ of all these crystals behave anomalously. This behavior and other data obtained have not been interpreted as yet.

Since the crystals of this class are widely used in practice, it is very important to establish the cause of these anomalies by studying experimentally both inactivated crystals and crystals activated by the dopants of the iron group.

We investigated the optical activity, including the circular dichroism, of chromium-, manganese-, and nickel-doped $La_3Ga_5SiO_{14}$ crystals and chromium-activated $Sr_3Ga_2Ge_4O_{14}$ crystals.

The crystals of high optical quality were grown by the Czochralski method with the use of high-frequency heating on a setup with a platinum crucible [8]. The dopant concentration in the melt was 0.1 wt %.

CIRCULAR-DICHROISM SPECTRA OF ACTIVATED $La_3Ga_5SiO_{14}$ CRYSTALS

The absorption spectra of $La_3Ga_5SiO_{14}$: Cr, $La_3Ga_5SiO_{14}$: Ni, and $La_3Ga_5SiO_{14}$: Mn crystals were measured on 2.4–3.5-mm-thick samples oriented normally to the optic axis on a Specord-40 spectrophotometer in the range from 250 to 900 nm. It was established that the bands observed in the spectra correspond to the Cr^{3+}- and Cr^{4+}-ions in the octahedral and the tetrahedral coordination, respectively, and to Mn^{2+} and Ni^{2+} ions in the octahedral coordination.

The circular-dichroism spectra of these crystals had the bands corresponding to the electron transitions in activating ions and were also present in the absorption spectra. Moreover, the circular-dichroism spectra of all

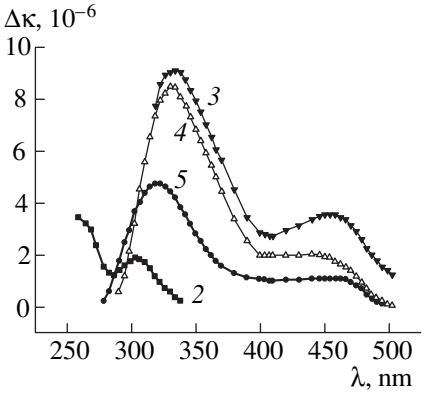

Fig. 1. Linear-dichroism spectra of (*2*) $La_3Ga_5GeO_{14}$, (*3*) $La_3Ga_{5.5}Nb_{0.5}O_{14}$, (*4*) $Ca_3Ga_2Ge_4O_{14}$, and (*5*) $Sr_3Ga_2Ge_4O_{14}$ crystals.

1063-7745/02/4703-0480$22.00 © 2002 MAIK "Nauka/Interperiodica"

the crystals had the maximum in the range 270–370 nm that cannot be attributed to the activating ions.

As an example, Fig. 3 shows the circular-dichroism spectrum of a $La_3Ga_5SiO_{14} : Ni^{2+}$ crystal. In the visible range of the spectrum, only the bands with the maxima at 400 and 650 nm are observed. These maxima correspond to two electron transitions of Ni^{2+} ions in the octahedral coordination, namely, ${}^3A_{2g} \longrightarrow {}^3T_{1g}(P)$ and ${}^3A_{2g} \longrightarrow {}^3T_{1g}(F)$. In addition, a complex band with the maximum at ~340 nm not associated with Ni^{2+} ions is observed in the ultraviolet range of the circular-dichroism spectrum. A similar band in the range of 330–340 nm is also observed in the spectra of $La_3Ga_5SiO_{14} : Mn^{2+}$ and $La_3Ga_5SiO_{14} : Cr^{3+}$ crystals and in the spectra of inactivated $La_3Ga_5SiO_{14}$ crystal (Fig. 4).

Similar bands in the circular-dichroism spectra were also observed in both inactivated and chromium-activated $Ca_3Ga_2Ge_4O_{14}$ and $Sr_3Ga_2Ge_4O_{14}$ crystals [9, 10]. It was assumed that the bands in the vicinity of 340 nm in circular-dichroism spectra of these crystals should be attributed to defects formed during the growth process. It seems that the bands observed in this range of the circular dichroism spectra of $La_3Ga_5SiO_{14}$ crystals are also associated with defects formed during crystal growth.

Comparing the data in Figs. 1, 2 and 3, 4, we can see that the regions of the anomalous behavior of dispersion in linear dichroism and linear birefringence of inactivated crystals coincide with the positions of the bands in the circular-dichroism spectra of both inactivated and activated crystals. The results obtained lead to the conclusion that all the crystals studied have "growth defects," which manifest themselves in the circular-dichroism spectra of these crystals obtained along the optic axis and in the linear-dichroism spectra obtained normally to it.

OPTICAL ACTIVITY OF CRYSTALS WITH Ca-GALLOGERMANATE STRUCTURE

Earlier [6], we obtained the dispersion dependence of the specific rotation of the polarization plane, $\rho(\lambda)$, for a number of inactivated crystals (Fig. 5). For comparison, Fig. 5 also indicates the values of specific rotation for quartz crystals. In a similar way, we measured the rotatory power along the optic axis for crystals activated by various ions, $La_3Ga_5SiO_{14} : Cr^{3+}$, $La_3Ga_5SiO_{14} : Ni^{2+}$, $La_3Ga_5SiO_{14} : Mn^{2+}$, $Ca_3Ga_2Ge_4O_{14} : Cr^{3+}$, and $Sr_3Ga_2Ge_4O_{14} : Cr^{3+}$. The values of specific rotation of the polarization plane practically coincide with the values obtained for transparent crystals.

Knowledge of the specific rotation $\rho(\lambda)$ allows the determination of only one component of the pseudogyration tensor, g_{33}. The second component, g_{11}, can be determined only upon the corresponding measurements on a plate cut out parallel to the optic axis [11]. While measuring the optical activity of the crystals along the directions that differ from the optic axis, it is necessary to take into account absorption and linear dichroism. For the azimuth of the transmitted light $\chi_{\parallel,\perp}$ and two

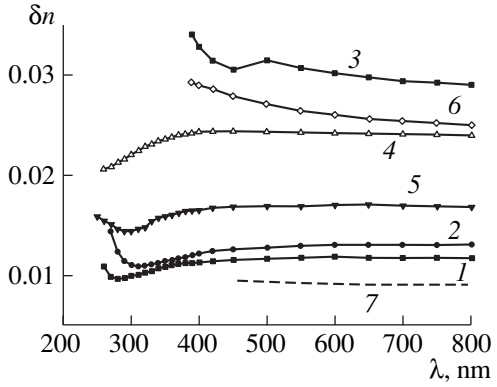

Fig. 2. Dispersion dependences of birefringence of (*1*) $La_3Ga_5SiO_{14}$, (*2*) $La_3Ga_5GeO_{14}$, (*3*) $La_3Ga_{5.5}Nb_{0.5}O_{14}$, (*4*) $Ca_3Ga_2Ge_4O_{14}$, (*5*) $Sr_3Ga_2Ge_4O_{14}$, (*6*) $La_3Ga_{5.5}Ta_{0.5}O_{14}$, and (*7*) SiO_2 crystals.

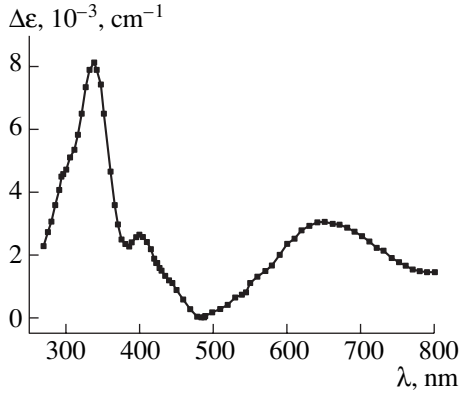

Fig. 3. Circular-dichroism spectrum of a $La_3Ga_5SiO_{14} : Ni^{2+}$ crystal.

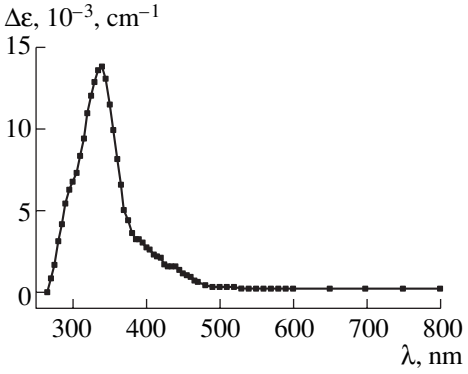

Fig. 4. Circular-dichroism spectrum of an inactivated $La_3Ga_5SiO_{14}$ crystal.

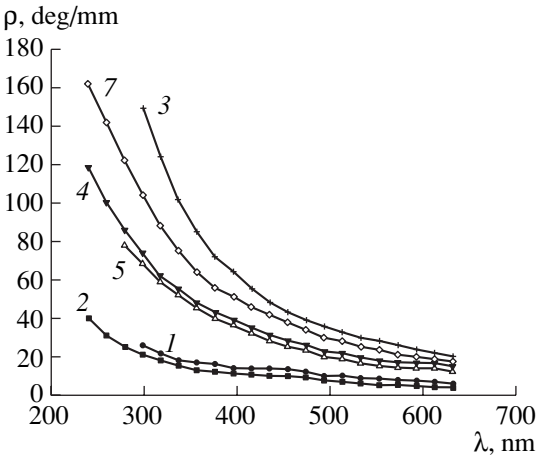

Fig. 5. Specific rotation of the polarization plane in (*1*) $La_3Ga_5SiO_{14}$, (*2*) $La_3Ga_5GeO_{14}$, (*3*) $La_3Ga_{5.5}Nb_{0.5}O_{14}$, (*4*) $Ca_3Ga_2Ge_4O_{14}$, (*5*) $Sr_3Ga_2Ge_4O_{14}$, and (*7*) SiO_2 crystals.

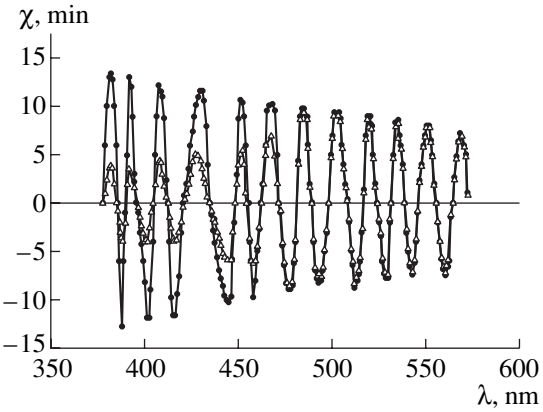

Fig. 6. Dependence of the polarization azimuth of the transmitted light for a plate cut out parallel to the optic axis of the $Sr_3Ga_2Ge_4O_{14} : Cr^{3+}$ crystal (d = 0.96 mm). Light polarization: ● normal to the optic axis and ▲ parallel to it.

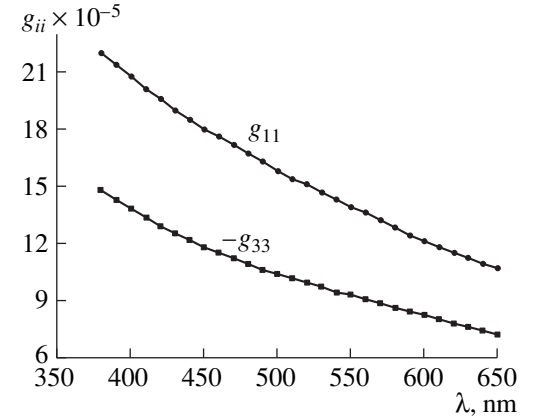

Fig. 7. Dispersion of the components of the gyration pseudotensor g_{11} and g_{33} in the $Sr_3Ga_2Ge_4O_{14} : Cr^{3+}$ crystal.

polarizations of the incident light (∥ and ⊥ denote the polarizations parallel to and normal to the principal plane), we have

$$\tan 2\chi_{\parallel,\perp} = -2k e^{\pm\delta} \sin\Delta,$$

where, for the plate cut out parallel to the optic axis, $k = g_{11}/2n_{av}\delta n$ is the ellipticity of the eigenwaves in the crystal, n_{av} is the average refractive index, and $\Delta = 2\pi d(\delta n)/\lambda$, $\delta = 2\pi d(\Delta\kappa)/\lambda$, where δn and $\Delta\kappa$ are birefringence and dichroism of the plate, respectively.

The azimuths of the transmitted light, $\chi_{\parallel}(\lambda)$ and $\chi_{\perp}(\lambda)$, in the wavelength range from 270 to 660 nm were measured on the plates cut out from $La_3Ga_5SiO_{14}$ crystals [7]. We made similar measurements on the plates cut out parallel to the optic axis of Cr-activated $Sr_3Ga_2Ge_4O_{14}$ crystals (Fig. 6). It is seen that in the ultraviolet range of the spectrum, the dependences $\chi_{\parallel}(\lambda)$ and $\chi_{\perp}(\lambda)$ are somewhat different, which is explained by the effect of linear dichroism. To determine the sign of g_{11}, the measurements were made on a thin (d = 0.01 mm) plate. It turned out that, for a right-handed crystal, g_{11} is positive, whereas g_{33} is negative. The dispersion of the components g_{11} and g_{33} for a $Sr_3Ga_2Ge_4O_{14} : Cr^{3+}$ crystal is shown in Fig. 7. The dopant in a concentration of up to 0.1 wt % does not change the gyration-tensor components, and, thus also the rotatory power of the crystals with the Ca-gallogermanate structure, since the dispersion of these quantities is determined by the bands located in the vacuum range of the spectrum.

CONCLUSION

The spectra of all the crystals with Ca-gallogermanate structure, both inactivated and activated by ions of the iron group, have a circular-dichroism band not associated with the electron transitions of doping ions. The nature of this band seems to be associated with the defects formed in the crystal structure during their growth. Linear dichroism and linear birefringence observed in the range 270–370 nm in inactivated crystals with the Ca-gallogermanate structure also confirm this assumption. It should be indicated that the study of the EPR spectra of inactivated $La_3Ga_5SiO_{14}$ crystals revealed no paramagnetic centers. Therefore, the defects observed in the circular-dichroism spectra of these crystals cannot be of a paramagnetic nature.

ACKNOWLEDGMENTS

We are grateful to B.V. Mill of Moscow State University for growing the crystals. The study was supported by the Russian Foundation for Basic Research, project no. 99-2-17242.

REFERENCES

1. A. A. Kaminskiĭ, *Laser Crystals* (Nauka, Moscow, 1975).
2. A. A. Kaminskiĭ, B. V. Mill', I. M. Sil'vestrova, and G. G. Khodzhabagyan, Izv. Akad. Nauk SSSR, Ser. Fiz. **47** (10), 1903 (1983).
3. I. A. Andreev and M. F. Dubovik, Pis'ma Zh. Tekh. Fiz. **10** (8), 487 (1984) [Sov. Tech. Phys. Lett. **10**, 205 (1984)].
4. A. A. Kaminskii, E. L. Belokoneva, B. V. Mill, *et al.*, Phys. Status Solidi A **86** (1), 345 (1984).
5. E. L. Belokoneva, M. A. Simonov, A. V. Butashin, *et al.*, Dokl. Akad. Nauk SSSR **255** (5), 1099 (1980) [Sov. Phys. Dokl. **25**, 954 (1980)].
6. O. A. Baturina, B. N. Grechushnikov, A. A. Kaminskiĭ, *et al.*, Kristallografiya **32** (2), 406 (1987) [Sov. Phys. Crystallogr. **32**, 236 (1987)].
7. A. A. Kaminskii, B. V. Mill, G. G. Khodzhabagyan, *et al.*, Phys. Status Solidi A **80** (1), 387 (1983).
8. E. L. Belokoneva and B. V. Mill', in *Crystallochemical Systematization of Minerals* (Mosk. Gos. Univ., Moscow, 1985), p. 140.
9. Z. B. Perekalina, T. F. Veremeĭchik, K. A. Kaldybaev, and A. D. Tynaev, Kristallografiya **45** (2), 337 (2000) [Crystallogr. Rep. **45**, 304 (2000)].
10. Z. B. Perekalina, V. P. Orekhova, and K. A. Kaldybaev, Kristallografiya **46** (5), 900 (2001) [Crystallogr. Rep. **46**, 826 (2001)].
11. A. F. Konstantinova, B. N. Grechushnikov, B. V. Bokut', and E. G. Valyashko, *Optical Properties of Crystals* (Nauka i Tekhnika, Minsk, 1995).

Translated by L. Man

Crystallography Reports, Vol. 47, No. 3, 2002, pp. 484–488. Translated from Kristallografiya, Vol. 47, No. 3, 2002, pp. 531–536.

PHYSICAL PROPERTIES OF CRYSTALS

Spontaneous Polarization of Fe-Doped $SbNbO_4$ Crystals

Yu. V. Shaldin

Shubnikov Institute of Crystallography, Russian Academy of Sciences, Leninskiĭ pr. 59, Moscow, 117333 Russia

e-mail: graimo@aha.ru

Received November 9, 2000; in final form, November 15, 2001

Abstract—The temperature dependence of spontaneous polarization in $SbNbO_4$: Fe crystals has been studied. The temperatures of the ferroelectric and the structural phase transitions (537 ± 1) K and (876 ± 1) K are determined from the permittivity data. The anomalies in the temperature dependence of P_s provided by the presence of the Fe_{Sb} and (O_iV_{Sb})-type impurity centers are observed in the whole range of ferroelectric ordering. In the $SbNbO_4$ structure, the macrofragments—two types of mesotetrahedra formed by Sb ions and NbO_6-octahedra—are established, which are responsible for the spontaneous polarization of the crystal. © *2002 MAIK "Nauka/Interperiodica".*

Spontaneous polarization P_s is the central problem in all the pyroelectric classes of crystalline media, because P_s is a physical parameter widely used in various phenomenological theories [1–3]. Therefore, the study of the specific features of its behavior under the action of various external factors is quite timely.

Unfortunately, the theoretically calculated data based on the model representations [1, 2] for such a complex dynamic system as a crystal are far from reliable. The model representations can be made more adequate to the real situation if one uses the crystallographic approach [4], which allows the description of the structure of noncentrosymmetric crystals by using the physical parameters that can be transformed as tensor quantities with weights, $L = 1$, 2, and 3. The structures of noncentrosymmetric crystals can be considered as mesofragments or various combinations of tetrahedra obeying certain symmetry requirements. Although this approach allows one to pass from the analysis of atomic displacements to the analysis of distortions of these mesofragments during phase transitions, the problem of the quantitative determination of spontaneous polarization is yet to be resolved. Therefore, the experimental studies of spontaneous polarization in a wide temperature range under the action of various external factors, and, especially, those of the selective change of the ferroelectric properties caused by the doping of crystals, has become very important.

Doping crystals, including ferroelectric ones, is accompanied by considerable changes in the energy spectrum of the crystal lattice [5]. On the one hand, the present defects break the translation symmetry of the crystal, which results in the delocalization of the wave functions of the atoms and the formation of tails of the function of electron-state density in the Brillouin zone penetrating deeply into the band gap. On the other hand, some defects can be charged more pronouncedly than the lattice and, thus, lead not only to the formation of impurity levels in the band gap, but also to depolarization of the crystal fields in the crystal bulk determined by the efficiency of the lattice–defect interactions. Despite the fact that, in both these cases, the translation symmetry of crystals is broken, the problem of phase transitions in the crystal-dopant systems with defects was theoretically considered in detail in monographs [6, 7]. In accordance with the terminology introduced in [7], the first defects are related to the "random local field" type, the second defects, to the "random transition temperature" type or *T*-defect. The expressions derived within the framework of this phenomenological approach that describe the order parameters as functions of the concentration of noninteracting defects have several parameters whose evaluation requires not only the conduction of some additional experiments, but also the development of new growth technology.

Nowadays, the great practical need for pyroelectric elements efficient at room temperatures makes it necessary to use the traditional methods of search for new media (matrices) and new methods of their doping. Of all the diverse methods of doping, one should pay special attention to isomorphous dopants, whose use at low concentrations corresponds to the formation of *T*-defects. Below, we consider the results obtained for $SnNbO_4$ crystals doped with isomorphous dopants. Thus, doping with Fe provides a considerable decrease in the phase-transition temperature. However, the pyroelectric data [8, 9] do not allow the detailed reconstruction of the behavior of spontaneous polarization in antimony orthoniobate in the whole range of ferroelectric ordering. The existence of impurity levels in the band gap against the background of the tails of the electron-state density function results in the complex temperature dependence of conductivity in $SbNbO_4$: Fe crystals, which makes the P_s data dubious in the whole

existence range of the ferroelectric state. This is also confirmed by the measurements of the pyroelectric coefficient $\gamma_s(T)$, which is practically constant in the whole range of T_c from 300 to T_c – 100 K. In the low-temperature range, the presence of a noncontrollable impurity and crystallization water and also the possible nonstoichiometry of the crystals result in the formation of some anomalies observed in some polar crystals [10–12]. Therefore, the study of spontaneous polarization at low temperatures is as important as the study of the influence of various isomorphous dopants on the $P_s(T)$ dependence in the vicinity of the phase transition. Below, we consider the ferroelectric properties of iron-doped antimony orthoniobate crystals studied in the temperature range from 4.2 to 900 K.

EXPERIMENTAL

A $SbNbO_4$ crystal (sp. gr. $Pna2_1$) is a representative of the ABO_4 family of ferroelectrics (A = Sb and Bi, B = Nb, Ta, and Sb). The $SbNbO_4$ single crystals were grown on a seed by the hydrothermal method [9] and had a rather low resistivity (10^5 Ω cm). Their impurity levels indicated the deviation of the crystal composition from stoichiometry $SbNbO_4$ because of the presence of Sb vacancies. The introduction of iron oxide into the charge changed the intensity of crystal color and provided the growth of large usually faceted single crystals, which considerably facilitated the orientation of the samples. We selected from a large number of crystals only slightly colored ones having a single-domain structure to cut out 3.2 × 4.2 × 1.1-mm^3 rectangular z-cut samples. The silver electrodes were applied onto the samples by vacuum sputtering. For the temperature measurements, we selected two $SbNbO_4$ samples grown from the charge containing ~1.6% iron oxide. The resistivity of the samples varied from 10^8 Ω cm at $T \sim 500$ K to 10^{10} Ω cm at $T \sim 300$ K. An increase in resistivity and the lower color intensity of the samples indicated the replacement of a large number of V_{Sb} vacancies by iron. The influence of fatigue caused by defect migration during crystal repolarization and the formation of spatial charge due to thermally-excited carriers on the reproducibility of the results did not exceed the measurement error (±5%).

METHODS AND MEASUREMENTS

In order to determine the temperature range of ferroelectric ordering in $SbNbO_4$: Fe crystals in a weak field with frequency of 10^3 Hz, we studied the temperature dependence of the coefficient ε_{33}^T of the permittivity tensor (or, more exactly, of its real part $\mathrm{Re}\,\varepsilon_{33}^T$). The behavior of ε_{33}^T as a function of T is shown in Fig. 1. The data obtained confirm the fact that doping with iron considerably (by ~140 K) decreases the temperature of the ferroelectric phase transition in comparison with the temperature of this transition in undoped crystal (T_C = 678 K) [9]. The incorporation of iron into the antimony orthoniobate lattice does not affect (within the measurement error) the temperature of another phase transition.

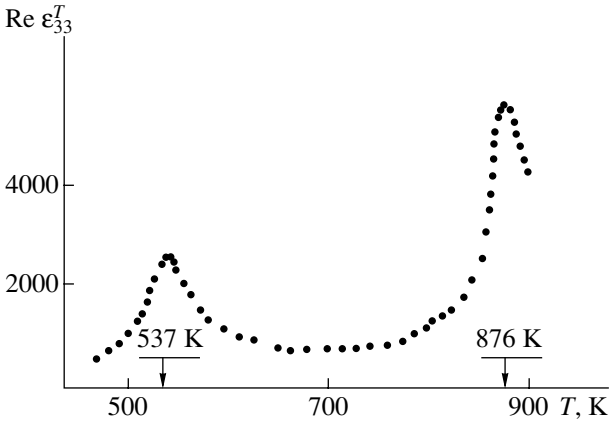

Fig. 1. Temperature dependence of the real part of the ε_{33}^T component of the permittivity tensor of $SbNbO_4$: Fe crystals. The indicated temperatures correspond to the ferroelectric (537 K) and the structural (876 K) phase transitions.

While studying $P_s(T)$ in the temperature range from 4.5 to 600 K, we encountered a number of technical problems associated with the equipment used and the specific features of the object. The preliminary experiments provided the solution of the methodical part of the problem. Thus, at temperatures lower than 350 K, i.e., the temperatures at which repolarization of the samples required the application of the fields comparable with the breakdown fields, we measured not $P_{s,d}(T)$ of the doped sample, but the difference $\Delta P_s = P_{s,d}(T) - P_s^0$, where P_s^0 is the spontaneous polarization at $T = 0$. The measurements were made in a flow-type helium cryostat by the standard quasi-continuous method. The sample was fixed on a cooling rod with the aid of a silver paste. The data obtained corresponded to the effective ΔP_s values for practically mechanically-free $SbNbO_4$: Fe samples. At the sample temperatures exceeding 350 K, the repolarization curves of the $SbNbO_4$: Fe samples were recorded by a storage oscilloscope and then were used to calculate their spontaneous polarization. To take account of the systematic errors caused by the change in the sample resistivity, we used the compensation method suggested in [13]. The measurement errors did not exceed ±5%.

The experimental data on the spontaneous polarization of $SbNbO_4$: Fe crystals in the temperature range from 4.5 to 600 K are shown in Fig. 2. The measurements indicate the existence of two temperature ranges, a and b, where the behavior of $P_{s,d}(T)$ is of anomalous character—(a) the range of low temperatures (Fig. 2a), where the measured data characterize the behavior of

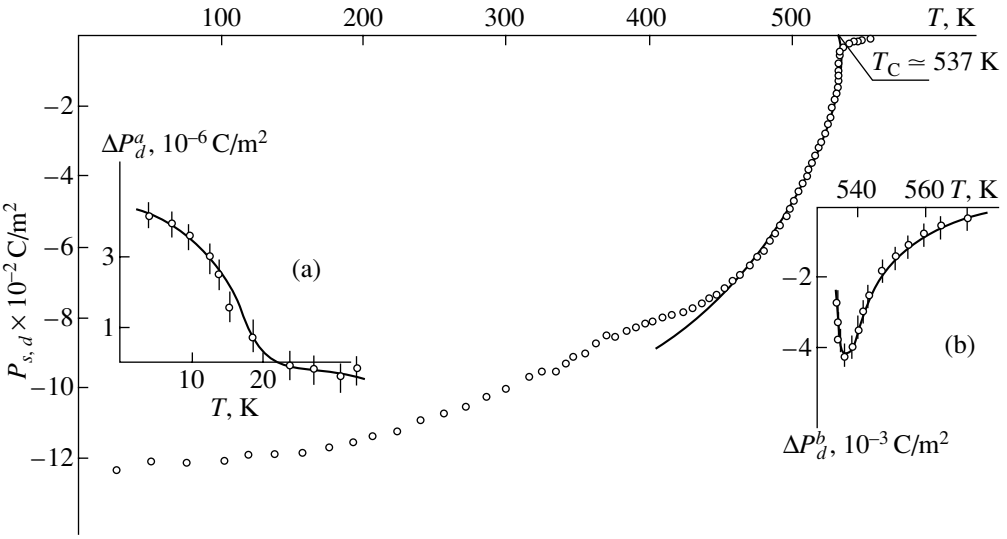

Fig. 2. Temperature dependence of spontaneous polarization of $SbNbO_4$ crystals. The solid line indicates the theoretically calculated curve. In the insets: the contribution of defects in the (a) low- and (b) high-temperature ranges.

ΔP_s with due regard for the contribution introduced by defects and (*b*) the temperature range corresponding to the range of the ferroelectric transition where the contribution from defects was calculated (Fig. 2b) (see below).

The tails of the spontaneous polarization curves do not allow the evaluation of the ferroelectric phase-transition temperature with sufficient accuracy from the experimentally measured spontaneous polarization. Therefore, we used the value $T_C = (537 \pm 1)$ K corresponding to the maximum of the ε_{33}^T function (Fig. 1). The spontaneous polarization in $SbNbO_4$: Fe corresponding to the practically mechanically-free state of the crystal at $T = 300$ K equals (0.10 ± 0.01) C/m^2 and has a tendency to increase at lower temperatures.

DISCUSSION

The above experimental data on the temperature dependence of spontaneous polarization confirmed by the measured coefficient $\varepsilon_{33}^T(T)$ of the permittivity tensor indicate the pronounced influence of doping on the parameters of ferroelectric ordering in antimony orthoniobate. The incorporation of iron into the $SbNbO_4$ lattice results in a considerable shift in the temperature of the second-order phase transition toward $T < T_C$ and the formation of two anomalies in the $P_{s,d}(T)$ dependence at high ($T > 537$ K) and low ($T < 20$ K) temperatures.

As was shown in [6, 7], a decrease in the phase-transition temperature by 141 K is explained by the presence of rigid or *T*-defects whose local symmetry remains unchanged also in the ferroelectric phase. It is most probable that these defects are Fe^{3+} ions occupying Sb vacancies. In this case, the doping-induced perturbation does not essentially change the behavior of the crystal–dopant system and, in the first approximation, allows the phase transition with the critical indices corresponding to the ideal crystal [7]. The approximation of the spontaneous-polarization tail at temperatures $T > 537$ K (Fig. 2b) yields the exponential dependence

$$\Delta P_d^b(T) = P_d^0 \exp[-\alpha(T/T_{c,d} - 1)],$$

where $P_d^0 = 5 \times 10^{-3}$ C/m^2, $\alpha = 20$, and $T_{c,d} = 537$ K is the phase-transition temperature in the crystal–dopant system. Since $\Delta P_d^b \ll P_{s,d}$, then, in the first approximation, the effect of the impurity can be ignored. Then, one can readily see that in the temperature range from $T_{c,d} - 100$ to $T_{c,d}$, the temperature dependence of spontaneous polarization obeys the power law

$$P_{s,d}(T) = P_{s,d}^0(1 - T/T_{c,d})^{1/2},$$

where $P_{s,d}^0$ is the constant equal to 0.18 C/m^2 and $T_{c,d} = 537$ K. This dependence is characteristic of ferroelectrics undergoing second-order phase transitions. Thus, one can readily calculate the contribution from defects (Fig. 2b).

The anomaly in the low-temperature range is associated with a completely different type of defects, whose contribution to the spontaneous polarization of $SbNbO_4$: Fe does not exceed 4×10^{-6} C/m^2 and, as is seen from the experimental data in Fig. 2a, decreases with an increase in the temperature. This behavior is characteristic of defects that are weakly bound to the lattice and possess a certain dipole moment. These defects can be interstitial oxygen vacancies forming donor–acceptor pairs with antimony atoms. This assumption is confirmed by the experimentally observed decrease in conductivities in iron-doped sam-

ples. Thus, for an ideal pyroelectric $P_s \sim T^4$ at $T \longrightarrow 0$ [14], it can be assumed that the changes in spontaneous polarization observed in this T range characterize, in the first approximation, the contribution of the defect subsystem to the total $P_{s,d}$ attaining its maximum value $p_d N$ at $T \longrightarrow 0$, where p_d is the effective dipole moment of a defect and N is the defect concentration. Assuming that the concentration of the donor–acceptor pairs does not exceed 10^{16} at/cm^3, we arrive at the estimate of p_d equal to ~100 D.

The incorporation of a dopant into the antimony orthoniobate lattice not only decreases T_C but also changes the spontaneous polarization of the doped crystal. There are no direct data on P_s for nominally pure samples. Our estimates of this quantity from the experimentally measured pyroelectric data [8, 9] for both doped and undoped samples range within 0.2–0.25 C/m^2 at T = 300 K. The discrepancies between these values and our data can be explained by a number of facts and, in particular, by the presence of defects and their associates with dopants. This results in the partial reduction of the polarization value observed during the recording of hysteresis loops and in the low accuracy of the measured pyroelectric coefficient, which is seen, first of all, from the spreading of the dependence of this coefficient in the vicinity of the phase transition and the almost constant value of $\gamma_s(T)$ in the temperature range from 300 K to $T_C - 100$ K [9].

Within the framework of the phenomenological theory [7], the change in the phase-transition temperature in a ferroelectric with T-defects is described as

$$\Delta T_C = -T_C A_1 N_t / A_0 (1 + \alpha'),$$

where N_t is the concentration of T-defects, A_0, A_1 are the coefficients of the expansion of the density function of the thermodynamic potential in the order parameter, and α' is a certain fitting parameter having the values less than unity in isomorphous substitutions. The substitution of the above values at the concentration of T-defects equal to ~10^{16}–10^{17} at/cm^3 yields the A_1/A_0 ratio equal to $2 \times (10^{-17}$–$10^{-18})$ cm^{-3}.

The theoretical calculations for the model crystal–dopant systems allow one to draw only qualitative conclusions based mainly on the fact of the loss of the translation symmetry of the medium [6]. In the general case, each defect breaking the translation symmetry can delocalize the wave functions of the atoms forming the lattice (matrix). At $T \longrightarrow 0$, the doping-induced static distortions of the lattice can have values comparable with the mean-square values of the thermal fluctuations of the atomic coordinates of the local order of the matrix, which promotes the formation of the defect subsystem in the $SbNbO_4$ structure. The formation of the local-disorder regions results in a reduction in the correlation length, which, in turn, decreases the temperature of the ferroelectric phase transition to $T_{c,d}$ at which the correlation length attains its critical value.

In the case of the $SbNbO_4$ structure (Fig. 3a), the iron dopant isomorphously replaces the antimony vacancies forming, according to [15], the ferroelectrically active sublattice of the initial matrix. This replacement is quite real, because the interatomic Sb–O distances vary within wide ranges with an increase in T. The incorporation of the impurities into the NbO_6-octahedra is hardly probable, because this structure is rather rigid. The presence of $SbNbO_4$ cavities provides the incorporation of interstitial oxygen into the sample, which, with a high degree of probability, should result in the formation of donor–acceptor pairs of the $(O_i V_{Sb})$-type.

It is also possible to consider the antimony orthoniobate structure in a different way [4], as a combination of two deformed mesotetrahedra A and B (Fig. 3b) sharing oxygen atoms in the (001) plane. The representation of any structure (and not only of $SbNbO_4$) as a combination of mesotetrahedra reveals the loss of the local symmetry with respect to the center of inversion (the opposite crystallographic directions from the center to the vertex and from the center to the tetrahedron base are not equivalent). Within the framework of this approach, the specific feature of the ⟨001⟩ directions in the structure can be preserved if one proceeds from the statement that the charge states of mesotetrahedra are characterized not only by different magnitudes, but also by different dipole moments aligned in two opposite directions. Only in this case, the dipole moments are linearly independent, i.e., preserve their orientations with respect to the symmetry operations in the group *mm*2 [16]. This motif in the $SbNbO_4$ structure allows the establishment of the character of medium distortion in its transition from the ferroelectric to the antiferroelectric (*Pnam*) phase (Fig. 3b). Thus, we can draw the conclusion that mesotetrahedra are strongly distorted because of the considerably different radii of antimony and iron.

In the first approximation, the deviation of the $SbNbO_4$ structure from centrosymmetricity can be represented not only graphically but can also be described analytically by introducing the physical parameters invariant with respect to the symmetry operations [4]. It was shown [16] that for crystals described by the point group *mm*2, there are five invariants—the first two, $P_3^{(1)}$ and $P_3^{(11)}$, are related to the subspace of vectors; the third one Q_{12}^*, to the subspace of pseudodeviators; and the fourth and the fifth ones, $S_{131}^{(I)}$ and $S_{232}^{(II)}$, to the subspace of septors (i.e., fully symmetric third-rank tensors). Thus, the second-order phase transition from the ferroelectric to the antiferroelectric phase (*mm*2–*mmm*) should be described by a multicomponent order parameter, because for the point group *mmm*, the subspaces of vectors, pseudodeviators, and septors are empty [16]. The first two invariants can be used to describe the spontaneous polarization of crystals. Therefore, one can single out at least two sublattices in the structure motif of any ferroelectric crystal possessing

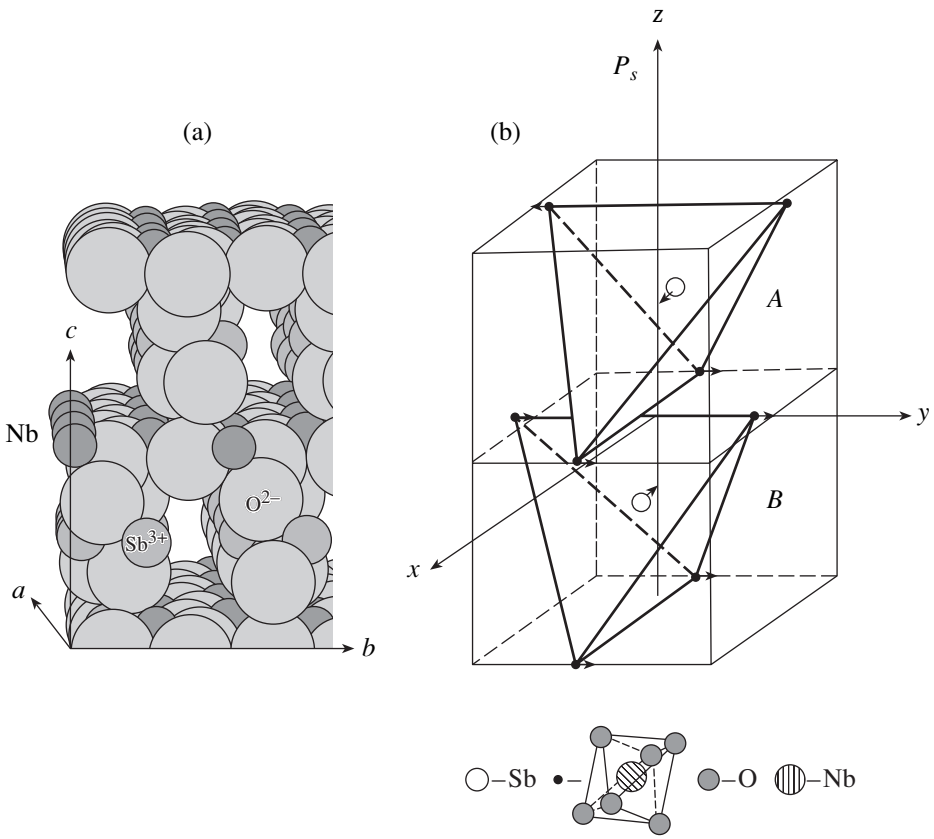

Fig. 3. (a) Structure of antimony orthoniobate and (b) its representation as a combination of two types of mesotetrahedra, *A* and *B*.

approximately equal spontaneous polarizations but oriented in two opposite directions. The same is true for antimony orthoniobate shown in Fig. 3b, where both sublattices formed by *A* and *B* mesotetrahedra are clearly seen.

ACKNOWLEDGMENTS

The author is grateful to the scientists of the International Laboratory of High Magnetic Fields and Low Temperature (Wroclaw, Poland) for their help in low-temperature experiments and, in particular, to A. Liber without whose active participation this study could hardly be performed. The samples for this study were kindly supplied by V.I. Popolitov.

REFERENCES

1. V. G. Vaks, *Introduction to the Microscopic Theory of Ferroelectrics* (Nauka, Moscow, 1973).
2. Yu. M. Gufan, *Structural Phase Transitions* (Nauka, Moscow, 1982).
3. M. DiDomenico and S. Wempl, J. Appl. Phys. **70** (2), 720 (1969).
4. Yu. V. Shaldin, Fiz. Tverd. Tela (Leningrad) **19**, 1580 (1977) [Sov. Phys. Solid State **19**, 922 (1977)].
5. Yu. I. Ukhanov, *Optical Properties of Semiconductors* (Nauka, Moscow, 1977).
6. A. D. Bruce and R. A. Cowley, *Structural Phase Transitions* (Taylor and Francis, London, 1981).
7. A. P. Levanjuk and A. S. Sigov, *Defects and Structural Phase Transitions* (Gordon and Breach, New York, 1988).
8. A. I. Leĭchenko, V. I. Popolitov, and V. F. Peskin, Pis'ma Zh. Tekh. Fiz. **4** (19), 1153 (1978) [Sov. Tech. Phys. Lett. **4**, 463 (1978)].
9. V. I. Popolitov and B. N. Litvin, *Crystal Growth under Hydrothermal Conditions* (Nauka, Moscow, 1986).
10. W. Minkus, Phys. Rev. **138**, 1274 (1965).
11. R. Popravski, Yu. Shaldin, and S. Matyjasik, Phys. Status Solidi A **90**, 167 (1985).
12. Yu. Shaldin and R. Popravski, Ferroelectrics **106**, 399 (1990).
13. H. Diamant, K. Drenck, and R. Pepinsky, Rev. Sci. Instrum. **28**, 30 (1957).
14. M. Born and K. Huang, *Dynamical Theory of Crystal Lattices* (Clarendon, Oxford, 1954; Inostrannaya Literatura, Moscow, 1958).
15. V. I. Ponomarev, O. S. Filipenko, L. O. Atovmyan, *et al.*, Kristallografiya **26**, 341 (1981) [Sov. Phys. Crystallogr. **26**, 194 (1981)].
16. J. A. Schouten, *Tensor Analysis for Physicists* (Clarendon, Oxford, 1954; Nauka, Moscow, 1965).

Translated by L. Man

Crystallography Reports, Vol. 47, No. 3, 2002, pp. 489–494. Translated from Kristallografiya, Vol. 47, No. 3, 2002, pp. 537–542.

PHYSICAL PROPERTIES OF CRYSTALS

Evolution of Twin-Boundary Geometry in Bismuth Crystals with an Increase of Load

V. I. Bashmakov and T. S. Chikova

Mozyr' State Pedagogical Institute, Mozyr', 247760 Belarus

e-mail:mozvuz@mail.gomel.by

Received June 6, 2000; in final form, September 6, 2001

Abstract—The effect of an increase in an external static load on the shape of wedgelike twins formed in the vicinity of stress concentrators in Bi crystals has been studied. A new method for investigating the intermediate stages of mechanical twinning in metals is suggested. It is shown that the applied load is not the determining factor in the development of plastic deformation via twinning in metal crystals. *© 2002 MAIK "Nauka/Interperiodica".*

FORMULATION OF THE PROBLEM

The concept of mechanical twinning in crystals was formed mainly on the basis of the data on plasticity of ionic crystals, where deformation via twinning occurs in its purest form, i.e., is not accompanied by gliding [1]. The description of the multistage formation of a twin interlayer is based on the data on the changes in the shape and dimensions of this interlayer with an increase of mechanical stresses in calcite and sodium nitrate crystals [2]. The dislocation theory of elastic twinning in crystals [3] is based on the reliably established experimental fact observed in calcite: the length of a wedgelike twin and its profile are uniquely determined by the applied concentrated load [4].

Obviously, similar studies are also very important for metals, where, usually, twinning and gliding occur simultaneously [5]. The mutual influence of these processes considerably changes the growth kinetics of deformation twins whose nucleation and further development in a real metal crystal containing defects of different nature and strengths under conditions of either preceding or simultaneous gliding are determined by a number of random factors and, thus, cannot be predicted [6]. Up to now, no rigorous characteristics of the kinetics of plastic deformation via twinning in loaded metal crystals have been established. This is explained, first and foremost, by the experimental difficulties: contrary to transparent ionic crystals, loaded metal crystals allow no direct observation of the growth dynamics of a mechanical twin. In this study, we observed for the first time the evolution of the shape of wedgelike twin interlayers in a metal crystal under conditions of a stepwise increase in the applied concentrated load.

Bismuth crystals were not selected by accident. Both calcite and bismuth crystals are classical materials for studying the laws of pure twinning in metal crystals. A number of publications are dedicated to twin interlayers in bismuth and their effect on the physical properties of twinned crystals, which is explained by a number of reasons.

At all the twinning stages in bismuth crystals over a wide range of temperatures, it is preceded and accompanied by gliding [7]. Both calcite and bismuth single crystals belong to the trigonal system. This allows one to compare the obtained experimental results with the known data on pure twinning, reveal the common features of this type of plastic deformation in various crystals, and study the specific features of restructuring caused by twinning accompanied by gliding.

The method of growth and preparation of Bi specimens is rather simple. Bismuth crystals have a low melting point and possess perfect cleavage. The (111)Bi cleavage is a natural metallographic section requiring no additional treatment and, therefore, can be studied directly under a microscope [8].

Finally, bismuth and bismuth-based alloys are promising materials for technology and, therefore, the study of their mechanical properties are of great practical interest.

EXPERIMENTAL

Bismuth single crystals were grown by the Kapitsa–Shubnikov method [9]. The necessary crystal orientation was set by the seed.

The specimens in the shape of rectangular $10 \times 10 \times$ 5-mm prisms were cleaved by a sharp knife along the (111) plane at liquid nitrogen temperature. To prevent the formation of relief waves on the specimen surface caused by the deceleration and arrest of cleavage-induced cracks [10], a shock stress was applied to the knife. The high velocity of the crack propagation along the cleavage provided a high quality of specimen surface.

The specimen structure was checked using the method of selective chemical etching [10]. The speci-

1063-7745/02/4703-0489$22.00

mens used in our experiments had an initial dislocation density in the non-basal planes of about ~10^6 cm^{-2}.

The setup for studying residual wedgelike twins in metal specimens was based on a PMT-3 metallographic microscope providing crystal deformation by the application of a concentrated load to the specimens and the control of the quantitative parameters of the external factors.

The major difficulty in recording intermediate stages of plastic deformation in metals was overcome by using the original method of the repeated specimen indentation. The studies were performed according to the following scheme: indentation (pointlike deformation of the crystal within the controlled time of loading) ⟶ specimen unloading ⟶ measurements of the dimensions of all the twins formed in the vicinity of the impression ⟶ the change of the external-load parameters (increase of the load) and the repeated indentation in the same pit ⟶ specimen unloading ⟶ measurements of the same parameters, etc. At each unloading stage, we took the photographs of the deformation zone.

The following notation is used. Twins generated in the vicinity of the impression upon the first indentation are called primary twins and twins formed upon the repeated indentation are called new twins.

Special experiments showed that the repeated indentation of the same pit by a constant load applied for the same time does not change the shape, dimensions, and number of primary twins. Specimen unloading at different stages of the formation of a twin interlayer fixes the positions of its boundaries for practically any period of time. An increase in the load during repeated indentation in the same pit results in the restoration of plastic shear at twin boundaries. This simple technique allows the direct observation of the effect produced by various factors on the formation of an ensemble of twins in the vicinity of a stress concentrator.

EXPERIMENTAL RESULTS AND DISCUSSION

Depending on the method of specimen deformation, mechanically-induced twin interlayers have different shapes. It is well known that a stable twin of finite dimensions can be formed only if the stresses are concentrated in the region containing a source of twinning dislocations [1, 3].

To obtain wedgelike twins in bismuth single crystals, the latter were deformed with the aid of a diamond prism of a PMT-3 apparatus (point loading) by indentation of the (111) plane at room temperature (Fig. 1). An external load was increased in a stepwise manner in the range from 0.05 to 0.9 N. The indentation time in each loading stage was 5 s.

Under these conditions, both types of plastic deformation occurred in the vicinity of the impression. Gliding proceeds along two systems: slight basal gliding along the $\{111\}\langle 1\bar{1}0\rangle$ system and secondary gliding with a higher yield stress along the $\{11\bar{1}\}\langle 110\rangle$ system [11], whereas twinning proceeds along the $\{110\}\langle 001\rangle$ system [12].

Twins formed under the action of concentrated mechanical stresses have a wedgelike shape both in the cleavage (111) and in the shear (110) planes. The angles formed by the cleavage plane and any of the three twinning planes in bismuth crystals equal 35° [13]. This signifies that the cleavage plane is the only crystallographic plane in which all three possible twinning planes are orientationally equivalent during indentation of a Bi specimen. The concentrated load applied normally to the (111) plane results in the formation of the maximum number of twins around the impression.

The properties of twin boundaries in the cleavage and shear planes are essentially different, which is associated with different behavior of the edge and the screw components of twinning dislocations [14]. The study of twins on the cleavage plane provides information on the screw dislocations forming the twin boundaries, whereas the study of twins on the shear plane provides information about the edge dislocations. Since we studied the (111)Bi plane, the information obtained characterizes the development of ensembles of screw components of twinning dislocations at the boundaries of wedgelike twins.

The single indentation of a bismuth specimen yields identical patterns irrespective of the load applied. In the vicinity of the pyramid impression, a number of wedgelike twins of different shapes and dimensions are formed (Figs. 1a–1e). The study of more than two thousand twins formed due to single loading of the specimens with an increasing load revealed a large variety of twin wedges; however no direct correspondence between the load value and the profiles of the residual twin interlayer was established. A twin of any shape can be formed at any load. Such a method of deformation does not allow the observation of the evolution and geometry of the interlayer boundary with an increase of the load, because all the twins formed upon single loading are primary twins.

Changing the diamond pyramid for a spherical indenter, we came to the same conclusions. There is only one characteristic feature established for the case of a diamond pyramid: the twins around the impression are nucleated at the concentrators of two types-stable ones, which are set by the indenter structure, and unstable ones, which are set by the defects of the crystal structure [15]. In our case, the stable concentrators were those which gave rise to the formation of twins *1–7* (Figs. 1a–1e).

The development of an ensemble of wedgelike twins was studied by the method of repeated indentation of bismuth specimens under an increasing load. The primary indentation resulted in the formation of twins *1–10* (Fig. 2a), with interlayers *1*, *3*, *4*, *6*, *8*, and *9* appearing in the vicinity of the same stable concentra-

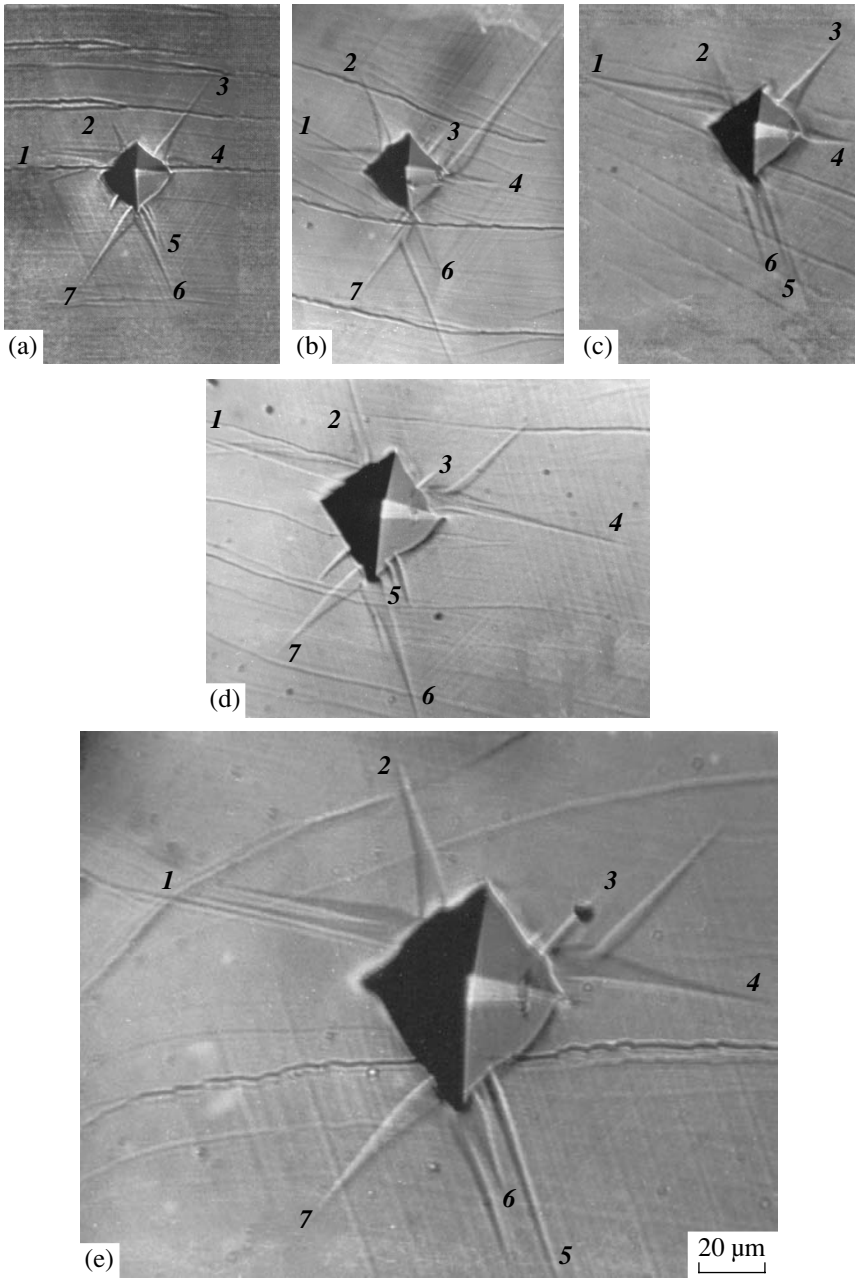

Fig. 1. Wedgelike twins in the vicinity of the impression in the (111) plane of a bismuth single-crystal specimen formed upon single loading: (a) 0.05, (b) 0.1, (c) 0.2, (d) 0.3, and (e) 0.9 N.

tors as in the case of single loading. With an increase in mechanical stresses, the geometrical parameters of the primary twins change and wedges *11–14* are formed (Figs. 2b–2e). Moreover, an increasing impression draws new portions of the crystal into the deformation zone, which, with due regard for the existence of structural defects in the vicinity of the indenter boundaries, is accompanied by a change in the strengths of the stable-concentrators—they either increase or decrease. This explains, in particular, the fact that nucleation of stable twin *1* occurs not during the primary indentation but in the course of the additional loading of the crystal.

It is well known that in pure twinning an increase in the deforming load increases the length and thickness of the interlayer proportionally so that the twin preserves its wedgelike shape with rectilinear boundaries at all stages of its development (Fig. 3a) [2, 4]. In metal crystals, the accompanying gliding provides the formation of the wedgelike configuration of the residual twin interlayer with one curved boundary (Fig. 3b) [7].

The studies showed (Figs. 1, 2) that a considerable number of twins in bismuth crystals, especially under low loads, had classical boundaries described in numer-

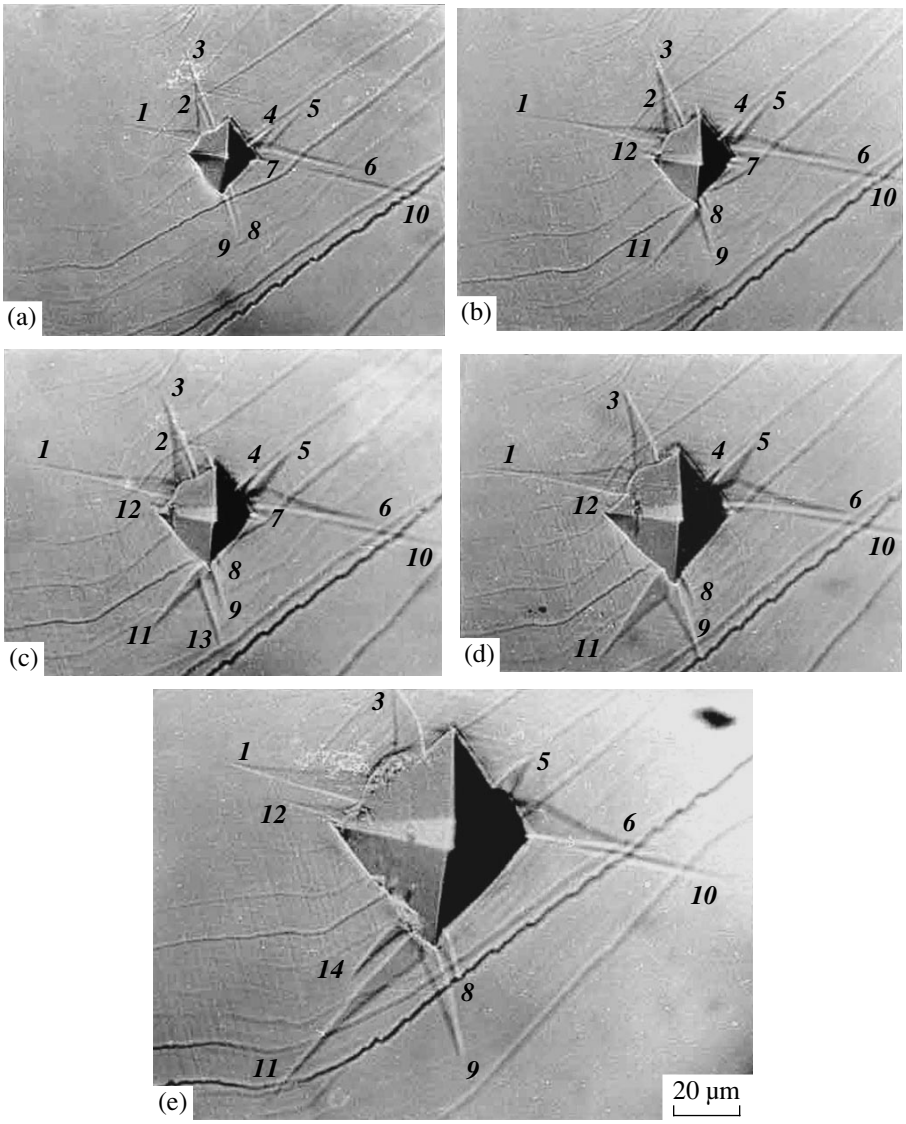

Fig. 2. Development of wedgelike twins in the vicinity of the impression in the (111) plane of a bismuth single-crystal specimen with an increase in the applied load upon repeated indentation. (a) 0.05, (b) 0.1, (c) 0.2, (d) 0.3, and (e) 0.9 N.

ous publications (Figs. 3a, 3b). However, even the minimum stresses gave rise to the formation of nonstandard twins. The group of twins *4*, *5*, and *6* (Fig. 2a) formed a branched structure in which interlayers *4* and *6* had a common "mouth," whereas twin wedge *5* was nucleated at the boundary of twin *6*. This is explained by the considerable strength of stable concentrators *4* and *6* and the complicated profile of the field of induced internal stresses in the specimen.

A pyramidal indenter creates a field of mechanical stresses in a crystal, decreasing radially in the crystal depth. Each wedgelike twin interlayer also gives rise to local internal stresses in the deformation zone. The formation of local internal stresses depends on the defects distributed arbitrarily over the crystal. Because of the random character of nucleation and the growth of wedgelike twins in metals, the total stress field in the vicinity of the impression cannot be predicted a priori. The fields created by the pyramidal indenter, the twins, and the structural defects are either summed up and enhance each other or are subtracted and weaken each other because of their different configurations, lengths, and strengths. In the first case, relaxation of the pronounced total internal stresses formed in the vicinity of the impression occurs via intense gliding and growth of twins. Twinning proceeds at a much higher rate than gliding [1] and, compared with material destruction, is energetically more favorable. This often results in the branching of the twin structure (twins *5* and *6* in Fig. 2a, twins *11* and *13* in Fig. 2c). Relaxation twins are always generated at the convex boundary of the wedge at the site of its maximum incoherence (Fig. 3c), i.e., at the site where the density of twinning disloca-

tions is maximal [3]. A pileup of twinning dislocations becomes the source of a new twin, which removes the energy from the overstressed zone.

Earlier [6, 16], we established that the nucleation of a twin and the formation of a wedgelike twin in metals consist of four elementary dislocation processes: (1) excitation of sources of twinning dislocations, (2) motion of twinning dislocations in the twinning plane with the formation of an interface, (3) generation of twinning dislocations at the formed interfaces, and (4) translation of twinning dislocations along the twinning boundaries.

An analysis of the twins formed at stable concentrators showed that the evolution of the shape of their boundaries with an increase in the load occurred in different ways. Primary wedgelike twins *1*, *6*, *7*, *8*, and *9* (Fig. 2a) only slightly changed their profiles with an increase in the load. The major part in the development of such twinning interlayers is played by the generation of twinning dislocations in the wedge mouth and their subsequent motion with the formation of an interface.

With an increase in the deforming stresses, interlayer *2* is "absorbed" by twin *3* (Figs. 2a–2d), which indicates the prevalent effect of the strength of the source which generates twinning dislocations in the wedge mouth *3*. The retwinning of the twinned region *2* and its incorporation into twin *3* is accompanied by interactions of twinning dislocations and also their interactions with dislocations in the crystal. As a result, both boundaries of interlayer *3* become curved (Figs. 2a–2e) and a new wedgelike twin is formed (Fig. 3d).

The merging of twins *4* and *5* (Fig. 2a) occurs for quite a different reason. The vertices of both wedges are completely stopped even at very low loads. With an increase in the load, the sources of twinning dislocations in the mouth continue "working," the interlayer width at the base increases, and, upon the attainment of the critical interboundary distance, they merge together in a jumpwise manner (Figs. 2d, 2e). Then, the source in the mouth of the left boundary of the twin wedge is blocked, and with a further increase in the stresses, the twinning dislocations are only translated along the boundary and the latter becomes convex (Fig. 2e). In contrast, at the right-hand boundary, the intense generation of dislocations in the mouth and their motion toward the stopped vertex of the twin make is wedge side concave (Fig. 2e). A similar twin interlayer is schematically depicted in Fig. 3e.

Twins simultaneously stopped in the wedge mouth and at its vertex do not develop any more under further loading and are completely "absorbed" by the impression as was observed for interlayer *7* (Figs. 2a, 2d).

Special attention should be given to twins *11* and *13* (Fig. 2c). With an increase in the load, the varying field of mechanical stresses at the impression pushes out twin *13* from the crystal (Fig. 2d). The twin branch *13* disappears and the shape of the initial interlayer *11* is restored. Thus, spontaneous local "untwinning" occurs.

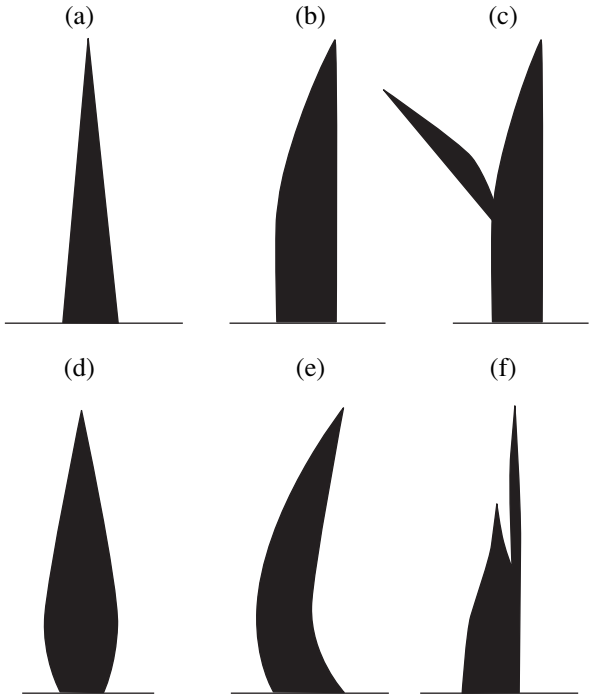

Fig. 3. Shapes of wedgelike twins in a bismuth single crystal specimen.

This phenomenon was observed in our study for the first time. Earlier, it was reported that under the action of the stress of the opposite sign the residual twin can leave the crystal [17]. In our case, an increase in the external mechanical stress of the same sign led to the reversible deformation.

In addition to wedgelike interlayers, Fig. 2 also shows a twin-satellite of lenslike shape, *10*. This twin is not directly associated with indentation and its appearance is explained by the "work" of the source of the twinning dislocations at an accidental concentrator in the crystal depth activated by an external factor. In the range of the loads studied, this twin interlayer was stable. However, the evolution of twin *6* located in the same twinning plane as interlayer *10* resulted in their merging with the formation of a two-vertex wedge (Fig. 3f).

Contrary to the case of pure twinning, we observed no unambiguous correlation between the mechanical stresses applied to the crystal and the shape of the twin interlayer. We did not establish any laws that would describe the change in the twin-boundary geometry with an increase in the load. The accompanying gliding and the defect structure of metal crystals give rise to the formation of wedgelike twins of peculiar forms (Figs. 3c–3f). Similar configurations of twin boundaries are also observed under conditions of both single and repeated loading of the specimens and cannot be interpreted within the framework of the dislocation theory of twinning [3]. The accumulation of the data on the evolution of the boundaries of twin interlayers with an

increase in mechanical stresses in metal crystals is a necessary stage in the creation of an adequate physical theory of mechanical twinning in defect-containing crystals.

CONCLUSIONS

The method of repeated indentation of crystals enables one to study the intermediate stages of the mechanical twinning in metals under conditions of varying parameters of deformation.

There is no direct correspondence between the external load and the shape of residual twin interlayers in bismuth single crystals. With an increase in the load, the configurations of the boundaries of wedgelike twins vary in different ways.

The evolution of the geometry of twin boundaries with an increase in the mechanical stresses in metals is explained by the accompanying gliding and the interactions between twinning dislocations forming the interlayer boundaries and the defects of the crystal structure.

Wedgelike twins of unusual shape with one or two curved boundaries and two vertices and also branching of the twin structure under static loading were observed.

The phenomenon of spontaneous untwinning with an increase in the load applied to the crystal was observed for the first time.

REFERENCES

1. M. V. Klassen-Neklyudova, *Mechanical Twinning of Crystals* (Akad. Nauk SSSR, Moscow, 1960; Consultants Bureau, New York, 1964).
2. R. I. Garber, Zh. Éksp. Teor. Fiz. **17**, 48 (1947).
3. A. M. Kosevich and V. S. Boĭko, Usp. Fiz. Nauk **104**, 201 (1971) [Sov. Phys. Usp. **14**, 286 (1971)].
4. R. I. Garber and E. I. Stepina, Dokl. Akad. Nauk SSSR **128**, 499 (1959) [Sov. Phys. Dokl. **4**, 1023 (1959)].
5. V. M. Kosevich and V. I. Bashmakov, Kristallografiya **4**, 749 (1959) [Sov. Phys. Crystallogr. **4**, 709 (1960)].
6. V. I. Bashmakov and T. S. Chikova, Fiz. Met. Metalloved. **51**, 1066 (1981).
7. V. M. Kosevich and V. I. Bashmakov, Fiz. Met. Metalloved. **9**, 288 (1960).
8. E. N. Glazkov, *Bismuth* (Fan, Tashkent, 1969).
9. L. Shubnikov and W. J. de Haas, Zh. Russ. Fiz.-Khim. O–va, Chast Fiz. **62**, 529 (1930).
10. V. M. Kosevich, Kristallografiya **7**, 97 (1962) [Sov. Phys. Crystallogr. **7**, 121 (1962)].
11. V. I. Bashmakov, M. E. Bosin, F. F. Lavrent'ev, and I. I. Papirov, Probl. Prochn., No. 1, 80 (1974).
12. O. Hall, *Twinning and Diffusionless Transformations in Metals* (Butterworths, London, 1954).
13. E. Schmid and W. Boas, *Kristallplastizät, mit besonderer berücksichtigung der Metalle* (J. Springer, Berlin, 1935; GONTI, Moscow, 1938).
14. F. Terasaki, Acta Metall. **15**, 1057 (1967).
15. V. I. Bashmakov and T. S. Chikova, Vesnik Mazyrskaga Dzyarzhanaga Pedagag. Inst., No. 1, 22 (1999).
16. V. I. Bashmakov and T. S. Chikova, Fiz. Met. Metalloved. **49**, 443 (1980).
17. V. I. Bashmakov, M. E. Bosin, and P. L. Pakhomov, Phys. Status Solidi A **9**, 69 (1972).

Translated by L. Man

Crystallography Reports, Vol. 47, No. 3, 2002, pp. 495–500. Translated from Kristallografiya, Vol. 47, No. 3, 2002, pp. 543–548.

PHYSICAL PROPERTIES OF CRYSTALS

Evolution of Dislocation Structures in a Crystal under Deformation

A. K. Emaletdinov

Ufa Technological Institute of Service, ul. Chernyshevskogo 145, Ufa, 450014 Russia

e-mail: emaletd@mail.ru

Received December 20, 1999; in final form, April 18, 2000

Abstract—The system of equations describing the dislocation kinetics which provides plastic deformation in fcc and bcc metal crystals over a wide range of temperatures and stresses has been studied. The general types of solution and the two-parameter diagram of solution bifurcation are obtained as functions of stresses and temperatures. The diagrams of various types of solution are compared with the diagram of experimentally observed dislocation structures. © *2002 MAIK "Nauka/Interperiodica".*

INTRODUCTION

The physical and chemical properties of structural materials are essentially dependent on their dislocation structures. Therefore, the study of the kinetics of the formation of dislocation structures under various thermal and mechanical conditions is of great importance, e.g., for the development of technologies for growing gradient single crystals and single crystals with low dislocation densities, the optimization of crystallization processes, the thermal and mechanical treatment of materials, etc. [1, 2]. The microstructural studies of plastic deformation in fcc and bcc poly- and single crystals over a wide range of temperatures and stresses [2–6] showed that the dislocation substructure is a complex function of the deformation process and, in particular, is essentially dependent on the degree of deformation ε_P, applied stresses σ, temperature T, and some other parameters. This fact underlies the basis for control of the structure of materials during their thermal and mechanical treatment. The generalized two-parameter diagram of dislocation states in the space of dimensionless parameters ($\sigma = \sigma/\sigma_P$ and $T = T/T_m$) [2–6] in the temperature range T/T_m = 0.2–0.4 is shown in Fig. 1, where σ_P is the breaking stress and T_m is the melting point. It is schematically shown that, in the process of deformation at the given dimensionless temperature T_{def}, different dislocation structures are formed. Their nucleation and self-organization occurs at stresses exceeding the critical dimensionless stresses σ_{Ci} at i = 1, 2, …. As is seen from Fig. 1, at stresses $\sigma < \sigma_{C1}$ ($\rho < \rho_{C1}$ is the dislocation density), dislocations are distributed uniformly (region I). With an increase in stresses $\sigma_{C1} < \sigma < \sigma_{C2}$ ($\rho_{C1} < \rho < \rho_{C2}$), dislocation pileups are formed (region II). At stresses $\sigma_{C2} < \sigma < \sigma_{C3}$ ($\rho_{C2} < \rho < \rho_{C3}$), a homogeneous network structure is formed (region III), which, at stresses $\sigma_{C3} < \sigma < \sigma_{C4}$ ($\rho_{C3} < \rho < \rho_{C4}$), is reorganized into a cellular structure (region IV). With a further increase in stresses $\sigma > \sigma_{C4}$ ($\rho > \rho_{C4}$), a fragmented striation is observed (region V). With a decrease in the temperature, the sequences of dislocation structures become simpler. The fast accumulation of the large volume of experimental material on dislocation substructures and the complex nature of these data resulted in such a situation that the reliable and consistent interpretation of the accumulated data and the classification of the material behavior during plastic deformation are impossible without the construction and study of various models of dislocation kinetics.

In terms of nonequilibrium thermodynamics and synergetics [2, 7, 8], the dislocation substructures formed can be considered as dissipative structures whose formation is associated with the collective motion modes in the dislocation kinetics. In a large number of relevant studies [9–17], the equations of the

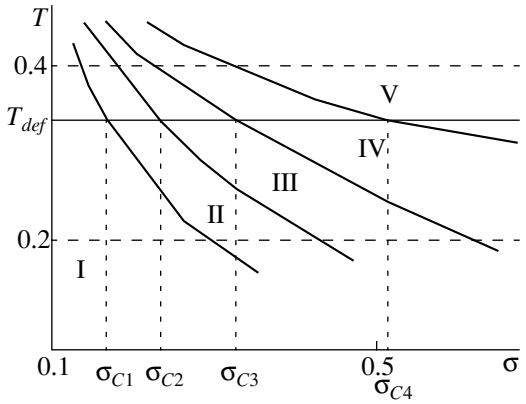

Fig. 1. Generalized qualitative diagram of the sequence of dislocation substructures formed in plastic deformation as a function of dimensionless temperature and stresses (deformation) [5, 6]; σ_{C1}, σ_{C2}, σ_{C3}, and σ_{C4} are the critical stresses providing changes of type of dislocation substructures. I–V are the regions of different types of substructures.

1063-7745/02/4703-0495$22.00 © 2002 MAIK "Nauka/Interperiodica"

dislocation kinetics were derived, which describe the major dislocation processes such as their multiplication, immobilization, diffusion, annihilation, etc. These equations are analyzed with the use of the principles of synergetics and nonequilibrium thermodynamics and are dedicated to some dislocation structures, e.g., of the dipole, cellular, and disclination types, under various deformation modes. The system of equations of dislocation kinetics was analyzed by the method of Liapunov's exponents and with the use of the harmonic approximation of the linearized system of equations at the given stress σ and temperature T. Nevertheless, only some of the types of the solution of kinetic equations and the sequence of their alternation are studied and only at the qualitative level. Up to now, no two-parameter diagram of the bifurcation points of the solutions as a function of temperature and stresses has been constructed and, therefore, no comparison of such diagrams with the diagram of dislocation substructure has been made (Fig. 1).

Below, we describe the numerical study of the two-parameter system of equations of dislocation kinetics during plastic deformation in the stress and temperature space (σ, T). We performed the complete qualitative analysis of the main types of the solution, constructed the diagram of solution bifurcation, and compared the diagram of the solution types with the experimental diagram of dislocation structures.

NUMERICAL MODELING

We consider a simplified model of crystal deformation in which dislocation slip is developed along two systems of planes (primary and secondary), which corresponds to the known microstructural data on plastic deformation in real materials over a wide range of stresses and temperatures. In both primary and secondary slip planes, the shear processes are developed in a similar way, and, therefore, the dislocation densities and the dimensions of the shear zones in these systems are the same. The "wood" dislocations ρ_L are distributed in a random way, whereas the stresses thus induced are taken into account via the effective stresses σ_S. The kinetic equation in the integro–differential form were formulated in [2, 15–17] with due regard for the changes in the densities of immobile dislocations. The allowance for the contribution of immobile dislocations to the kinetics equation via the integral term or the internal stresses are equivalent. The problems associated with averaging the ensemble of dislocations were considered elsewhere (see, e.g., [2, 17]). None of the approximations were rigorous enough; however, they allowed one to take into account all the important qualitative aspects of the dislocation kinetics.

Consider the kinetics of infinite rectilinear dislocations in two families of intersecting slip planes that provide the plastic deformation in a two-dimensional crystal. The dislocation density in the primary slip system is equal to $\rho_1(x_1, x_2, t)$, whereas in the secondary slip system it equals $\rho_2(x_1, x_2, t)$. The x_1- and x_2-axes are directed along the slip planes of the primary and the secondary systems, respectively. The immobile dislocations give rise to certain internal stresses, which are taken into account via the effective stress. This model was considered in a large number of studies [9–17]. The kinetic equations for the dislocation density have the conventional form, $\dot{\rho}_i + \nabla v\rho_i = I_S - I_A$ ($i = 1, 2$), where I_S and I_A are the collision integrals of the processes of dislocation multiplication and annihilation, respectively. The rigorous description of the elementary processes of dislocation kinetics—multiplication and annihilation, mutual trap, translation, "diffusion," etc.—is a problem yet to be resolved [2–6, 9–17] and, therefore, we consider here these processes in a semiphenomenological way. The equations of dislocation kinetics have the form [17]

$$\frac{\partial\rho_1}{\partial t} = A_1(\sigma - \sigma_{I1}) - M_1\rho_1^2 - K_1\rho_1\rho_2 + D_1\Delta\rho_1 + m_{11}\rho_1 - m_{12}\rho_1, \quad (1)$$

$$\frac{\partial\rho_2}{\partial t} = A_2(\sigma - \sigma_{I2}) - M_2\rho_2^2 - K_1\rho_1\rho_2 + D_2\Delta\rho_2 + m_{22}\rho_2 - m_{21}\rho_2, \quad (2)$$

where A_i is the rate of dislocation generation by various sources and σ_{Ii} ($i = 1, 2$) are the stresses that provide the activity of the sources in the primary and secondary slip planes, respectively; M_i is the constant of mutual annihilation of dislocations which is dependent on temperature and the physical characteristics of dislocations [17]; K_1 is the constant that describes the mutual reactions of dislocations from different slip systems [9, 17]; m_{ii} ($i = 1, 2$) are the constants that describe the dislocation multiplication via double transverse slip [11]; $\Delta = \partial^2/\partial x_1^2 + \partial^2/\partial x_2^2$ is the Laplacian; D_i ($i = 1, 2$) are the "diffusion" coefficients of fluctuations in dislocation densities [17]; and m_{12} and m_{21} are the constants that describe absorption of dislocations at the interfaces.

For the system of equations (1) and (2), the theorem on the existence and uniqueness of the solution satisfying the initial conditions is valid [18]. The system of equations (1) and (2) can have both homogeneous and inhomogeneous solutions depending on time and coordinates. Therefore, in the analysis of the stationary dislocation structures, only the second type of coordinate-dependent solution is important, and, therefore, it is sufficient to consider only the stationary equations. Since all the primary and secondary slip planes are equivalent, one can pass to the averaged dislocation

densities in both slip systems $\bar{\rho}_1(x_1) = \int_0^{L_0}\rho_1(x_1, x_2)dx_2/L_0$, $\bar{\rho}_2(x_2) = \int_0^{L_0}\rho_2(x_1, x_2)dx_1/L_0$, where L_0 is the sample size.

In what follows, we omit the bar above the $\rho_1(x_1)$ and $\rho_2(x_2)$ variables. Then, if $\sigma > \sigma_{i1}, \sigma_{i2}$, the system of stationary equations (1) and (2) takes the form

$$D_1\frac{\partial^2}{\partial x_1^2}\rho_1 + A_1\sigma - M_1\rho_1^2 - K_1\rho_1\rho_2 + m_{11}\rho_1 - m_{12}\rho_2 = \alpha_1\dot{\varepsilon}, \quad (3)$$

$$D_2\frac{\partial^2}{\partial x_2^2}\rho_2 + A_2\sigma - M_2\rho_2^2 - K_1\rho_1\rho_2 + m_{21}\rho_1 - m_{22}\rho_2 = \alpha_2\dot{\varepsilon}, \quad (4)$$

where $\dot{\varepsilon} = D_i(\partial\rho_i/\partial x_i)|_0^L/L_0$ ($i = 1, 2$) is the rate of crystal deformation, $\alpha_1 = \cos(\varphi)$, $\alpha_2 = \sin(\varphi)$, and φ is the angle formed by the tension direction and the normal to the primary slip plane.

To obtain the solutions in the form $\rho_i(x_i, T)$ ($i = 1, 2$) and construct a two-parameter diagram, one has to take into account the dependence of the system coefficients on temperature. In the general case, this dependence for the coefficients A_i, M_i, K_1, m_{ij}, and D_i is of a complex nonlinear nature; e.g., it can be described by the Arrhenius-type relationship $D_i \propto \exp(-1/T)$. In the range of dimensionless temperatures $0.2 \le T/T_m \le 0.4$ (Fig. 1), we used the linear approximation $M_i \approx M_{0i}T$, $m_{ii} \approx m_{0ii}T$, and $D_i \approx D_{0i}T$ ($i = 1, 2$).

The types of solution of the system of stationary equations (3) and (4) were analyzed by the finite differences method [18], by constructing phase trajectories and diagrams, and by calculating Liapunov's exponents [19, 20] and Poincaré mappings [21]. In modeling, we transformed Eqs. (3) and (4) to the equations with the dimensionless variables x/b, ρ_i/ρ_c, $\sigma/\sigma_p = 0.1$–0.6, and $T/T_m = 0.2$–0.4, where b is the magnitude of the Burgers vector. The coefficients A_i, M_i, K_1, m_{ij}, and D_i in the system of equations (3) and (4) were evaluated for Al, Cu, and Fe crystal lattices: $A_i \approx 10^4$–10^5 s^{-1} Pa^{-1} ($\varepsilon \approx 0.02$–0.05), $\sigma/\sigma_P \approx 0.1$), $A_1 = 0.1A_2$ is the rate of dislocation nucleation at the initial stage of deformation [11]; $M_i \approx 10^{-12}$–10^{-13} m^2 s^{-1} K [17]; $K_1 \approx 10^{-14}$–10^{-15} m^2 s^{-1} [17], $D_i \approx 10^{-14}$–10^{-15} m^2 s^{-1} K^{-1} [17]; $D_2 = 0.1D_1$; m_{11}, m_{12}, m_{21}, and m_{22} are equal to m_{11}, $m_{22} \approx 10$–100 m^2 s^{-1} and $m_{21} = 0.1m_{12}$, m_{12}, $m_{21} \approx 0.1$–1.0 m^2 s^{-1} [17]. We used the typical values $\dot{\varepsilon} = 0.001$ s^{-1} and $\rho_c = 10^{12}$ m^{-2}. The stationary points of the system were determined by the Newton–Rafson method [19]. Now, represent the system of equations (3) and (4) in the vector form

$$\nabla X = F(X), \quad (5)$$

where

$$\nabla = \begin{pmatrix} \frac{\partial}{\partial x_1} \\ \frac{\partial}{\partial x_2} \\ \frac{\partial}{\partial x_1} \\ \frac{\partial}{\partial x_2} \end{pmatrix}, \quad X = \begin{pmatrix} \rho_1 \\ \rho_2 \\ \rho_3 \\ \rho_4 \end{pmatrix},$$

and

$$F = \begin{pmatrix} \rho_3 \\ \rho_4 \\ \frac{1}{D_1}[\alpha_1\dot{\varepsilon} - A_1\sigma + M_1\rho_1^2 + K_1\rho_1\rho_2 - m_{11}\rho_1 + m_{12}\rho_1] \\ \frac{1}{D_2}[\alpha_2\dot{\varepsilon} - A_2\sigma + M_2\rho_2^2 + K_2\rho_1\rho_2 - m_{22}\rho_2 + m_{21}\rho_2] \end{pmatrix}.$$

As is seen from Eq. (5), the equilibrium positions are the zeroes of the vector field F, $F(X) = 0$. Therefore, constructing the Jacobian $DF = |\partial F/\partial X|$, we arrive at the iteration procedure for determining the equilibrium position X_*

$$X_{(i+1)} = X_{(i)} + DF(X_{(i)})^{-1}F(X_{(i)}), \; i = 0, 1, 2, \ldots . \quad (6)$$

The nature of stability of the stationary point X_* was established from the analysis of the eigenvalues of the matrix $A = DF(X_*) = \partial F(X_*)/\partial X$. With this aim, we linearized the system of equations (5) in the (σ, T) space and studied the dependence of the parameters of the eigenvalues of the matrix A. The change in the nature of stability of an immobile point is associated with direct or inverse Turing bifurcations such that $\mathrm{Re}\lambda_i = 0$, where λ_i are the eigenvalues of the matrix A.

RESULTS OF NUMERICAL MODELING

The stationary points and their stability are important characteristics of the system of equations (3) and (4). In the initial range of the parameters (σ, T), the system of equations (3) and (4) has only one unstable immobile point O_1 of the node–saddle type. The unstable stationary point O_2 of the saddle–focus type dependent on the value of the parameter T appears in the intermediate range of the system. The two-parameter diagram of the system states in the space of dimensionless parameters ($\sigma = \sigma/\sigma_P$, $T = T/T_m$) is shown in Fig. 2. Curve *1* is the line of bifurcation of the stationary point O_1 of the system from the node to the saddle. Curve *2* of the Turing bifurcation separates the stable and unsta-

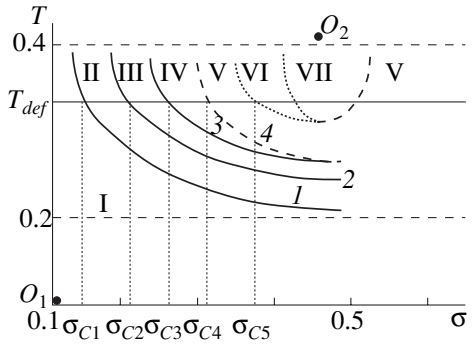

Fig. 2. Generalized qualitative phase portrait of the main states of the system of equations (3) and (4) depending on dimensionless temperature and stresses; σ_{C1}, σ_{C2}, σ_{C3}, σ_{C4}, and σ_{C5} are the critical stresses (points of bifurcation of the types of inhomogeneous solutions or dissipative structures). Curves *1–4* are the approximate lines of solution bifurcation. The point O_1 is of the node–saddle type, the point O_2 is of the saddle–focus type.

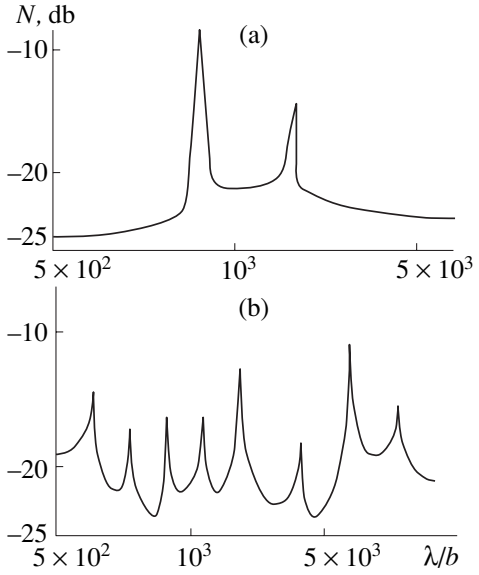

Fig. 3. Spectra of relative power N (db) of (a) biharmonic and (b) subharmonic waves. The parameters used in calculations: $T/T_m = 0.35$, $M_i \approx 5 \times 10^{-12}$ m^2 s^{-1} K, $K_1 \approx 8 \times 10^{-14}$ m^2 s^{-1}, $D_1 = 6 \times 10^{-14}$ m^2 s^{-1} K, and $m_{11}, m_{22} \approx 3 \times 10$ m^2 s.

ble regions of the system. Curve *3* is the line of the change of the stability type of the stationary point O_2 from the saddle to the focus accompanied by the generation of wave solutions and dissipative structures in the system. As is seen from Fig. 2, the theoretical curves of solution bifurcation describe the experimental diagram of dislocation substructures (Fig. 1) quite adequately. In the region central with respect to the parameter T, the system has only one unstable stationary point and, thus, various inhomogeneous spatial periodic dislocation structures. The numerical modeling yielded the main types of solution of the system of equations (3) and (4) dependent on the parameters σ and T, namely: (I) stable stationary homogeneous solutions, (II) quasi-harmonic waves, (III) biharmonic states, (IV) alternation [19], (V) subharmonic states, (VI) nonlinear waves [20], and (VII) random waves [20]. At the fixed T_{def} temperature, the following hierarchic sequences of critical stresses

$$\sigma_{C1} < \sigma_{C2} < \sigma_{C3} < \sigma_{C4} < \sigma_{C5} < \ldots$$

and new types of solutions

$$\text{I} \longrightarrow \text{II} \longrightarrow \text{III} \longrightarrow \text{IV} \longrightarrow \text{V} \longrightarrow \text{VI} \longrightarrow \text{VII} \longrightarrow \text{V} \longrightarrow \ldots$$

were obtained.

This sequence of secondary bifurcations is the generalized one and is constructed under the normal conditions at $T/T_m = 0.35$. At higher and lower temperatures, simpler sequences are possible. At the temperatures $0.2 \le T/T_m \le 0.35$, simpler types of the development of solutions types, such as I ⟶ II ⟶ V ⟶, etc., were obtained. At the temperatures $T/T_m \le 0.2$, only the homogeneous solution was obtained.

At $\sigma < \sigma_{C1}$, the dislocation density is homogeneous ($\rho_1, \rho_2 \cong$ const); this is the solution of type I. At $\sigma > \sigma_{C1}$, the system shows Turing bifurcation which results in the spatially inhomogeneous quasi-harmonic wave solution of type II with the formation of a dissipative structure. The phase portraits show that this solution has the form of closed elliptic trajectories. The corresponding power spectra clearly show the only peak indicating the existence of only one critical mode. The calculated first Liapunov's coefficient $\lambda_1/b \cong 823$ at $T/T_m = 0.3$. Therefore, the period length (dimension) of the dissipative structure $l_d \cong 1/\lambda_1 \approx 3 \times 10^{-6}$ cm, which is consistent with the experimental data [2–6]. The Poincaré section has a characteristic pointlike form. At $\sigma > \sigma_{C2}$, solutions of type III are two-frequency waves with different periods. The kinetic curves of such solutions have the form of periodic oscillations modulated by the low-frequency component. The power spectra of these modes have two clear peaks corresponding to the modes λ_1 and λ_2 (Fig. 3a). The corresponding phase portraits have the corresponding attracting set—a torus of dimension two. With a further increase in the stresses, the amplitude of the second harmonic increases. The torus on the phase portrait changes its shape, which is accompanied by periodic stratification associated with the appearance of additional harmonics. An increase in the periodic stratification and the appearance of a number of additional harmonics resulted in the disappearance of the torus in the system. The torus destruction resulted in an increase in the correlation dimension, which indicated the transition from two-periodic vibrations to the alternation mode (at $\sigma > \sigma_{C3}$, the distribution of type IV arises). The characteristic feature is the periodic repetition of the regions characterized by different modes. The kinetic curves have

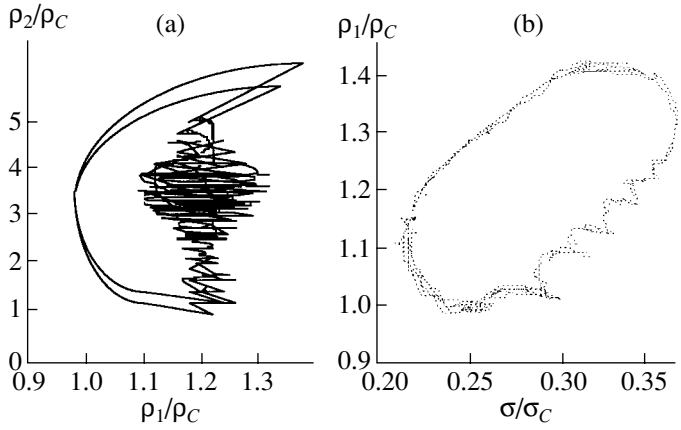

Fig. 4. Alternation mode: (a) phase trajectories, (b) Poincaré sections. The parameters used in the calculation are the same as in Fig. 3.

segments with different wavelengths periodically following one another. The phase portrait in Fig. 4a illustrates the stratification of the torus into layers corresponding to the modes with different wavelengths in the vicinity of the separatrix connecting the stationary point and the saddle–focus manifold. The narrow regions with the short wavelengths are associated with the "unwinding" in the vicinity of the unstable stationary point, whereas the long wavelength regions are associated with the "winding" far from this point. This trajectory is called the loop-type *E*-homoclinic trajectory of the separatrix of the equilibrium state. The characteristic feature of the homoclinic trajectories is their nonrigidity. Therefore, the *E*-homoclinic trajectories play the role of boundaries separating the systems showing different behavior and indicate the presence of bifurcations. In accordance with one of the Shil'nikov theorems [22] that is valid in this case (on the structure of the phase space in the vicinity of the *E*-homoclinic trajectory), there is a denumerable set of periodic motions in the vicinity of this trajectory. In turn, this generates quasi-attractors—the complex attracting sets containing saddle and stable (with a small attraction region) periodic trajectories. The Poincaré section for the thus formed attractor shown in Fig. 4b is related to the helical Ressler attractors [19]. Under conditions exceeding critical, $\sigma > \sigma_{C4}$, the subharmonic waves are generated in the system, which are, in fact, complex oscillations consisting of *K* harmonics (Fig. 3b). The phase portrait is a *K*-dimensional torus. The generation of subharmonic waves in the system is caused by synchronization of the first harmonics. The system dimension becomes equal to *K*, e.g., to four or six. At stresses exceeding critical, $\sigma > \sigma_{C5}$, an obviously inhomogeneous structure is formed, which is similar to the cnoidal waves [19]. The cnoidal waves on the phase diagram can be considered as the limiting case of the alternation mode (Fig. 5). In this case, we observe the formation of segments with very small wavelength and a complicated spectrum. The broad smooth segments

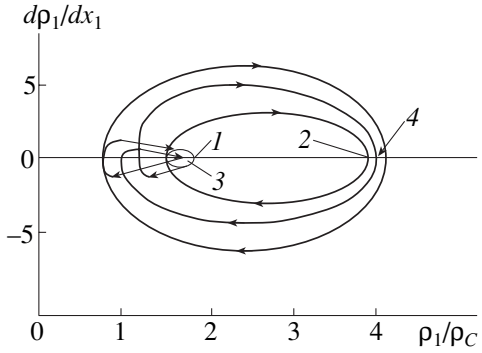

Fig. 5. Mode of cnoidal waves. Phase trajectories *1–4* indicate the successive points of the motion along the trajectory. The parameters used for the calculation are the same as in Fig. 3.

have a narrow spectrum with a small amplitude (almost one mode) and a large wavelength. With an increase in the stresses, $\sigma > \sigma_{C6}$, random solutions are formed due to the action of different mechanisms [20]. In this model, a random attractor generated via a "cascade" of period doublings has a multiband form. The phase trajectories have the shape of a bent and twisted band. The power spectrum of the mode reminds one of the flicker-noise spectrum, which indicates its pronounced aperiodicity. The random solutions have the form of helical Ressler attractors. With a further increase in the stresses, $\sigma > \sigma_{C7}$, no random behavior is observed any more, and the system acquires complex subharmonic state (V) again. With a still further increase in the stresses, new solution bifurcations indicate the complex kinetic behavior, but they have no clear physical sense and seem to be associated with the approximate nature of the system of equations (1) and (2).

CONCLUSION

Finally, compare the complete qualitative diagram of self-organization of inhomogeneous solutions (dissi-

pative structures) of the equations of dislocation kinetics (Fig. 2) with the diagram of dislocation states (Fig. 1). Proceeding from the graphical analogy, we can interpret the dislocation structures as follows. At stresses $\sigma < \sigma_{C1}$, the dislocations are distributed homogeneously, and therefore the corresponding homogeneous solution exists. At the stresses $\sigma_{C1} < \sigma < \sigma_{C2}$, polygonal and net structures are formed, which can be described by quasi-harmonic solutions. Biharmonic solutions at $\sigma_{C2} < \sigma < \sigma_{C3}$ can be interpreted as possible dipole structures. At stresses $\sigma_{C3} < \sigma < \sigma_{C4}$, cellular structures with possible dislocation-free channels are formed. These states can be described as the structure of the alternating type. If the condition $\sigma_{C4} < \sigma < \sigma_{C5}$ is fulfilled, coiled cellular structures are formed, which can be described by subharmonic waves. If the condition $\sigma_{C5} < \sigma < \sigma_{C6}$ is fulfilled, fragmentation or striation is observed described by cnoidal waves. The random solutions can be interpreted as intermediate and random structures. Thus, the dislocation substructures observed experimentally in fcc and bcc poly- and single crystals are self-organizing dissipative states generated at stresses and temperatures exceeding their critical values and developing by the mechanism of a kinetic transition.

In order to construct the quantitative two-parameter thermal–mechanical diagrams of dislocation states, one has to set the exact expressions for the slip systems, collision integrals, and the coefficients in the equations of dislocation kinetics for the materials under study.

REFERENCES

1. I. A. Kasatkina and T. I. Ivanova, Kristallografiya **43** (6), 1073 (1998) [Crystallogr. Rep. **43**, 1015 (1998)].
2. V. S. Ivanova, A. S. Balankin, I. Zh. Bunin, and A. L. Oksolaev, *Synergetics and Fractals in Materials Science* (Nauka, Moscow, 1994).
3. L. A. Shuvalov, A. A. Urusovskaya, I. S. Zheludev, *et al.*, *Modern Crystallography*, Vol. 4: *Physical Properties of Crystals*, Ed. by B. K. Vainshtein, A. A. Chernov, and L. A. Shuvalov (Nauka, Moscow, 1981; Springer-Verlag, Berlin, 1988).
4. B. I. Smirnov, *Dislocation Structure and Strengthening of Crystals* (Nauka, Leningrad, 1981).
5. *Deformation Strengthening and Fracture of Polycrystalline Materials*, Ed. by V. I. Trefilov (Naukova Dumka, Kiev, 1987).
6. V. A. Likhachev, V. E. Panin, V. I. Vladimirov, *et al.*, *Cooperative Deformation Processes and Localization of Deformation* (Naukova Dumka, Kiev, 1989).
7. H. Haken, *Synergetics: An Introduction* (Springer-Verlag, Berlin, 1977; Mir, Moscow, 1980).
8. G. Nicolis and I. Prigogine, *Self-Organization in Non-Equilibrium Systems* (Wiley, New York, 1977; Mir, Moscow, 1979).
9. V. L. Indenbom and A. N. Orlov, Metallofizika, No. 35, 3 (1971).
10. *Elementary Processes of Plastic Deformation in Crystals*, Ed. by V. I. Startsev (Naukova Dumka, Kiev, 1978), p. 188.
11. V. I. Vladimirov and A. A. Kusov, Fiz. Met. Metalloved. **39** (6), 1150 (1975).
12. B. A. Greenberg, M. A. Ivanov, Yu. N. Gornostirov, and L. E. Karkina, Phys. Status Solidi A **47**, 731 (1978).
13. E. É. Zasimchuk and S. I. Selitser, Dokl. Akad. Nauk SSSR **276** (6), 1125 (1984) [Sov. Phys. Dokl. **29**, 500 (1984)].
14. V. E. Panin, V. A. Likhachev, and Yu. V. Grinyaev, in *Structural Levels of Deformation in Solids* (Nauka, Novosibirsk, 1986), p. 226.
15. A. N. Orlov and Sh. Kh. Khannanov, Poverkhnost **4** (1), 71 (1986).
16. A. L. Gaĭkov and A. E. Romanov, Fiz. Tverd. Tela (St. Petersburg) **33**, 2772 (1991) [Sov. Phys. Solid State **33**, 1569 (1991)].
17. G. A. Malygin, Fiz. Tverd. Tela (St. Petersburg) **37** (1), 3 (1995) [Phys. Solid State **37**, 1 (1995)].
18. A. A. Samarskiĭ, *The Theory of Difference Schemes* (Nauka, Moscow, 1977).
19. A. A. Andronov, E. A. Leontovich, I. I. Gordon, and A. G. Maĭer, *Qualitative Theory of Second-Order Dynamic Systems* (Nauka, Moscow, 1966; Wiley, New York, 1973).
20. T. S. Akhromeeva and S. P. Kurdyumov, Zh. Vychisl. Mat. Mat. Fiz. **25** (9), 1314 (1985).
21. M. Henon, Physica D (Amsterdam) **5** (2), 412 (1982).
22. L. P. Shil'nikov, Dokl. Akad. Nauk SSSR **160** (3), 54 (1967) [Sov. Phys. Dokl. **10**, 1 (1967)].

Translated by L. Man

Crystallography Reports, Vol. 47, No. 3, 2002, pp. 501–506. Translated from Kristallografiya, Vol. 47, No. 3, 2002, pp. 549–554.

LIQUID CRYSTALS

Domain Structure in a Nematic Layer under Oscillatory Couette Flow

E. N. Kozhevnikov

Samara State University, ul. Akademika Pavlova 1, Samara, 443011 Russia

e-mail: kozhev@ssu.samara.ru

Received January 10, 2001

Abstract—The formation of a spatially modulated structure (domains) in a homeotropically aligned layer of a nematic liquid crystal (NLC) under an oscillatory Couette flow are described theoretically by using the hydrodynamic equations for an NLC which are linearized with respect to perturbations. The shear frequencies at which the phenomenon is determined by the inertial properties of the medium are considered. It is shown that the domain size is equal to the thickness h of an NLC layer and that the dependence of the threshold value of the shear amplitude u_{th} on the frequency ω and the layer thickness h is described by the expression $u_{th} = \text{const}/(\omega h^2)$. The calculated results are compared with the experimental data. © *2002 MAIK "Nauka/Interperiodica".*

INTRODUCTION

A periodic shear on a layer of a nematic liquid crystal (NLC) results in the deformation of the uniaxial structure of the crystal and thus also changes its optical properties [1]. At low shear amplitude, the molecules in the crystal oscillate about their initial equilibrium state. An increase in the amplitude can give rise to the formation of a spatially modulated structure that is optically observed in the form of domains. In this case, one observes the vortex motion of the liquid in the layer, and the molecules start oscillating about a new equilibrium direction, periodically changing along the layer. The ability of nematic single crystals to change their optical properties under periodic deformation is used in acousto-optical sensors, modulators of laser radiation, etc. [2–4], which, in turn, stimulates theoretical studies of structural transformations in crystals under conditions of periodic compression and shear.

The spatially modulated structures formed under the effect of periodic shear in a homeotropically aligned NLC layer were repeatedly studied. The modulated structure depends on the initial geometry of the sample, the shear polarization and frequency, and the absence or presence of a magnetic or an electric field and its orientation. The ellipticity of the boundary-plate motion results in the formation of roll domains [5, 6] whose direction and formation threshold depend on the ellipticity of the plate motion. According to the theory suggested in [5, 6], the transition to the in-plane shear results in the disappearance of the domains. The application of an electric field normal to the layer results in the formation of a cellular domain structure under the action of viscous waves. In each cell, the nematic director deviates from its initial orientation and slowly rotates, which results in the formation of disclinations and their subsequent growth [7]. The domain structure was also studied experimentally in a homeotropically aligned NLC layer under the action of plane oscillatory Couette flows in the absence of electric and magnetic fields in various frequency ranges [8–10].

The stability of the homeotropic structure of a nematic liquid crystal under the action of an in-plane periodic shear was studied in a number of works. The loss of crystal-structure stability at high [11] and low [12] frequencies was described with the use of multimode analysis. However, the excessive simplification of the basic equations in these studies lead to a theoretical description of the effect that is inconsistent with the experimental data. The formation of a domain structure in a homeotropically aligned NLC layer under the action of a periodic shear caused by the in-plane motion of one of the boundary plates was described theoretically in [13], where it was shown that the formation of the domain structure is associated with the inertia of the medium, which leads to the phase delay of the liquid velocity in the vortex flows relative to the shear velocity in the Couette flow and, as a result, to stationary flows and torques that destabilize the initial crystal structure. The results obtained in [13] qualitatively agree with the experimental data. At the same time, the simplifications made in the equations and the boundary conditions result in discrepancies between the theory and the experiment (the values of threshold shear amplitude and the domain width). The formation of a domain structure under the action of a periodic shear in the NLC layer with initial planar orientation was described theoretically in [14]. Using the equations from [13], Hogan *et al.* [14] obtained results which agree only qualitatively (but not quantitatively) with the experimental data considered in the same paper. The experimental studies of the domain structure in the NLC layer at frequencies <200 Hz [15, 16] were inconsistent, both qualitatively and quantitatively, with the theoretical

1063-7745/02/4703-0501$22.00

data [13, 14] and showed that the inertial properties of the medium are not responsible for the domain formation in the NLC layer at low frequencies. In the above publications, computer simulation of the domain structure was performed by the multimode Galerkin method, and the threshold of domain formation and their spatial period were determined numerically (the inertia of the medium was ignored). The results of the computer simulation are close to the experimental data obtained only at the frequencies <100 Hz, whereas at higher frequencies, these results disagree both qualitatively and quantitatively with the experimental data.

Thus, at present, there is no adequate theory of the formation of a spatially modulated structure in the NLC layer under the action of a planar periodic shear. Below, we develop such a theory for a homeotropically aligned NLC layer. The phenomenon is analyzed with the use of hydrodynamic equations for an NLC in which the quadratic terms proportional to the product of the angle of molecule rotation and the liquid velocity are retained. Following [13, 14], we consider the formation of the structure given the inertial delay in the velocity of the vortex flow with respect to the velocity of the Couette flow. The analysis is made in the single-mode approximation. Unlike [11–16], the velocities of the flows and the rotation angle of the molecules are described with the use of the real velocity profile of the unperturbed Couette flow and the exact boundary conditions for the velocities of vortex flows. In addition, the equations of perturbations are refined and the frequency range of the validity of the results is also determined.

Now, calculate the effect assuming the rigid orientation of the molecules at the boundaries of the NLC layer in the one-constant approximation of Frank elastic energy. The rotation and motion of NLC molecules are described by the equations [17]

$$\begin{gathered}\gamma[\mathbf{N} - \hat{V}\cdot\mathbf{n} + (\hat{V}\cdot\mathbf{n}\cdot\mathbf{n})\mathbf{n}] - [\mathbf{h} - (\mathbf{h}\cdot\mathbf{n})\mathbf{n}] = 0,\\ \rho\dot{\mathbf{V}} = -\nabla P + \nabla\hat{\sigma}.\end{gathered} \tag{1}$$

Here, $\mathbf{n}$ is the director, $\mathbf{V}$ is the velocity of the liquid, $\hat{V}$ is the strain-rate tensor, $\mathbf{N} = \dot{\mathbf{n}} - \frac{1}{2}(\mathrm{curl}\,\mathbf{V}\times\mathbf{n})$ is the velocity of the molecule rotation relative to the surrounding liquid, ρ is the density, P is the pressure, $\hat{\sigma}$ is the viscous-stress tensor, γ is the coefficient of rotational viscosity, $\mathbf{h}$ is the Frank elastic force,

$$\mathbf{h} = \nabla_i\frac{\partial g}{\partial(\nabla_i\mathbf{n})} - \frac{\partial g}{\partial\mathbf{n}},$$

g is the volume density of the Frank elastic energy equal, in the one-constant approximation, to

$$g = \frac{1}{2}K_{33}\sum_i(\nabla n_i)^2, \quad i = x, y, z,$$

and K_{33} is the Frank elastic constant. Ignoring viscosity coefficients, i.e., assuming α_3 and α_1 to be zeroes, we have $\gamma = \alpha_5 - \alpha_6$. Then, the components of the viscous-stress tensor acquire the form

$$\begin{aligned}\sigma_{ij} &= \alpha_4 v_{ij} + \alpha_6(v_{ik}n_kn_j + v_{jk}n_kn_i)\\ &\quad + \gamma v_{km}n_kn_mn_in_j - h_in_j.\end{aligned}$$

Now, consider the domain formation in the shear plane specified by the shear direction (the X-axis) and the layer normal (the Z-axis) under the assumption that the molecules are rotated in the XZ plane and that all the variables are independent of the coordinate Y. We obtain $V_y = 0$. This arrangement of the molecules in the domains was justified theoretically in [13]. Now, specify the shear deformation in the layer by the in-plane motion of the upper ($Z = h/2$) boundary plate at frequency ω and the shear amplitude, with the lower $Z = -h/2$ boundary plate being immobile:

$$\begin{gathered}U_x|_{Z=h/2} = u_0h\sin\omega T,\\ V_x|_{Z=-h/2} = V_z|_{Z=-h/2} = V_z|_{Z=h/2} = 0.\end{gathered}$$

Here, u_0 is the dimensionless shear amplitude of the boundary plate and T is the time.

Now, consider small shear amplitudes, $u_0 < 1$. In this case, the angles θ of the deviation of the molecules from the Z-axis are also small, which allows the linearization of the motion equations with respect to angles and the assumption that the director components are $n_x \approx \theta$ and $n_z \approx 1$.

In what follows, we use the dimensionless coordinates $x = X/n$ and $z = Z/h$, the time $t = \omega T$, and the dimensionless velocities $v_k = V_k/(\omega h)$. Retaining the terms proportional to the product of the angle θ and the velocity v in the motion equations, we arrive at the following system of equations for θ, v_x, and v_z:

$$\begin{gathered}\partial_t\theta - \varepsilon\Delta\theta - v_{x,z} = -\theta_{,x}v_x - \theta_{,z}v_z - 2\theta v_{zz},\\ (\eta\sigma^2\Delta\partial_t - \hat{D})v_x + \varepsilon\Delta\partial_z^3\theta\\ = [\partial_z(\partial_z^2 - \partial_x^2)(v_{z,z}\theta) - 2\partial_x\partial_z^2(v_{xz}\theta)]\\ + \eta\sigma^2\partial_z[\Delta v_zv_{1x} - v_zv_{x,z^2}],\\ \mathrm{div}\,\mathbf{v} = 0,\end{gathered} \tag{2}$$

where $\hat{D}$ is the differentiating operator

$$\hat{D} = \eta\Delta^2 + \partial_z^2\partial_x^2,$$

and ε and σ are the dimensionless parameters determining the dependence of the effect on the nematic-layer thickness h and the shear frequency ω via the scaling parameter ωh^2,

$$\varepsilon = \frac{K_{33}}{\gamma\omega h^2}, \quad \sigma^2 = \frac{\rho\omega h^2}{\eta} = \frac{\lambda}{\varepsilon}, \quad \lambda = \frac{\rho K_{33}}{\gamma\eta} \sim 10^{-6},$$

where $\eta = \frac{\alpha_4 + \alpha_6}{\gamma}$ is the dimensionless viscosity in a viscous wave propagating along the crystal axis.

Now, represent the hydrodynamic variables by the expansions

$$\mathbf{v} = \mathbf{v}_1 + \mathbf{v}_2 + \mathbf{v}', \quad \theta = \theta_1 + \theta_2 + \theta',$$

where subscript 1 identifies the solution of the linearized Eqs. (2) with the initial boundary conditions for $\mathbf{v}$ and θ, and subscript 2 and the prime identify the stationary and the oscillatory parts of the perturbations, respectively. In the perturbation equations, the velocity v_1 and the angle θ_1 play the role of an external factor. The appearance of the nonzero stationary angle θ_2 in the solution indicates the transition of the crystal into a new orientational state.

Consider system (2) and single out the equations for the external factor,

$$\begin{cases} (\sigma^2\partial_t - \partial_z^2)v_x - \dfrac{\varepsilon}{\eta}\partial_z^3\theta_1 = 0 \\ \theta_{1,t} - \varepsilon\partial_z^2\theta_1 - v_{1x} = 0 \\ \theta|_{z=\pm1/2} = 0, \ v_{1x}|_{z=-1/2} = 0, \ v_{1x}|_{z=1/2} = u_0\cos t; \end{cases} \tag{3}$$

the equations for oscillating variables,

$$\begin{cases} \partial_t\theta' - \varepsilon\Delta\theta' - v'_{x,z} = -\theta_{2,x}v_{1x} \\ (\eta\sigma^2\Delta\partial_t - \hat{D})v'_z - \varepsilon\Delta\partial_z^2\partial_x\theta' = \partial_x^2\partial_z(\theta_2 v_{1x,z}) \\ \operatorname{div}\mathbf{v}' = 0 \\ \theta'|_{z=\pm1/2} = v'_z|_{z=\pm1/2} = v'_{z,z}|_{z=\pm1/2} = 0; \end{cases} \tag{4}$$

and the equations for stationary variables,

$$\begin{cases} \varepsilon\Delta\theta_2 + v_{2x,z} = \langle\theta'_{,x}v_{1x} + 2\theta_1 v'_{zz} + \theta_{1,z}v'_z\rangle \\ \hat{D}v_x - \varepsilon\Delta\partial_z^3\theta_2 = -\partial_z(\partial_z^2 - \partial_x^2)\langle v'_z\theta_1\rangle \\ + \partial_x\partial_z^2\langle\theta' v_{1x,z} + \theta_1 v'_{x,z} + \theta_1 v'_{z,x}\rangle \\ -\eta\sigma^2\partial_z[\langle\Delta v'_z v_{1x}\rangle + \langle v'_z v_{x,z^2}\rangle] \\ \operatorname{div}\mathbf{v}_2 = 0 \\ \theta_2|_{z=\pm1/2} = v_{2x}|_{z=\pm1/2} = 0, \ \int\limits_{-1/2}^{1/2} v_{2x}dz = 0. \end{cases} \tag{5}$$

Here, the angular brackets indicate averaging over the oscillation period.

The stationary stresses and torques destabilizing the initial structure are associated with the phase delay in the displacement of the particles in the medium in the oscillatory flows with respect to the displacement of the boundary plate. This delay is determined by the inertia of the medium and the boundary effects in the thin layers (of the order of the orientational-wave length); the ratio of their contributions to the velocity v'_z is determined by the quantity $\sigma^2\sqrt{\varepsilon} = (\rho\omega h^2/\gamma)^{3/2}\lambda^{-1/2}$. Analyzing the phenomenon, we limit our consideration to the frequencies at which this ratio is pronounced and at which the inertial effects prevail over the boundary effects. In this case, the boundary conditions for the angles θ_1 and θ' can be ignored and can be defined as the gradients of the displacements $u_{1x,z}$ and $u'_{x,z}$. Moreover, the frequencies are limited from above by the condition $\sigma^2 < 15$, which allows us to change the functions $\sin(\sigma z)$ and $\cos(\sigma z)$ by their expansions in the argument retaining only two terms of these expansions. The above constraints on the frequency lead to the inequality

$$\lambda^{1/3} \approx 10^{-2} \ll \frac{\rho\omega h^2}{\gamma} < 15. \tag{6}$$

The solution of system (3) can be written as

$$v_{1x} \approx u_0\left\{\cos t + \frac{\sigma^2}{6}[1 - (z+1/2)^2]\sin t\right\}(z+1/2), \tag{7}$$

$$\theta_1 = u_{1x,z} \approx u_0[\sin t - \sigma^2 H(z)\cos t],$$

where

$$H = H(z) = \frac{1}{6} - \frac{1}{2}(z+1/2)^2.$$

Eliminating the angles θ' and θ_1 and their time derivatives from the equations for the stationary variables and rejecting the terms of the smallness order ε, we arrive at the following equation for the stationary angle of the molecule rotation:

$$\varepsilon\Delta\theta_2 + v_{2x,z} = \partial_z^2\langle v'_z u_{1x}\rangle.$$

Introducing the function $w = v_{2x} - \partial_z\langle v'_z u_{1x}\rangle$, we can transform this equation into the form

$$\varepsilon\Delta\theta_2 + w_{,z} = 0. \tag{8}$$

Because of the boundary conditions for v'_z and v_{2x} in Eqs. (4) and (5), the function w should satisfy the conditions

$$w|_{z=\pm1/2} = 0; \quad \int\limits_{-1/2}^{1/2} w dz = 0 \tag{9}$$

and can be regarded as the reduced flow velocity.

Now, proceed to the equation for the stationary flows in system (5). Expressing the average product in

terms of the second equation of system (4), we obtain

$$-\eta\sigma^2\partial_z\langle\Delta v_z' v_{1x}\rangle = \partial_z\langle(\eta\sigma^2\Delta\partial_t v_z')u_{1x}\rangle$$

$$= \partial_z\langle u_{1x}\hat{D}v_z'\rangle + \varepsilon\langle u_{1x}\Delta\partial_z^2\theta_{,x}'\rangle + \langle\partial_x^2\partial_z(\theta_2 v_{1x})u_{1x}\rangle.$$

Taking into account inequalities (6), we can transform the equations for flows into the form

$$(\hat{D} + \partial_z^4)w$$

$$= -[(4\eta + 1)\partial_z^4 + 4\eta\partial_x^2\partial_z^2]\langle v_z' u_{1x,z}\rangle \qquad (10)$$

$$+ \sigma^2\{[(6\eta + 1)\partial_z^3 + 2\eta\partial_x^2\partial_z]\langle v_z' v_{1x}\rangle - 4\eta\partial_z^2\langle v_z' v_{1x,z}\rangle\}.$$

Assuming the perturbations to be periodic along the layer, we can represent the angle θ_2 and the velocities w and v_z' as

$$\begin{pmatrix}\theta_2\\ w\\ v_z'\end{pmatrix} = \begin{pmatrix} f_\theta(z)\\ a f_w(z)\\ \varphi(t) f_v(z)\end{pmatrix}\theta_0\cos(kx). \qquad (11)$$

In the single-mode approximation, the angle θ_2 is represented by an even function of the coordinate z, whereas the flow velocities w and v_z' are represented by the odd functions. The functions f_w and f_v are selected so as to ensure the smooth dependence of the perturbations on z and the fulfillment of the boundary conditions for the velocities

$$f_w = \sin(2\pi z),$$
$$f_v(z) = \sin(\pi z) + \sin(3\pi z). \qquad (12)$$

The coefficient a is assumed to be equal to

$$a = \frac{4\pi^2 + k^2}{2\pi}.$$

The function f_θ is determined by the solution of Eq. (8). For strong surface anchoring of the NLC molecules with the substrates, the function f_θ has the form

$$f_\theta(z) = \cos(2\pi z) + \frac{\cosh kz}{\cosh k/2}.$$

Substituting Eqs. (11) for v_z' and θ_0 into Eq. (4) for oscillatory flows, multiplying both sides of the equation by $f_v(z)$, and integrating the result with respect to the layer thickness, we can separate the equation for $\varphi(t)$ as follows:

$$(D_s + \eta\sigma^2\Delta_s\partial_t)\varphi$$
$$= -\pi k^2 u_0\theta_0\{\nu\cos t + \sigma^2\psi\sin t\}. \qquad (13)$$

Hereafter, we use the following notation:

$$\Delta_s = \Delta_1 + \Delta_3, \quad D_s = D_1 + D_3,$$
$$\Delta_n = k^2 + n^2\pi^2, \quad D_n = \eta\Delta_n^2 + n^2k^2\pi^2,$$

where n is an integer,

$$\nu = \nu(k) = \int_{-1/2}^{1/2}[\cos(\pi z) + 3\cos(3\pi z)] f_\theta(z)dz$$

$$= \frac{36}{15\pi}\frac{36 + 25\xi + 4\xi^4}{(\xi + 1)(\xi^2 + 9)},$$

$$\psi = \psi(k)$$

$$= 2\int_{-1/2}^{1/2}[\cos(\pi z) + 3\cos(3\pi z)]H(z) f_\theta(z)dz \qquad (14)$$

$$\approx [0.03\xi^{12} + 1.7\xi^{10} + 31\xi^8 + 135\xi^6 + 133\xi^4$$
$$- 135\xi^2 + 106 - (3\xi^9 + 32\xi^7$$
$$- 292\xi^3 - 262\xi)\tanh(\pi\xi)]/[(\xi^2 + 1)(\xi + 9)^3],$$
$$\xi = k/\pi.$$

The constraint imposed on frequency (6) results in the inequality $\sigma^2|\Delta| < |\hat{D}_s|$, which allows one to represent the solution of Eq. (13) in the form

$$\varphi(t) = -\frac{\pi k^2 u_0\theta_0}{D_s}\left\{\nu\cos t + \sigma^2\left(\frac{\nu\eta\Delta_s}{D_s} + \psi\right)\sin t\right\}.$$

Substitute the velocity v_z' with the function φ determined to Eq. (10) and write the averaged moments in the right-hand side of the equation as

$$\langle v_z' u_{1x,z}\rangle = -\frac{k^2\pi\sigma^2 u_0}{2}$$

$$\times\left\{\frac{f_v(z)}{D_s}\left[\frac{\nu\eta\Delta_s}{D_s} + \psi - \nu H(z)\right]\right\}\theta_0\cos kx,$$

$$\langle v_z' v_{1x,z}\rangle = -\frac{k^2\pi\sigma^2 u_0}{2D_s} f_v(z)\theta_0\cos kx,$$

$$\langle v_z' v_{1x}\rangle = -\frac{k^2\pi\sigma^2 u_0}{2D_s} f_v(z)(z + 1/2)\theta_0\cos kx.$$

Multiplying both sides of Eq. (10) by w in form (13) and performing the integration over the layer thickness, we arrive at the following equation for θ_0:

$$\frac{(D_2 + 16\pi^4)\Delta_3}{4\pi^2}\theta_0 = \frac{\sigma^2 u_0^2}{\varepsilon}A(k)\theta_0, \qquad (15)$$

where

$$A(k) \approx \frac{k^2\Delta_2}{\pi D_s}\left\{\left[\ 33(1+4\eta)\pi^4 + 17\eta\pi^2k^2\right]\right.$$
$$\times\left(\frac{\eta\nu\Delta_s}{D_s} + \psi\right) + \ \nu[2.7(1+4\eta)\pi^4 - 16(\pi^2 + \eta k^2)$$
$$\left. - 72\eta\pi^2 + 1.4\eta\pi^2k^2]\right\}.$$

Equation (15) has a nonzero solution for θ_0 if the shear amplitude is

$$u_0 = \frac{\sqrt{\varepsilon}}{\sigma}F(k),$$

where

$$F(k) = \frac{(\eta\Delta_2 + 4\pi^2)\Delta_2^2 D_s}{4\pi k^2}$$
$$\times\left\{\left[\ 33(1+4\eta)\pi^4 + 17\eta\pi^2k^2\right]\left(\frac{\eta\nu(k)\Delta_s}{D_s} + \psi(k)\right)\right.$$
$$+ \nu(k)\left[2.7(1+4\eta)\pi^4 - 16(\pi^2 + \eta k^2)\right. \quad (16)$$
$$\left.\left. - 72\eta\pi^2 + 1.4\eta\pi^2k^2\ \right]\right\}^{-1}.$$

The threshold amplitude $u_{0,th}$ is determined by the u_0 value with the minimum k as follows:

$$u_{0,th} = \frac{\sqrt{\varepsilon}}{\sigma}F_{th} = \sqrt{\frac{\rho K_{33}}{\eta\gamma}}\frac{\eta}{\rho\omega h^2}F_{th}. \quad (17)$$

Here, k_{th} is the k value which minimizes the function $F(k)$; $F_{th} = F(k_{th})$.

Now, analyze the results obtained. The inertial properties of the medium lead to the formation of a domain structure in the NLC layer in a planar oscillatory Couette flow. The threshold of the effect depends on the frequency and the layer thickness via the scaling parameter ωh^2:

$$u_{th} \sim 1/(\omega h^2).$$

The k_{th} and F_{th} values were calculated numerically by Eqs. (16) and (14) using the typical parameters of a nematic crystal: $\rho = 1$ g cm^{-3}, $\alpha_4 = 0.104$ Pa, $\alpha_6 = -0.034$ Pa, $\gamma = 0.078$ Pa, and $K_{33} = 7 \times 10^{-12}$ N [17]. The k_{th} value was determined to be 3.1, and therefore the theoretical domain width, $d = \pi/k_{th}h = 1.01h$, is the same as the thickness of the NLC layer and does not depend on frequency. The minimum $F(k)$ value equals $F_{th} = 63.3$ and is also independent of w. It should be indicated that differently selected functions $f_w(z)$ and $f_v(z)$ (e.g., Chandrasechar functions) and the account for the difference in the Frank elastic constants ($K_{11} \neq K_{33}$) in the calculations produce almost no effect on the k_{th} and F_{th} values.

The experimental data on domains in a homeotropically aligned NLC layer under oscillatory Couette flow are given for both high frequencies, 10^2–10^4 Hz (the inequality $\rho\omega h^2/\gamma \gg \lambda^{1/3}$ is satisfied) [9, 10], and low frequencies ($\rho\omega h^2/\gamma \ll \lambda^{1/3}$) [15, 16]. In these cases, different dependences of the amplitude of the threshold shear u_{th} on the layer thickness and frequency were reported. The threshold amplitude in [9, 10] was approximated by Eq. (17), while the F_{th} values were equal to $F_{th} \approx 7.5$ and $F_{th} \approx 6$ at layer thicknesses 100 and 10 μm, respectively. The data [15, 16] for the frequencies and layer thicknesses satisfying inequality (6) and the condition $\varepsilon^{-1} = \gamma\omega h^2/K_{33} > 10^5$ can also be approximated by the expression $u_{th} \sim 1/(\omega h^2)$. However, insufficient data for the above range of parameters do not allow the unambiguous establishment of this dependence. Thus, the theoretical dependence of the threshold amplitude on frequency and the thickness of the nematic layer is consistent with the experimental data within the frequency range considered above. At low frequencies, where $\varepsilon^{-1} = \gamma\omega h^2/K_{33} < 10^5$, the envelope of the experimental curves obtained in [15, 16] for various thicknesses of the layer is approximated by the relationship $u_{th} \sim \omega^{-1/4}h^{-1/2}$. In this frequency range, the effect should be subjected to a more thorough theoretical analysis.

The theoretical width of the domain structure, $d = h$, agrees with the data in [15, 16], where, at frequencies $\omega/2\pi > 100$ Hz, it was obtained that $d \approx h$.

The theoretical account for the real (nonlinear in z) velocity profile of the oscillatory Couette flow and the exact boundary conditions imposed on the velocities of the vortex flow increases by an order of magnitude the theoretical values of u_{th} with respect to the threshold amplitude obtained in the simplified calculation [14]. Compare these values with the experimental data obtained in [9, 10] and [15, 16]. The threshold amplitude u_{th} in the cited studies was determined in different frequency ranges. In the region of their overlap (100–200 Hz), the u_{th} values reported in [9, 10] and [15, 16] at the same layer thickness differs by an order of magnitude. The theoretical u_{th} values obtained in the present work exceed the experimental data [9, 10] but are consistent with the data from the later publications [15, 16]. This is confirmed by the same theoretical value $u_{th} = 0.22$ determined at the parameter ratio $\varepsilon = K_{33}/\gamma\omega h^2 = 0.5 \times 10^{-5}$ and the experimental value $u_0 = 0.2$ at the same ε reported in [15, 16]. A more detailed comparison of the theoretical and experimental data requires the performance of additional experiments at frequencies exceeding 100 Hz and with layer thicknesses $h \sim 10^2$ μm.

To determine the influence of the surface density of anchoring energy on the formation of the domain structure, we also calculated the threshold of the phenomenon observed given a weak orienting effect of the layer boundaries (the validity of the inequality $g_S h/K_{33} \ll 1$, where g_S is the surface density of the anchoring energy). Using the above reasoning and the functions f_v and f_w in the form (12), we arrived at the following simple expression for f_θ:

$$f_\theta(z) = \cos 2\pi z.$$

The threshold parameters of the phenomenon vary only slightly in the transition from strong surface anchoring of NLC molecules at the boundaries to weak anchoring—the domain size becomes equal to $d \approx 0.9h$ and the threshold amplitude increases by 13%. Therefore, the orienting effect of the boundaries of the nematic layer on the molecules in the crystal is not essential for the theoretical analysis of the effect. It is important only for the selection of their initial orientation.

REFERENCES

1. A. P. Kapustin and O. A. Kapustina, *Acoustics of Liquid Crystals* (Nauka, Moscow, 1986).
2. V. N. Reshetov, I. V. Sytin, and G. N. Yakovenko, in *Problems of Shipbuilding* (Sudostroenie, Moscow, 1985), Vol. 20, p. 59.
3. E. I. Remizova and V. N. Reshetov, in *Proceedings of the VI All-Union Conference "Liquid Crystals and Their Practical Use" (*Chernigov, 1988), Vol. 4, p. 529.
4. G. N. Yakovenko, Akust. Zh. **40**, 851 (1994) [Acoust. Phys. **40**, 754 (1994)].
5. E. Dubois-Violette and F. Rothen, J. Phys. (Paris) **39** (10), 1039 (1978).
6. E. Guazelli and E. Guyon, J. Phys. (Paris) **43**, 915 (1982).
7. V. K. Kondratenko, M. M. Fardzitov, and A. N. Chuvyrov, Fiz. Tverd. Tela (Leningrad) **17**, 795 (1975) [Sov. Phys. Solid State **17**, 506 (1975)].
8. G. N. Belova and E. I. Remizova, Kristallografiya **31**, 517 (1986) [Sov. Phys. Crystallogr. **31**, 304 (1986)].
9. G. N. Belova and E. I. Remizova, Akust. Zh. **31**, 289 (1985) [Sov. Phys. Acoust. **31**, 171 (1985)].
10. G. N. Belova and E. I. Remizova, Kristallografiya **30**, 343 (1985) [Sov. Phys. Crystallogr. **30**, 198 (1985)].
11. I. A. Chaban, Akust. Zh. **24**, 200 (1978) [Sov. Phys. Acoust. **24**, 115 (1978)].
12. I. A. Chaban, Akust. Zh. **31**, 132 (1985) [Sov. Phys. Acoust. **31**, 77 (1985)].
13. E. N. Kozhevnikov, Zh. Éksp. Teor. Fiz. **91**, 1346 (1986) [Sov. Phys. JETP **64**, 793 (1986)].
14. S. J. Hogan, T. Mullen, and P. Woodford, Proc. R. Soc. London, Ser. A **441**, 559 (1993).
15. T. Börsönyi, Á. Buka, A. P. Krekhov, and L. Kramer, Phys. Rev. E **58**, 7419 (1998).
16. A. P. Krekhov, T. Börsönyi, P. Tóthc, *et al.*, Phys. Rev. **337**, 171 (2000).
17. P. de Gennes, *The Physics of Liquid Crystals* (Clarendon, Oxford, 1974; Mir, Moscow, 1977).

Translated by A. Zolot'ko

Crystallography Reports, Vol. 47, No. 3, 2002, pp. 507–513. Translated from Kristallografiya, Vol. 47, No. 3, 2002, pp. 555–561.

THIN FILMS

X-ray Diffraction Study of Gadolinium Stearate Langmuir–Blodgett Films

É. K. Kov'ev*, S. N. Polyakov, A. M. Tishin***, T. V. Yurova***, and G. B. Khomutov*****

** Shubnikov Institute of Crystallography, Russian Academy of Sciences, Leninskiĭ pr. 59, Moscow, 117333 Russia*

*** Research Institute of Physics, Moscow State University, Vorob'evy gory, Moscow, 119899 Russia*

e-mail: cryo161a@nabla.phys.msu.su

**** Faculty of Physics, Moscow State University, Vorob'evy gory, Moscow, 119899 Russia*

e-mail: tanya@phys.msu.su

e-mail:gbk@phys.msu.su

Received December 20, 2000; in final form, June 20, 2001

Abstract—The comparative structural studies of gadolinium stearate Langmuir–Blodgett films prepared with the use of two different subphases (aqueous solutions of gadolinium chloride and gadolinium acetate) have been performed by the methods of X-ray diffractometry. The films were applied onto single-crystal silicon substrates coated with a native-oxide layer either with the use of buffer molecular stearic-acid layers or without such layers. It was established that the films obtained with the use of gadolinium acetate and the preliminarily formed buffer layers are, in fact, single-phase *Y*-type films with highly ordered molecular structure, and the thickness of the bimolecular layer $d = (51.3 \pm 0.5)$ Å. © *2002 MAIK "Nauka/Interperiodica".*

INTRODUCTION

Langmuir–Blodgett (LB) films of fatty acids are highly ordered two-dimensional layered structures with periods of the order of several nanometers [1]. Their physicochemical properties depend, to a large extent, on the metal cations incorporated into the molecular matrix. Langmuir–Blodgett films are very promising materials for molecular electronics, nanotechnology, and various quantum devices [2–5], as well as for the modeling of two-dimensional physical systems, because the material of these films can be considered as a certain layer matrix. Metal ions incorporated into Langmuir–Blodgett films form two-dimensional arrays distributed with a certain spatial periodicity. The incorporation into the films of metal cations possessing intrinsic magnetic moments make them similar to two-dimensional magnetic films. One of the first studies along these lines [6–9] was performed on manganese stearate [$Mn(C_{18}H_{35}O_2)_2$] Langmuir–Blodgett films. It was established that manganese stearate could be deposited onto the substrate either as an individual monolayer or as a multilayer film with a period of ~50 Å. It was also shown that the magnetic moments of manganese ions are ordered as in antiferromagnetic compounds and that the magnetic phase transition temperature equals ~10 K.

Possible magnetic ordering at high temperatures in gadolinium stearate films was indicated in [10, 11]. Magnetic ordering in Langmuir–Blodgett films containing gadolinium ions occurs up to a temperature of ~500 K [12]. Gadolinium is a ferromagnetic with a Curie temperature ~294 K and a hexagonal close-packed lattice [$Mg(A3)D^4_{6h} - P6_3/mmc$] with the unit-cell parameters $a = 3.636$ Å and $c = 5.783$ Å. The electronic structure of a gadolinium atom is such that 4*f*-electrons are inside the filled 5*p*-shell and the wave functions of the 4*f*-levels of the nearest neighboring atoms from different coordination spheres do not overlap. As a result, the indirect exchange interactions in metal Gd occur via conduction electrons [13, 14]. The local intrinsic magnetic moment of Gd atoms is created by seven 4*f*-electrons and equals $7_{\mu B}$. The wave functions of the 5*d*- and 6*s*-electrons of the neighboring atoms considerably overlap and provide chemical bonding between these atoms.

Along with thin epitaxial metal films and surface layers of various magnetics, the LB films can be considered as a promising model for studying two-dimensional magnetism. However, it should be remembered that the preparation of quasi-two-dimensional epitaxial films is associated with considerable technological difficulties in the preparation of substrates with atomically pure surfaces and the growth of perfect thin films and atomic layers. It should also be indicated that the methodological aspect of the preparation of a two-dimensional magnet based on a gadolinium-containing LB

1063-7745/02/4703-0507$22.00 © 2002 MAIK "Nauka/Interperiodica"

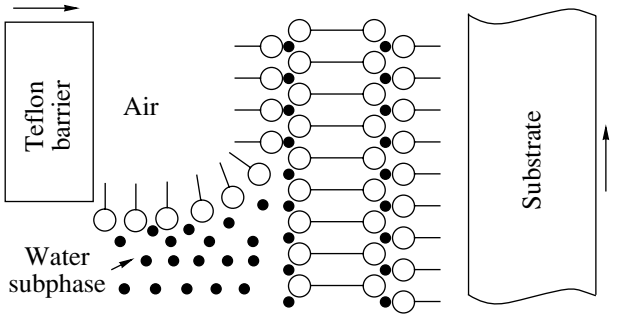

Fig. 1. Scheme of preparing gadolinium stearate LB films and their molecular structure.

film depends, first and foremost, on the technology of its growth, the choice of the organic matrix, and the incorporation of gadolinium atoms into the film [15]. All these problems are the subject of the present study.

Below, we consider the results of X-ray diffraction studies of the structural characteristics of gadolinium stearate LB films formed on single-crystal silicon substrates coated with a layer of native oxide obtained with the use of two different subphases—aqueous solutions of gadolinium chloride and gadolinium acetate.

EXPERIMENTAL

Preparation of Langmuir–Blodgett Films

We used stearic acid $C_{18}H_{36}O_2$ (Serva, Germany) and gadolinium chloride and gadolinium acetate (Aldrich, USA). Water was deionized with the aid of a MilliQ system for water purification (Millipore, USA). Langmuir monolayers were transferred onto solid substrates and were studied on an automated setup described elsewhere [16]. In order to obtain a stearic-acid monolayer the stearic acid (SA) solution in 4×10^{-4} M chloroform was spread onto a clean surface of the subphase. Ten minutes later (upon the evaporation of the solvent and the attainment of the adsorption equilibrium), the monolayer was compressed at a rate of 3 Å^2/(SA molecule) × min with a simultaneous record of the compression isotherm. The monolayer was transferred from the surface of the aqueous phase onto a solid substrate [a polished (100)Si surface] by the method of vertical lifting of the substrate under a surface pressure of 30 mN/m at a temperature of 20°C. The velocity of substrate immersion was 5 mm/min, the concentration of gadolinium salts [$GdCl_3$ and $Gd(CH_3COO)_3$] was 10^{-4} M at pH 5.5. Figure 1 illustrates the formation of gadolinium stearate Langmuir–Blodgett films onto the substrates and shows their possible three-dimensional structure.

Table 1. Structural parameters of various phases of stearic acid

Phase	Parameters, Å	Card JCPDS
B-monoclinic	$a = 5.710$, $b = 7.390$, $c = 50.70$, $\beta = 119.9°$	9-622
C-monoclinic	$a = 9.378$, $b = 7.390$, $c = 39.960$, $\beta = 94.81°$	38-1923
E-orthorhombic	$a = 15.00$, $b = 22.50$, $c = 22.50$	8-594
F-orthorhombic	$a = 16.50$, $b = 24.70$, $c = 24.700$	8-668

X-ray Diffraction Measurements

The integral diffraction patterns (θ/2θ scan) were recorded on a multicrystal X-ray spectrometer based on the Rigaku D/max-RC diffractometer with a 12 kW X-ray radiation source with a rotating anode. We used the $K_{\alpha 1}$-line of a copper-anode radiation. The primary radiation was monochromatized by a tunable double-reflection silicon crystal–monochromator. Depending on the angular resolution required, different single- and triple-reflection silicon crystal analyzers were used. Weak signals were recorded according to the classical scheme with the use of the pyrolytic graphite crystal (with an angular resolution of ≤0.1°).

RESULTS AND DISCUSSION

The surface-active substance forming a Langmuir monolayer on the aqueous-phase surface was stearic acid because of the highly ordered and compact arrangement of its carboxyl groups in the monolayer. According to the X-ray diffraction data for powder crystals, the solid phase of this compound can exist in four polymorphous modifications, *B*, *C*, *E*, and *F*, with different spatial orientations of C–H bonds with respect to the molecule axis (Table 1).

Only the *B* and *C* phases are present in multilayer stearate LB films, in which the pairs of molecules are aligned to form bimolecular layers. The length of these dimers depends not only on the tilt of the molecules and their mutual arrangement, but also on the packings of atoms (especially carbons) in the tails of methyl groups. Unlike the situation in single crystals, SA molecules in LB films form an independent triclinic *A* phase with the thickness of the bimolecular layer equal to (46.1 ± 0.5) Å [17, 18]. The space group of the packing of SA molecules in the films was determined from the transmission electron diffraction patterns. The spot-type electron diffraction patterns showed that the *A* phase is either monoclinic or orthorhombic with the unit-cell parameters $a = 5.0$ Å and $b = 7.5$ Å [19, 20]. In actual fact, LB films consist of different mixtures of the *A* and *C* or the *B* and *C* phases or of all three phases simultaneously, which, no doubt, changes the period of the layered structure of the film and provides its local variations. This should always be kept in mind while interpreting the X-ray diffractometric data.

The characteristic diffraction pattern from the 11-layer LB films of the stearic acid (θ/2θ scan) is shown in Fig. 2a. The thicknesses of the bimolecular layer or the periods of the films measured from diffraction patterns range within 46–48 Å. It should be emphasized that the experimental values considerably differ from the known powder diffractometric data for the *B* phase but are close to the measured period of layer alternation (46.1 ± 0.5) Å in the LB films consisting of the molecules of the *A* phase [17]. Thus, it can be assumed that the stearic-acid films obtained in our experiments are formed mainly by the molecules of the *A* phase. However, the question of whether the films really consist of only one phase or not is still open.

It is interesting to compare the structural perfection of the films prepared by the transfer of SA monolayers from the surface of the aqueous solutions of various gadolinium salts onto substrates. We did experiments on gadolinium chloride $GdCl_3$ and gadolinium acetate [$Gd(CH_3–COO)_3$] (the salts of the acetic acid). It turned out that the structure of the LB films obtained at the same pH and the gadolinium salt concentration in the aqueous subphase depended on the nature of the acidic residue of the salt. The diffraction patterns from LB films obtained with the use of a gadolinium chloride solution (θ/2θ scan) clearly show only one considerably broadened peak (the second one) with the integrated halfwidth $W_R = 0.794°$ (Fig. 2b), whereas the other narrow peaks characterized by $W_R = 0.2°$, including the first one, are very weak. X-ray diffraction from thin LB films is described by the kinematical theory of scattering. Therefore, the diffraction pattern can be considered as two overlapped independent series of reflections due to two independent phases having different molecular structures. It is also necessary to take into account the superposition of individual reflections, which makes the interpretation of the diffraction pattern even more difficult.

The intensities at the maxima (*I*) and the integrated intensities ($I_i = kN_i$), the halfwidths (W_R) of the reflection curves, and the layer periods (*d*) calculated from the experimental values of the Bragg angles are indicated in Table 2 (series 1). These data show that the gadolinium stearate LB films consists of two phases having different periods, d_1 = 25.2 or 50.4 Å and d_2 = 47.6 Å. However, since the first reflection is very weak, the structure of such films can be described by two models. In the first model, the reflection formed at the Bragg angle 2θ = 3.5° is assumed to be the 001 reflection and, therefore, the film should consist of the *E* or *F* phase and not the *A* phase, because almost the whole integrated intensity is concentrated in this reflection. In the second model, this reflection is indexed like the second, 002, reflection of the *A* phase, but the first peak due to this phase is practically invisible on the diffraction pattern because of pronounced diffuse scattering from the molecular distortions of the film. The second phase

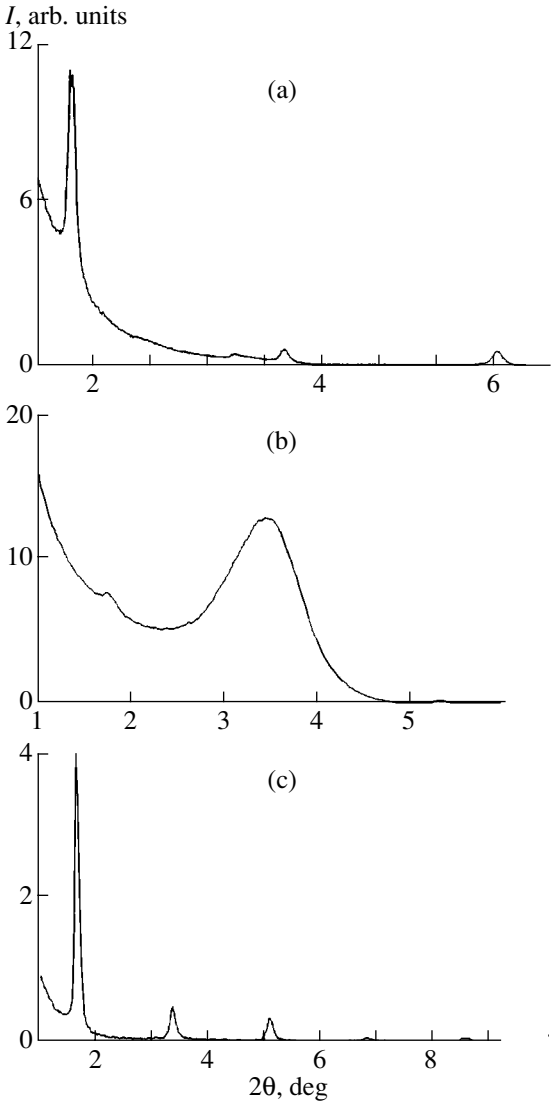

Fig. 2. Diffraction pattern (θ/2θ scan) of LB films of (a) the stearic acid (five bilayers, the period d = 47.6 ± 0.5 Å), (b) gadolinium stearate on the polished silicon substrates coated with a layer of native oxide obtained with the use of an aqueous gadolinium chloride solution (the film thickness is up to 20 bilayers, pH 5.5), and (c) gadolinium stearate on the polished silicon substrates coated with a layer of native oxide obtained with the use of an aqueous gadolinium acetate solution (the film thickness is 80 bilayers, pH 5.5).

observed most probably corresponds to the stearic acid with the bimolecular-layer thickness d_2 = 47.6 Å.

The integrated intensities (I_i) show that the fraction of the second phase is insignificant (about 0.7%). The second phase is more probable and, therefore, we assume that the LB films consist mainly of molecules of the *A* phase.

The reflection broadening (W_R) is associated with the finite dimensions of the coherent-scattering region, $l = \lambda/(W_R \cos\theta)$. This corresponds to l_1 = 110 Å for the

Table 2. Results of X-ray diffraction study of Longmuir–Blodgett films

Sample series	*hkl*	*I*, pulse/s	N_i, pulse	W_R, deg	2θ, deg	Interlayer period *d*, Å
1	001	4064	–	–	2.86	42.9
	002	7526	162311	0.79	3.50	50.4
	003	75	687	0.21	5.62	47.1
	004	25	158	0.17	7.42	47.6
	005	30	309	0.22	9.20	48.1
2	001	3921	25558	0.10	1.69	52.5
	002	509	4417	0.11	3.40	52.2
	003	284	2899	0.13	5.11	51.7
	004	58	738	0.15	6.85	51.8
	005	50	687	0.20	8.56	51.6
3	001	464	24561	0.55	1.73	51.1
	002	324	9728	0.19	3.74	47.2
	003	2144	61198	0.19	5.46	48.5
	004	729	19498	0.18	7.23	48.9
	005	702	18288	0.19	9.00	49.1
	006	122	1938	0.17	10.79	49.2
	007	101	2461	0.18	12.58	49.2
4	001	21115	382444	0.16	1.80	49.1
	002	1897	31011	0.19	3.62	49.2
	003	1113	23559	0.19	5.37	49.6
	004	153	3148	0.18	7.18	49.5
	005	159	3083	0.20	8.94	49.0
	006	28	446	0.10	10.73	49.4
	007	33	3031	0.19	12.30	49.4

first phase, and, according to the data for the (003), (004), and (005) reflections, to $l_2 = 420$ Å for the second phase. It is interesting that the experimental l_1 value equals double the period of the film, $2d_1 = 101$ Å, whereas the l_2 value is close to the film thickness (500 Å). The coherent-scattering regions for LB films are the regions with characteristic molecular structures. Therefore, the molecular structure of the LB films obtained with the use of the aqueous $GdCl_3$ solution as a subphase is represented by the following model. Gadolinium cations interacting with the stearic-acid molecules of the film form the complexes and, thus, bind two molecular bilayers, thus forming stable "chains" of SA molecules. In this case, the chain consists of four SA molecules, e.g., SA–SA–Gd–SA–SA. In the film bulk, these chains are arranged randomly and form a characteristic "texture." Between the regions of phase 1, one can also encounter the regions of phase 2—long chains of stearic acid molecules which have not reacted with gadolinium cations (SA–SA–SA–SA…). Thus, the results obtained indicate that the use of gadolinium chloride as a source of gadolinium ions in the aqueous phase under the conditions of our experiments (pH 5.5, gadolinium concentration 10^{-4} M) does not lead to the formation of perfect gadolinium stearate LB films. This can be explained by the complicated processes of formation of complexes by gadolinium cations on the monolayer surface, including the interaction with hydroxide and chloride ions, and also the specific mechanical properties of the monolayer and the interactions occurring during the monolayer transfer onto the substrate and the formation of the multilayered structure of the LB film. A similar dependence was also observed for cadmium stearate films [4].

The diffraction pattern from the films obtained with the use of the gadolinium acetate aqueous solution as a subphase is quite different. Figure 2c shows the typical X-ray diffraction patterns (θ/2θ scan) from a thick (80 bilayers) gadolinium stearate film deposited onto the polished silicon substrate from the surface of the aqueous subphase by the method of vertical immersion of the substrate.

In the angular range 2θ = 1°–10°, one can clearly distinguish narrow Bragg reflections of various orders. The characteristic feature of such diffraction patterns is the occurrence of the Bragg diffraction only in the angular range whose values are higher than the critical

angle (θ_{cr}) against the background of the X-ray specular reflection from the substrate and the successive decrease in the peak intensities of the diffracted beams with an almost constant width of Bragg reflections. The number of the recorded peaks is fully determined by the intensity of the primary X-ray beam.

The intensities (I) and (I_i), the halfwidths (W_R), and the layer periods (d) calculated from the Bragg angles (2θ) are indicated in Table 2 (series 2). The average value of the period of multilayer films determined from different values of the Bragg angles equals $d = (51.30 \pm 0.5)$ Å.

It should be indicated that the X-ray diffraction patterns were measured at a high source power (6–8 kW) at an angular resolution of $\cong 0.1°$ insufficient for studying gadolinium stearate LB films. The halfwidths and the maximum reflection intensities are also considerably affected by the apparatus function.

However, the incorporation of heavy gadolinium ions with a radius of 1.78 Å into the layered stearic acid matrix consisting of light H, C, and O atoms with the covalent radii $R_H = 0.30$, $R_C = 0.77$, and $R_O = 0.74$ Å, respectively [21], can give rise to pronounced deformations and distortions of the matrix structure and its fragmentation, i.e., formation of regions similar to domains in the bulk ferromagnetics. Therefore, the Bragg diffraction in LB films can be accompanied by diffuse scattering from these individual structural inhomogeneities. The study of such fine structural problems requires qualitatively new X-ray experiments at a higher angular resolution ($\leq 0.01°$).

The structural perfection of LB films considerably depends on the state of the substrate surface (its purity, relief, etc.). To avoid these effects, we used the molecular layers of the pure stearic acid as buffer layers. Figure 3 shows the diffraction patterns of gadolinium lead stearate LB film deposited directly onto a clean substrate (Fig. 3a) and onto a substrate coated with a buffer layer (Fig. 3b). The X-ray diffraction data obtained from these specimens are listed in Table 2 (series 3 and 4).

Comparing the diffraction patterns, we see that the relief of the substrate with the applied LB film considerably influences the film structure. The diffraction pattern in Fig. 3a shows not only a newly appeared broadened (001) reflection, but also shows that the dependence of the peak intensities on the reflection order is also changed. Unlike the diffraction pattern in Fig. 2a, we see that the first and not the third reflection that is broadened. The characteristic dimension of the coherent-scattering region determined from the peak halfwidth ($W = 0.55°$) corresponds to the length of the molecular chain of gadolinium stearate, 160 Å, which corresponds to the triple period $3d_{001} = 153$ Å. Therefore, the fragmentation of the LB film structure is accompanied by the formation of complexes in the form of molecular chains of the SA–SA–Gd–SA–SA–Gd–SA–SA-type. This is the shortest possible molecular chain. If there are ten layers, the chain length ranges from 3d to 10d.

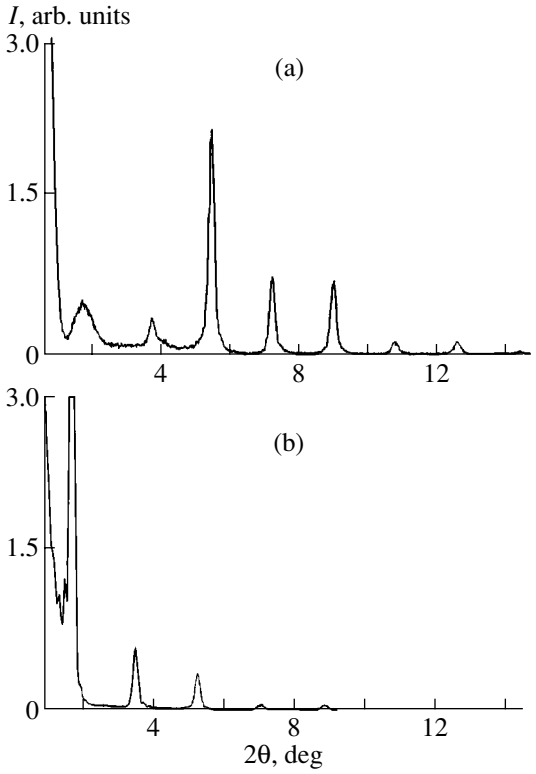

Fig. 3. Diffraction pattern ($\theta/2\theta$ scan) of a gadolinium stearate LB film (10 bilayers) on polished silicon substrates coated with layer of native oxide (a) without a buffer molecular layer of stearic acid and (b) with such a buffer layer. The thickness of the buffer layer equals three bilayers.

The molecular 3d-chains can form clusters possessing a certain short-range order, which can result in a considerable decrease in the peak intensity of the (001) reflection. These clusters may comprise up to 18% of the total volume. In a similar way, it is also possible to explain the anomalous changes in the intensities of other reflections on the diffraction pattern.

The stearic acid molecules located on the substrate surface of the buffer layer smoothen this surface and thus facilitate the formation of the regions with extended ordered chain structures built from gadolinium-stearate molecules during the film application. The halfwidths of all the reflections on the diffraction pattern (Fig. 3b) are almost equal, $W = 0.18°$. This value corresponds to the dimension of the coherent-scattering region equal to 512 Å or $l = 10d$. It follows from the diffraction data that in the LB films studied there are no molecular chains shorter than $l = 10d$. Therefore, the studies performed allow us to state that the gadolinium stearate LB films obtained from the subphase of the aqueous gadolinium-acetate solution onto the single-crystal silicon substrates consist of only one phase and have homogeneous composition and perfect structure. The average period of the layers determined from the differences of the Bragg angles is $d = (50.1 \pm 0.5)$ Å.

Figure 4 shows X-ray specular reflection curves in the vicinity of the critical angles for a silicon substrate (curve *1*) and gadolinium stearate LB films [series 3

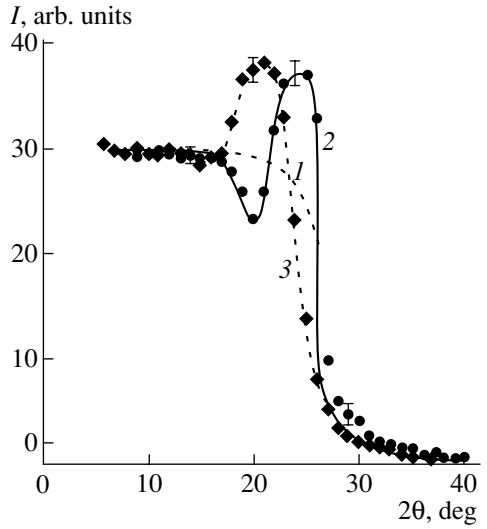

Fig. 4. X-ray specular reflection curves for (*1*) single-crystal silicon substrate and (*2*, *3*) gadolinium stearate films (ten bilayers) (*2*) with a stearic acid buffer layer and (*3*) without a buffer layer.

and 4 (curves *2* and *3*)]. For the single-crystal silicon substrate (curve *1*), no specific features in X-ray specular reflection were revealed, and the angular dependences are described by the well-known Fresnel expressions [22] with the critical reflection angle $\theta_{cr} \sim 13'$–$14'$. The application of an LB film onto the substrate results, on the one hand, in a slight decrease in the critical angle, and, on the other hand, in the dispersion form of the angular dependence of the reflection intensity, i.e., in the appearance of the corresponding minimum and maximum.

This X-ray scattering pattern can be explained on the basis of the following simple model [22]. Assuming that in the gadolinium stearate–silicon substrate system the refractive index of the film is less than that of the substrate, we can state that the incident X-ray beam (at the incidence angles exceeding the critical angle for the film) propagates in the film bulk, and, if the film is inhomogeneous, is scattered by various structural defects or electron-density inhomogeneities. The refracted waves are reflected by the substrate and emerge to the surface, where they interfere with the waves reflected from the film. In the vicinity of the critical angle, the phase of the reflected waves is changed by π [22, 23], and, therefore, the angular dependence of the X-ray specular reflection at the angles $\theta \sim \theta_{cr}$ acquires the dispersion form (curves *2* and *3*).

One can evaluate the angle θ_{cr} for gadolinium stearate Langmuir–Blodgett films. The critical angle of the total external reflection of the X-ray radiation and the refractive index are determined by the material polarizability χ as follows: $\theta_{cr} = (|\chi_{r0}|)^{1/2}$, $n^2 = 1 - |\chi_{r0}|$, $\chi_0 = r^e(\lambda^2/\pi\Omega)\sum_j f_0^j$, where $|\chi_0|$ is the modulus of the real part of the Fourier coefficient of the crystal polarizability, f_0 is the atomic scattering factor, $r^e = e^2/mc^2 = 2.8 \times 10^{-13}$ cm is the classical radius of an electron, Ω is the unit cell volume, and λ is the radiation wavelength.

For silicon crystals whose unit-cell volume $\Omega = 161$ Å^3 contains eight atoms, the critical angle at the wavelength $\lambda = 1.5405$ Å equals $13.37'$ at $|\chi_{r0}| = 15.127 \times 10^{-6}$. The calculation of the Fourier coefficients of molecular-crystal polarizability involves certain difficulties. Their rigorous calculation should be made by the formula of the structure factor including the atomic coordinates in the molecule. However, this requires knowing the model of the packing of the atoms in the molecule, whose determination itself is a complicated problem of the X-ray diffraction analysis of organic materials. Therefore, we assume that the $|\chi_0|$ values for gadolinium stearate and the stearic-acid crystals differ only insignificantly. Then, one molecule of the *A*-phase occupies the volume with a base of $5.0 \times 7.5 = 37.5$ Å^2 and a height equal to a half-thickness of the bimolecular layer ($d/2$) of the film. In this case, the critical angle equals $\theta_{cr} = 6.84'$, i.e., has a value lower than the critical angle for silicon $\theta_{cr} = 13.37'$.

It should be indicated that interference can occur only in single-phase homogeneous LB films. Therefore, the films of series 4 prepared with the use of an aqueous gadolinium acetate solution as a subphase on a single-crystal silicon substrate coated with a buffer molecular layer satisfy this condition (curve *2* in Fig. 4). If LB films are inhomogeneous and have some "defect regions," diffuse (small-angle) scattering takes place and suppresses the X-ray specular reflection (curve *3*). In this case, interference is weakened and a peak with an anomalous intensity is formed in the vicinity of the critical angle of the film due to the "condensation" of diffuse scattering [24]. Measuring the angular range of nonspecular reflection, one can determine the linear dimensions of these inhomogeneities, $D \le \lambda/2\Delta\theta_{cr} = 400$ Å. The defect structure is characteristic of LB films of series 3 obtained with the use of gadolinium acetate solution and single-crystal silicon substrate without a buffer molecular layer. The study of the nature of these defects is a separate problem. However, we assume that these defects can be certain complexes of gadolinium atoms formed at the interface between the bimolecular layers.

CONCLUSION

Our studies showed that gadolinium stearate LB films obtained with the use of aqueous solutions of gadolinium chloride and gadolinium acetate as subphases are characterized by different degrees of structural perfection. The films obtained with the use of the $GdCl_3$ solution consist of two phases, whose layers are disordered and bimolecular layers are considerably distorted. The films obtained with the use of gadolinium acetate and single crystal silicon substrates with buffer molecular layers are practically of single phase, are characterized by a high degree of perfection of molec-

ular structure, and can be used for creating two-dimensional magnets.

ACKNOWLEDGMENTS

This study was supported by the Russian Foundation for Basic Research, project no. 99-03-32218.

REFERENCES

1. G. L. Gaines, *Insoluble Monolayers at Liquid-Gas Interfaces* (Wiley, New York, 1966).
2. G. G. Roberts, *Langmuir-Blodgett Films* (Plenum, New York, 1990).
3. L.M. Blinov, Usp. Khim. **52**, 1263 (1983).
4. V. Klechkovskaya, M. Anderle, R. Antolini, *et al.*, Thin Solid Films **284–285**, 208 (1996).
5. G. B. Khomutov, E. S. Soldatov, S. P. Gubin, *et al.*, Thin Solid Films **327–329**, 550 (1998).
6. M. Pomerantz, A. Segmiller, and F. Dacol, Phys. Rev. Lett. **40**, 246 (1978).
7. M. Pomerantz, Solid State Commun. **27**, 1413 (1978).
8. A. Aviram and M. Pomerantz, Solid State Commun. **41**, 297 (1982).
9. R. M. Nicklow, M. Pomerantz, and A. Segmiller, Phys. Rev. B **23**, 1081 (1981).
10. A. M. Tishin, Yu. A. Koksharov, G. B. Khomutov, *et al.*, Phys. Rev. B **55**, 11064 (1997).
11. O. A. Aktsipetrov, N. V. Didenko, G. B. Khomutov, *et al.*, Mater. Sci. Eng. C **8–9**, 411 (1999).
12. G. B. Khomutov, Yu. A. Koksharov, I. L. Radchenko, *et al.*, Mater. Sci. Eng. C **8–9**, 299 (1999).
13. K. A. MeEwen, in *Handbook on the Physics and Chemistry of Rare Earths*, Ed. by K. A. Gschneidner and L. Eyring (North-Holland, Amsterdam, 1991), Vol. 1.
14. R. J. Weiss, *Solid State Physics for Metallurgists* (Pergamon, New York, 1963).
15. G. B. Khomutov, Macromol. Symp. **136**, 33 (1998).
16. G. B. Khomutov, S. A. Yakovenko, E. S. Soldatov, *et al.*, Biol. Membr. **13**, 612 (1996).
17. E. Von Sydov, Appl. Crystallogr. **8**, 557 (1955).
18. A. Relini, R. Rolandi, F. Ciuchi, *et al.*, Thin Solid Films **284–285**, 216 (1996).
19. J. P. Stefens and C. Tuck-Lee, J. Appl. Crystallogr. **2**, 1 (1969).
20. I. R. Peterson, Appl. Phys. **23**, 379 (1990).
21. C. A. Coulson, *Valence* (Clarendon, Oxford, 1961; Mir, Moscow, 1965).
22. M. Born and E. Wolf, *Principles of Optics* (Pergamon, Oxford, 1969; Nauka, Moscow, 1973).
23. M. A. Krivoglaz, *Theory of X-Ray and Thermal Neutron Scattering by Real Crystals* (Nauka, Moscow, 1967; Plenum, New York, 1969).
24. Y. Yoneda, Phys. Rev. B **113**, 2010 (1963).

Translated by L. Man

Crystallography Reports, Vol. 47, No. 3, 2002, pp. 514–518. Translated from Kristallografiya, Vol. 47, No. 3, 2002, pp. 562–566.

SURFACE

General Orientational Characteristics of Heteroepitaxial Layers of $A^{II}B^{VI}$ Semiconductors on Sapphire and Semiconductor Substrates with Diamond and Sphalerite Structures ($A^{III}B^{V}$)

G. F. Kuznetsov and S. A. Aĭtkhozhin

Institute of Radio Engineering and Electronics, Russian Academy of Sciences (Fryazino Branch), pl. Vvedenskogo 1, Fryazino, Moscow oblast, 141120 Russia

e-mail: gfk217@ire216.msk.ru

Received October 31, 2000; in final form, August 2, 2001

Abstract—X-ray reflection and transmission diffractometric studies of nonisostructural heteroepitaxy showed that the spatial rotation of the crystal lattice of the grown heteroepitaxial layer with respect to the substrate lattice about the crystallographic direction common for both lattices is the most general characteristic feature of their mutual crystallographic orientation. This feature leads to the coincidence of the ⟨0001⟩ polar axis of the heteroepitaxial layer of the $A^{II}B^{VI}$ compounds with one of the ⟨111⟩ polar axes of the cubic substrate. The 30° and 90° rotations in the plane of heteroepitaxy and the vernier-type conjugating of the planar nets of the heteroepitaxial layer and the substrate are the particular cases of their mutual crystallographic orientations. © *2002 MAIK "Nauka/Interperiodica".*

INTRODUCTION

The discovery of acousto-electric phenomena and effects in piezoelectric–insulator [1, 2] and piezoelectric–semiconductor [3–5] systems required the preparation of heterostructures with definite mutual crystallographic orientations of the epitaxial layers of $A^{II}B^{VI}$ piezoelectrics on sapphire substrates or semiconductor substrates with diamond (Ge, Si) and sphalerite ($A^{III}B^{V}$) structures. The mutual crystallographic orientations determine the type and number of exited bulk and, especially, the surface acoustic waves in piezoelectric–insulator and piezoelectric–semiconductor systems. It also affects the accuracy and reliability of the measurements of the acousto-electric effects [1, 2] that allow these effects to be used in various devices. All these facts were an incentive to study the general features of the mutual crystallographic orientations of conjugating crystal lattices.

As a rule, mutual crystallographic orientations were studied by transmission electron diffraction [4], Laue X-ray diffraction in the transmission geometry in the case of low X-ray absorption in the substrates, and the method of back Laue scattering in the case of highly absorbing substrates [5]. The data in Manasevit's famous review article [6] demonstrate that, in many instances, the mutual crystallographic orientation could not be completely determined, because only one system of parallel crystallographic planes was determined for conjugating crystal lattices of the heteroepitaxial layer and the substrate.

The substrates with surface orientation along the {111}, {110}, {001}, and {112} planes and wedge-shaped model substrates were prepared by the method reported in [7, 8], which involved the X-ray orientation of bulk single crystals and the preparation of oriented cuts in a unified orientation–cutting cycle.

EXPERIMENTAL TECHNIQUES FOR MEASURING THE MUTUAL CRYSTALLOGRAPHIC ORIENTATIONS IN THE CASE OF NONISOSTRUCTURAL HETEROEPITAXY

The orientation of the CdS epitaxial layer on the Ge substrate in the heteroepitaxial CdS/(111)Ge system was determined by X-ray topography using a divergent beam from a quasipoint source [4, 9–11] as $(0001)[11\bar{2}0]\mathrm{CdS} \parallel (111)[1\bar{1}0]\mathrm{Ge}$. However, since the operating speed of the X-ray topography was insufficient for the analysis of the mutual crystallographic orientation, we suggested [3, 12] using faster X-ray diffractometric methods such as Bragg diffraction in the reflection geometry in combination with Laue diffraction in the transmission geometry. These methods provide a record of reflections from crystal planes both parallel and perpendicular to the heteroepitaxial layer–substrate interface. We used DRON-1,2,3,4 or DRON-

1063-7745/02/4703-0514$22.00 © 2002 MAIK "Nauka/Interperiodica"

4M diffractometers (CuK_{α_1} radiation) and recorded the intensities in the angular ranges $0° \le 2\theta \le 164°$ and $0° \le 2\theta \le 70°$ in the reflection and transmission geometries, respectively. The monochromatic radiation was obtained using the 004 Bragg reflection from the plane-parallel plate (cut out of a (001)Ge single crystal) on a standard crystal holder of the goniometer.

In the case of heteroepitaxial layers on highly absorbing substrates, the mutual crystallographic orientations were determined from the difference in the angular positions of the sample while recording the reflections from the selected crystal planes. In these cases, the counter was rigidly fixed at the corresponding Bragg angles 2θ. If necessary, the X-ray diffraction methods were supplemented by recording back Laue scattering [5] and the analysis of growth-pyramid orientations [3, 9] often observed on the surfaces of heteroepitaxial layers.

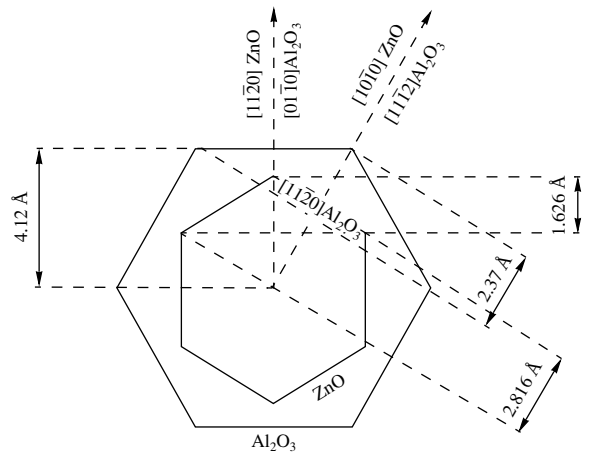

Fig. 1. Scheme illustrating the 30° rotation of the lattice of the (0001)ZnO crystal layer relative to the lattice of the (0001)Al_2O_3 substrate in the plane of heteroepitaxy.

MUTUAL CRYSTALLOGRAPHIC ORIENTATIONS OF HETEROEPITAXIAL ZnO LAYERS AND DIFFERENTLY ORIENTED SAPPHIRE (Al_2O_3) SUBSTRATES

Sapphire (Al_2O_3) belongs to the trigonal system, sp. gr. $R3c$, and has the lattice constants $a_1 = 0.476$ nm and $c_1 = 1.297$ nm. Zinc oxide (ZnO) crystals belong to the hexagonal system, sp. gr. $P6mc$, and has the lattice constants $a_2 = 0.32492$ nm and $c_2 = 0.52053$ nm. An analysis of the ZnO heteroepitaxial layers grown on differently oriented sapphire substrates [12] gave the following results.

As a rule, an epitaxial ZnO layer is oriented on the (0001)Al_2O_3 substrates in such a way that its basal plane (0001)ZnO is parallel to the substrate surface [3, 12] so that, in the plane of heteroepitaxy, the ZnO lattice is rotated by an angle of 30° with respect to the Al_2O_3 lattice. The schematic in Fig. 1 clearly demonstrates that in both hexagonal lattices the following directions coincide: $[11\bar{2}0]$ZnO $\parallel$ $[01\bar{1}0]Al_2O_3$ and $[10\bar{1}0]$ZnO $\parallel$ $[11\bar{2}0]Al_2O_3$. Because of the 30° rotation, the lattice mismatch decreased from 37.8% at the parallel arrangement of directions with the same indices to 17%. Such a lattice rotation in the plane of heteroepitaxy was first observed in the experimental growth of ZnO layers on a mica substrate [13].

At $(11\bar{2}0)Al_2O_3$-oriented substrates, the vernier-type conjugating of the net of zinc atoms of the heteroepitaxial ZnO layer with the net of oxygen atoms on surface of the sapphire substrate (Fig. 2) was found. In this case, the sum of four interatomic distances along the $[1\bar{2}10]$ZnO direction (12.96 Å) is almost equal to the sum of three interatomic distances along the $[0001]Al_2O_3$ direction (12.95 Å). This leads to a substantial reduction in the mismatch in lattice periods (down to about 7%) also in the perpendicular direction.

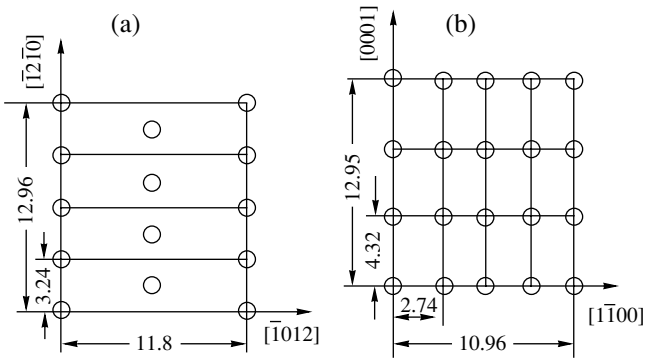

Fig. 2. Scheme illustrating the vernier-type conjugating of (a) the planar net of Zn atoms in the heteroepitaxial $(10\bar{1}1)$ZnO layer with (b) the atomic net of oxygen atoms on the sapphire substrate in the $(11\bar{2}0)Al_2O_3$ plane.

In ZnO layers on $(\bar{1}012)Al_2O_3$ substrates, the ZnO lattice is rotated about the coinciding $[1\bar{1}00]$ZnO and $[\bar{1}2\bar{1}0]Al_2O_3$ directions. As a result, the lattice mismatch in this direction decreases from 38 to 16%, whereas in another pair of coinciding directions, [0001]ZnO and $[10\bar{1}1]Al_2O_3$, it decreases as low as 1.6%.

The growth of a thin (1 μm) intermediate ZnS layer at the sapphire (0001)Al_2O_3 substrate leads to the formation of a ZnO layer oriented with its (0001) plane along the substrate. In this case, the mutual orientation was $(0001)[11\bar{2}0]$ZnO $\parallel$ $(111)[0\bar{1}1]$ZnS $\parallel$ $(0001)[11\bar{2}0]Al_2O_3$. Here, the total mismatch equals 38% and is the sum of the 22% mismatch at the (0001)Al_2O_3/(111)ZnS interface and the 16% mismatch at the (111)ZnS/(0001)ZnO interface.

Mutual crystallographic orientation of $A^{II}B^{VI}$ (CdS, CdSe, and ZnO) heteroepitaxial layers on the substrates with diamond- and sphalerite-type hcp crystal structure

Substrate orientation	(111)	(001)	(110)	(112)	$(\bar{1}\bar{1}\bar{2})$
Substrate material	Orientation of $A^{II}B^{VI}$ heteroepitaxial layers				
Ge	(0001)	$(30\bar{3}4)$	$(10\bar{1}3)$	$(10\bar{1}5)$	$(10\bar{1}5)$
GaAs	(0001)	$(30\bar{3}4)$	$(10\bar{1}3)$	$(10\bar{1}5)$	$(20\bar{2}5)$
InSb	(0001)	$(30\bar{3}4)$	$(10\bar{1}3)$	$(10\bar{1}5)$	$(20\bar{2}5)$

ORIENTATIONS OF HETEROEPITAXIAL $A^{II}B^{VI}$ LAYERS ON SEMICONDUCTOR SUBSTRATES WITH DIAMOND AND SPHALERITE ($A^{III}B^{V}$) CUBIC LATTICES

The $A^{III}B^{V}$ materials with face-centered cubic (fcc) lattices of sphalerite type have no center of symmetry and, therefore, are polar crystals, whereas silicon and germanium with centrosymmetric fcc lattices of diamond type are not polar crystals. The $A^{II}B^{VI}$ materials with hexagonal close-packed (hcp) lattices of wurtzite type have no center of symmetry and are polar. The anisotropy of physical characteristics in these crystals is even more pronounced than in the sphalerite-type materials.

The $A^{II}B^{VI}$ semiconductor compounds (CdS, CdSe, and ZnO) are piezoelectrics. In our experiments, these materials were obtained on Ge, GaAs, and InSb substrates by chemical vapor deposition.

The indices of the crystal planes in single-crystal CdS, CdSe, and ZnO layers coinciding within an angular minute with the crystallographic planes closest to the substrate surface are indicated in the table. The analysis of the tabulated data with due regard for the results obtained from back Laue patterns shows that one of the $\langle 111\rangle$ directions of the substrates coincides with the [0001] polar axis of the wurtzite-type structure of the heteroepitaxial layers.

Below, we formulate the most general features of the mutual crystallographic orientation in nonisostructural heteroepitaxy of $A^{II}B^{VI}$ compounds with hcp lattices on substrates with diamond-(Ge) or sphalerite-type ($A^{III}B^{V}$) fcc lattices.

The polar [0001]A axis coincides with the $\langle 111\rangle$A direction in sphalerite or the $\langle 111\rangle$Ge direction.

The polar [0001]A axis coincides with that of the $\langle 111\rangle$A direction that forms the maximum angle of deviation from the substrate surface and the boundary of the heteroepitaxial layer.

The crystallographic directions $\langle 11\bar{2}0\rangle$ (at least one of these directions) in heteroepitaxial layers are strictly parallel to the $\langle 110\rangle$ directions of the substrates.

The most severe constraint is the first one. If this condition is met in the heteroepitaxial growth of $A^{II}B^{VI}$ compounds on $A^{III}B^{V}$ substrates, condition two can be violated. The fulfillment of condition one causes the mutual 90° rotation of the crystal lattices of the layers on the opposite sides of the plane-parallel (001)GaSb and (001)InSb substrates. This result is supported by the different orientations of the growth pyramids in the heteroepitaxial layers grown on the opposite surfaces of one substrate [3, 14]. Here, the $(30\bar{3}4)$ plane of the $A^{II}B^{VI}$ layer coincides with the plane of the (001) cut of $A^{III}B^{V}$ substrates.

Two directions of the same polarity ($[1\bar{1}1]$B and $[\bar{1}11]$B) emerge at the $\{112\}A^{III}B^{V}$ substrate surface at an angle of 71°32′, whereas the direction of the opposite polarity, [111]A, emerges at an angle of 28°28′. In diamond-type structures, these directions differ only in inclination angle. In the heteroepitaxially grown layers on the opposite (112)Ge and $(\bar{1}\bar{1}\bar{2})$Ge planes, the crystal lattices of the heterolayers have a common [0001] axis parallel to the [111]Ge direction forming an angle of about 71° to the surface of the boundary of the heteroepitaxial layer. This is also confirmed by the same indices of strictly coinciding crystallographic planes (columns 5 and 6 in the table).

In CdS, CdSe, and ZnO heteroepitaxial layers grown on the opposite surfaces of the {112}GaAs and {112}InSb substrates (three-layer "sandwiches"), conditions one and two are met only for the heteroepitaxial layers grown on one surface of the substrate, whereas in the heteroepitaxial layers grown on the opposite surface ($\{\bar{1}\bar{1}\bar{2}\}$) of the plane-parallel substrates, the coincidence of the directions of polar axes, [0001]A ∥ [111]A, resulted in the spatial rotation of the crystal lattice of the heteroepitaxial layer and the violation of the second condition. In this case, the polar [0001] axis of the heteroepitaxial layer with the wurtzite structure coincides with the [111]A axis of the opposite polarity emerging at the surface at an angle of 28°28′ and not with the directions $[1\bar{1}1]$B or $[\bar{1}11]$B characterized by the maximum inclination (71°) from the substrate surface. This fact is also confirmed by the different indices of strictly coinciding planes: instead of a $(10\bar{1}5)$ layer orientation on the (112) surface of the substrate, the layer

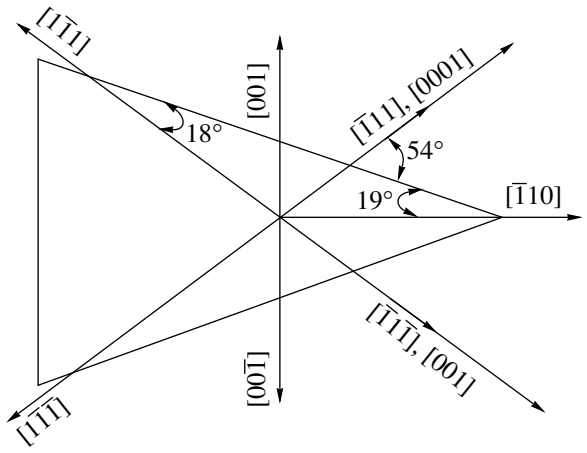

Fig. 3. Orientation of crystallographic directions in the wedge-shaped Ge substrate and the orientation of the crystal lattices with respect to these directions of the heteroepitaxial CdS layers grown on the (221) and ($22\bar{1}$) surfaces of the wedge-like Ge substrate.

has a ($20\bar{2}5$) orientation on the opposite ($\bar{1}\bar{1}\bar{2}$) surface parallel to the heteroboundary (see table).

The second condition is confirmed in the model experiment of the growth of CdS heteroepitaxial layers on a wedge-shaped Ge substrate with (221) and ($22\bar{1}$) wedge surfaces.

The crystallographic orientation determined is illustrated by Fig. 3. It is clear that the polar [0001] axes in the CdS layers on both surfaces of the wedgelike substrate coincide with the [$\bar{1}$11] and [$\bar{1}1\bar{1}$] directions in the Ge substrate, which deviate by ~54° and not 18°, as is characteristic of their extensions on the opposite surfaces of the wedge-like substrate.

The above general characteristics of the mutual crystallographic orientations were partly confirmed in experiments [14, 15] and [16, 17]. The experimentally observed 30° rotation of the heteroepitaxial layer in the plane of heteroepitaxy [16] was earlier predicted by the authors on the basis of the two-dimensional point symmetry of the bicrystal. It seems that this result was first obtained experimentally in [13]. The method for avoiding this 30° rotation of a heteroepitaxial layer with an hcp lattice on a sapphire substrate with the basis orientation and the reduction of the mismatch by introducing a thin intermediate cubic layer was suggested in [12]. This method is successfully used to grow gallium and aluminum nitrides on sapphire substrates [17]. The same authors used the advantages of vernier conjugating arising from the lattices described in [12] in nonisostructural heteroepitaxy in order to reduce the lattice mismatch and to attain a higher crystallinity of the active layer of the device-oriented structures.

CONCLUSIONS

The spatial rotation of the crystal lattice in heteroepitaxial ZnO layers and, probably, in the layers of other $A^{II}B^{VI}$ compounds with respect to the lattice of the sapphire substrate is the most general characteristic of the mutual lattice orientations of these materials. This rotation occurs around the directions common to the layer and the substrate. As a result, the elastic-strain energy in the heteroepitaxial system is decreased. The 30° rotation of the layer lattice in the plane of heteroepitaxy in the case of coinciding basis planes of the layer and the substrate and vernier-type conjugating of their planar atomic nets also reduces the elastic-strain energy and is a particular case of the mutual crystallographic orientation. The growth of a thin (1 μm) intermediate, e.g., ZnS, layer on a sapphire (0001)Al_2O_3 substrate prevents the 30° rotation of the ZnO layer in the plane of heteroepitaxy and ensures the (0001)ZnO orientation over the whole substrate area.

In the nonisostructural heteroepitaxy of $A^{II}B^{VI}$ compounds on substrates with diamond-(Ge) or sphalerite-type ($A^{III}B^{V}$) structure, the most general characteristic of the mutual crystallographic orientations is the coincidence of the [0001]A polar axis either with the [111]A direction of $A^{III}B^{V}$ substrates or with [111]Ge.

If several axes of the same polarity emerge at the substrate surface of sphalerite structure, the polar [0001]A axis of the wurtzite structure coincides with the ⟨111⟩A axis with the maximum deviation angle from the substrate surface.

The 30° rotation of the lattice of the heteroepitaxial layer on sapphire and the 90° rotation on $A^{III}B^{V}$ substrates, as well as the vernier-type conjugating of the planar atomic nets of $A^{II}B^{VI}$ materials on substrates with diamond- and sphalerite-type structures, are particular cases of the mutual crystallographic orientation.

REFERENCES

1. Yu. V. Gulyaev, A. M. Kmita, I. M. Kotelyanskiĭ, and A. V. Medved', Fiz. Tekh. Poluprovodn. (Leningrad) **5**, 80 (1971) [Sov. Phys. Semicond. **5**, 66 (1971)].
2. Yu. V. Gulyaev and A. V. Medved', Élektron. Prom-st', No. 6 (60), 83 (1977).
3. G. F. Kuznetsov, Doctoral Dissertation in Physics and Mathematics (Moscow, 1989).
4. G. F. Kuznetsov and S. A. Semiletov, in *Reviews on Electronics. Series Microelectronics* (TsNII "Élektronika," Moscow, 1975), Vol. 1 (280).
5. A. Guinier, *Théorie et Technique de la Radiocristallographie* (Dunod, Paris, 1956; Fizmatgiz, Moscow, 1961).
6. H. M. Manasevit, J. Cryst. Growth **22** (2), 125 (1974).
7. B. V. Ganichev, V. P. Moiseev, and G. F. Kuznetsov, Appar. Metody Rentgenovskogo Anal., No. 11, 28 (1972).
8. B. V. Ganichev and G. F. Kuznetsov, Élektron. Tekh., Ser. 7: Tekhnol. Org. Proizv., No. 2 (54), 73 (1973).

9. G. F. Kuznetsov, *Structural Defects in Semiconductors* (Inst. Fiz. Problem Sib. Otd. Akad. Nauk SSSR, Novosibirsk, 1973), p. 24.
10. G. F. Kuznetsov, in *Proceedings of the All-Union Conference on Structural Defects in Semiconductors (*Novosibirsk, 1970), Part 2, p. 24.
11. G. F. Kuznetsov, Appar. Metody Rentgenovskogo Anal., No. 12, 162 (1973).
12. S. A. Semiletov, G. F. Kuznetsov, A. M. Bagamadova, *et al.*, Kristallografiya **23**, 357 (1978) [Sov. Phys. Crystallogr. **23**, 197 (1978)].
13. S. A. Semiletov and R. A. Rabadanov, Kristallografiya **16**, 1012 (1971) [Sov. Phys. Crystallogr. **16**, 878 (1971)].
14. I. M. Kotelyanskiĭ, V. D. Strygin, and G. F. Kuznetsov, *Growth and Synthesis of Semiconductor Crystals and Films* (Nauka, Novosibirsk, 1975), Part 2, p. 337.
15. O. Igarashi, J. Appl. Phys. **42**, 4035 (1971).
16. A. N. Efimov, A. O. Lebedev, V. V. Lundin, and A. S. Usikov, Kristallografiya **45**, 345 (2000) [Crystallogr. Rep. **45**, 312 (2000)].
17. M. I. Kotelyanskiĭ, I. M. Kotelyanskiĭ, and V. B. Kravchenko, Pis'ma Zh. Tekh. Fiz. **26**, 62 (2000) [Tech. Phys. Lett. **26**, 163 (2000)].

Translated by K. Kugel

Crystallography Reports, Vol. 47, No. 3, 2002, pp. 519–523. Translated from Kristallografiya, Vol. 47, No. 3, 2002, pp. 567–571.

CRYSTAL GROWTH

Effect of Low-Frequency Vibration on Nucleation of Crystals in Supercooled Melts

O. P. Fedorov and E. L. Zhivolub

Institute of Metal Physics, National Academy of Sciences of Ukraine, pr. Vernadskogo 36, Kiev, 252680 Ukraine

e-mail: fedorov@imp.kiev.ua

Received June 18, 1999; in final form, September 6, 2001

Abstract—Nucleation of transparent organic substances in supercooled melts under vibration (50 Hz, 1–5 mm) has been studied experimentally. In the absence of a seeding crystal, vibration did not affect nucleation within the whole range of melt supercoolings studied, $\Delta T = 0.1$–10 K. The introduction of a seeding crystal provides a threshold supercooling ΔT^* below which no nucleation occurs at all, whereas above it, an explosion-like nucleation is observed. It is shown that mass growth of small crystals at $\Delta T > \Delta T^*$ is not associated with the detachment of growing-crystal fragments and seems to be explained by three-dimensional nucleation on the surface of a seeding crystal. © *2002 MAIK "Nauka/Interperiodica".*

INTRODUCTION

Crystallization of melts under vibration is one of the traditional methods of controlling the solidification structure under the action of various external factors. In particular, the methods of fragmentation of a cast structure under ultrasonic or low-frequency vibration are widely used in metallurgy [1]. However, the technological use of these methods is limited to a relatively small number of alloys, whereas the mechanisms suggested for the interpretation of the effects observed are developed insufficiently. This is true, in particular, for interpretation of the role of vibration in nucleation and growth of crystals. The present study is dedicated to the direct observation of the processes of nucleation and mass growth of crystals under vibration.

EXPERIMENTAL

The schematic of a setup used in our experiments is shown in Fig. 1. A working chamber with an object is placed onto a vibration-testing machine providing a constant vibration frequency of 50 Hz and an amplitude ranging within 0.1–5.0 mm. A distributing valve provides the supply of water from thermostats to the working chamber. One of these thermostats (a hot one) is used for remelting crystals in the sample in order to attain the size necessary for the experiment, whereas the cold one maintains the necessary temperature in the sample, $T < T_L$ (where T_L is its liquidus temperature).

We studied one-component compounds and binary alloys of transparent low-melting compounds (see table) whose growth was studied in detail elsewhere [2–4].

The alloys were sealed in hermetic glass vessels in the shape of flattened cylinders. The experimental procedure reduced to the following. A vessel with a compound was fixed in the working chamber placed on the vibration-testing machine. The temperature T_L and the solidus temperature T_S of the alloy were measured prior to and upon vibration. The alternative connection of the chamber to the hot and the cold thermostats resulted in the formation of an initial crystal of a desirable size (the optimum size was dictated by the convenience of obser-

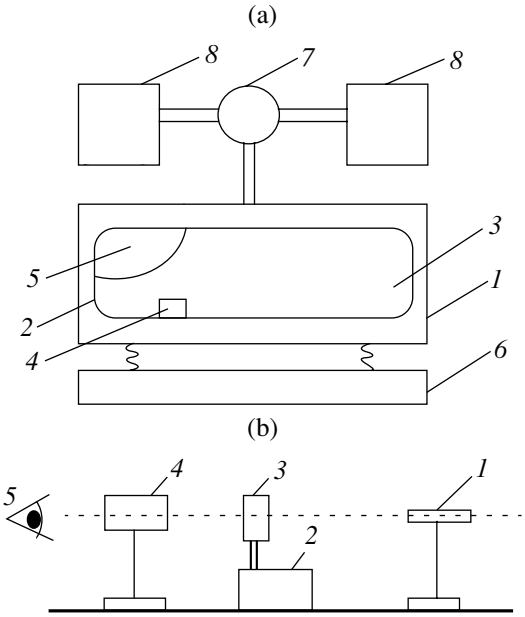

Fig. 1. (a) Schematic of the experimental setup: *1* working chamber, *2* glass vessel, *3* supercooled melt, *4* crystals, *5* air bubble, *6* vibration-testing machine, *7* distributing valve, *8* thermostat U-10; (b) schematic of observation: *1* source of light, *2* vibration-testing machine, *3* working chamber with glass vessel, *4* MBS-2 microscope, *5* camera.

Substances studied

Substance	Growth mechanism	Liquidus temperature T_L, °C
Succinonitrile	Normal	57.6
Salol	Layer	46.0
Benzophenone		48.0
Paradibromobenzene		89.0
Naphthalene		83.0
Thymol		49.9
Thymol + 1 wt % salol		49.2
Thymol + 2 wt % salol		48.8
Thymol + 5 wt % salol		48.5
Thymol + 6.5 wt % salol		47.8

vation and the necessity of providing growth under the same conditions for a sufficiently long time). Special precautions were made to fix seeding crystals at the same place of the vessel. We also studied the effect of the vibration onto the nucleation of crystals in a supercooled melt without the introduction of a seeding crystal.

In all the experiments, the axes of cylindrical vessels coincided with the direction of the application of vibration accelerations that gave rise to the melt flow, which was characteristic of the given geometry and provided the vibration of free surfaces (as was described in [1]). Irrespective of the vibration parameters used, the melt flow had the same closed configuration whereas its intensity depended on the vibration amplitude.

EXPERIMENTAL RESULTS

The experiments were performed in three stages:

—the study of the effect of vibration on supercooling of melts without the introduction of a seeding crystal;

—the observation of the mass growth of crystals in melts with a preliminarily introduced seeding crystal;

—the study of the growth stages for a fixed seeding crystal under vibration.

Supercooled melts of salol, benzophenone, paradibromobenzene, naphthalene, and succinonitrile in the vessels described above were subjected to vibration. Earlier, it was established that the melts of these substances (except for succinonitrile) have a tendency to supercooling and, under certain conditions, can acquire a glassy state. The experiments were made in the supercooling range ΔT = 0.1–10.0 K. In all the cases including keeping the samples at ΔT = 10 K and then subjecting them to at least 3-h-vibration, no nucleation was observed in the salol, benzophenone, and thymol melts. For paradibromobenzene and succinonitrile, the ΔT^* values at which crystals appeared in the melts, coincided with the values recorded in the absence of vibration. Thus, for the substances characterized by different growth mechanisms, vibration did not affect nucleation within the parameters used (a frequency of 50 Hz, an amplitude of 5 mm).

In melts with one seeding crystal obtained upon multiple remelting–growth cycles, an explosion-like mass growth of crystals occurred within several seconds. Switching-off vibration during the experiment, we established that the mass growth of crystals was preceded by a stage of formation of small crystals on the vessel walls as a result of the collisions of the seeding crystal with these walls. The reduction of the vibration amplitude below a certain threshold value (providing the absence of collisions of a crystal with the vessel walls) eliminated this effect. Thus, the presence of a crystal with a diameter less than 100–150 μm in the salol–thymol system under vibration with an amplitude less than 1 mm did not lead to the mass growth of crystals within the observation time of up to 30 min.

The explosion-like formation of a large number of small crystals was observed for all the substances studied (see table) irrespective of their growth mechanisms and nucleation rate. The observation showed that this effect is associated only with collisions between the crystal and vessel walls and, therefore, is not associated with nucleation in the melts and the mechanisms determining this nucleation.

The specific features of nucleation in a vessel with a fixed seeding crystal are essentially determined by the melt motion in the vessel under vibration. Usually two characteristic melt flows arise—the first flow caused by the vibration of a free surface and the second less intense flow in the whole volume, which is induced by the first (surface) flow. The intensities of both flows are determined by the sample geometry, with all the other conditions being the same. Therefore, we prepared a vessel of a standard shape and fixed the seeding crystal there at a certain constant distance from the melt surface in the vessel. Below, we consider the results obtained in the case where a growing crystal interacted with the first-type flow at a constant vibration frequency (50 Hz) and the maximum vibration amplitude (5 mm).

The results obtained can be summarized as follows. For all the substances growing by the layer mechanism (salol, thymol, benzophenone, paradibromobenzene, and naphthalene), the range of supercoolings is revealed within which the introduction of a seeding crystal did not give rise to nucleation of new crystals during its growth under vibration. These substances can be divided into two groups depending on type of the manifestation of this effect:

—paradibromobenzene and haphthalene (Fig. 2) in which no mass crystallization was observed in the whole range ΔT = 0.1–3 K (the upper limit of ΔT is determined by a dramatic increase in growth rate at ΔT = 4.0–4.5 K);

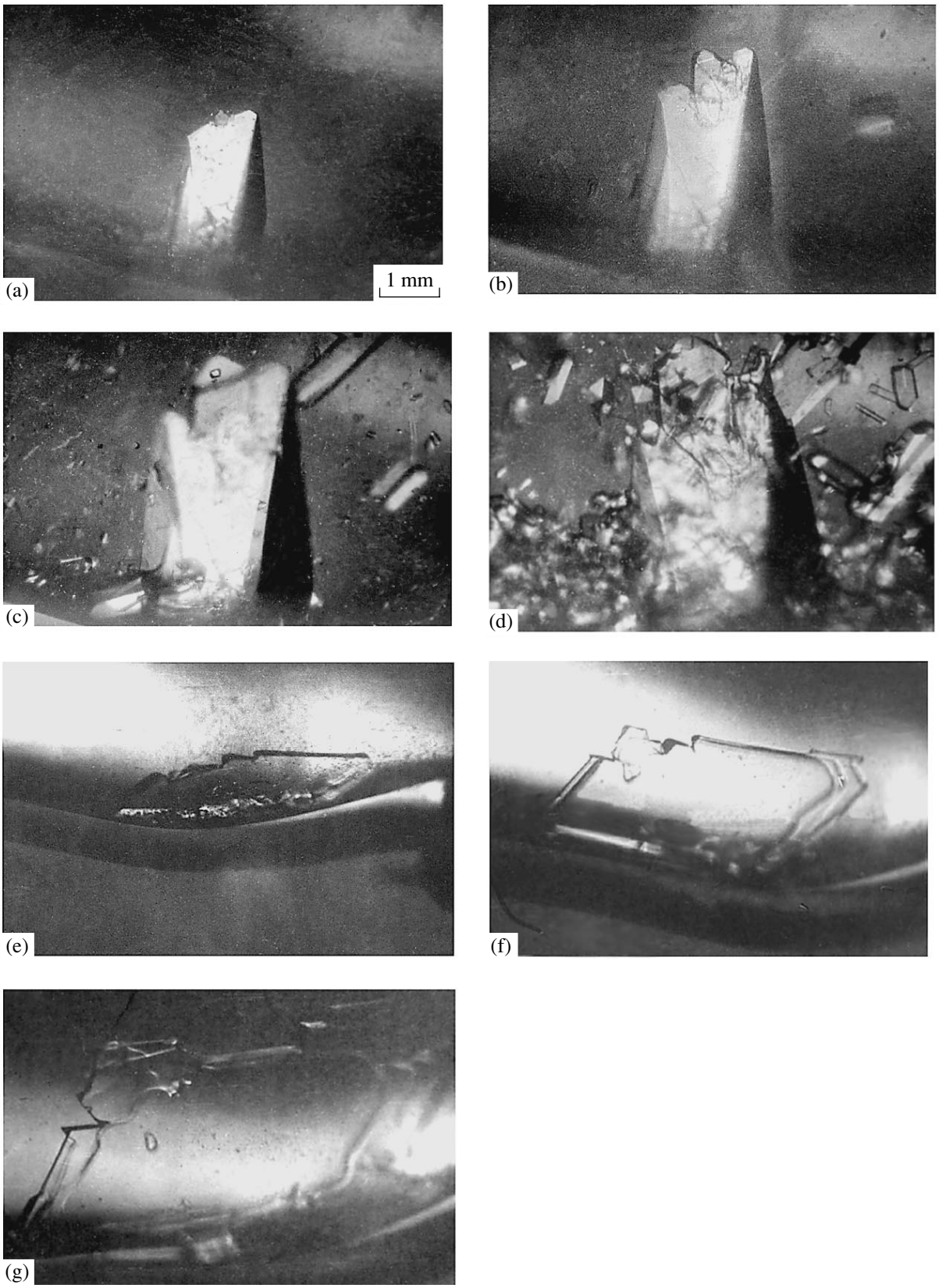

Fig. 2. Grows of (a–d) thymol and (e, g) naphthalene crystals from a one-component melt under vibration; (a–d) $\Delta T = 0.5$ K; the time between frames: (a, b) 5 min, (b, c) and (c, d) 1 min, (e, g) $\Delta T = 0.8$ K with a 30 s interval between the frames.

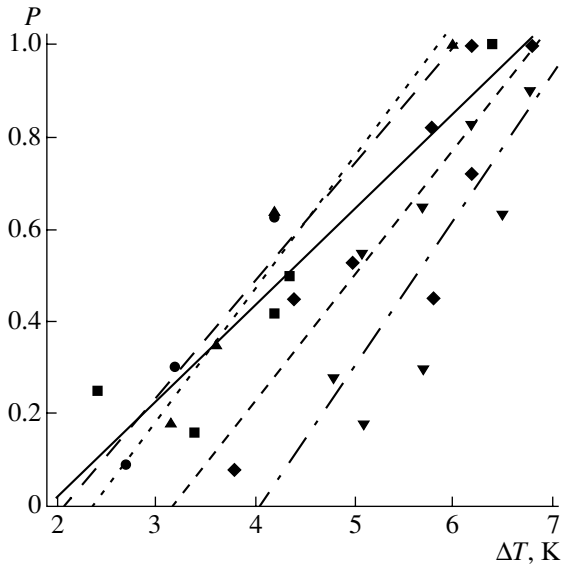

Fig. 3. Dependence of P on ΔT for the thymol–salol alloys. The straight lines were obtained by the least squares method. The salol content in the alloy: ■ 0, ● 1, ▲ 2, ▼ 5, and ◆ 6.5 wt %.

—salol, benzophenone, and thymol (Figs. 2a–2d) characterized by the well-pronounced threshold supercooling ΔT^* upon the attainment of which nucleation of new crystals is observed under vibration.

The existence of ΔT^* was established as a result of multiple experiments on growth of a fixed single crystal under different supercoolings. Thus, the observation of a sample of the alloy thymol + 1 wt % salol under 3-h-vibration at ΔT = 0.2–1.0 K showed no formation of new crystals.

With an increase of ΔT by not more than 0.1 K with respect to ΔT^*, the mass crystallization of new crystals was observed. Such a behavior was characteristic of all the above-mentioned faceted crystals. We performed the most detailed study of thymol and the binary thymol–salol system. The salol concentration in the alloys and their T_L are indicated in the table. It turned out that there exists a supercooling range where, under vibration at a frequency of 50 Hz and an amplitude of 5 mm, growth of a seeding crystal and the appearance of new crystals are of a probabilistic character. The experimental ΔT^* value was obtained by studying the probability P of the appearance of new crystals (the quantity inversely proportional to the expectation time). The corresponding curves are shown in Fig. 3. The extrapolation of these curves to the point $P = 0$ provided the determination of the ΔT^* value under the assumption that the $P(\Delta T)$ function is linear. It is seen that the character of the dependence $P(\Delta T)$ remains unchanged with an increase in the second-component content in the melt.

It should be indicated that similar experiments with substances growing by the normal mechanism (succinonitrile, camphene, and cyclohexasanol) are impossible because of their low adhesion that did not allow one to fix a seeding crystal on a wall of a glass vessel.

DISCUSSION OF RESULTS AND CONCLUSIONS

The fragmentation of casted alloy under vibration is often considered as a result of pronounced nucleation under vibration. The data obtained in the present study lead to the conclusion that the explosion-like fragmentation of the structure occurs under conditions where the formed (introduced into the melt) crystals repeatedly collide either with one another or with the vessel walls. If such crystals are absent, vibration (in the range of the parameters used) produces no effect on the propensity of the melts to supercooling. Moreover, if a seeding crystal is introduced into the melt, the mass crystallization occurs in the range of the parameters exceeding the critical ΔT^* value.

The existence of ΔT^* is also of importance for understanding some characteristics of the growth mechanism of crystals with flat surfaces. In our experisents, the effect of vibration reduces to the formation of a flow around the crystal in the melt. Consider briefly the effect of such a flow on the changes in the temperature, the processes at the interface, and the mechanical action on a crystal.

Melt mixing in the vicinity of a growing crystal caused by vibration results in a higher rate of interface growth. The additional supercooling evaluated from these data does not exceed 0.1 K. Obviously, such a reduction of the melt temperature in the vicinity of the interface cannot give rise to nucleation in the melt that can readily be supercooled by several degrees centigrade.

For paradibromobenzene and haphthalene in the range ΔT = 0.5–1.5 K, where the initial crystal looses stability and is covered with macrosteps, neither macrostep break nor the formation of new crystals were observed. At the same time, for salol and thymol crystals with flat surfaces (without macrosteps), mass nucleation of crystals was observed. Thus, this effect cannot be explained by the loss of the morphological stability of a growing crystal and the mechanical break of macrosteps.

As is well known [2], salol, thymol, naphthalene, and paradibromobenzene under low supercooling of the melt acquire planar growth shapes and grow by the layer mechanism. This mechanism is implemented via the growth of steps formed either by dislocations (the dislocation mechanism) or by two-dimensional nucleation on the faces (the mechanism of two-dimensional nucleation). It was also indicated [2] that the dislocation mechanism prevails in the range of low supercoolings, whereas beginning with ΔT = 1.0–1.5 K, the main contribution to the growth rate comes from the processes of facets nucleation. At ΔT > 6–7 K, the crystals

with flat facets are transformed into spherulites consisting of thin needles of the same orientation continuously reproduced during the process of crystal growth. We believe that the most probable mechanism of spherulite formation is the continuous nucleation of three-dimensional nuclei on the growth surface of crystals. The sequences of shape formation for naphthalene and paradibromobenzene is quite different. In [3], the conclusion is drawn regarding the formation of kinetic roughness and the change of layer growth to normal growth under comparatively low supercoolings. A similar conclusion was also drawn for naphthalene crystals [4]. With an increase in the melt supercooling, the flat facets of naphthalene and paradibromobenzene acquire a pronouncedly anisotropic needlelike shape and not a spherulitic one as in salol. The essential difference in the morphology of the above two groups of crystals reduces to the fact that the change in the growth shapes in salol and thymol is accompanied by the transition from the growth of single crystals to the growth of polycrystals, whereas the change in the growth mechanism for naphthalene and paradibromobenzene occurs within the growth of single crystals.

The above facts allow the following interpretation of the differences observed in mass crystallization in the melt flow for different crystals. Under melt supercooling, where the interface growth is controlled by the formation of three-dimensional nuclei, the melt flow provides the detachment of the nuclei and their further individual growth. In other words, for salol- and thymol-type crystals, the melt flow shifts the transition from growth of single crystals to growth of polycrystals toward lower supercooling values.

REFERENCES

1. O. V. Abramov, *Crystallization of Metals in Ultrasonic Field* (Metallurgiya, Moscow, 1972).
2. D. E. Ovsienko and G. A. Alfintsev, *Crystals. Growth. Properties and Application* (Springer-Verlag, Berlin, 1980), Vol. 2, p. 119.
3. O. P. Fedorov and D. E. Ovsienko, Metallofizika **6** (2), 56 (1984).
4. A. M. Ovrutskiĭ and V. V. Podolinkiĭ, *Crystal Growth* (Erevanskiĭ Gos. Univ., Yerevan, 1975), p. 293.

Translated by L. Man

Crystallography Reports, Vol. 47, No. 3, 2002, pp. 524–525. Translated from Kristallografiya, Vol. 47, No. 3, 2002, pp. 572–573.

JUBILEE

Vadim Robertovich Regel (on the Occasion of His 85th Birthday)

In sympathy with Vadim Robertovich Regel and feeling deep gratitude to him, we cannot resist the temptation to begin this article with a quite unusual fact—Regel's grandfather, the well-known botanist Eduard Lyudvigovich Regel, was invited from Switzerland to organize the Imperial Botanical Gardens in St. Petersburg. It was not easy to change the well-tended and cared-for alpine valleys for the "wild" Baltic sea open to all winds. But luckily, the hereditary nobility promised to him in Russia took precedence over all other considerations, and Regel the eldest continued his work on the banks of the Neva river. The advantage of this Swiss investment in Russian science became even more obvious when his son Robert became the head of the Bureau of Applied Botany (the future world-renowned All-Union Institute of Plant Breeding) and became the supervisor of the diploma work of future great geneticist Nikolai Ivanovich Vavilov, and Regel's grandsons Anatolii and Vadim decided to become physicists.

Vadim Regel's life was, to a large extent, determined by the friendly relations of his youth. In times much harder than ours, Regel's mother, Elizaveta Andreevna, rented a room to a girl, who soon acquired an admirer that often visited her either via the drainpipe or the window. This could not passed unnoticed and the curiosity of little Vadim grew. From that time onward, the admirer and Vadim Regel became friends for life. The admirer was none other than Anatolii Petrovich Aleksandrov, the future President of the USSR Academy of Sciences. It was Aleksandrov who later invited Regel, who was then (1939) a postgraduate of the Polytechnic Institute, to participate in work on the demagnetization of ships. The method that they developed soon became very popular. In 1941, when the Baltic fleet was blockaded in the Finish bay by German minefields, this method helped to free the battleship *Marat* and the part of the Baltic fleet that had survived German bombing. The physicists worked onboard naval ships together with sailors and the quality of their work was verified by risking their lives. During the war with Germany, the German name Regel could hardly be a letter of safe conduct, and Aleksandrov did his best to protect Regel from the interest of the "competent government organs." Immediately after the war, Aleksandrov invited Regel to participate in a study associated with the use of thermal diffusion in the separation of uranium isotopes (which then was part of the Soviet project on the creation of atomic weapons). This work involved great risks. Then, no safety measures were known and they were only established in the process of the work, which was part of the development of the strategy of nuclear deterrence. This research concluded the heroic chapter of Regel's life.

In 1952, Vadim Regel started working at the Institute of Crystallography, where he studied the nature of the strengthening and plasticity of materials. He was the first to establish experimentally the role of the thermal motion of atoms in crystals and polymers during their plastic deformation and destruction.

Regel continued these studies at the Ioffe Physicotechnical Institute, where he was a vice director, and, in 1964, he defended his doctoral dissertation (in physics and mathematics) and became a professor. He also initiated the study of the physical characteristics of the deformation and fracture of composite materials. Under his guidance, a new technology for producing profile composites was developed. As one of the most prominent experts in this field, Regel also studied the durability of polymers and the physical mechanisms of their destruction.

Regel spent most of his scientific life in Leningrad and Moscow. By invitation of Academician B.K. Vainshtein, he returned to the Institute of Crystallography in

1063-7745/02/4703-0524$22.00 © 2002 MAIK "Nauka/Interperiodica"

1980 and became the head of the Laboratory of the Mechanical Properties of Crystals, where he continues to work as a leading scientist to this day. From the very beginning of this period, Regel supported all the scientific projects of the laboratory, in particular, the study of the role of point defects in the deformation of crystals under concentrated loads. These studies allowed us to establish that the mass transfer caused by the collective motion of point defects results in the formation of a nanocrystalline state. In radiation physics, Regel studied the effect of beams of accelerated ions on crystals, the effect of irradiation on the defect structure, the physical properties of alkali-halide crystals, and the behavior of various materials under the simultaneous action of mechanical loading and irradiation with an ion beam. His methodological studies include a modernization of the classical device for the active loading of crystals, the so-called Regel–Dubov relaxometer (in cooperation with the Design Bureau of the Institute of Crystallography).

In the following years, Regel concentrated on studying the evolution of the defect structure of crystals in the mechanical stress fields. In addition to the conventional objects of such studies, he also considered new substances that were very promising for use in optoelectronics and acousto-optics. Regel's investigations of the stability and durability of materials were aimed at establishing the physical mechanisms of plasticity and the fracture of solids. One of the questions most often asked by Regel is, "And what is the *mechanism* of this phenomenon?"

Regel has always been a model of self-discipline, responsibility, conscientiousness, and precision in his experimental work, his work with students, and in his scientific-organizational activity. He manages to do everything not only on time but *ahead of time*. He has supervised numerous candidate and doctoral dissertations and is highly esteemed in Moscow, St. Petersburg, and in all the ex-Soviet republics. Regel was recently head of the Scientific Council on the problems of strength and plasticity of materials and today he is a member of several scientific councils of the Russian Academy of Sciences, a member of the editorial board of the journal *Solid State Physics*, and an editor of the journal *Physical Abstracts*.

A man of enormous charisma, with an easy and cheerful disposition and exceptional goodwill, Professor Regel quite lives up to his family name (in German, Regel means a rule). His *correctness*, *nobleness*, and *accuracy* are evident in everything he does. If he decides to get acquainted with Moscow theater, he starts going to the theater every Saturday and continues for the whole season. If he becomes interested in the arts, he *systematically* visits all the museums and exhibitions. The order underlying his "grandfather's botany" and the systematic nature of his personality were inherited by Regel from his ancestors but are luckily balanced by his Epicurean attitude to life, i.e., the perception of all its manifestations with an unchanging sense of the joy, sense, and harmony of existence. His favorite toast at friendly gatherings is "Let us drink to life because, despite everything, life is beautiful!"

The editorial board of the journal *Kristallografiya* (Crystallography Reports) applauds this toast, all the more so because Professor Regel himself is an excellent illustration of its truth.

Translated by L. Man

Crystallography Reports, Vol. 47, No. 3, 2002, p. 526. Translated from Kristallografiya, Vol. 47, No. 3, 2002, p. 574.

INFORMATION

The 2002 Koptyug Prize Competition to Be Held by the Russian Academy of Sciences

The Russian Academy of Sciences announces the Koptyug Prize competition. This prize is awarded for outstanding studies in chemistry that contribute to the protection of the environment and the development of science.

Submissions will be accepted no later than March 9, 2002.

GENERAL RULES

For the purpose of encouraging outstanding scientific studies, discoveries, and inventions that are of great importance for science and practice, the Russian Academy of Sciences awards the Koptyug Prize.

The prize is awarded for the best separate scientific study, discovery, or invention, or the best series of studies on the same subject.

A study or a series of studies on the same subject are submitted, as a rule, on behalf of a separate author. Only the leading authors (no more than three persons) can be proposed as candidates.

The right to propose candidates is granted to the following:

(a) academicians and corresponding members of the Russian Academy of Sciences;

(b) scientific institutions and schools of higher learning;

(c) scientific societies and technical societies of engineers;

(d) scientific councils of the Russian Academy of Sciences or of other departments on the most important scientific problems;

(e) scientific and technical councils of state committees, ministries, and departments, technical councils of industrial enterprises, and designer's offices.

The organizations or the persons that propose candidates for the competition should present to the Russian Academy of Sciences (Leninskiĭ pr. 14, GSP, Moscow V-71, 117901 Russia) the following documents no later than March 9, 2002:

(a) a presentation justifying the nomination and detailing the scientific characteristics of the study and its significance for the development of science and the national economy;

(b) three copies of a published scientific paper (or a series of papers) or data on the scientific discovery or invention (for restricted studies, one copy of a typescript can be presented);

(c) information about the authors, including a list of their main scientific papers, discoveries, and inventions, affiliation and post, and home address.

The document should be addressed "To the Koptyug Prize Competition."

Studies that were earlier awarded State Prizes or named state prizes are not accepted by the Koptyug Prize competition.

The scientists who are awarded the prize are granted the right to note "Awarded the 2002 Koptyug Prize of the Russian Academy of Sciences" in the titles of the papers published.

The resolution of the Presidium of the Russian Academy of Sciences and the abstract of the study that was awarded the prize are published in *Vestnik Rossiĭskoĭ Akademii Nauk* (*Herald of the Russian Academy of Sciences*), the corresponding series of *Izvestiya Rossiĭskoĭ Akademii Nauk* (*Izvestiya of the Russian Academy of Sciences*), and the newspaper *Poisk* (*Search*). *Vestnik Rossiĭskoĭ Akademii Nauk* also prints the portraits of the scientists that are awarded the prize.

The published scientific papers discussed at the session of the Presidium of the Russian Academy of Sciences and for which the prize is awarded will be turned over to the Library of the Russian Academy of Sciences for preservation.

Certificates will be presented to the winners of the Koptyug Prize at a session of the Presidium of the Russian Academy of Sciences.

Further information is available via tel. 237-99-33, 237-99-65, and 952-25-86.

Translated by I. Polyakova

1063-7745/02/4703-0526$22.00 © 2002 MAIK "Nauka/Interperiodica"